'LASER APPLICATIONS TO ANALYTICAL ULTRACENTRIFUGATION'

A THESIS PRESENTED TO

MASSEY UNIVERSITY, PALMERSTON NORTH,

NEW ZEALAND

IN

PARTIAL FULFILMENT OF THE REQUIREMENTS

OF

DOCTOR OF PHILOSOPHY

BY

JAMES ANTHONY LEWIS

MAY, 1972.

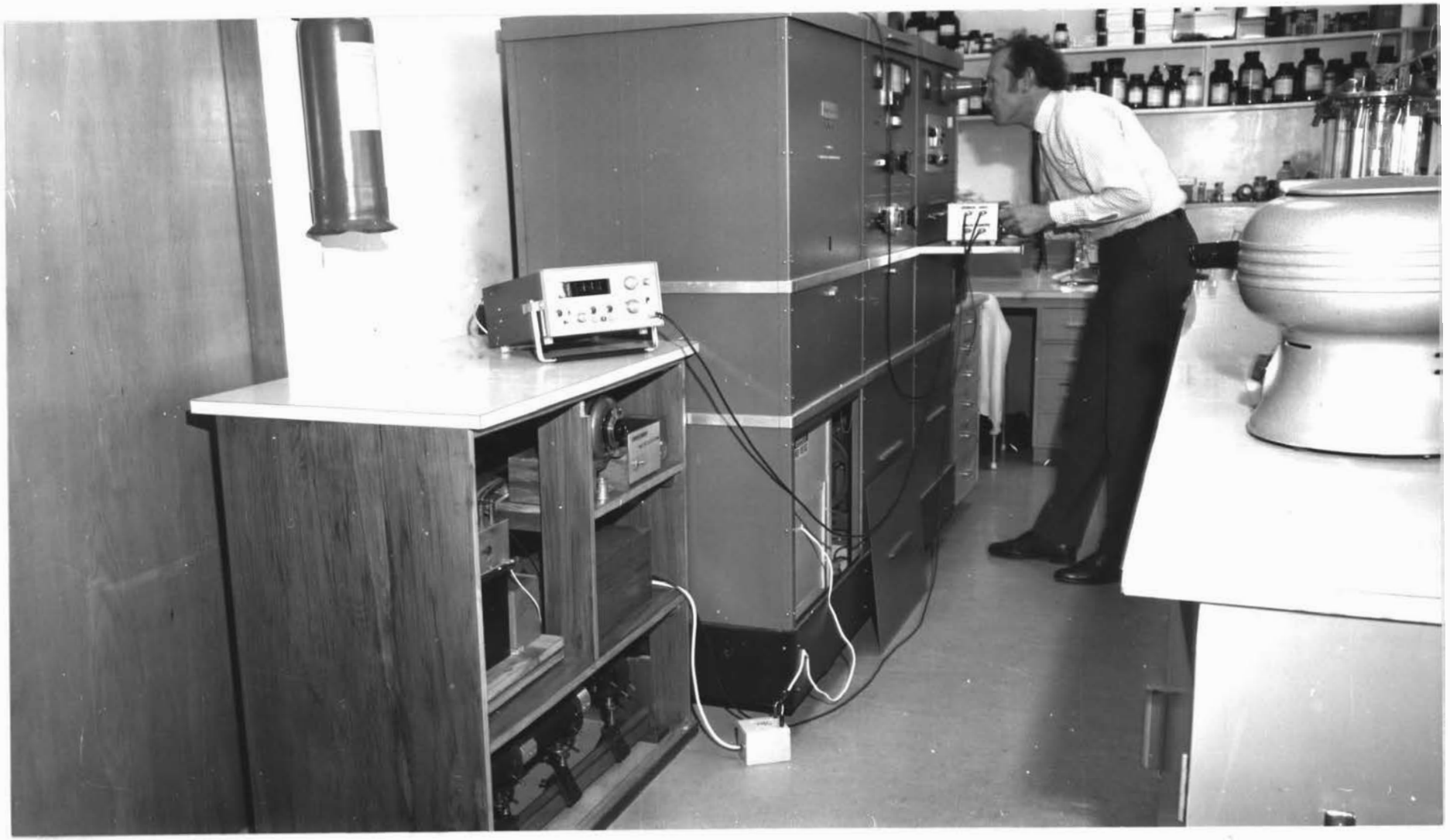

F R O N T I S P I E C E : A GENERAL VIEW OF THE ANALYTICAL ULTRACENTRIFUGE WITH THE LASER AND ITS ASSOCIATED MODULATION EQUIPMENT.

ACKNOWLEDGEMENTS

I should like to express my sincere thanks to Doctor John W. Lyttleton of the Applied Biochemistry Division, Department of Scientific and Industrial Research, Palmerston North, for his friendship and guidance during these past four years. I am particularly grateful for the many hours he has spent with me in adapting the analytical ultracentrifuge for use with the laser system when he was always available with both practical assistance and constructive advice.

I am greatly indebted to Professor Norman F. Barber, of the Physics Department, Victoria University of Wellington, Wellington, New Zealand who was my major theoretical advisor. His interest and enthusiasm could not fail to stimulate constructive ideas and my discussions with him have been most rewarding.

In addition, I would like to thank Professor Geoffrey N. Malcolm, Professor of Physical Chemistry, Massey University who has co-ordinated this research for the Department of Graduate Studies. His interest and friendship during the course of this research project has been of great assistance, and I am indebted particularly for his aid and support in obtaining funds for the project.

Finally, I would like to thank all persons both at Massey and D.S.I.R., whom it has been my privilege to know and who have contributed their advice and assistance at various times.

The assistance of grants (URC 68/337 and URC 70/314) from the University Grants Committee of New Zealand is acknowledged.

TABLE OF CONTENTS

LIST OF ILLUSTRATIONS

PREFACE.

PREFACE

The work of Svedberg[1] and his collaborators in the early 1920's heralded the use of centrifugal fields for the study of macromolecular systems. Following this work the developments in both theoretical and experimental aspects have been dramatic, so much so that the majority of current researchers take the use of the analytical ultracentrifuge for granted as a basic tool for the determination of molecular weights of macromolecules. The latter is justified in view of the theoretical and experimental evidence to date, and reviews citing original references and covering the state of the art from its inception to the present day are available.[2-8]

Physically, the problem associated with a study involving the analytical ultracentrifuge is to obtain measurements that will enable a specific solution of the Lamm[9] equation to be obtained. For an ideal two-component system in which the partial specific volumes $\bar{v}_o$ (solvent) and $\bar{v}_1$ (solute) are constant the Lamm equation may be written[5]

$$\frac{\partial c_1}{\partial t} = \frac{1}{x} \frac{\partial}{\partial x} \left[xD\left(\frac{\partial c_1}{\partial x}\right) - s\omega^2 x^2 c_1 \right] \qquad \text{(P1)}$$

where c_1 represents the concentration of solute (component 1) with respect to solvent (component o), at a radial position x in a centrifuge cell. D and s represent the diffusion and sedimentation coefficients respectively for component 1, and ω is the angular frequency of the rotor. Lamm's[9] original derivation of this second order partial differential equation was non-rigorous, but the work of Goldberg[10] using the concepts of irreversible thermodynamics has established clearly the conditions under which the equation applies. Similar equations exist for more complex molecular systems, but exact analytical solutions are difficult since the coefficients D and s are not constant but functions of the variables. Thus workers with the ultracentrifuge are confronted with the all too familiar problem in science of attempting the solution of partial differential equations with non-constant coefficients. Naturally, attempts have been made to derive analytical solutions to the Lamm equations

under specified conditions, and the monograph by Fujita[5] contains a useful summary of work in this area.

Of particular interest both theoretically and in the context of this present study is the concentration distribution in a centrifuge cell at sedimentation-diffusion equilibrium. This is a thermodynamic equilibrium state and is defined as the state in which the total potential of any component in a solution being centrifuged is constant, and where the temperature is uniform throughout the centrifuge cell. Experimentally, this state is achieved under isothermal conditions when the concentration distribution no longer changes with time within the accuracy of the experiment. Obviously, this allows the time dependent terms in the solution of the relevant equations to be equated to zero. The latter condition greatly simplifies the analysis and the solutions then obtained are the most rigorous theoretically.

It is shown by Creeth and Pain[6] and elsewhere[3-5] that the ideal two component system considered in equation (P1) is distributed at sedimentation equilibrium according to the expression

$$M(1-\bar{v}\rho)\omega^2 x = \frac{\partial \mu}{\partial c_1}\left(\frac{\partial c_1}{\partial x}\right) \qquad (P2)$$

where M is the molecular weight of the solute (component 1) and μ and $\bar{v}$ the chemical potential and partial specific volume respectively of the solute at concentration c_1 (measured on a scale mass/ unit volume). The standard relationships between μ and c lead to the fundamental expression that is used in all experiments at sedimentation equilibrium

$$\text{i.e.} \qquad \frac{1}{xc_1}\frac{dc_1}{dx} = \frac{M(1-\bar{v}\rho)\omega^2}{RT(1+d\ell ny/d\ell nc_1)} = \frac{Mapp(1-\bar{v}\rho)\omega^2}{RT} \qquad (P3)$$

Here R is the universal gas constant, T is the absolute temperature, y is the activity coefficient on the c scale, and M_{app} is the apparent molecular weight of the solute. The latter may be related to the true molecular weight by use of the thermodynamic non-ideality

$$\ell n\, \gamma = BMc + \ldots\ldots\ldots \qquad (P4)$$

in which B is an empirical coefficient and where higher terms in the series can frequently be neglected. Using equations (P3) and (P4) we note that

$$M_{app} = \frac{M}{1 + BMc} \qquad (P5)$$

The importance of equations (P3) and (P5) is that the molecular weight is determinable from measurements of c(x) at equilibrium.

The ultracentrifuge operator has the choice of three separate optical techniques in the modern instrument for the evaluation of the concentration distribution in the centrifuge cell. Firstly, there is the Schlieren system that relies on the refractometric properties of the solution and gives a record of refractive index gradient versus radial position for a cell. Here it is assumed that the incremental solution refractive index is proportional to the solute concentration. Secondly, there is the Rayleigh interference system which again relies on the refractometric properties of the solution but gives a photographic record of difference in refractive index between the solution and solvent (solute concentration) versus the radial position in the cell. The interference and Schlieren systems commonly share the same optical components in the ultracentrifuge. Finally, there is the ultraviolet absorption system that utilises the specific absorption of radiation at 254 nm by macromolecules such as nucleic acids and proteins as the sensing phenomena for determining the solute concentration.

The comparative merits of the three systems have been evaluated by Schachman[4,11,23] but the interference system is the primary concern of the present study. It has been demonstrated adequately[12] that the interference system is capable of giving simple and accurate data that is suited particularly for sedimentation diffusion equilibrium work. To a physicist this is not surprising, since interferometry has provided the means of making some of the most precise measurements available to man. However, with the advent of the first operational gas laser

by Javan et al[13] in 1961, the whole field of interferometry has undergone a revolution. This thesis is the culmination of a study initiated by the author in late 1967 into the possible applications of a gas laser to interference studies in the analytical ultracentrifuge.

Dr. J. F. Lyttleton of the Applied Biochemistry Division, D.S.I.R., Palmerston North, was kind enough to allow the use of his Beckman Model 'E' analytical ultracentrifuge to be used for this work, and also agreed to act as one of the supervisors for the author when the work was deemed appropriate as a staff Ph.D. project by Massey University. Obviously, the ultracentrifuge was in routine laboratory use, and any modifications to the instrument had to be compatible with this usage.

In chapter 1, a theoretical study of the Rayleigh interference optics in the analytical ultracentrifuge is undertaken. Extensive use is made of the Fourier theory of optics, and the basis upon which the refractometric measurements are made in the instrument is firmly established.

A discussion of coherence theory is included in chapter 2. The theoretical findings are applied to the conventional mercury source and a helium-neon gas laser employed in the work, allowing a definitive comparison between the two light sources to be made.

Chapter 3 includes a description of the actual instrumentation that was designed and constructed by the author, for use in the ultracentrifuge. A discussion of the optical alignment procedure is given and experimental results obtained both with the modulated laser and mercury sources are compared and discussed.

The design and construction of a new type of interference cell is the concern of chapter 4, together with the theory upon which the measurements using this cell are based. Ancilliary equipment necessary for the use of the new cell in the ultracentrifuge is described, together with a critical analysis of the results so far obtained.

Chapter 5 is a detailed theoretical analysis of the effects of the refractive index gradients on the

experimental data derived from the interference system in the analytical ultracentrifuge. The study indicates that the effects are small for the assumptions made, but the analysis does provide correction procedures based on the raw experimental data that can be applied in practice.

Finally, in chapter 6 the effects of cell distortion in the centrifugal field are evaluated mathematically. Its importance in the context of this thesis is that sedimentation equilibrium studies frequently require a precise knowledge of the radial positions of the meniscus and base of the solution column. The theoretical and experimental work shows that the laser gives sharper definition of the menisci than does the mercury source, and this increased precision gained by the laser could well be lost if the menisci positions vary owing to extraneous unknown factors. The work in this chapter has been published[14] by the author in conjunction with Professor N.F. Barber who is acting as a second supervisor for this project. A reprint of the publication is included in an appendix to this work.

CHAPTER 1

THE RAYLEIGH INTERFERENCE OPTICAL SYSTEM IN THE ANALYTICAL ULTRACENTRIFUGE

1. HISTORICAL INTRODUCTION

The Rayleigh Interferometer was invented by Lord Rayleigh[15] in the late nineteenth century for the study of the refractivities of argon and helium, and owing to his ingenuity he was able to show by his experiments that argon was not an allotropic form of nitrogen as had been supposed erroneously at that time. A diagram of the basic interferometer is shown in figure 1-1, and it should be noted that the astigmatic cylindrical lens used for the telescope was introduced into the original instrument by Lord Rayleigh to improve the quality of the fringe system. This latter lens gives differential magnification of the horizontal and vertical coordinates, and forms an integral part of the Schlieren/Interference optical system in modern analytical ultracentrifuges. Philpot and Cook[16] in England were the first to adapt the Rayleigh Interferometer for use directly in the ultracentrifuge, and carried out pioneer sedimentation measurements with their interference optics.

Concurrently with Philpot and Cook, Svenssen[17,18] had introduced the same optical system for electrophoretic and diffusion studies and these systems are essentially the same as exist in current analytical ultracentrifuges. A diagram of the system used in the Beckman Model 'E' ultracentrifuge is depicted in figure 1-2.

Johnson and Kraus[19] were the first to appreciate that the precision and accuracy of the interference optics were superior to those of the older Schlieren optics, and with Scatchard[20] showed how a baseline could be obtained by running water - water centrifugations in the same cell - a routine procedure in modern high precision work. Richards and Schachman[21] made an initial critical study of the Rayleigh optics in the analytical ultracentrifuge using a standard sucrose solution and this was followed by a detailed experimental study of the overall system by LaBar[12] who extolled its advantages over the older Schlieren system, that had been the subject of a study undertaken sometime previously by Van Holde and Baldwin[22].

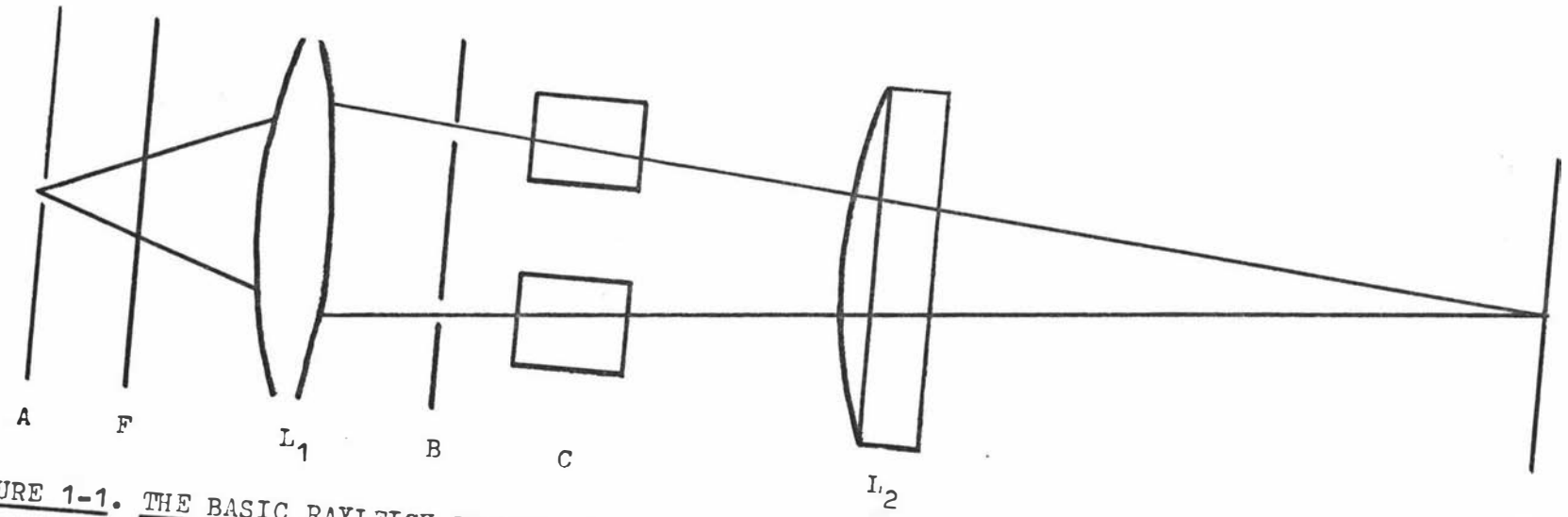

FIGURE 1-1. THE BASIC RAYLEIGH INTERFEROMETER.

A. SOURCE SLIT, F. FILTER, L_1. COLLIMATING LENS, B. RAYLEIGH APERTURE MASK, C. CELLS, L_2. CYLINDER LENS, I. IMAGE PLANE.

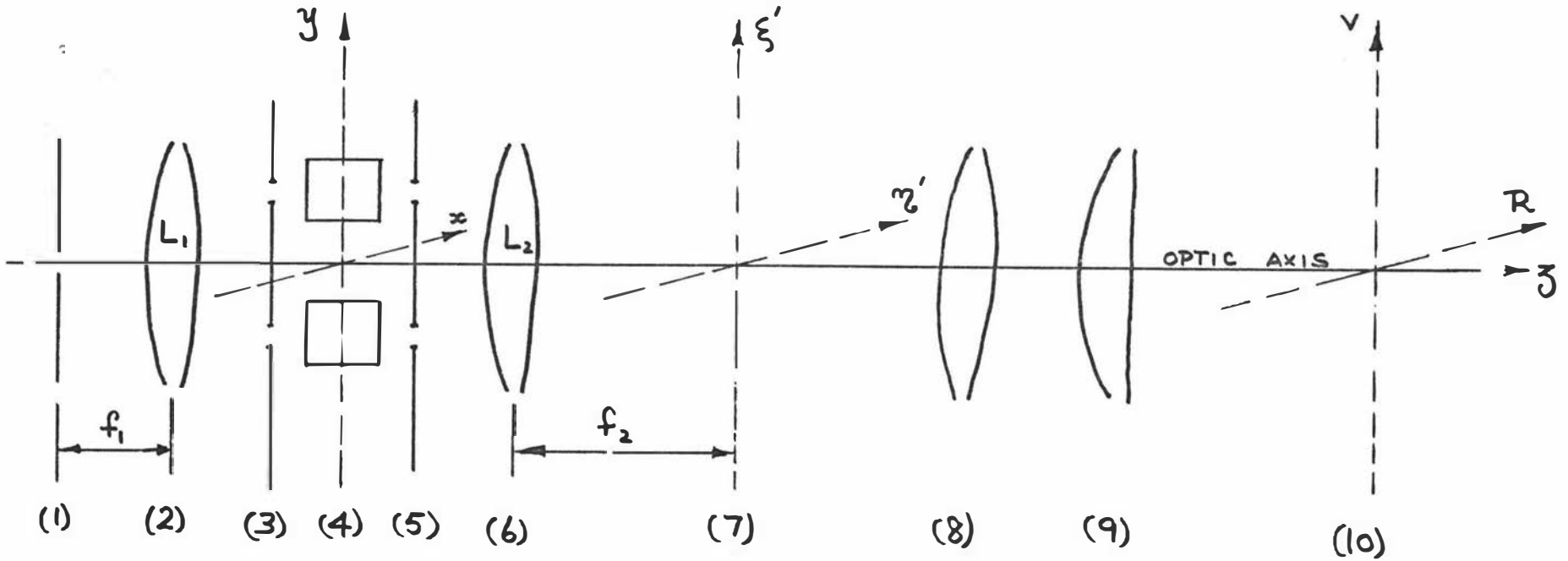

FIGURE 1-2. THE INTERFERENCE OPTICAL SYSTEM IN THE ANALYTICAL ULTRACENTRIFUGE.

(1) SOURCE (2) LOWER COLLIMATING LENS L_1 (3)CELL DIAPHRAGM IN LOWER WINDOW HOLDER (4)CENTRIFUGE CELL CENTRE (5) APERTURE MASK (6) UPPER COLLIMATING LENS L_2 (7) FOCAL PLANE OF LENS L_2 (8) CAMERA LENS (9) CYLINDER LENS (10) PHOTOGRAPHIC PLATE.

In particular LaBar[12] showed how the interference system gave simpler and more accurate measurements that were suitable particularly for sedimentation equilibrium studies which are very important theoretically. Furthermore, Schachman[23] has made a critical appraisal of the various optical systems in use currently in analytical ultracentrifugation, and the reviews of Williams et al[3], Fujita[5], and Creeth and Pain[6] have established theoretically the validity of observing sedimentation using interference techniques.

2. THEORETICAL ANALYSIS OF BASIC RAYLEIGH INTERFEROMETER

Consider initially the source and collimating lenses L_1 and L_2, shown in figure 1-3.

The diagram defines the relevant coordinate axes in both the pupil (wavefront) and image planes. It is shown by Born and Wolf[24] that a Fourier-transform relation holds between the complex amplitude distribution of the electric field vector in the pupil or wavefront domain (xy) and the complex amplitude distribution at a point $P(\eta', \xi')$ in the focal plane of lens L_2

$$\text{i.e.} \quad E_p'(k\alpha, k\beta) = \iint_{\text{pupil}} f(xy) \exp\left[\frac{2\pi i}{\lambda}(\beta x + \alpha y)\right] dx\, dy \qquad (1\text{-}1)$$

where $\alpha = \frac{\xi'}{f_2}$; $\beta = \frac{\eta'}{f_2}$ and $k = \frac{2\pi}{\lambda}$ with λ being the wavelength of the radiation used. Using the notation of Stroke[25] it is useful to define reduced coordinates such that

$$u' = k\beta \quad \text{and} \quad v' = k\alpha$$

and equation (1-1) becomes

$$\bar{E}(u'v') = \iint_{\text{pupil}} f(xy) \exp\left[i(u'x + v'y)\right] dx\, dy = \mathcal{F}\{f(xy)\} \qquad (1\text{-}2)$$

where $\mathcal{F}$ stands for 'Fourier transform of'.

As seen from figure 1-3 an image of the source appears in the focal plane of lens L_2. The physical significance of the relationship in equation (1-2) is that the image of a point source located in this plane is

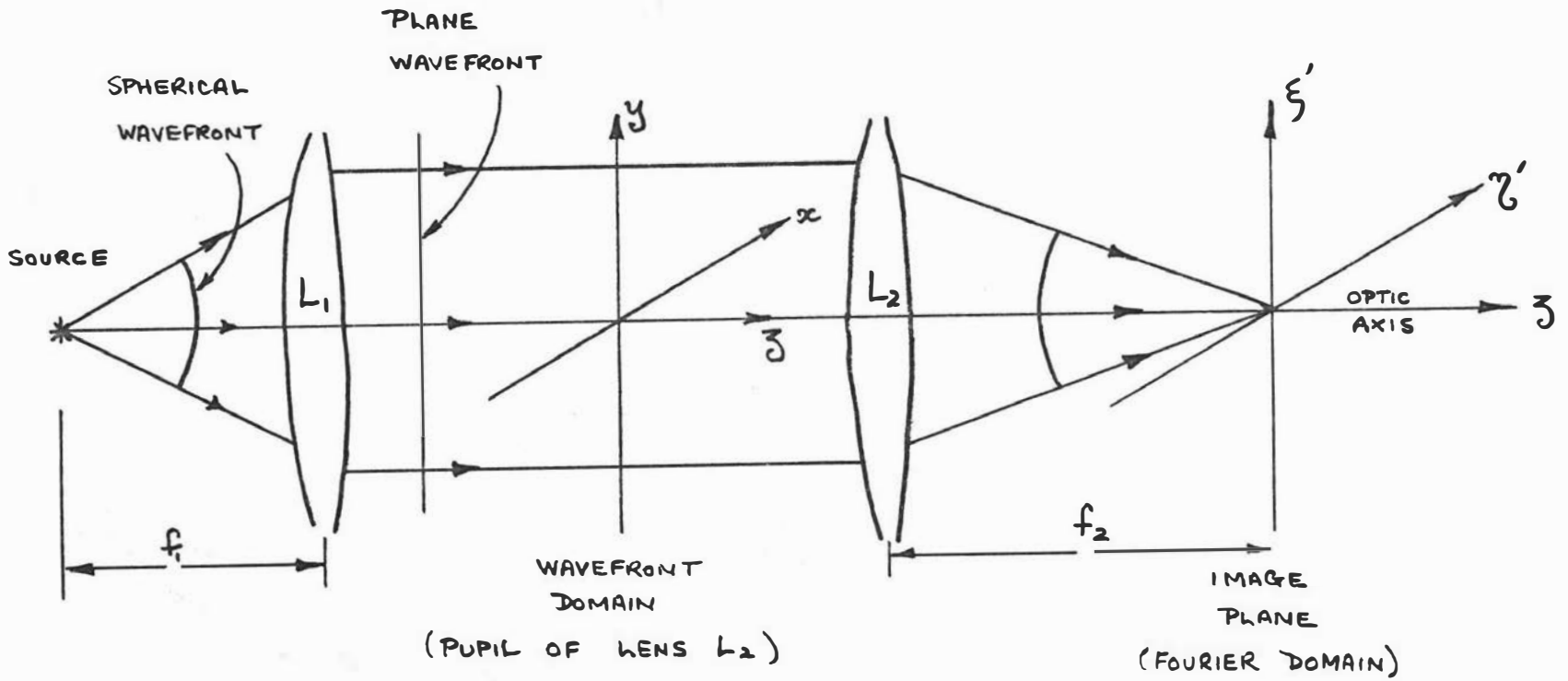

FIGURE 1-3. THE BASIC COLLIMATING SYSTEM DEFINING THE COORDINATE AXES.

not a point source as indicated by the theory of geometrical optics, but owing to the electromagnetic nature of light and the finite dimensions of the pupil, the light from a point or line source is spread out into a diffraction pattern.

A physical receptor (e.g. eye or photographic plate) is sensitive to the electric field and detects intensity (Ip') at best where

$$Ip' = \bar{E}\,\bar{E}^* = |E|^2 \tag{1-3}$$

Here $\bar{E}^*$ is the complex conjugate of $\bar{E}$.

In general light from more than one source point may reach any point in the image and if $\bar{E}_1$ and $\bar{E}_2$ are two light amplitude vectors reaching the point p' from two different source points then for a non-coherent source if used in the current Schlieren/ Interference system (e.g. white light).

$$I_{p'} = \bar{E}_1^{\,2} + \bar{E}_2^{\,2} = I_1 + I_2 \tag{1-4}$$

whereas for a coherent source (e.g. laser),

$$I_{p'} = (\overline{E_1 + E_2})\ (\overline{E_1 + E_2})^* = \overline{E_1 + E_2}^{\,2} \tag{1-5}$$

Considering the current system initially (i.e. non-coherent source) the intensity distribution at p' follows from above to be given by

$$I_{p'} = s(u',v') = \mathcal{F}\{f(xy)\}\ \mathcal{F}^*\{f(xy)\} \tag{1-6}$$

where s(u',v') is known as the spread function and is (as we shall see) the image of a point source located at infinity.

When the light intensity at an image point (u'_o, v'_o) in the presence of spreading is computed it is convenient as shown by Stroke[25] to define the image formed by geometrical optics or perfect lens system O(u',v') in conjunction with the spread function s(u',v'). Whence it is shown[25] that

$$I(u'_o,v'_o) = \iint_{-\infty}^{+\infty} O(u',v')\,s(u'_o-u',v'_o-v')\,du'dv' \qquad (1\text{-}7)$$

and equation (1-7) is recognised as a convolution integral which is conveniently written as

$$I(u'_o v'_o) = O(u',v') \circledast s(u'v') \qquad (1\text{-}7a)$$

It is useful frequently in optics to analyse image formation in terms of 'spatial Fourier space', or by analogy with electronics the 'spatial frequency domain'. This is achieved by taking the Fourier transforms of equations applicable to the image domain (η' ξ') since this Fourier transform operation will transfer the above equations to the pupil or wavefront domain with coordinates (xy). This is particularly relevant for equation (1-7a) since

$$\mathcal{F}\{I(u'_o,v'_o)\} = \mathcal{F}\{O(u'v') \circledast s(u'v')\} = \mathcal{F}\{O(u'v')\}\,\mathcal{F}\{s(u',v')\} \qquad (1\text{-}8)$$

where use has been made of the first form of the convolution theorem[26]. Thus the Fourier transform of the image intensity distribution is given by the product of the Fourier Transforms of the object intensity distribution with that of the spread function. For the noncoherent point or line source employed in the current interference/Schlieren work we can consider the geometric image O(u') to be adequately represented by the Dirac delta function $\delta(u')$, where

$$\delta(u') = \lim_{\delta \to 0} \int_{-\delta/2}^{+\delta/2} \frac{1}{\delta}\, du' \qquad (1\text{-}9)$$

and using this one dimensional form in equation (1-7a) we get

$$I(u'_o) = \delta(u'_o) \circledast s(u') = s(u'_o) \qquad (1\text{-}10)$$

i.e. the spread function is the image of a point source, as anticipated.

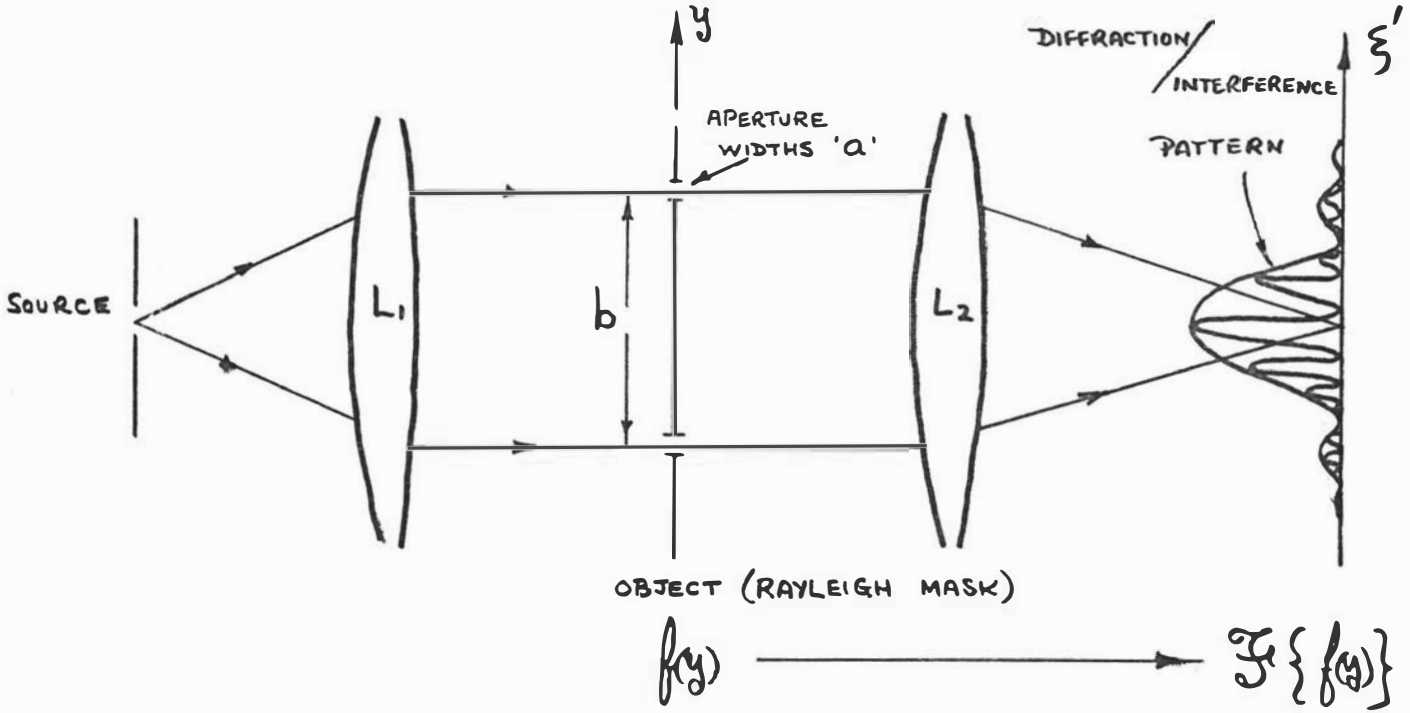

FIGURE 1-4. BASIC SYSTEM WITH RAYLEIGH MASK.

The fact that this image of the source slit is located in the focal plane of the lens L_2 when the Raylwigh system is being used was pointed out by Philpot and Cook[16] and is important as we shall later see since the fringe pattern is also located in this plane, and for this reason the fringes observed in the Rayleigh interferometer are known as source fringes.

If now the Rayleigh mask is inserted into the pupil as shown in figure 1-4 then the intensity pattern observed in the focal plane of lens L_2 will be modified. For Rayleigh interference work it is essential that the effective source should have sufficient spatial and temporal coherence and as we shall see later the latter requirement necessitates the use of monochromatic radiation as stressed by Philpot and Cook[16]. Again we shall also see later that the spatial coherence is achieved by having a point or line source at the focal point of the lens L_1, and for analysis it is useful to conceive that the coherent source is now the aperture of lens L_1. Thus as can be seen from figures (1-3) and (1-4) the aperture of the lower Schlieren lens L_1 acts effectively as a source of spatially and temporally coherent plane wavefronts. Now if an object is placed in the pupil (xy) of the lens L_2 then a Fraunhofer diffraction pattern of that object will be observed in the focal plane of the lens L_2. It is shown by Born and Wolf[24] that the Fraunhofer diffraction pattern of an object $f(y)$ is given by the Fourier transform $\mathcal{F}\{f(y)\}$ of that object.

i.e. $$\mathcal{F}\{f(y)\} = \int_{-\infty}^{+\infty} f(y) \exp^{iuy} dy \qquad (1\text{-}9)$$

where $u = k \sin\alpha \approx k\alpha$ for small angles (see equations (1-1) and (1-2). Now the Rayleigh aperture mask in one dimensional form is depicted in figure 1-4 and is obviously an intensity object. The apertures of width 'a' may be represented by $\Pi(y)$ as defined in figure 1-5(a), whereas the Rayleigh aperture mask can be represented as the convolution of the aperture function $\Pi(y)$ with a pair of δ-functions ($\emptyset_2$) with a symmetrical separation 'b' - assuming the

Rayleigh mask to be symmetrical. The pair of δ -functions are shown schematically in figure 1-5(b).

$$\therefore \quad f(y) = \Pi(y) \circledast \phi_2(y) \tag{1-10}$$

where $\phi_2(y) = \delta(y-y_2)$ and from figure 1-5(b) $y_2 = \pm b/2$. Hence the complex amplitude of the electric field vector ($\bar{E}$) in the focal plane of lens L_2 is given by

$$\mathcal{F}\{f(y)\} = \mathcal{F}\{\Pi(y) \circledast \phi_2(y)\} = \mathcal{F}\{\Pi(y)\}\,\mathcal{F}\{\phi_2(y)\} \tag{1-11}$$

where again use has been made of the convolution integral[26] . Using equation (1-9) it may be shown that

$$\mathcal{F}\{\Pi(y)\} = \int_{-\infty}^{+\infty} \Pi(y) \exp^{iuy} dy = \frac{a \sin\left(\frac{ua}{2}\right)}{\left(\frac{ua}{2}\right)} \tag{1-12}$$

where (1-12) represents the Fraunhofer diffraction function for a single slit aperture.

Now $$\mathcal{F}\{\phi_2(y)\} = \exp\frac{iub}{2} + \exp\frac{-iub}{2} = 2\cos\left(\frac{ub}{2}\right) \tag{1-13}$$

and this represents the interference function.

Substituting equations (1-12) and (1-13) into equation (1-11) we obtain the complex amplitude of the electric field vector in the focal plane of lens L_2 ,

i.e. $$\bar{E} = \frac{2a \sin\left(\frac{ua}{2}\right)}{\left(\frac{ua}{2}\right)} \cos\left(\frac{ub}{2}\right) \tag{1-14}$$

As usual the detected intensity I_2 is given by equation (1-3)

i.e. $$I_2 = \frac{4a^2 \sin^2\left(\frac{ka \sin\alpha}{2}\right)}{\left(\frac{ka \sin\alpha}{2}\right)^2} \cos^2\left(\frac{k b \sin\alpha}{2}\right) \tag{1-15}$$

in practice α is small and hence $\sin\alpha = \alpha$ and equation (1-15) becomes

$$I_2 = \frac{4a^2 \sin^2\left(\frac{ka\alpha}{2}\right)}{\left(\frac{ka\alpha}{2}\right)^2} \cos^2\left(\frac{k b\alpha}{2}\right) \tag{1-16}$$

Now $b \gg a$ and hence the interference ($\cos^2$) term varies more rapidly than the diffraction term and the

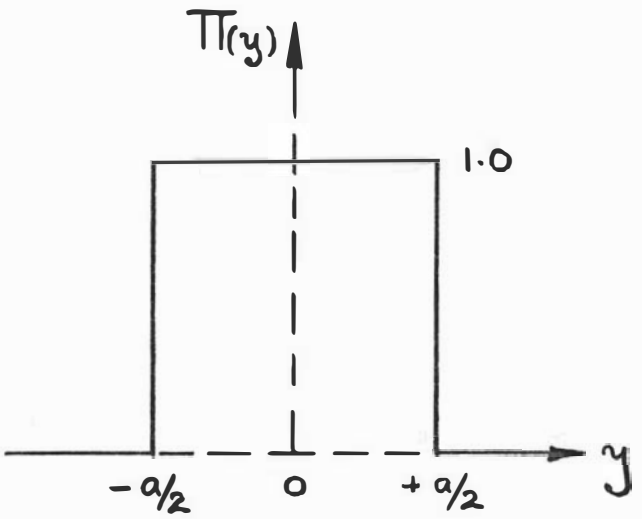

(a) RAYLEIGH APERTURE $\Pi(y)$.

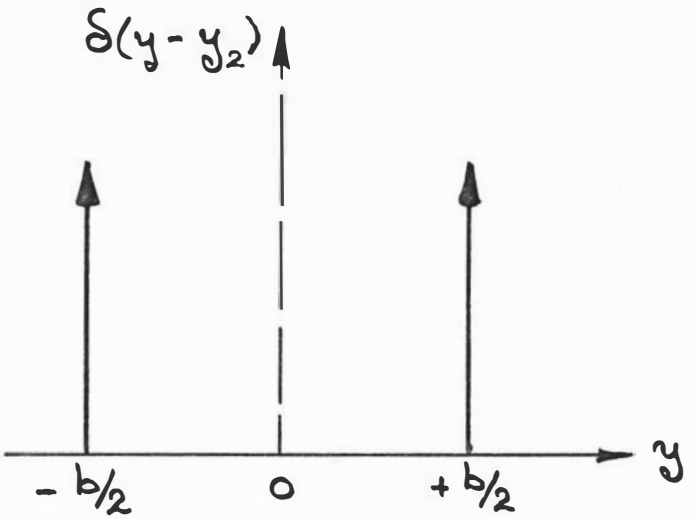

(b) PAIR OF DIRAC δ - FUNCTIONS.

RAYLEIGH APERTURE MASK $f(y) = \Pi(y) \otimes \delta(y - y_2)$.

FIGURE 1-5. MATHEMATICAL REPRESENTATION OF THE RAYLEIGH APERTURE MASK.

observed intensity pattern approximates that of figure 1-6 where we note that physically the interference fringes are intensity modulated by the single slit diffraction pattern. If finer slits are employed as proposed by Schachman[11] one gets more fringes within the central maximum of the diffraction envelope, but naturally owing to the reduced aperture the overall intensity which is proportional to a^2, according to equations (1-15) and (1-16), is reduced.

An analysis using an asymmetrical mask as proposed by Richards and Schachman[21] is of interest and is accomplished readily since the object $f(y)$ can still be represented as a convolution of a symmetrical aperture $\Pi(y)$ and two delta (δ) functions.

$$\text{i.e.} \qquad f(y) = \Pi(y) \circledast \delta(y) + \Pi(y) \circledast \delta(y-b) \qquad (1\text{-}17)$$

and since convolution is distributive over addition equation (1-17) becomes

$$f(y) = \Pi(y) \circledast \left[\delta(y) + \delta(y-b)\right] \qquad (1\text{-}17a)$$

whence

$$\mathcal{F}\{f(y)\} = \frac{a \sin\left(\frac{ua}{2}\right)}{\left(\frac{ua}{2}\right)} \left[1 + \exp^{iub}\right] \qquad (1\text{-}18)$$

and the observed intensity pattern is similar to that given by equation (1-16)

$$\text{i.e.} \qquad I = 4a^2 \operatorname{sinc}^2\left(\frac{ua}{2}\right) \cos^2\left(\frac{ub}{2}\right) \qquad (1\text{-}19)$$

$$\text{where } \operatorname{sinc} A = \frac{\sin A}{A} \qquad (1\text{-}20)$$

Naturally, this was to be expected since offset and symmetrical masks are used routinely in the laboratory, and similar patterns are observed.

If now we consider our aperture mask to be the optically active element as proposed by Schachman and introduce a filled two compartment cell into the pupil of the lens L_2, it will have the effect of producing a phase advance (θ) in the radiation emanating from one of the

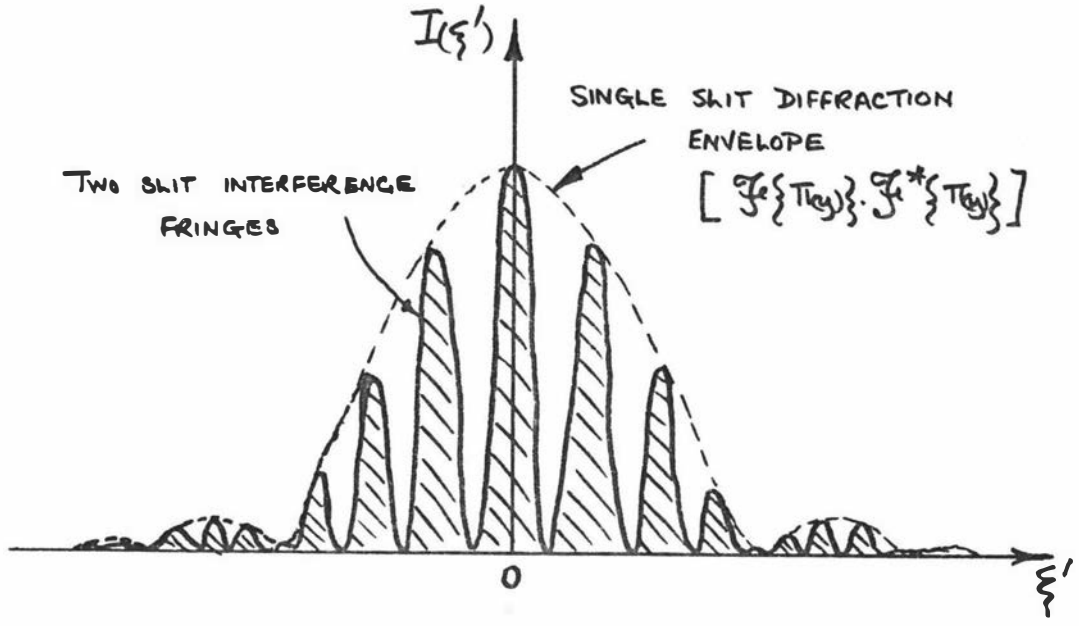

FIGURE 1-6. THE INTENSITY PATTERN OBSERVED IN THE FOCAL PLANE OF LENS L_2 OWING TO THE RAYLEIGH MASK.

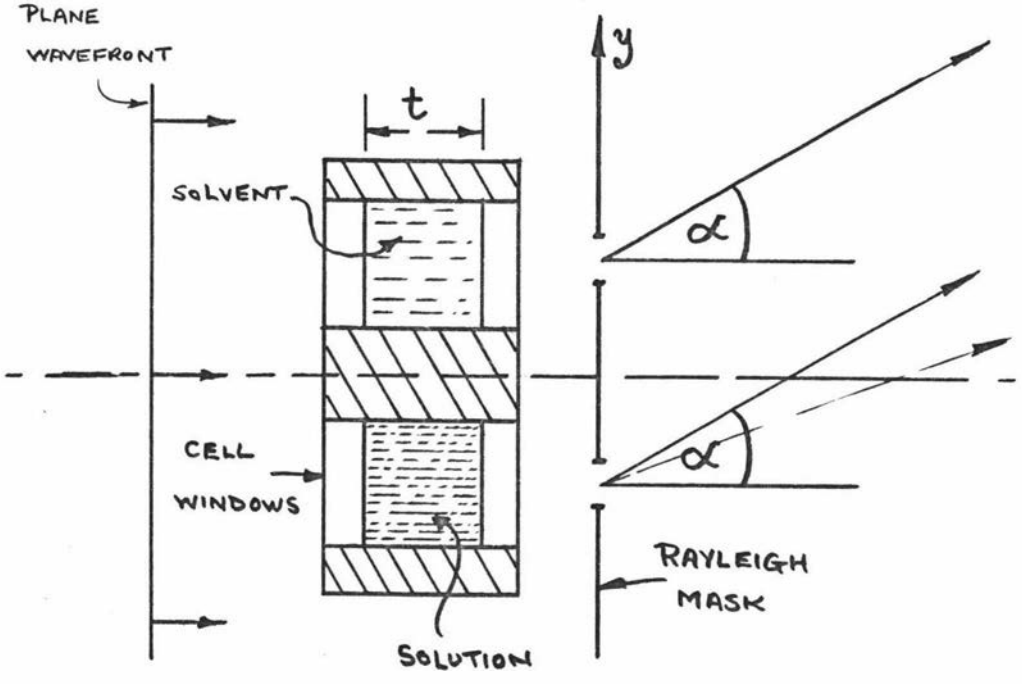

FIGURE 1-7. SCHEMATIC DIAGRAM OF THE CELLS AND APERTURE MASK.

apertures relative to that from the other.

i.e., $$\Theta = \frac{2\pi}{\lambda} t n \qquad (1\text{-}21)$$

Here t = cell thickness, n is the refractive index difference between the solution in one sector and solvent in the other, and λ is the wavelength of the radiation. In practice n is a function of the solute concentration (c), with the functional relationship being normally linear, and hence Θ carries the relevant information.

A descriptive diagram of a cell and aperture is shown in figure 1-7. Now the path difference (Δy) for waves scattered at an angle α from the solution aperture for points distance y apart is

$$\Delta y = y \sin\alpha - t n \qquad (1\text{-}22)$$

and if each point has a scattering amplitude $f(y)$ then the wave diffracted at angle α is given by

$$\psi = \int_{-\infty}^{+\infty} f(y) \exp^{ik\Delta y} dy = \int_{-\infty}^{+\infty} f(y) \exp^{ik(y\sin\alpha - tn)} dy$$

i.e., $$\psi = e^{-i\theta} \int_{-\infty}^{+\infty} f(y) \exp^{iuy} dy = e^{-i\theta} \mathcal{F}\{f(y)\} \qquad (1\text{-}23)$$

The cell and solutions above are assumed to constitute a pure phase pbject and as such have an amplitude transmission factor (S) of 1.0. Naturally, the cell and Rayleigh aperture mask together constitute a simple amplitude and phase object in the pupil of lens L_2.

Consider now the offset mask as proposed by Richards and Schachman[21] in conjunction with the filled cell. The complex amplitude distribution of the electric field vector in the focal plane of the lens L_2 may be written down directly from equations (1-17 and (1-23).

i.e., $$\bar{E} = \mathcal{F}\{\Pi(y)\} \cdot e^{-i\theta} \mathcal{F}\{\delta(y)\} + \mathcal{F}\{\Pi(y)\} \cdot \mathcal{F}\{\delta(y-b)\}$$

$$= a \operatorname{sinc} \frac{ua}{2} \left[e^{i\theta} + e^{iub} \right] \qquad (1\text{-}24)$$

whence by trigonometric manipulation (1-24) becomes

$$\bar{E} = 2a \operatorname{sinc}\left(\frac{ua}{2}\right)\left[\cos\left(\frac{ub+\theta}{2}\right)\cos\left(\frac{ub-\theta}{2}\right) + i\cos\left(\frac{ub+\theta}{2}\right)\sin\left(\frac{ub-\theta}{2}\right)\right] \tag{1-25}$$

The observed intensity will be $|\bar{E}|^2$ hence

$$I = \bar{E}\ \bar{E}^* = 4a^2 \operatorname{sinc}^2\left(\frac{ua}{2}\right)\cos^2\left(\frac{ub-\theta}{2}\right) \tag{1-26}$$

and by substitution of values for known terms above we obtain

$$I = 4a^2 \operatorname{sinc}^2\left(\frac{ua}{2}\right)\left[\cos^2\frac{\pi}{\lambda}(b\sin\alpha - tn)\right] \tag{1-27}$$

Equation (1-27) depicts explicitly the behaviour of the Rayleigh interferometer and shows that the information desired lies in the $\cos^2$ interference term. In practice the apertures, source intensity and coherence are chosen so as to render the interference fringes visible from which the phase delay introduced within the interferometer may be evaluated.

It is of interest to use equation (1-27) to determine the location of the achromatic white/light fringe since this only occurs when phase difference between the two beams producing interference in the interferometer is zero - providing of course that dispersion is not too severe. Without the cell in position we see from equation (1-19) that the achromatic fringe occurs when $\alpha = 0$. However, with the cell in position we see from equation (1-27) that the achromatic fringe will occur when

$$\sin\alpha = \alpha = \frac{tn}{b} \tag{1-28}$$

Now $\alpha = \frac{\xi'}{f_2}$, and so the introduction of the filled cell into the interferometer has given rise to a fringe displacement in the focal plane of the lens L_2.

i.e. $$\xi' = \frac{f_2 t}{b} n \tag{1-29}$$

The above is a basic theoretical analysis of the Rayleigh interference system in the analytical ultracentrifuge. In practice b and f_2 are fixed whereas the choice of cell dimensions t may be chosen from a

given range (e.g. 3.0 cm, 1.2 cm, etc.) to suit the concentration of solution under investigation. When the cell is placed in a rotor and subjected to a centrifugal gravitational field the solute sediments in the radial direction (x) giving rise to a concentration gradient, and the refractive increment (n) becomes a function of the radial coordinate 'x' of the rotor i.e. $n(x)$.

Hence the fundamental problem in a given sedimentation study is to evaluate $n(x)$, and we note from the above that the parameter ξ' which determines the dependent variable (n) is located at a different position along the optic axis (z) of the optical system from that of the independent variable (x) - these being the focal plane of lens L_2 and the mid-plane of the cell respectively. Fortuitously, ξ' and x are spatially orthogonal and as such may be considered to exist in two independent channels which by means of the astigmatic cylinder lens shown in figure 1-2 are recorded independently and simultaneously in the two orthogonal directions on a photographic plate, or alternatively may be viewed in the observation telescope.

3.SUMMARY

The basic interference system in the analytical ultracentrifuge has been described, together with a brief survey of its history. A theoretical analysis has been made of the optics and the basis upon which measurements are made has been established. Extensive use has been made of the Fourier theory of optics in the above, and this will be further developed and employed in the next chapter of this work concerned with the light source coherence.

CHAPTER 2.

THE COMPARISON OF MERCURY ARC AND HELIUM-NEON GAS LASER LIGHT SOURCES

1. INTRODUCTION

It has been pointed out by Kuhn[27] that the most serious and inherent weakness of the Rayleigh interferometer is the lack of intensity and visibility of the fringes - this fault being aggravated further in the ultracentrifuge owing to the movement of the cell[4]. In chapter 1 it was shown that the mean phase differences containing the desired information is measured by virtue of fringe displacement, and hence fringe visibility is of paramount importance. Basically, the observed fringe pattern can be improved by (a) increasing the coherence of the source illumination, (b) increasing the intensity of the interferometer illumination, and (c) having a stationary cell in the interferometer.

In general perfect coherence is not required for interferometry, and light is considered sufficiently coherent provided (i) its temporal coherence length is large compared with the optical path differences in the interferometer, and (ii) that adequate spatial coherence exists. It is well known that the existing Rayleigh system in the analytical ultracentrifuge employing the AH-6 high pressure mercury lamp and filter to isolate the 546.1nm emission line, has insufficient temporal coherence when concentrated solutions are studied, and some form of compensation such as that of Richards and Schachman[21] has to be employed to achieve clear fringes. Furthermore, the fringe pattern observed has very low intensity owing to the small source aperture, which as will be shown is so necessary to achieve adequate spatial coherence with the mercury source.

From the above it will be apparent that a knowledge of coherence theory is essential in any meaningful discussion or analysis of an interferometer. Indeed as stated succinctly by Steel[28], the theory of coherence explains what an interferometer can measure, the errors it commits and how these errors may be corrected. In other words interferometry is the experimental side of coherence theory. Mielenz[29] has made a pertinent review of coherence theory in conjunction with a relevant

discussion on the use of gas lasers and conventional sources in interferometry, and is appropriate in the context of the present work.

2. BASIC COHERENCE THEORY

Briefly, coherence may be considered by using the optical arrangement depicted in figure 2-1. If the source is infinitesimally small and the light emitted is perfectly monochromatic, then the electric field vectors ($E_1(t)$ and $E_2(t)$) at the two apertures of the Rayleigh mask in the pupil of lens L_2 will be in complete agreement, since they belong to the same wavefront at any instant of time. Hence, the complex amplitude of the electric field vector $E_R(t)$ at a point $P(\xi')$ in the focal plane of a perfect lens L_2 will be the result of the superposition of the two interfering waves.

i.e.,
$$E_R(t) = E_1(t) + E_2(t)$$
$$= A_1 \exp^{i(\omega t + k\delta_1 + \delta)} + A_2 \exp^{i(\omega t + k\delta_2 + \delta)} \qquad (2\text{-}1)$$

Where 'A' and 'δ' are the respective amplitude and path lengths in the interferometer, and δ is the common phase difference at time $t = 0$. Here it is assumed that $E_1(t)$ and $E_2(t)$ have a common plane of polarization.

The observable intensity at P is

$I = \overline{E_R(t).E_R(t)^*}$ i.e., the time averaged intensity (cfeq(1-3)) given by

$$\overline{E_R(t).E_R(t)^*} = \frac{1}{2T} \int_{-T}^{+T} E_R(t).E_R(t)^* \, dt \qquad (2\text{-}2)$$

where $T >> T_o = \frac{2\pi}{\omega}$ the period of oscillation.

Hence
$$I_R = A_1^2 + A_2^2 + 2A_1A_2 \cos k\ell \qquad (2\text{-}3)$$

in which $\ell = \delta_2 - \delta_1$, <u>the optical path difference</u> of the two interfering waves at P.

Obviously maxima of intensity, $I_{max} = (A_1 + A_2)^2$, occurs at all points P for which ℓ is an integral multiple of the wavelength ($\ell = N\lambda$) or

$$k\ell = 2\pi N \tag{2-4}$$

whereas minima $I_{min} = (A_1 - A_2)^2$ are observed wherever $\ell = (N + \frac{1}{2})\lambda$.

Now intermediate points are characterized by their order number (m) , which has an important role in this elementary discussion of coherence.

$$m = \frac{\ell}{\lambda} = \frac{k\ell}{2\pi} = N + \varepsilon \quad (0 \leq \varepsilon < 1) \tag{2-5}$$

where N and ε are the integral and fractional order number respectively.

The visibility of the pattern is given by

$$V = \frac{I_{max} - I_{min}}{I_{max} + I_{min}} = \frac{2A_1A_2}{A_1^2 + A_2^2} \tag{2-6}$$

and obviously if the two interfering waves have equal amplitude ($A_1 = A_2$) then maximum visibility is achieved throughout the field of view, i.e., V = 1.0 .

This ideal case is never achieved in practice and although sharp fringes of reduced visibility are found for small path differences ℓ , and fringes fade out as ℓ is increased for observation points farther away from the central fringe. The reasons for this are essentially twofold in a real source, since (a) any real source has finite extension, and (b) always emits light of finite spectral width. Thus the assumptions made in the analysis of equations (2-1) through to (2-6) above are invalid. Now for any real source there exists uncertainty in the order number

$$\Delta m = \left[\left(\frac{\partial m}{\partial \ell}\right)^2 . \Delta\ell^2 + \left(\frac{\partial m}{\partial k}\right)^2 . \Delta k^2 \right]^{\frac{1}{2}} \tag{2-7}$$

which is associated with every point of observation (P). Equation (2-7) is useful since it shows that the uncertainty in the order number arises from an uncertainty

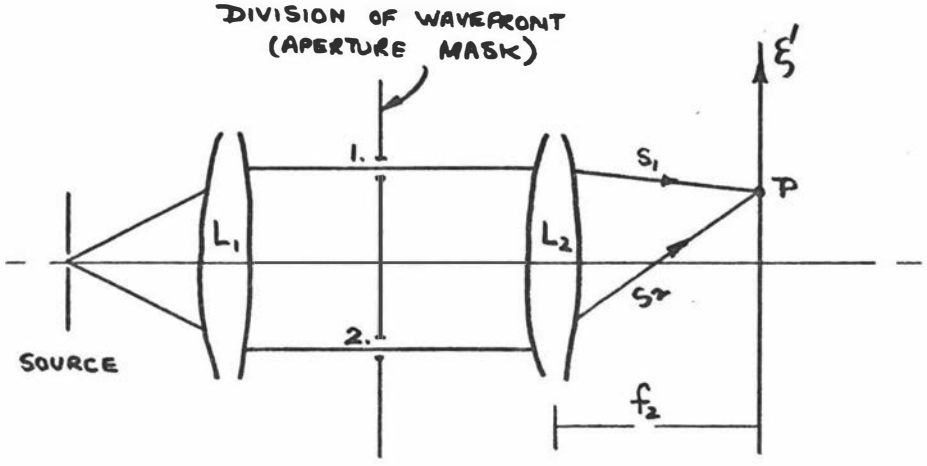

FIGURE 2-1. DIAGRAM FOR BASIC COHERENCE THEORY.

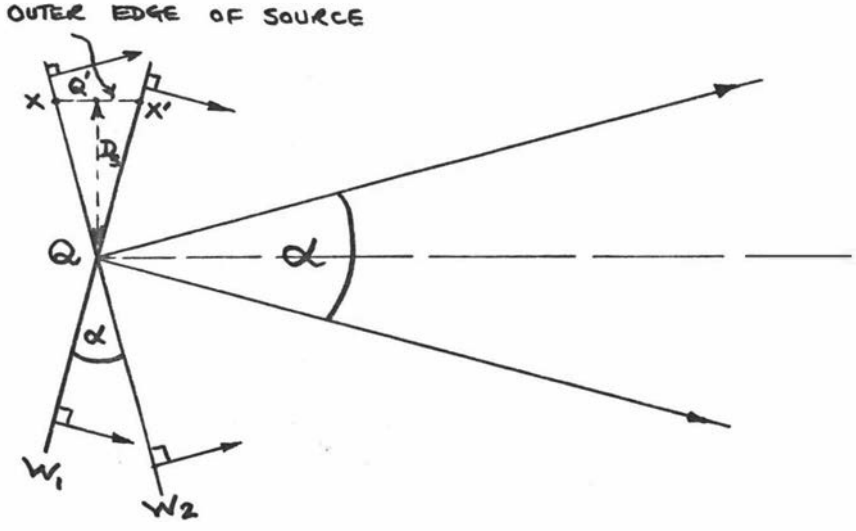

FIGURE 2-2. DIAGRAM FOR THE DERIVATION OF THE SPATIAL COHERENCE CONDITION.

in path difference ($\Delta\ell$) caused by the finite extension of the source, and the lack of monochromaticity given by the uncertainty in the wavenumber (Δk). Obviously, if $|\Delta m| \geq \frac{1}{2}$, no interference fringes will be observed and the two light beams are said to be mutually noncoherent. For the limiting case $|\Delta m| = \frac{1}{2}$ we obtain from equations (2-5) and (2-7), that

$$\left[(k\Delta\ell)^2 + (\ell\Delta k)^2\right]^{\frac{1}{2}} = \pm \pi \qquad (2\text{-}8)$$

which defines the limit of coherence.

Naturally, if $|\Delta m| \leq 1/4$ i.e., $|\Delta m|$ is small compared with the half width of the fringes, then there will be no appreciable reduction in the visibility of the fringes from the coherence point of view, and this defines the desired coherence condition.

i.e., $$\left[(k\Delta\ell)^2 + (\ell\Delta k)^2\right]^{\frac{1}{2}} \ll \pi/2 \qquad (2\text{-}9)$$

If equation (2-9) is satisfied then the two light beams are said to be mutually coherent.

In this analysis we will consider the two limiting cases separately where $\Delta k = 0$ and $\Delta\ell = 0$ respectively. This is experimentally and theoretically convenient, and allows a meaningful comparison of the two interferometer sources under discussion to be made.

(a) SPATIAL COHERENCE

Initially, consider an extended source emitting perfectly monochromatic light ($\delta k = 0$). In this case, the order number uncertainty ($\Delta m = \pm k\Delta\ell$) is caused by the extension of the source, and the source is said to have perfect temporal coherence but limited spatial coherence. The condition for spatial coherence was derived by Verdet[30] in 1869, and may be obtained readily from figure (2-2). Here W_1 and W_2 represent two wavefronts emanating at a small angle α to each other from a point source at Q. Consider the two beams to interfere at a distant point P and let ℓ be the path difference at P owing to the finite source point Q. Now at the other edge of the source remote from Q

the path difference between the two wavefronts will be $\ell' = \ell + XX' = \ell + D_S\,\alpha$ owing to the source dimension D_S in the direction normal to the line of intersection of the two wavefronts. Whence the path uncertainty at P owing to the outer source points Q and Q' is $\Delta\ell = \pm \frac{1}{2}(\ell' - \ell) = \pm \frac{1}{2} D_S\,\alpha$. Using equation (2-9) we obtain the spatial coherence condition

i.e., $$D_S\,\alpha \ll \lambda/2 \qquad (2\text{-}10)$$

From equation (2-8) we see that the largest source size for which fringes may be observed is given by

$$D_{S(coh)} = \frac{\lambda}{\alpha} \qquad (2\text{-}11)$$

This result is important in the context of the Rayleigh refractometer since α is obviously a function of the geometry of the interferometer. Now the Rayleigh interferometer is a division of wavefront interferometer as will be apparent from chapter 1, and hence α being significant necessitates the use of a small source width D_S and this results in the inherent low intensity of illumination in the interferometer.

Of interest is the observation from figure (2-2) that the two wavefronts have a common intersection for all points of observation, and so a line source extending along this intersection will produce fringes of perfect visibility. Naturally in practice the source width is determined from equation (2-11), but line sources are frequently employed to improve the intensity of interferometer illumination. However, it will be appreciated from the above that the alignment of the slit source is critical.

Rempel[31], has used Young's experiment as a typical division of wavefront interferometer to compare the performance of lasers and conventional sources in such an interferometer as the Rayleigh, and is applicable with few modifications to the task in hand. A diagram of the basic apparatus is shown in figure (2-3) .

The laser used in the present work was a single mode helium-neon gas laser of output power.

$$P = 4mw \qquad (2\text{-}12)$$

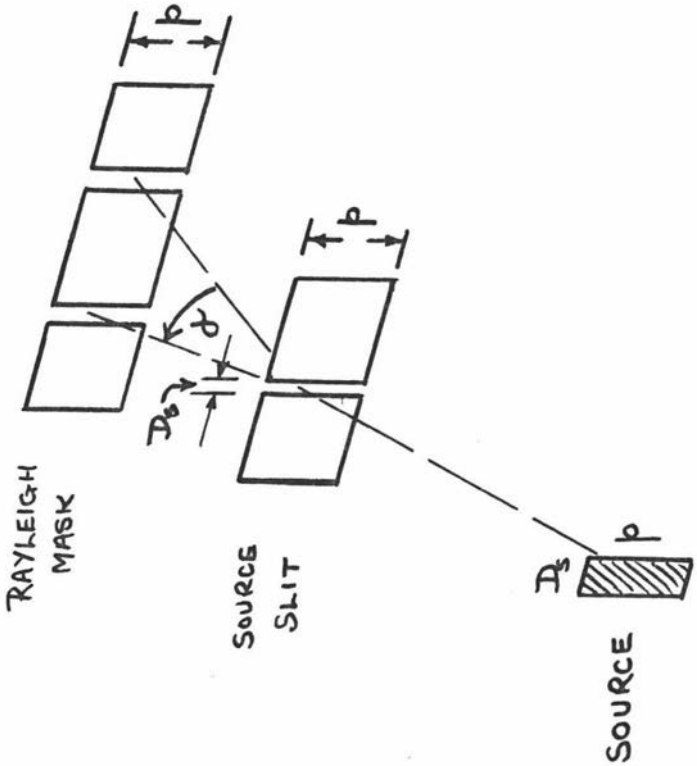

FIGURE 2-3. THE INTERFEROMETER ILLUMINATION.

The conventional high pressure (AH-6) mercury arc lamp has an approximate radiant emittance

$$M = 17 \text{ W/cm}^2 \tag{2-13}$$

in a 10 nm range about 546 nm (isolated by a green filter). Assuming that the arc length (P) is 2.5 mm and the slit width (D_S) is as defined by equation (2-11), we obtain by neglecting slit edge diffraction effects, that the maximum power derived from the arc lamp is

$$P' = \left(\frac{M}{\pi}\right) p D_S \sin\alpha = \frac{\lambda M p}{\pi} \tag{2-14}$$

i.e., $P' = 0.1$ mW

With the gas laser no source slit is necessary, since it has been shown by Fox and Li[32] and Boyd and Gordon[33] that the light from a gas laser in axial mode operation is effectively space coherent, and without limiting apertures the total laser power is available for interferometer illumination, i.e., $P_{laser} = 4$ mW . Thus this simple analysis has shown that laser light results in much brighter fringes, with the ratio P/p', being approximately 40 for our case.

A more rigorous analysis by Born and Wolf[24] and elsewhere[25,28] develops a partial coherence factor (γ_{12}) as the quantitative measure of spatial coherence. Using the notation defined in equation (2-1) this partial coherence factor is given by

$$\gamma_{12} = \frac{\overline{E_1 E_2^*}}{(\overline{E_1 E_1^*})^{\frac{1}{2}}(\overline{E_2 E_2^*})^{\frac{1}{2}}} = |\gamma_{12}| \exp^{i\Theta'} \tag{2-15}$$

whence equation (2-3) becomes

$$I_R = A_1^2 + A_2^2 + 2 \gamma_{12} A_1 A_2 \cos(k\ell + \Theta') \tag{2-16}$$

From equations (2-15) and (2-16) we see that (a) perfect spatial coherence exists when $|\gamma_{12}| = 1.0$, (b) no spatial coherence exists when $|\gamma_{12}| = 0$, and

(c) partial spatial coherence exists when $0 < |\gamma_{12}| < 1$. The latter is the usual case with the observation of fringes in the Rayleigh interferometer and physically from above the magnitude $|\gamma_{12}|$ is a measure of the contrast of the fringe system, whereas the phase θ' is a measure of the phase shift of the fringe maxima with respect to the phase obtained using light with perfect spatial coherence. Fortunately, in the Rayleigh instrument the spatial coherence of the radiation in the pupil of the lens L_2 does not vary with time since it is a function of the interferometer geometry and so fringe shifts from this source are not a problem!

Furthermore, it is shown[24,25] that the degree of partial coherence (γ_{12}) between two points S_1 and S_2 (say) in the pupil of lens L_2 is given by Fourier transform of the intensity distribution $I_S(\alpha,\beta)$ of the source as seen from the S_1S_2 plane.

i.e., $$\gamma_{12} = \frac{\text{source}\iint I_S(\alpha,\beta)\, \exp^{ik(\alpha x + \beta y)}\, d\alpha\, d\beta}{\text{source}\iint I_S(\alpha,\beta)\, d\alpha\, d\beta} \qquad (2\text{-}17)$$

and this can be used as shown below in the evaluation of the fringe contrast in the present Rayleigh interferometer.

With reference to figure 2-1, let $I_S(\alpha,\beta) = I_S$ a constant, where $I_S(\alpha,\beta)$ is the energy per unit angular area of the source at a given α,β.

Assuming the asymmetrical Rayleigh mask, the intensity of the fringe pattern located in the focal plane of lens L_2 is given by equation (1-19)

i.e., $$I = 4a^2\text{sinc}^2\left(\frac{ua}{2}\right)\cos^2\left(\frac{ub}{2}\right) = 2a^2\text{sinc}^2\left(\frac{ua}{2}\right)\left[1+\cos ub\right] \qquad (2\text{-}18)$$

From (2-17) the contrast in this fringe system may be obtained as

$$\gamma_{(x)} = \frac{\int_{-\alpha max}^{+\alpha max} I_S \exp^{ik\alpha x}\, d\alpha}{\int_{-\alpha max}^{+\alpha max} I_S\, d\alpha} = \frac{\mathcal{F}\{I_S(\alpha)\}}{\int_{-\alpha max}^{+\alpha max} I_S\, d\alpha} \qquad (2\text{-}19)$$

whence

$$\gamma_{(x)} = \frac{\sin(k\,\alpha max.x)}{k\,\alpha max\,x} = \frac{\sin\left[\frac{2\pi}{\lambda}\,\alpha max\,x\right]}{\frac{2\pi}{\lambda}\,\alpha max\,.x} \qquad (2\text{-}20)$$

Now x is measured in the pupil of lens L_2 and from (2-20) we see that the fringe visibility depends on the slit separation 'b' and incidentally equation (2-20) forms the theoretical basis of a stellar interferometer.

Now the data relevant to the interferometer used in the Beckman Model 'E' analytical ultracentrifuge are as follows:

Source width ($\mathcal{W}$) = 2.5×10^{-3}cm. Slit separation (b) = 0.4cm
Wavelength (λ) = 5.461×10^{-5}cm.
Focal length of the lower collimating lens (f_1) = 58 cm
Now α_{max} is given by

$$2\alpha_{max} = \frac{\mathcal{W}}{f_1} \qquad (2\text{-}21)$$

Hence by substitution,

$$\frac{2\pi}{\lambda}\,\alpha_{max}\,b = 0.99 \text{ radians} = 56.8^{\circ}$$

and $$\gamma_{12} = \frac{\sin 56.8^{\circ}}{0.99} = 0.84 \qquad (2\text{-}22)$$

Whereas for the laser source employed which operates in the axial mode the illumination is effectively space coherent,[32,33]

i.e., $\gamma_{12} = 1.0$.

The above analysis has indicated clearly that the fringe pattern obtained by the use of a laser source should be improved markedly in comparison with that achieved with the conventional AH-6 high pressure mercury discharge lamp and filter, owing to (a) greater interferometer illumination intensity, and (b) improved spatial coherence.

(b) TEMPORAL COHERENCE

Finally, consider an infinitesimally small source which emits a spectrum of finite width (δk). From the

above it will be apparent that the path difference ℓ is completely specified since $\Delta\ell = 0$, but now the time specification of the interfering light will be uncertain owing to the wavenumber uncertainty $\Delta k = \pm \frac{1}{2} \delta k$. This light is said to have perfect spatial coherence, but limited temporal coherence. From equation (2-7) the order number uncertainty $\Delta m = \pm \frac{1}{2} \ell \delta k$ may be considered to arise from the supposition of many mutually displaced fringe patterns in the plane of observation. Again from equation (2-9) the light will be effectively time coherent if

$$|\ell| \ll \frac{\pi}{\delta k} \tag{2-23}$$

and indicates that the observation of white light fringes or achromatic fringe pattern is possible at very short path differences ℓ, as discussed previously. From equation (2-8) we obtain the important temporal coherence length of the source which is defined by

$$\ell_{coh} = \frac{2\pi}{\delta k} \tag{2-24}$$

Michelson[34] was the first to explain the effect of spectral purity of the source on the path difference, and demonstrated with his interferometer the decrease in fringe system visibility with increasing path difference. It is shown[24,25] that for two beams with collinear polarizations arriving at a point of observation P (say) from a common point source that

$$\bar{E}_R(t) = \bar{E}_1(t) + \bar{E}_2(t) = \bar{E}(t) + \bar{E}(t - \tau) \tag{2-25}$$

where τ is the time delay. For the Rayleigh instrument

$$\tau = \frac{tn}{c} \tag{2-26}$$

Where in this case c is the velocity of light. As usual the observed intensity $I(t)$ is given by equation (2-2) and may be shown to be

$$I(t) = I(\tau) = |\overline{E(t)}|^2 + |\overline{E(t-\tau)}|^2 + 2\,|\overline{E(t)\,E(t-\tau)}| \tag{2-27}$$

where the source is assumed to be stationary.

The terms on the R.H.S. are recognised as auto-correlation functions, conveniently written as

$$I(t) = 2\,\phi(o) + 2\,\phi(\tau). \qquad (2\text{-}28)$$

Now from equation (2-3) and for convenience assuming $A_1 = A_2 = 1$ we get for a given position

$$I(\tau) = 2(1 + \cos 2\pi\nu\tau) \qquad (2\text{-}29)$$

where ν is the frequency.

Now for a polychromatic non-coherent source with a spectral energy distribution $\phi(\nu)$ per unit frequency interval $\Delta\nu$ equation (2-29) becomes

$$I(\tau) = 2\int_{\nu}\phi(\nu)\left[1 + \cos 2\pi\nu\tau\right]d\nu$$

$$= 2\int_{\nu}\phi(\nu)\,d\nu + 2\int_{\nu}\phi(\nu)\cos 2\pi\nu\tau\,d\nu \qquad (2\text{-}30)$$

Whence by comparison of equations (2-28) and (2-30) we obtain the varying quantity to be

$$\phi(\tau) = \int_{\nu}\phi(\nu)\cos 2\pi\nu\tau\,d\nu = \mathcal{F}_c\left\{\phi(\nu)\right\} \qquad (2\text{-}31)$$

This states that the autocorrelation function of the electric field in the light beam is equal to the Fourier cosine transform of the energy distribution in the spectrum. Thus from a knowledge of the spectral energy distribution in the source the temporal coherence length may be determined by direct application of equation (2-31). Incidentally, in experiment the inverse problem is the more common since equation (2-31) forms the basis for Fourier-transform spectroscopic analysis. However, multiple beam interference methods have largely superceded two beam interference in the practical analysis of spectra.

Candler[35] has stated that the temporal coherence of the mercury green line (λ = 546.1 nm) is limited by hyperfine structure, and for comparison with our laser source it is convenient to consider the spectral energy

distribution to be Gaussian of width 10 nm - this being typical[29] for a high pressure mercury arc lamp and filter as used in the analytical ultracentrifuge. A diagram of $\phi(\nu)$ is shown in figure 2-4(a) and may be represented mathematically as the convolution of a delta function with the relevant Gaussian function

i.e.,

$$\phi(\nu) = \delta(\nu - \nu_o) \circledast \exp(-a^2\nu^2) \qquad (2\text{-}31)$$

Now $$\mathcal{F}_c\{\delta(\nu - \nu_o)\} = \cos 2\pi\tau\nu_o \qquad (2\text{-}32)$$

and $$\mathcal{F}_c\{\exp^{-a^2\nu^2}\} = \frac{\sqrt{\pi}}{2a}\exp(-\frac{\pi^2\tau^2}{a^2}) \qquad (2\text{-}33)$$

Hence from equation (2-31) and the use of the convolution relationship[26] it may be shown that

$$\phi(\tau) = \frac{\sqrt{\pi}}{2a}\exp(-\frac{\pi^2\tau^2}{a^2})\cos 2\pi\nu_o\tau \qquad (2\text{-}34)$$

whereas

$$\phi(o) = \int_\nu \exp^{-a^2\nu^2} d\nu = \frac{\sqrt{\pi}}{2a} \qquad (2\text{-}35)$$

Substituting equations (2-34) and (2-35) into (2-30) we obtain the intensity of the fringe pattern owing to limited temporal coherence

i.e. $$I(\tau) = \frac{\sqrt{\pi}}{a}\left[1 + \exp(-\frac{\pi^2\tau^2}{a^2})\cos 2\pi\nu_o\tau\right] \qquad (2\text{-}36)$$

which is depicted in figure (2-5a). It can be seen that the visibility curve of the fringes is the envelope of the normalised intensity curve.

i.e. $$V(\tau) = \frac{I_{max} - I_{min}}{I_{max} + I_{min}} = \exp(\frac{-\pi^2\tau^2}{a^2}) \qquad (2\text{-}37)$$

This shows that theoretically the fringes arising from the use of a source with a Gaussian spectral distribution are visible even when τ is very large, since $\exp(\frac{-\pi^2\tau^2}{a^2})$ is never zero. However, for all practical purposes the

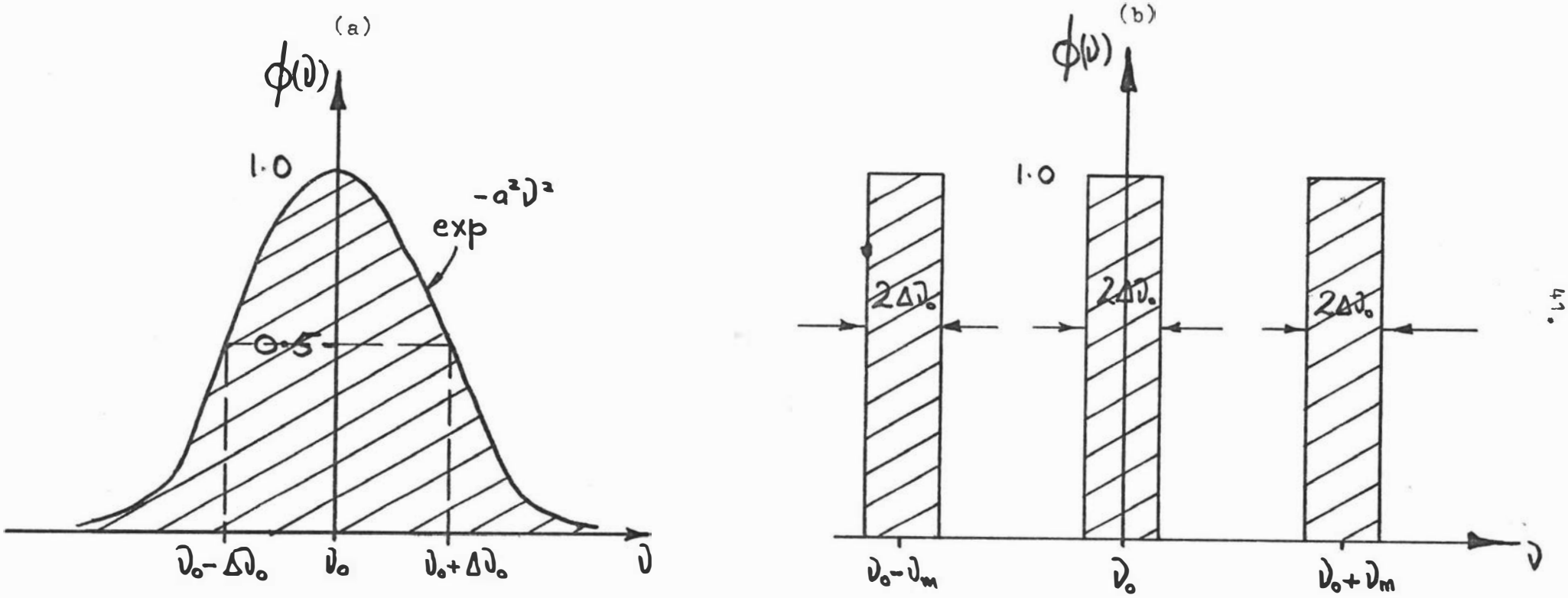

FIGURE 2-4. SPECTRAL ENERGY DISTRIBUTIONS OF THE INTERFEROMETER SOURCES:

(a) MERCURY ARC AND FILTER. (b) HELIUM-NEON GAS LASER.

fringes vanish for τ_o given by

$$\tau_o = \frac{1}{2\Delta\nu_o} \tag{2-38}$$

where $2\Delta\nu_o$ is the width of the Gaussian spectral energy distribution of the source.

Now the temporal coherence of the laser source used in the analytical ultracentrifuge under study was limited by three (3) axial modes spaced 450 Mhz apart centred on the wavelength $\lambda_o = 632.8\,nm$. The normalised spectral energy distribution is shown in figure (2-4b). It may be considered as the convolution of a single narrow spectrum of width $2\Delta\nu_o$ with three δ -functions, which is further convoluted with a δ -function

i.e. $$\phi(\nu) = g \circledast h \circledast \ell \tag{2-39}$$

where the functions g, h and ℓ are defined as follows:

$$g = \delta(\nu - \nu_o) \tag{2-40}$$

$$h = \Pi(\nu) \tag{2-41}$$

and $$\ell = \delta(\nu) + \delta(\nu + \nu_m) + \delta(\nu - \nu_m) \tag{2-42}$$

Now from the convolution theorem[26]

$$\mathcal{F}_c\{\phi(\nu)\} = \mathcal{F}_c\{g \circledast h \circledast \ell\} = \mathcal{F}_c\{g\}\,\mathcal{F}_c\{h\}\,\mathcal{F}_c\{\ell\} \tag{2-43}$$

It may be shown by integral calculus that

$$\mathcal{F}_c\{g\} = \int_{-\infty}^{+\infty} g.\cos 2\pi\nu\tau\, d\nu = \cos 2\pi\tau\nu_o \tag{2-44}$$

$$\mathcal{F}_c\{h\} = 2\Delta\nu_o \frac{\sin 2\pi\Delta\nu_o\tau}{2\pi\Delta\nu_o\tau} = 2\Delta\nu_o\,\mathrm{sinc}\,(2\pi\Delta\nu_o\tau) \tag{2-45}$$

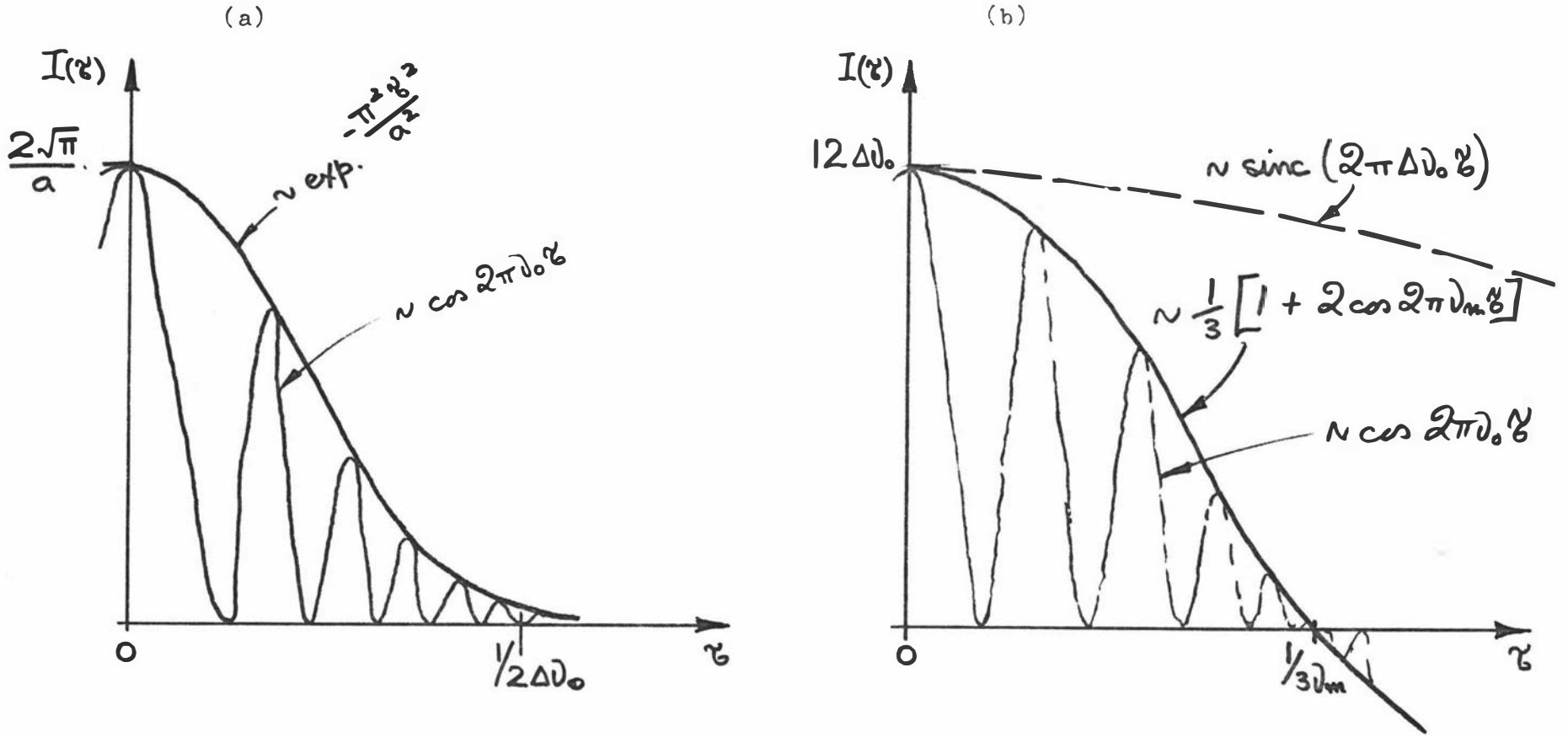

FIGURE 2-5. FRINGE INTENSITY PATTERNS OWING TO LIMITED TEMPORAL COHERENCE.

(a) GAUSSIAN MERCURY SOURCE. (b) TRIPLE AXIAL-MODE LASER SOURCE.

and $\mathcal{F}_c\{\mathcal{E}\} = 1 + 2\cos(2\pi\tau\nu_m)$ (2-46)

Now $\int \phi(\nu)\,d\nu = 6\Delta\nu$ (2-47)

since (2-47) represents the area under the spectrum

Substituting equations (2-43 - (2-47) into equation (2-30) we obtain the desired fringe intensity pattern for our laser source.

i.e. $I(\tau) = 12\Delta\nu_o\left[1 + \frac{1}{3}\,\mathrm{sinc}(2\pi\Delta\nu_o\tau)\left[1 + 2\cos 2\pi\tau\nu_m\right]\cos 2\pi\nu_o\tau\right]$ (2-48)

and this is shown in figure (2-5b).

The desired fringe visibility curve is given by

$$V(\tau) = \frac{1}{3}\,\mathrm{sinc}(2\pi\Delta\nu_o\tau)\left[1 + 2\cos 2\pi\tau\nu_m\right] \quad (2\text{-}50)$$

Here we note that the fringe visibility is characterized by the product of two distinct functions giving rise to two independent coherence times τ_{o1} and τ_{o2} respectively. Where the coherence times are defined as the time delays corresponding to zero visibility.

From $\mathrm{sinc}(2\pi\Delta\nu_o\tau)$ we determine τ_{o1} to be given by

$$\tau_{o1} = \frac{1}{2\Delta\nu_o} \quad (2\text{-}51)$$

whereas from $(1 + 2\cos 2\pi\tau\nu_m)$ we find that τ_{o2} is given by

$$\tau_{o2} = \frac{1}{3\nu_m} \quad (2\text{-}52)$$

In practice $\nu_m \gg \Delta\nu_o$ and hence from equations (2-51) and (2-52) the temporal coherence is characterized by τ_{o2}.

Thus the temporal coherence of the conventional mercury arc discharge and laser sources may be compared by application of equations (2-38) and (2-52) respectively.

For the mercury source and assuming a wavelength spread ($\Delta\lambda$) of 10 nm about the 546.1 nm emission line

we get from equation (2-38) that

$$\tau_o = \frac{1}{2\Delta\nu_o} = \frac{\lambda_o^2}{c(\Delta\lambda)} \cong 10^{-13}\ s \qquad (2\text{-}53)$$

whereas for our laser source with ν_m = 450 Mhz we get from equation (2-52) that

$$\tau_{g2} = \frac{1}{3\nu_m} \cong 7 \times 10^{-10}\ s \qquad (2\text{-}54)$$

Thus it will be appreciated that the temporal coherence of the laser source is orders of magnitude greater than the conventional mercury arc lamp and filter, and so with reference to equation (2-26) defining the coherence time for the Rayleigh interferometer, the laser will allow greater refractive increments i.e. solute concentrations, to be studied without compensation.

SUMMARY

In this chapter we have been concerned with a brief survey of coherence theory. The analysis has been applied to the mercury arc and laser sources, and has enabled a quantitative comparison of the two to be made. The findings indicate that the laser source should overcome some of the inherent disadvantages associated with the mercury arc. In addition, as will be shown in the next chapter, the highly collimated and coherent laser beam lends itself to electro-optical shuttering. The latter enables the rotor to be strobed, and this results in an effectively stationary cell in the interferometer which enhances even further the clarity of the fringe patterns whilstat the same time giving greater instrumental flexibility.

CHAPTER 3.

A MODULATED LASER SYSTEM FOR ANALYTICAL ULTRACENTRIFUGE INTERFERENCE STUDIES

1. INTRODUCTION

It has been shown[12,21] that the Rayleigh interference optical system in the analytical ultracentrifuge yields simple and accurate experimental data. However, the discussion and analysis in chapter 2 has indicated that the current system using the unmodulated AH-6 mercury arc discharge lamp and filter suffers from certain inherent disadvantages. The outcome from the above is that the fringe pattern observed from which pertinent data are obtained can suffer from a lack of visibility and overall intensity owing to (a) lack of coherence (both spatial and temporal) of the source, and (b) movement of the interference cell during the recording of the fringe pattern. The theoretical analysis of chapter 2 has indicated clearly that a laser source will overcome the drawback of the lack of source coherence and inadequate interferometer illumination. The problem of cell movement during the recording of the fringe pattern may be obviated by strobing the rotor with a suitably synchronised light source. Fortunately, the highly collimated and monochromatic laser light beam lends itself readily to electro-optical modulation as will be described below, and hence a suitably modulated laser system should overcome the inherent disadvantages of the conventional system. Furthermore, the versatility of the instrument will be enhanced in that the multiple cell rotors may be used without wedge windows with their associated inaccuracies. In this chapter a system is evolved wherein a continuous wave helium-neon gas laser replaces the conventional mercury lamp in a Beckman Model E instrument and the ancillary equipment necessary to pulse modulate this light in synchronism with the rotor is described.

2. DESCRIPTION OF SYSTEM (see FRONTISPIECE)

Figure 3-1 depicts a simplified block diagram of the basic units, in which the Rayleigh/Schlieren and ultraviolet optical systems of the analytical ultracentrifuge are separated laterally for ease of presentation.

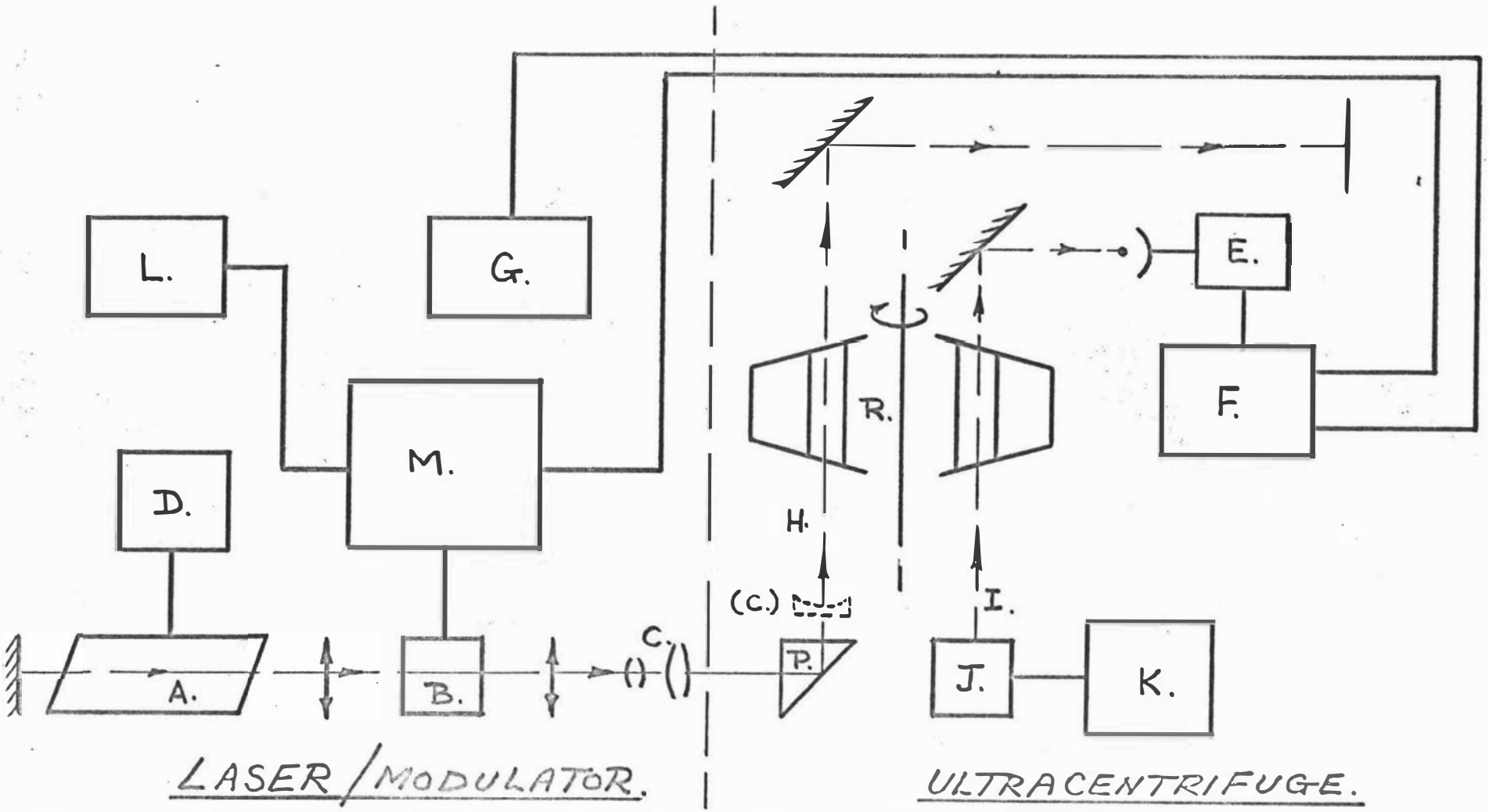

FIGURE 3-1. SCHEMATIC BLOCK DIAGRAM OF THE ULTRACENTRIFUGE AND MODULATED LASER SYSTEM.

A.LASER, B.POCKEL CELL, C.SOURCE OPTICS, D.LASER SUPPLY, E.ROTOR PICK-UP, F.ELECTRONIC CONTROL UNIT, G.DIGITAL FREQUENCY METER, H.SCHLIEREN/INTERFERENCE OPTICAL SYSTEM, I.ULTRAVIOLET OPTICAL SYSTEM, J.PICK-UP LIGHT SOURCE, K.LAMP POWER SUPPLY, L.VARIAC d.c. CONTROL, M.E.H.T.MODULATOR UNIT, P.PRISM, and R.ROTOR.

The laser, together with the E.H.T. supply and optical modulation units were situated to the left of the ultra-centrifuge when facing the front of the machine,and were housed in a specially constructed cupboard used for stowing other units when they were not in use. The laser (A), and the electro-optic light modulater (B) were aligned on a triangular section optical bench that was securely fastened to the laboratory floor. Source optics(C), associated with the production of a line source for the system were also aligned on this bench (when in use), and all units were held in adjustable mounts for alignment purposes.

The laser light entered the ultracentrifuge through a 1" diameter hole drilled through casing of the ultracentrifuge and was deflected through the conventional optical system (H) by an adjustable prism or diffusing device (K). The rotor pick-up (E) - so necessary for synchronism - was housed near the optical track of the ultraviolet system (I) at the top left-hand side of the ultracentrifuge. The removable light source (J) for the photo-cell sensor was fixed in position above the ultra-violet light source housing on a special mount fixed to one of the supports of the chain guides of the rotor chamber lifting mechanism. An electronic control unit (F) was semi-portable and was conveniently placed near the viewing telescope for ease of manipulation during operation. A digital frequency meter (G) used for monitoring the rotor frequency was placed normally on the bench top of the cup-board. A more detailed description of the operation and construction of the individual special units is given below.

I. THE LASER

This was a University Laboratories/Spectra-Physics Model 261, polarised helium-neon gas laser. It was constructed with a con-focal cavity and produced 4.0 mw continuous wave output at a wavelength (λ) of 632.8 nm. As mentioned in chapter 2, the temporal coherence was characterized by three axial modes spaced 450 MHz, and the spatial coherence was characterized by

the fundamental TEM_{oo} mode. The intensity distribution across a beam diameter was Gaussian and the diameter at the aperture ($\frac{1}{e^2}$ points) was 1.4 mm.

II. THE ELECTRO-OPTIC LIGHT MODULATOR

This was obtained from ISOMET Corporation, Palisades Park, New Jersey, U.S.A., and was their model EOLM 400. An optically matched Glan-Thompson analyser was obtained also from the same source. An elementary review of the applications of these devices together with appropriate references has been made by Goldstein[38]. Briefly, the active element was a Pockel[39] cell which in the EOLM 400 consisted of two precisely orientated potassium dideuterium phosphate (KD*P) crystals enclosed in an hermetically sealed package with antireflection coatings on the windows for 632.8 nm which gave an 8% insertion loss for the units. This unit is designed specifically for lasers and its half-wave voltage was about 1.8 kV at the wave-length used.

The mode of operation of the electro-optic shutter in the present system was as follows. The plane polarised and highly collimated monochromatic light from the laser was arranged so that its direction of polarisation was parallel to either the X- or Y- axis of the crystal. The Z-axis which was also the optic axis of the crystal was the direction of propagation of the light. The direction of polarization of the Glan-Thompson analyser was positioned parallel to that of the laser input. This orientation gives a transmission maximum when there is no voltage applied to the crystal. On application of a d.c. voltage to the crystal the light transmitted decreased until a minimum was reached at the so-called half-wave retardation voltage. At this voltage the orthogonal components of the light beam had undergone a relative phase shift of 180° in passing through the crystal and in doing so the plane of polarization had been rotated through 90°. This new direction of polarization was now at 90° to that of the Glan-Thompson analyser, and light transmission was restricted.

In the current system the d.c. half-wave

voltage was maintained on the Pockel cell from an E.H.T. supply unit for the greater period of time, thus restricting transmission of light to a minimum - indeed the laser beam was effectively extinguished. Electrical pulses that were suitably synchronized to the rotor frequency (obtained via the photocell pick-up, control unit and E.H.T. Modulator) were applied to the Pockel cell, reducing its voltage to zero for controlled periods. Naturally, the latter action had the effect of pulse modulating the light source as was desired. A schematic diagram of the electro-optical system is shown in figure 3-2.

III. THE ROTOR PICK-UP

The purpose of this unit was to provide electrical pulses that were synchronised to the rotor frequency and that were also shaped suitably for acceptance by the electronic control unit. The sensor transducer was a gas photo-tube (RCA 5582) mounted on an adjustable mechanical arm inserted into the optical track of the ultraviolet system of the ultracentrifuge. The sensor light was a 50W tungsten-halogen projector lamp (ATLAS A1/220) mounted above the normal ultra-violet source, with the conventional bayonet mounted chlorine-bromine filter removed to enhance the phototube illumination during operation. The high output impedance of the phototube was matched to a solid state Schmitt trigger circuit through a FET pulse amplifier. This circuitry was necessary to standardise in both height and width the pulses arising from the various cell types and counter balances employed in a rotor during operation. The sensitivity of the system was adjusted electronically so that each cell position in a rotor produced one pulse, e.g., double sector cells had to produce one pulse only.

IV. THE ELECTRONIC CONTROL UNIT

This unit modified the standardised pulses that it received from the rotor pick-up unit before passing a signal pulse to the E.H.T. modulator. Essentially, this unit selected individual pulses by means of appropriate division circuitry and then the pulse was delayed and modified in width by controllable electronic means prior to actuating the interferometer illumination control system.

FIGURE 3-2. DIAGRAMS SHOWING THE MODE OF ACTION OF THE ELECTRO-OPTIC MODULATOR.

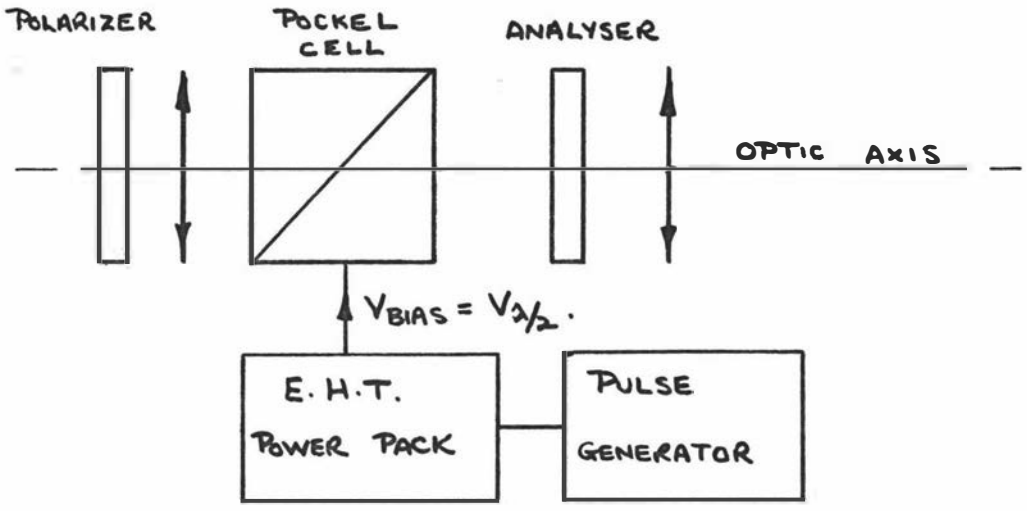

(a) BASIC EXPERIMENTAL COMPONENTS.

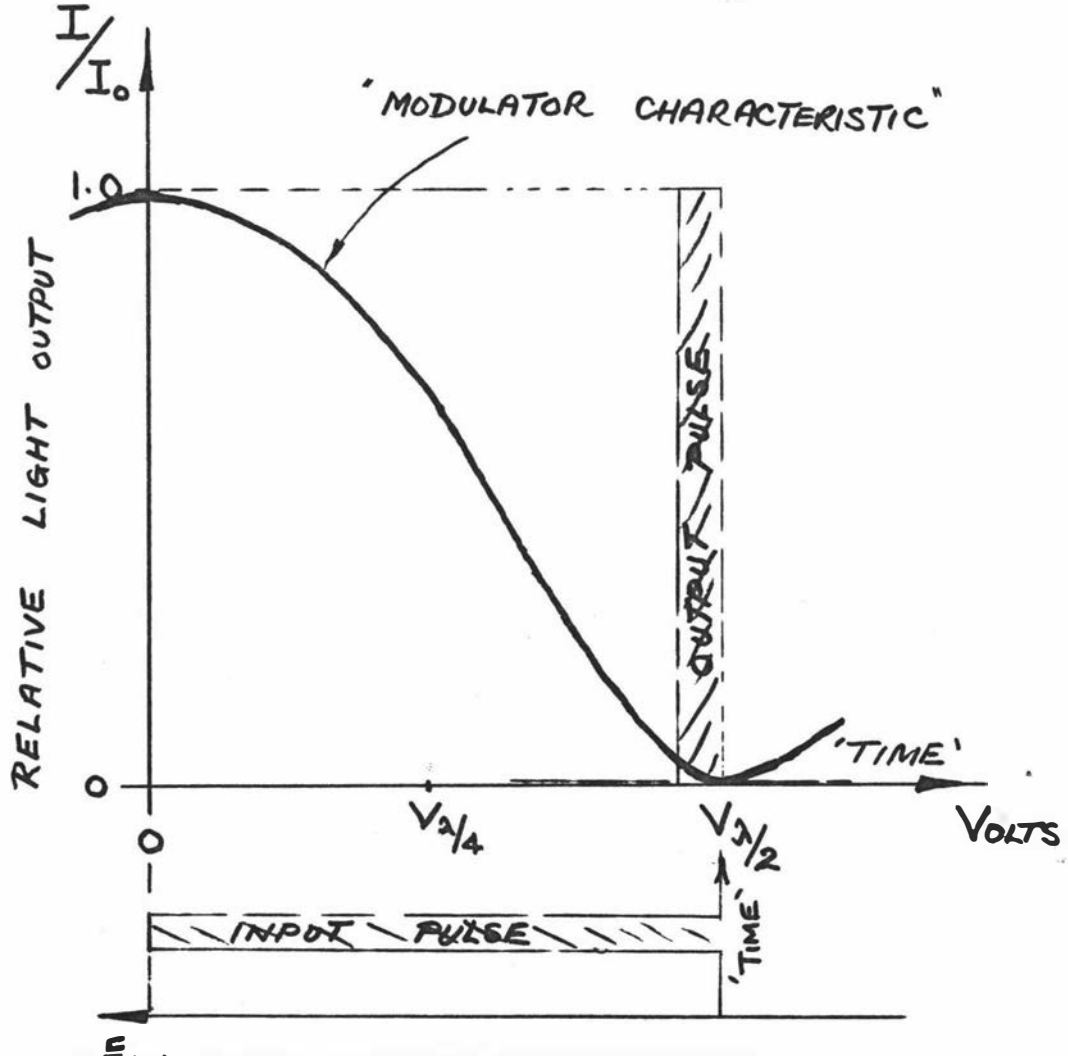

(b) TYPICAL WAVEFORM CHARACTERISTICS.

Hence this facility allowed individual cells in a rotor to be selected at will for observation, and the pulse delay and width control permitted considerable control over the position and time of viewing of the cell as it passed through the interferometer.

The unit had an additional output facility for use in conjunction with a digital frequency meter from which the mean rotor frequency and its flunctuations could be determined accurately at all times, and monitored as a routine measure. The 'Marconi' TF2414 Counter/Timer proved eminently suitable for this application, but any general purpose frequency meter would suffice.

The only rotors used in our laboratory were the two and four cell varieties, and the control unit was designed around these. However, with appropriate modifications to the frequency division circuitry the system could be used with six cell or other multicell rotors.

The circuitry was designed and built by the author using discrete components, and a block diagram and legend is shown in figure 3-3. Each block represents a conventional digital circuit unit, and the variable components were designed specifically to cover all the possible speed ranges of the ultracentrifuge with liberal overlap. In operation the counterbalance served as the reference cell from which the individual cells in the two or four cell rotors were numbered and thence selected for viewing and recording by means of an appropriate cell selection switch.

V. THE E.H.T. MODULATOR

This unit was designed and built with the dual purpose of providing (a) the high voltage necessary to actuate the Pockel cell, and (b) suitable modulation circuitry that could be controlled by the electronic control unit. A circuit diagram of the unit is shown in figure 3-4, and consists basically of a variable high voltage supply obtained from a half-wave rectifier and reservoir capacator, in conjunction with appropriate vacuum tube pulse circuitry. The former could be used independently from the modulation circuitry, and in conjunction with the laser and Pockel cell provided a useful means of controlling manually the intensity of the interferometer light source. The manual

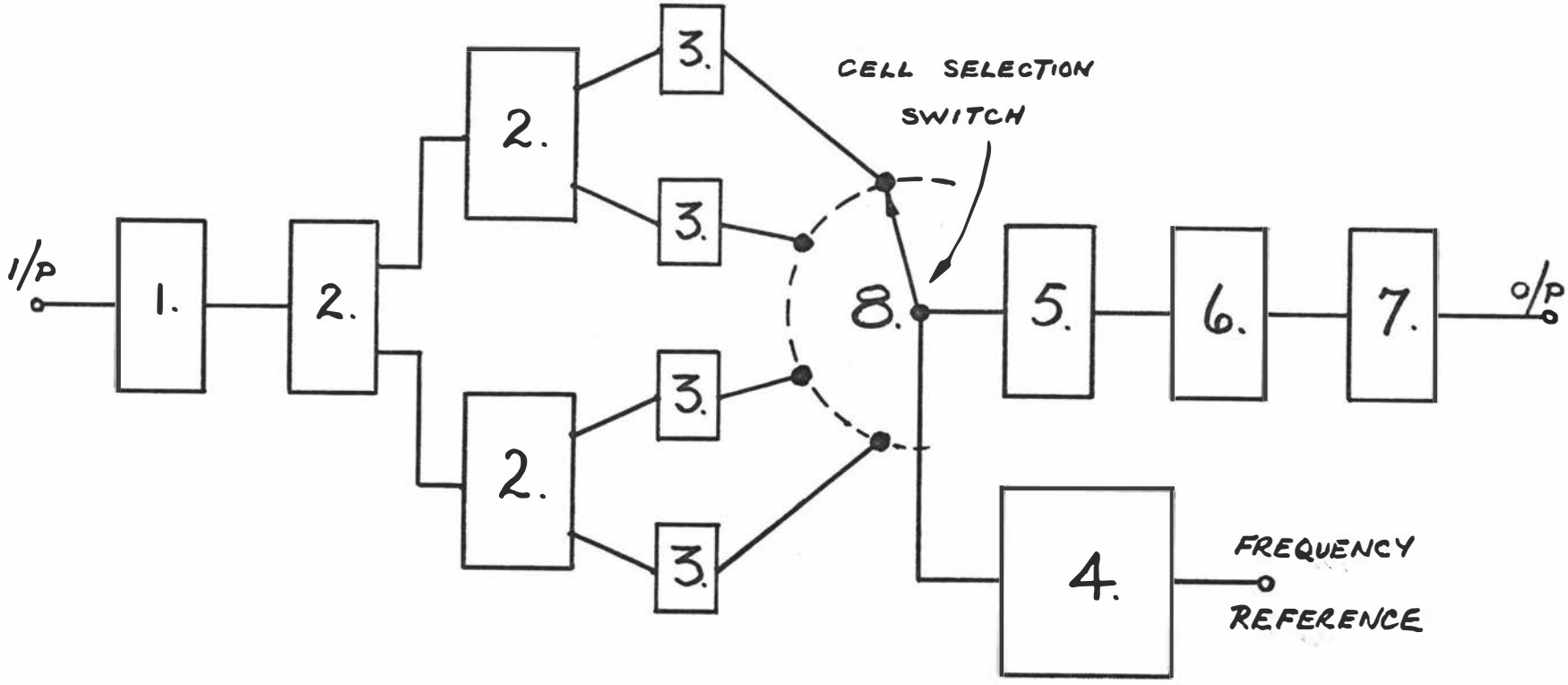

FIGURE 3-3. BLOCK DIAGRAM OF THE ELECTRONIC CONTROL UNIT.

1.SCHMITT TRIGGER, 2.BISTABLE 'FLIP-FLOP' CIRCUITS, 3.BUFFER CIRCUITS, 4.BUFFER CIRCUIT and EMITTER FOLLOWER, 5.MONOSTABLE CIRCUIT (Pulse Delay), 6.MONOSTABLE (Pulse Width), 7.EMITTER FOLLOWER (Impedance Matching).

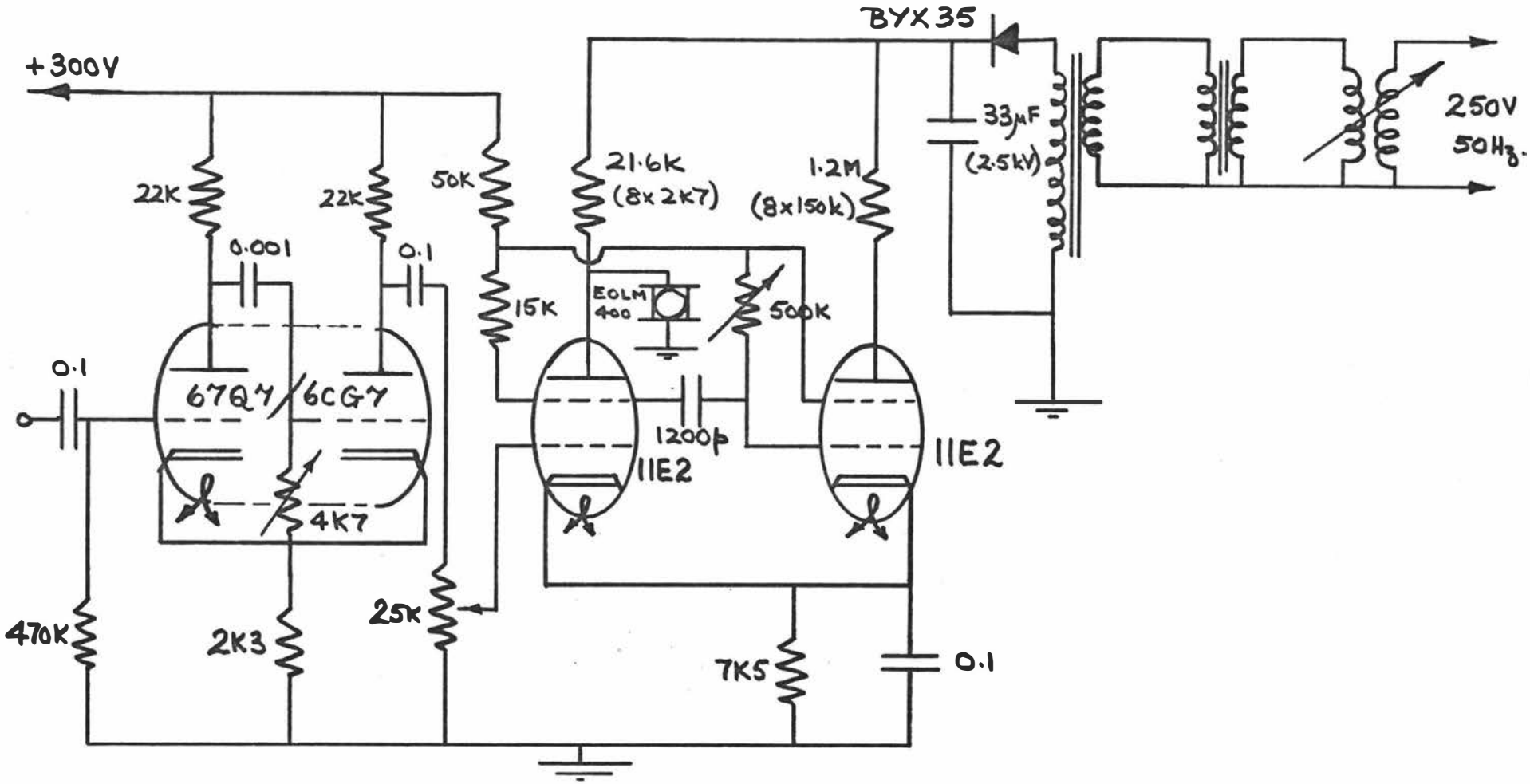

FIGURE 3-4. CIRCUIT DIAGRAM OF THE E.H.T. SUPPLY AND THERMIONIC VALVE MODULATOR.

control was achieved conveniently by varying the supply voltage by means of a variac autotransformer to which a special vernier control knob had been affixed. A calibration graph of d.c. voltage versus vernier control position was made as shown in figure 3-5, and this was used to estimate the approximate half-wave retardation voltage (1.8kV) for the Pockel cell, since as mentioned above this was the designed applied voltage when the equipment was in operation.

The vacuum tube circuitry consisted of a pulse control pre-amplifier designed around the twin triode (RCA 6707/6CG7) followed by a break modulator employing two high voltage tetrodes (AEI-11E2). The E.H.T. transformer and the high voltage silicon rectifying diode (Philips-BYX35) were oil immersed in the same tank. The former was obtained from an obsolete foot X-ray machine by appropriate alteration to the primary circuit windings and the use of the aforementioned variac autotransformer to produce the required secondary voltages. However, naturally a commercial high voltage supply with sufficient power and regulation could be substituted. The modulation unit described was capable of applying high voltage pulses to the pockel cell of variable duration in the range from 5.0μs to less than 1.0μs - the latter being controlled from the electronic control unit as was also the pulse timing.

VI. THE SOURCE OPTICS

The purpose of these were to make the highly collimated laser beam compatible with the Rayleigh Interference optics in the analytical ultracentrifuge. To this end, it was necessary to expand the beam and at the same time produce an effective source on the optic axis in the focal plane of the lower collimating lens L_1. During the development of the system various techniques were evolved to fulfil the above criteria. The most successful, and that in current use, involved the use of a right angled glass prism in conjunction with a plano-concave lens, that were aligned and focussed in a block similar to that housing the conventional mercury source. A photograph

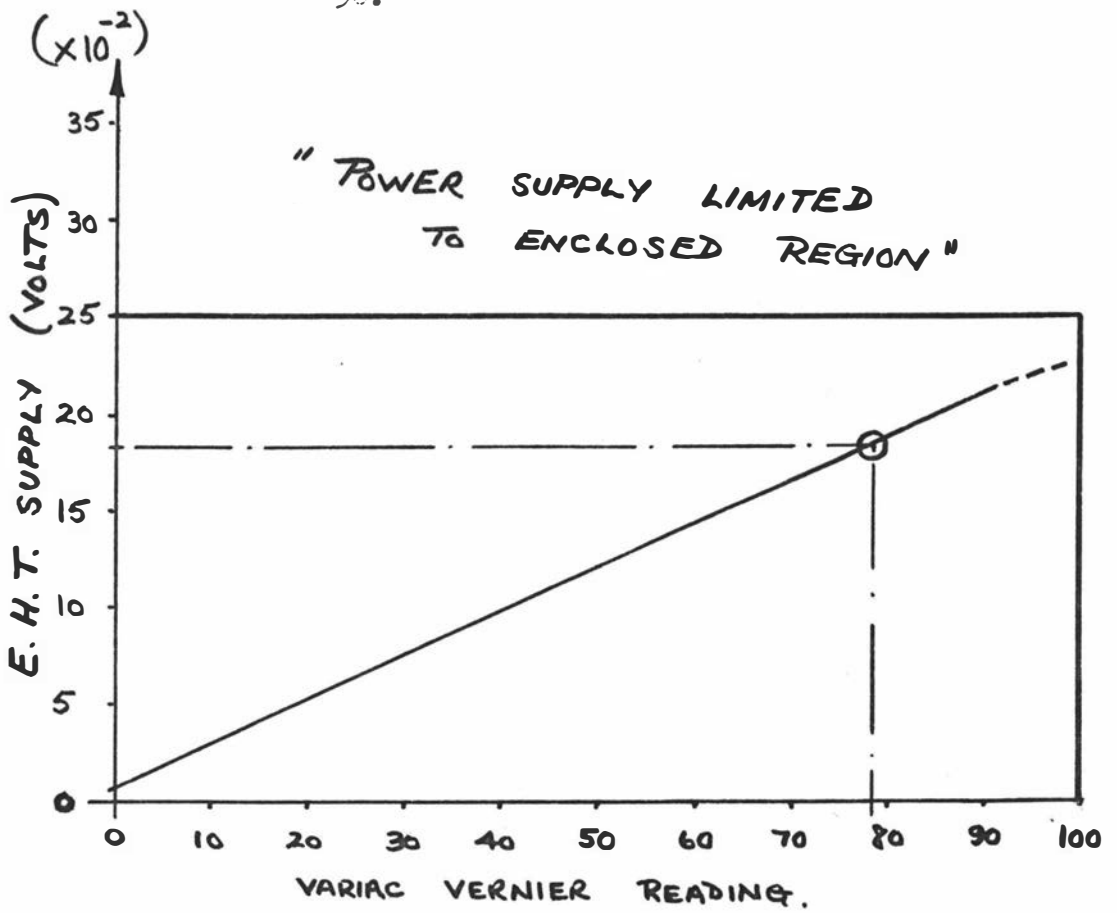

FIGURE 3-5. CALIBRATION GRAPH: E.H.T. Volts v. VARIAC READING.

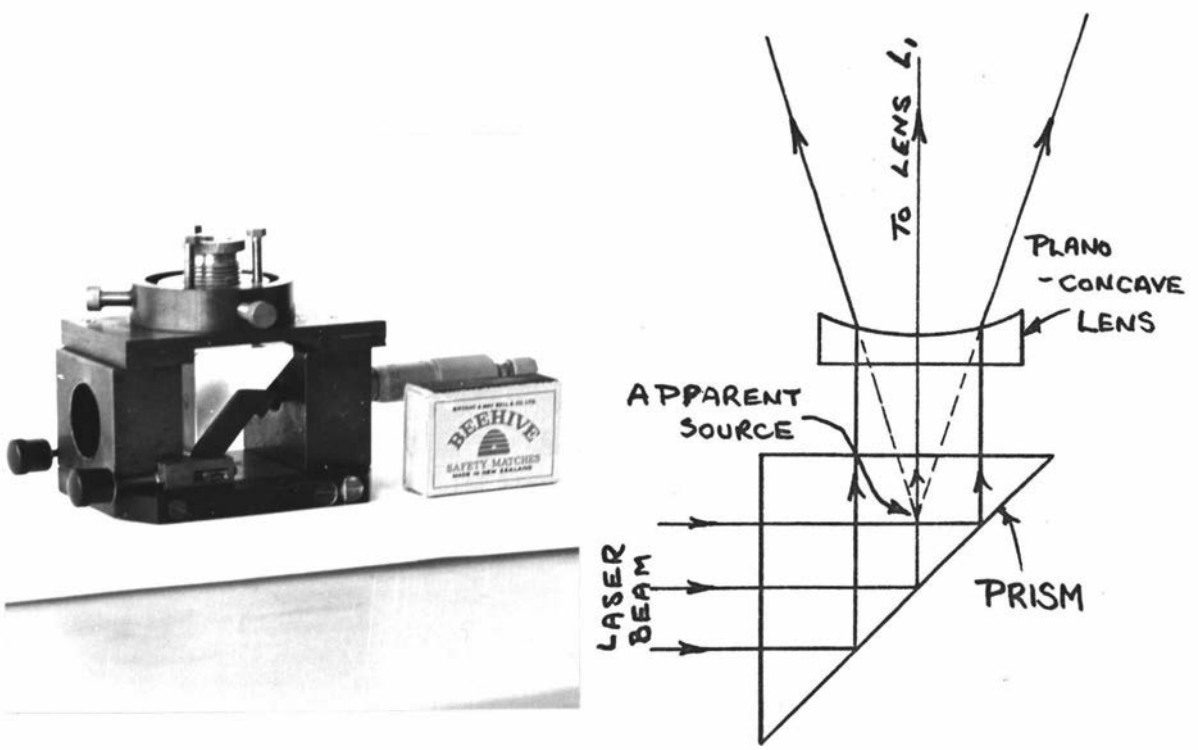

FIGURE 3-6. THE LASER SOURCE OPTICS AND PRISM.

(a) PHOTOGRAPH OF THE PRISM AND SOURCE OPTICS USED CURRENTLY IN THE CENTRIFUGE.

(b) SCHEMATIC PICTURE OF THE MODE OF ACTION OF THE LASER SOURCE OPTICS.

of this source assembly is shown in figure 3-6(a) and its mode of operation will be apparent from the diagram in figure 3-6(b). The mounting of the prism in this block assembly enabled the normal adjustable source mounts for the instrument to be used both for the conventional mercury source as well as for the laser, and facilitated a rapid and dependable interchange between the two when desired.

Rempel[40] has considered in some detail the problems associated with the focussing of laser light in comparison with that from conventional sources, and these were taken into account in the design of the special plano-concave lens. The latter simulated a point source at the focal point of the lower collimating lens L_1 and at the same time diverged the laser beam so that the aperture of lens L_1 was illuminated adequately. For the instrument used the focal length of lens L_1 was 59.4 cm and its diameter was about 3 cm. From geometrical optics and the work of Rempel[40] a centred plano-concave lens was designed by the author and manufactured by Barnes Optical Co., Ltd., Wellington, New Zealand. The adjustable lens assembly was also designed by the author and manufactured within the physics department using available technical assistance.

Prior to the introduction of the above special lens, a line source was used with some success. This was produced by a telescope arrangement consisting of a microscope objective and perspex cylinder lens (see figure 3-1). This was held in adjustable mounts on the optical track following the electro-optic modulater. The objective expanded the laser beam, and by means of a telescope adjustment and cylinder lens a suitably oriented line source was effectively focussed in the focal plane of lens L_1 and the laser light was projected into the conventional optical system by the prism depicted in figures (2-1) and (2-6). However, the focussing and alignment of this arrangement was not as precise as that attained with the plano-concave lens, although the qualitative appearance of the interference patterns obtained were comparable. The latter could be attributed to the averaging effect of the line source.

Diffuse sources together with the techniques

proposed by Steel[41] were also tried at various stages in the development, but these have met with only limited success. However, they are theoretically sound and with more development may prove useful since they may enable one to use the modulated system with Schlieren optics.

The prism was adjustable in all planes by means of screws and the micrometer shown in figure (3-6) and these were used in conjuction with the adjustable optical mounts in the optical alignment of the system as described below.

3. THE OPTICAL ALIGNMENT AND FOCUSSING

The correct alignment and focussing of the interference optics in the analytical ultracentrifuge is of paramount importance if the full potential of the system is to be realised. This has been appreciated from early times, and numerous procedures have been devised[21,42-46], for optimising the alignment and focussing of the various optical components in the instrument. Indeed a precise and detailed procedure and analysis has been published recently by Richards et al,[47,48] but these were not available at the time of our alignment.

The instrument in our laboratory was aligned and focussed accurately according to the procedures of LaBar and Baldwin[44] and Gropper[45] for use with the conventional mercury source, and was tested for accuracy and final adjustment using the boundary-cancelling test in conjunction with the methods proposed by Dyson[46] (see photographs in appendix). Having completed the focussing and alignment for the mercury source as mentioned above the objective was to replace the mercury source by the laser source, and this was accomplished according to the procedure outlined below.

(a) LASER ALIGNMENT ON OPTIC AXIS

The interference optics in the ultracentrifuge had been aligned as mentioned above and so it was convenient to use the laser to define the optic axis of this aligned system. To this end, the mercury source was switched on and the phase plate and cylindrical lens were removed from the system as they were replaceable owing to being mounted on a calibrated optical track in the instrument. A small pinhole was made in a black card and this was lightly affixed

by means of tape to the camera lens holder across its aperture. The camera lens and holder were loosened and moved towards the position of the phaseplate on the calibrated optical track, where a sharp image of the point mercury source became apparent on the card. The camera lens and holder were then fixed in this position, and the card was adjusted so that the pinhole and image of the source were superimposed. The small 50W tungsten-halogen light source, used in the optical pickup of the modulation system, was clamped on the optic axis in a position close to that normally occupied by the camera lens. When this was switched on an image of the pinhole was in focus in the actual mercury source aperture, and was clearly seen in this position when the mercury source was switched off. The mercury source had been accurately positioned in the focal plane of the lower collimating lens L_1 and on the optical axis of the system according to the procedure of Gropper[45] and so the optical axis was well defined by the position of the pinhole and its image near the mercury source.

The mercury source was removed by loosening its locking screw, and replaced by the prism in the assembly similar to that of the mercury source (see figure 3-6). However the beam expanding lens and mount were removed. The orientation of the prism was adjusted, by means of the special adjustment screws in the assembly, so that the images of the pinhole source from the two prism faces at right angles were reflected back through the system, along the same path. Then the prism was locked in position. The laser was now inserted onto the optical track in its adjustable mounts. A piece of tissue paper was placed on top of the prism so that an image of the pinhole was clearly visible. The laser was switched on, and adjusted by means of its mounts so that the beam coincided with the pinhole image mentioned above and at the same time all spurious reflections from the right angled faces of the prism were reflected back down the laser beam. The laser was then locked in position, and the tissue paper removed from the top surface of the prism. A high quality right-angled glass prism was used in this work,

and the adjustments proved so precise that it was found that the highly collimated and intense laser beam now passed through the actual pinhole in the card on the camera lens mount. The tungsten-halogen lamp was switched off and removed from the optical track, and the special target provided by Spinco was inserted at the camera end of the optical system. The undeviated laser beam proved to be slightly off centre but a very small adjustment to the 45^{o} mirror above the upper collimating lens L_2 soon remedied this minor fault.

The above adjustments had effectively placed the laser on the optic axis of the aligned interference optical system in the ultracentrifuge, and the undeviated laser beam defined this axis precisely. Indeed symmetrical and circular interference fringes associated by reflection with the collimating lenses L_1 and L_2 were clearly visible on the aperture of the laser. The pattern associated with lens L_1 was optimumly placed whereas that due to the upper lens L_2 was slightly displaced. The latter could not be improved upon, and since this laser test is so critical it was assumed to be caused by an inherent but noncritical alignment fault in the instrument.

The laser beam was used to check that all the optical components were symmetrically aligned on the optic axis, and it was found that only very minor adjustments were required.

(b) ADJUSTMENT OF ELECTRO-OPTIC MODULATOR

This was inserted with its adjustable mount on the optical track immediately following the laser, and consisted of the EOLM 400 modulater and optically matched Glan-Thompson prism analyser. The alignment of this device was achieved by means of its mounting so that the laser beam passed through it on the optic axis of the system as described above. However the rotational position of the plane of polarization was adjusted so that the radiation emanating from the modulater in its " on" position was aligned radially when passing through the cell in the roter. This plane of polarization was chosen so as to optimise the fringe patterns as suggested from the work of Ansevin et al[49]. The adjustment necessitated a very small rotational movement of the laser, since

the desirability of this additional criterion had been anticipated during the initial alignment of the laser itself.

(c) FOCUSSING THE LASER LENS OPTICS

The initial use of a radially inclined line source has been mentioned above wherein a suitable source was obtained through the use of a microscope objective and cylindrical lens in a telescope arrangement on the optical track. This system also provided a point source when the cylindrical lens was replaced by suitable spherical lens. The focussing and alignment was achieved by adjustments to the telescope and to the mount on which it was fixed. The telescope was inserted onto the optical track immediately following the modulator. Alignment and focussing were achieved by use of the pinhole and its image as mentioned earlier. Here the telescope was aligned so that the beam passed symmetrically through the pinhole itself and its image on the prism, and was focussed so that a sharp line or point image appeared on the card containing the pinhole in the plane of the Schlieren diaphragm. In this adjustment, and those following, the chromatic variations in the positions of focus lay within the precision of adjustment for the optical system employed.

The current optics employing the specially designed plano-concave lens above the prism as depicted in figure (3-6) was aligned and focussed by a different and more precise procedure. Here the lateral position and inclination of the lens was adjusted so that the laser beam entered this lens symmetrically and the reflections from the plano-surface were reflected back down the laser beam. This being the case, the diverged beam was found to illuminate the aperture of the lower collimating lens L_1 in a uniform manner, The focussing made use of the tungsten-halogen lamp and pinhole used previously. In this case, the light from this lamp and pinhole source was projected back through the system as described earlier. The focus of this lens was adjusted by a vertical screw (see figure 3-6), and correct focus was obtained when a sharp image of the illuminated pinhole was obtained at all distances back along the optical track between the prism and the laser source. Indeed a sharp image of this pinhole was formed within the aperture of the laser itself,

and this was substantial evidence that the system was both aligned and focussed for this white light. By using red perspex in front of the tungsten-halogen lamp the system was focussed for red light, but the focus adjustment between the optimum positions for this and the white light were found to lie at the limits of experimental precision. A mirror was inserted between the modulator and prism for the arrangement above which projected the pinhole image across the laboratory and this proved a convenient and critical test for the focussing described. The procedure is based on the fact that if the lens is correctly focussed in the system described above, then reversed light from the plano-concave lens should form a parallel beam assuming light to be reversible as required by the theory of geometrical optics. Obviously in practice a highly collimated and parallel laser beam enters the system.

(d) ADJUSTMENT OF THE APERTURE MASK

The plano-concave lens assembly was removable from the prism block on which it was located by means of steel pins. This was convenient since it gave ready access to the undeviated laser beam which served as the reference to the optical axis of the system. When used, it was found that the symmetrical Rayleigh aperture mask, fixed under the upper collimating lens L_2, was not symmetrical about the optic axis of the instrument. The reason for this was soon discovered when the mask alignment tool was examined and found to have a slight curvature. The effect of this in the initial alignment had been to cause an error in the radial alignment of the mask, but this had been corrected in the boundary cancelling test by a translational movement of the mask as shown by the work of Dyson[46]. This was not serious since the system was correctly aligned as shown by the boundary cancelling procedure. However it was irksome and since the laser had provided a useful alignment tool it was decided to realign this mask symmetrically upon the optic axis. The method by which this was acheived is described in chapter 4 of this thesis in which use was made of a triple-slot aperture mask and cell assembly. The slots in the aperture mask and in the lower window holder

were radially inclined, and by use of the modulation system with the cylinder lens removed for the ultracentrifuge it was possible to adjust the radial position of this mask with it in its optimum translational position on the optic axis. Further details and photographs are included in chapter 4 and in an appendix to this work.

The alignment of the aperture mask achieved with the laser source proved compatible with the mercury source without further adjustment. The replacement of the mercury source was a relatively simple procedure in that the locking screw on the conventional source baseplate was merely loosened allowing the prism or mercury source to be interchanged at will.

During the alignment, it was frequently found convenient to employ a laser beam of greatly reduced intensity and this was achieved with the system using the modulator and the variac autotransformer. The laser has proved very useful in the critical alignment of the optical system, and the author feels that alignment is more important than correct focussing. The reasons for this are that an out of focus image is not necessarily inaccurate, whereas impaired alignment always results in distortion even with good image quality.

The camera/cylinder lens combination was focussed on the midplane of the cell using the special cell assembly supplied by Spinco and the procedure of Gropper[45]. This focussing was adopted as routine for all interference studies since the locations of the meniscus and base are optimumly defined as indicated by Trautman[43]. Again, the chromatic variations in positions of focus of the lenses for the red laser light (λ=632.8 nm) and the green mercury light (λ=546.1 nm) were small and the same fixed focus position was used for both sources.

4. EXPERIMENTAL

To test the above modulated laser system in the analytical ultracentrifuge, it was decided to use a standard sucrose in distilled water. This critical test is well established [12,21,44], and is based on the physical data of sucrose solutions of Gosting and Morris[50].

(a) MATERIAL AND METHOD

Standard sucrose was purchased from the National Bureau of Standards, Washington, D.C. 20234, U.S.A., and was their standard sample 17, lot No. 6340. Solutions were made up and corrected for air bouyancy according to the well document -ed procedure of La Bar[12]. However, owing to the long temporal coherence of our laser source (equation 2-54) it was not necessary to compensate the reference solution with a 1,3-Butanediol, and this was an immediate experimental advantage of laser usage. Fluoro-chemical FC 43 was used as a base for the solution column, and a 2.5^{o} double sector epoxy-resin cell was filled to the required levels according to the procedures of Van Holde[51] and/or Chervenka[52].

The sedimentation equilibrium experiments were carried out with the temperature control set at 25^{o} and a two cell An-D rotor was used with an appropriately weighted interference counterbalance. Sapphire windows were used throughout this work, and the physical length of the cell along the optic axis was a nominal 1.2 cm. The fringe patterns were photographed using Ilford HP3 hypersensitive panchromatic backed plates. The reason for using these plates were that they were obtainable in New Zealand and could be used to record both the laser and mercury patterns. However, the choice was an expedient compromiseand the author is well aware that other high contrast plates should be more suited to laser usage, and some thought is being given to this problem with particular reference to the requirements of the cell discussed in chapter 4.

The cells were torqued to 135 in-lbs using a " torqometer" serial number 1460. The length of the cell centrepiece was measured accurately in a micrometer and the compression was assumed to be similar to that quoted by La Bar[12]. These measurements were used in the evaluation of j^{o}, the fringe number corresponding to the initial concentration c^{o} which was itself computed from the weights of solute and solvent. In the evaluation of j^{o} it was assumed that the specific refractive increment of sucrose at the wavelength used (λ=632.8 nm) , was the same, within the required accuracy of the experiment, as that for the mercury green line (λ=546.1 nm) . The justifications for this assumption were

based on interference boundary forming experiments with sucrose solutions of lower concentrations from that used in the actual experiments ($c^{o} \sim 5.4 g/d\ell$), which indicated this to be the case. However, the accuracy of these measurements were not of the same order as those of Gosting and Morris[50] whose value for the specific refractive increment was 1.431×10^{-1} $m\ell/g$ under the applied conditions. Furthermore, the results obtained in the sucrose studies substantiated this assumption, since they were within the anticipated accuracy.

The plates were developed according to the manufacturers' instructions, and were measured with a Topcan Measuring Projector Model PP-30E fitted with a Type D two dimensional micrometer object table. The latter had a 50 x 25 mm movement with a least count of 0.005 mm, and could be revolved through 360^{o} with a 2' angular reading. A special perspex holder and clamps was designed and fitted to the object table to take the 10" x 2" plates from the analytical ultracentrifuge. In addition the author had access to a Gaertner two dimensional microcomparator that was used in the early studies. The profile projector was fitted with three magnifications (x10,x20,x50) with bayonet mounted projection lenses in a turret assembly for ease of change, and these projected object sizes of diameter 30 mm, 15 mm and 6 mm respectively onto a screen of effective diameter 300 mm.

The profile projector was fitted with a photographic attachment that replaced the projection screen, and this used $4\frac{3}{4}$" x $6\frac{1}{2}$" plates that were eminently suited for the densimetric measurements described in chapter 4.

The methods of analysis and the theory upon which these were based for the sucrose equilibrium studies are adequately explained in the thesis by LaBar[12], and will not therefore be repeated here in detail. Indeed the analysis of sedimentation-diffusion equilibrium studies employing interference optics is now sufficiently well established that it exists as a routine procedure in most laboratories employing an analytical ultracentrifuge.

A sucrose equilibrium fringe pattern that is

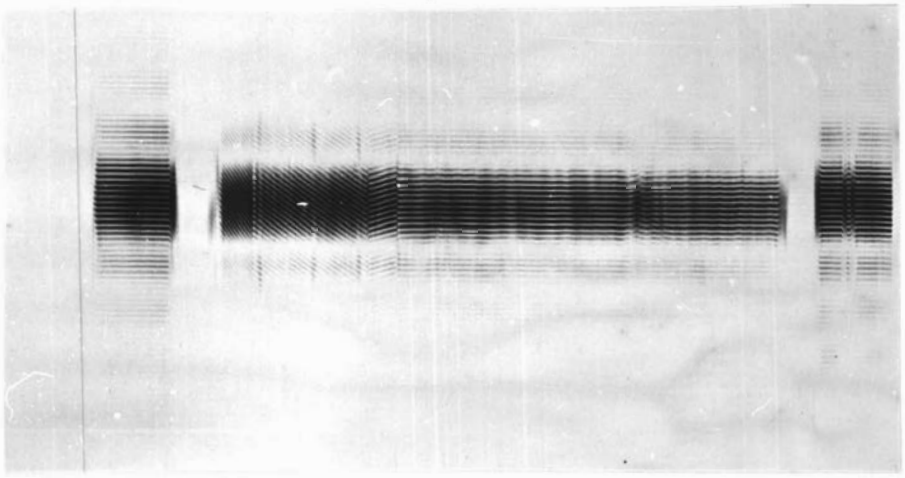

FIGURE 3-7(a): SUCROSE EQUILIBRIUM RAYLEIGH INTERFERENCE PATTERN WITH MODULATED LASER SOURCE. PHOTOGRAPHIC EXPOSURE 3 SECONDS.

Note: Pattern is the mirror image of the observed pattern owing to reproduction error.

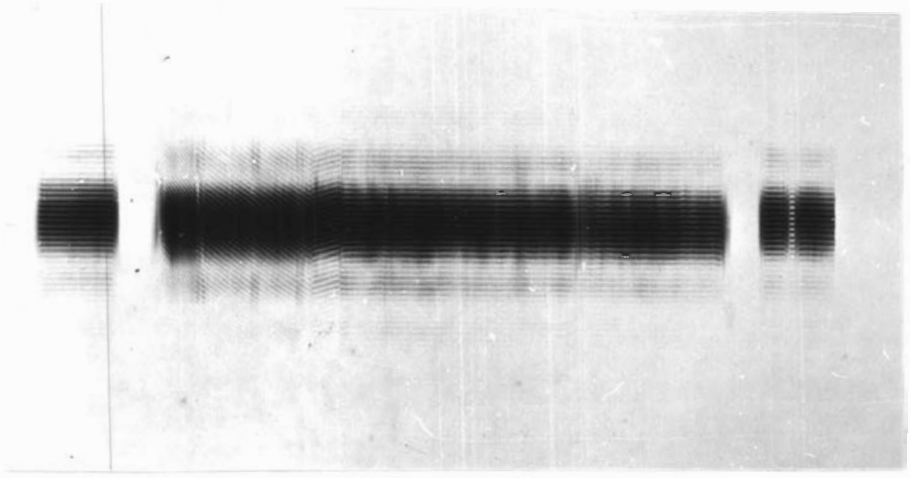

FIGURE 3-7(b): SUCROSE EQUILIBRIUM RAYLEIGH INTERFERENCE PATTERN (AS ABOVE) WITH NON-MODULATED LASER SOURCE. EXPOSURE 0.5 SECONDS.

Note: Pattern is again the mirror image of the observed pattern in the centrifuge.

typical of those obtained for both the modulated and non-modulated laser system is shown in figure (3-7). Unfortunately, owing to the limited temporal coherence of the mercury source it was impossible to obtain a fringe pattern with this source for comparison, owing to the concentration used. However, those familiar with the conventional interference optics will appreciate the additional clarity of the menisci associated with the use of the laser when compared with mercury patterns.

The relevant and typical experimental data applicable to the study shown are as follows:

Run No.18; Plate III(e); Date 27.2.70;

$j^o = 146 \pm 0.6$ fringes Density of Solution $\rho = 1.086$ g/mℓ

$\bar{v} = 0.618$ mℓ/g; $T = 298\ ^oK$ $(\Delta j)_{eq} = 33.8 \pm .1$ fringes.

$\omega^2 = 1.7447 \times 10^7\ s^{-2}$ $R = 8.314 \times 10^7$ ergs K^{-1} $mole^{-1}$

$(r_b^2 - r_m^2) = 5.8036 cm^2$

$$M^{app} = \frac{2RT}{\omega^2(1-\bar{v}\rho)(r_b^2 - r_m^2)} \frac{(\Delta j)_{eq}}{j^o} = 342.8\ (\pm\ 0.5\%)$$

(cf 342.3)

The more precise method of analysis using the slope of the $\ell n(c)$ versus r^2 graph gives an equally acceptable result, but the method of measuring the total corrected fringe count across the solution column at equilibrium $(\Delta j)_{eq}$ and the spread in its value for different measurements of the same experiment is a good quantitative measure of the possible experimental accuracy. An experimental survey of the accuracy with which the solution base (r_b) and meniscus (r_m) could be measured from different patterns of the same experiment showed these to be reproducible within the precision of the instruments, and indeed the major source of error was the exact location of the reference wire and not the solution menisci. This contrasts with the mercury patterns in which some subjective judgement is required in the determination of the exact locations of these important positions, and this introduces uncertainty in their location.

5. DISCUSSION

The sucrose equilibrium studies indicated, to our satisfaction, that the modulated laser system was capable of giving accurate experimental data from precise measurements

of the interference patterns. Indeed the accuracy with which the meniscus and base could be determined on the patterns is such as to leave little to be desired compared with the experimental accuracy with which other parameters may be measured currently. It would be wrong to imply that the current accuracy and excellent quantitative results were achieved without any problems. Although excellent fringe patterns were obtained for the system from the outset, the analysis revealed systematic errors in both the analysis and optical alignment. However, by careful and thorough checking of the instrument and data analysis these have been overcome and the author feels that the experimental data obtained from the instrument is now not far from optimum with the present ultracentrifuge.

The modulated laser system described herein has been in use in the ultracentrifuge since early 1969 in various forms. During this time it has been used in many different macromolecular studies and the results achieved have been comparable and in most cases superior to those obtained with the non-modulated mercury source. In certain cases where the fringe patterns with the mercury source have been poor and indistinct, the polarized laser source has produced excellent patterns from which quantitative measurements could be made. This has been particularly useful in high speed equilibrium work when the steep gradients have rendered the conditions too severe for the mercury source, (see appendix for Yphantis patterns).

A good example of the use of the laser system, for comparison with the mercury system, in a low speed equilibrium study is given in Figure (3-8). Here the system was a chinese gooseberry (Kiwi fruit) enzyme protein ($M \sim 27{,}000$) in a suitable buffer. The plates show the equilibrium patterns obtained both with the laser and the mercury source. The synthetic boundary patterns used in the evaluation of j° for the system are shown in figure (3-9). The ratio of the fringe counts $j^{\circ}He/Ne : j^{\circ}Hg$ measured from these patterns were found to be in the same ratio as $\lambda_{Hg} : \lambda_{He/Ne}$ within experimental accuracy of the experiment. This indicates

(a) (b)

FIGURE 3-8 COMPARISON OF THE MERCURY AND LASER SOURCES USING AN ENZYME PROTEIN SEDIMENTATION DIFFUSION EQUILIBRIUM EXPERIMENT. (a) CONVENTIONAL MERCURY SOURCE AND (b) MODULATED HELIUM-NEON GAS LASER SOURCE. Note fringe patterns in the air/solvent and oil/solvent regions owing to the long temporal coherence of the laser light source.

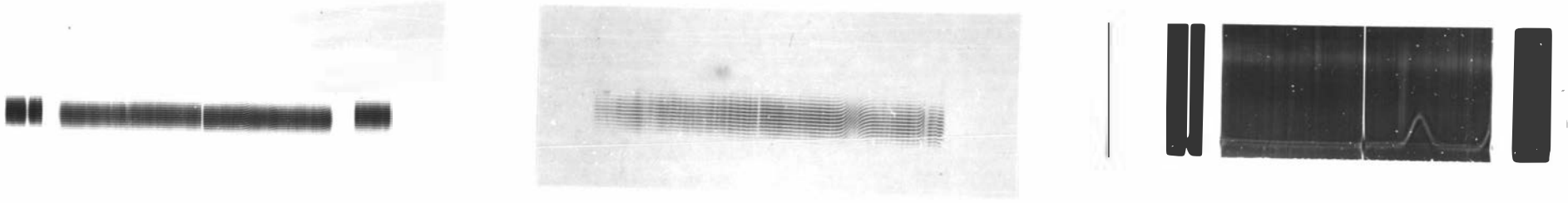

(a) (b) (c)

FIGURE 3-9

SYNTHETIC BOUNDARY PATTERNS FOR THE ENZYME PROTEIN DEPICTED IN FIGURE 3-8. (a) MERCURY SOURCE (b) MODULATED LASER SOURCE. Note that this exposure was taken without a reference cell pattern. (c) SCHLIEREN PATTERN OF THE BOUNDARY TAKEN WITH THE MERCURY SOURCE.

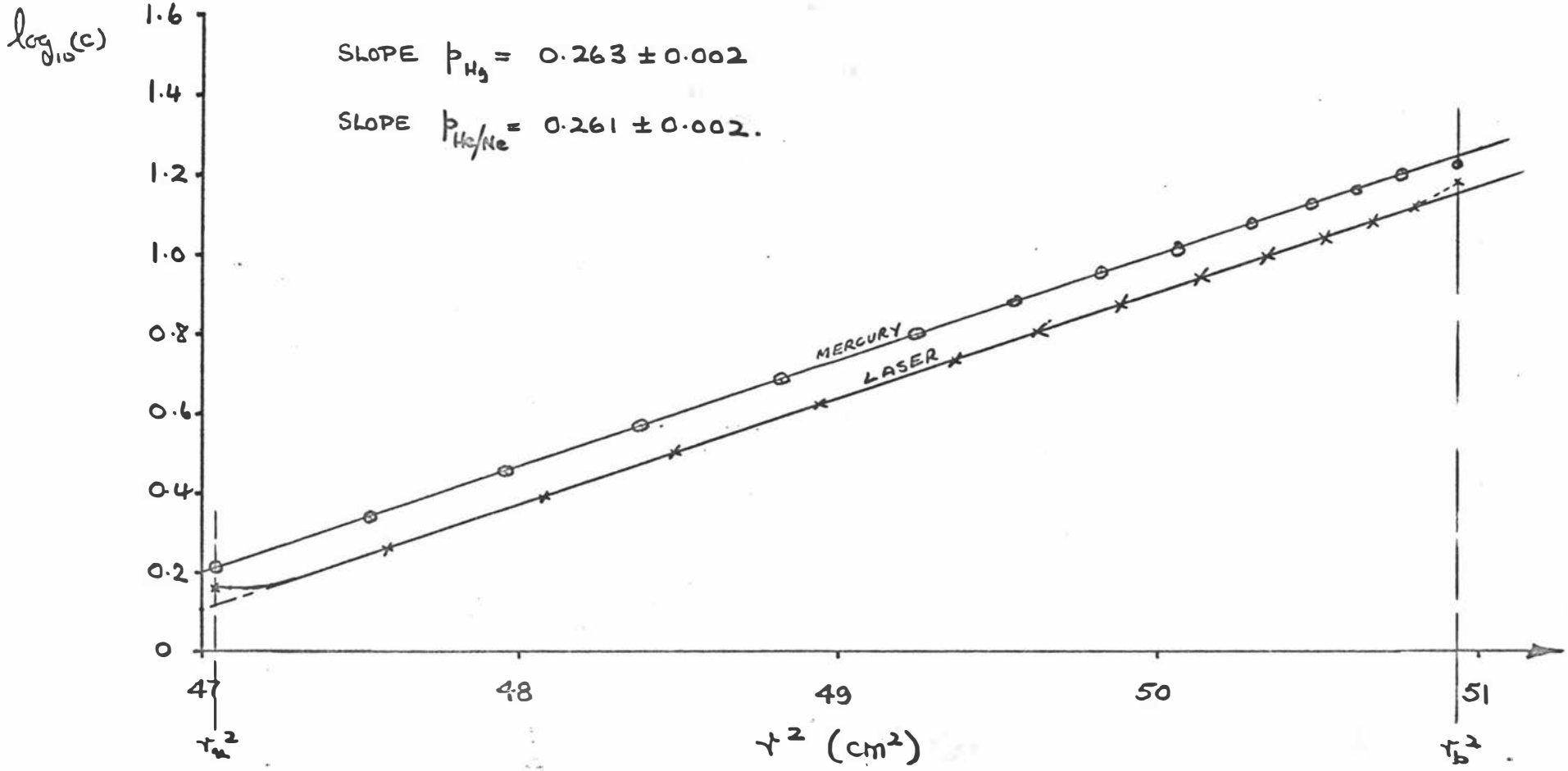

FIGURE 3-10. COMPARATIVE PLOTS OF $\log_{10} c$ versus r^2 FOR THE MERCURY AND LASER SOURCES.

that for this protein system, as was found for sucrose, that the specific refractive increment has a neglible chromatic variation between the green and red regions of the visible spectrum. The graphs of log j(r) versus r^2 are drawn on the same diagram in figure (3-10) for comparison and are seen to be linear and of the same slope within the errors of experiment. However, the upward curvature at the meniscus for the laser plot may be significant since the log c plot is accurate to within $\pm$ .006 and suggests that low molecular weight component was present in very small quantities. This was not important in the study being undertaken, but would have been missed if the mercury source alone had been used, and is an indication of enhanced sensitivity of the optics with the laser source. The latter measurements were made for a colleague, and so were not pursued by performing the experiment again at a higher speed to test this initial finding. However, all the experimental plots for the sucrose equilibrium work of log c versus r^2 were characterized by " perfect" linearity from the equivalent base to meniscus positions, and this substantiates in a small measure the conclusion drawn.

At this stage it is convenient to consider the effect of changing the wavelength of the interferometer light from the green (λ=546.1 nm) to the red (λ=632.8 nm). Our studies have shown from synthetic boundary cell measurements that the specific refractive increment remains constant within the accuracy of the experiments.

The changes in concentration at a radial position x are measured in terms of fringe difference ($\Delta j(x)$) given by

$$\Delta j(x) = \frac{t.\Delta n(x)}{\lambda} \qquad (3\text{-}1)$$

Here t is the cell thickness (often 1.2 cm in the current work), λ is the wavelength used and $\Delta n(x)$ is the refractive index difference change between solution and solvent corresponding to a solute concentration change $\Delta c(x)$. Obviously, $\Delta n(x)$ is given by

$$\Delta n(x) = \left(\frac{\partial n}{\partial c}\right) \Delta c(x) \qquad (3\text{-}2)$$

where $(\frac{\partial n}{\partial c})$ is the specific refractive increment. If the latter is a constant, as the available evidence indicates, it will be apparent from equations (3-1) and (3-2) that

$$\Delta j(x) \alpha \frac{1}{\lambda} \qquad (3\text{-}3)$$

for a given fixed concentration change, and hence the sensitivity of the system is reduced for the longer wavelengths. In a 1.2 cm cell a displacement of 1 fringe ($\Delta j = 1$) corresponds to a concentration change of about 0.25 mg/mℓ for most proteins when the mercury green line (λ = 546.1 nm) is used. The above analysis indicates that change of 1 fringe with the laser source corresponds to a concentration change of about 0.29 mg/mℓ, i.e., a reduction of about 8% in the sensitivity, since for both systems the precision of fringe measurement is similar i.e., $\pm$ 0.02 fringes. However, the advantages of the laser, explained above, more than compensate for this inherent disadvantage. Moreover, the system described would be compatible with the use of the newly developed helium-selenium laser[53] which has suitable outputs at 497.6n m, 4.99.3 nm, 506.9 nm, 522.8 nm and 530.5 nm. The blue laser light would be superior to the mercury green, and have all the advantages of the laser,

The modulation facility enables individual sectors in the double sector cell to be viewed independently during an experiment owing to the various permissible orientations between the cell diaphragm in the lower window holder and the fixed aperture mask. Examples of the patterns achieved using this facility are shown in figure (3-11) for interest — (see also figure 3-12). In particular the "fine aperture" slit pattern should be noted, and results from an alignment between cell and aperture mask slightly before or after the optimum alignment is reached. Indeed the optimum alignment experimentally, is characterized by the narrowest diffraction envelope, since as the effective slit aperture decreases the diffraction envelope widens and vice versa, as indicated in the theory of chapter 1 of this work.

The ability to view the cell in its various

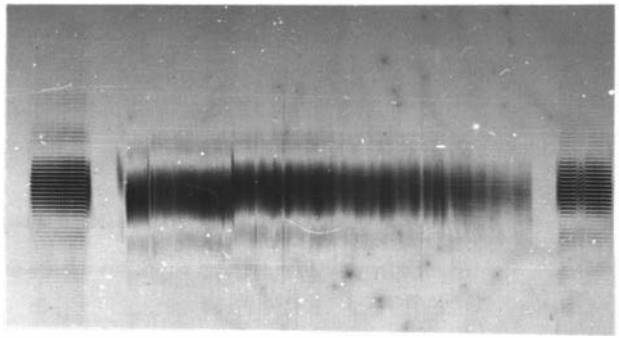

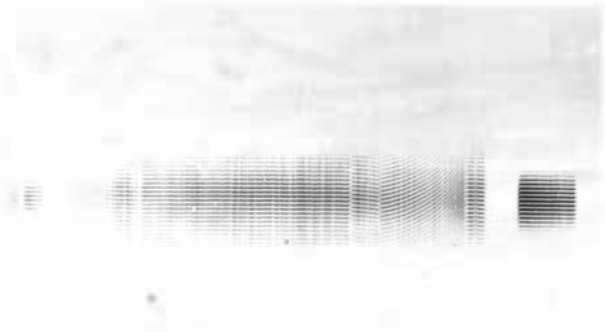

(a) (b)

FIGURE 3-11 TYPICAL EXAMPLES OF THE MODULATION FACILITY IN THE ULTRACENTRIFUGE.

(a) VIEW OF THE SOLUTION COLUMN ONLY IN A RAYLEIGH INTERFERENCE EXPERIMENT. Note absence of fringes and the normal interference pattern that has been exposed separately on the plate.

(b) 'FINE' SLIT INTERFERENCE PATTERN OBTAINED BY VIEWING THE CELL IN THE INTERFEROMETER IN A POSITION SLIGHTLY AWAY FROM OPTIMUM.

Note normal interference pattern and (in this case) nonuniform light intensity.

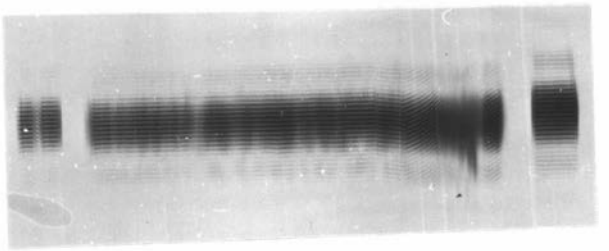

(a)

(b)

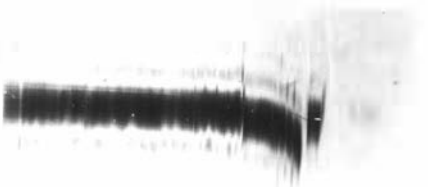

(c)

(d)

FIGURE 3-12 PATTERNS OBTAINED WITH THE LASER SYSTEM DURING A VERY HIGH SPEED EQUILIBRIUM EXPERIMENT, SHOWING THE ORIGIN OF THE FLOGGING FLARE ASSOCIATED WITH ASYMMETRICAL APERTURE MASK USAGE.

(a) NON-MODULATED PATTERN.

(b) MODULATED PATTERN

(c) SOLUTION SECTOR VIEWED THROUGH OFF-AXIS APERTURE.

(d) SOLVENT SECTOR VIEWED THROUGH RADIAL APERTURE.

orientations with the fixed aperture mask enables us to explain a phenomenon sometimes observed in high speed equilibrium studies using the asymmetrical mask. This was the appearance of a flare in the recorded patterns when extreme concentrations or speeds were being employed. This flare was obviously associated with the steep concentration gradients present and was troublesome with the mercury system since one was uncertain of its origin and effects on the fringe data, as the patterns under these conditions were invariably poor. An example of the occurence of this phenomenon is shown in figure (3-12) in which a low speed equilibrium experiment was inadvertently run at too high a speed. Indeed the mercury source was incapable of giving a worthwhile fringe pattern in this case but the modulated laser pattern indicates the fringe pattern (for what it is worth), since packing at the base of the solution column is evident. However, the non-modulated laser pattern (a) clearly shows the flare whereas in the modulated pattern (b) it is obviously absent. Its origin is clear in pattern (c) which is a picture of the solution sector viewed through the asymmetrical aperture of the mask and is caused by a steep gradient viewed by the system non-radially and off-axis. The solvent sector viewed through the radial aperture is seen in pattern (d), and in this case no flare is present. This phenomena is frequently observed in high speed equilibrium studies employing the multichannel Yphantis type cells with the asymmetrical aperture, but the above experimental evidence has shown that it is only troublesome in that it masks the fringe pattern, and does not upset the basic reliability of data obtained from the pattern. It was the observation of this gradient together with the diffraction effects at the solution base that prompted the author to undertake the theoretical study recorded in chapter 5 of this thesis, concerned with the effects of refractive index gradients.

The routine monitoring of the rotor frequency via the modulator unit and digital frequency meter introduced an additional facility for the performance of time dependent experiments. This is especially useful in the determination of the diffusion coefficients from the approach

to equilibrium measurements by procedures such as that of LaBar[12]. The timing of an experiment with the system can be determined to an accuracy of a few seconds if desired with the photographic exposures required being about one second. Furthermore, the enhanced precision with which the meniscus and/or base position can be measured holds promise of applications in various proposed techniques for the evaluation of molecular weights at early times in these regions before the system attains equilibrium throughout.

In addition, the system stressed the desirability of positioning the cell and counterbalance in precise radial alignment in the rotor. We do not as yet possess a microscope aligning tool (Spinco part 332 308), and had to be content with aligning the cells and counterbalances according to the scribe marks on the various assemblies. For the counterbalance small inaccuracies in the alignment became apparent during the course of experiments, since it was found that optimum timing for the inner reference invariably did not coincide with that for outer reference and the order varied from experiment to experiment. An explanation for this phenomenon is that the reference cell is slightly non-radial, and the variation in times between which the two reference holes are optimumly aligned in the interferometer, is an indication of the non-radiality of the counterbalance. The effect is obviously small, and indicates the sensitivity of the modulation timing circuitry that allows such observations to be made, and infers that cell alignment could be improved.

Finally, it is appropriate to mention some of the problems associated with optical imaging using the highly coherent laser illumination. The problems associated with large scale intensity variation across the image have been overcome to a large extent (see figure 3-7), but problems inherent to the high degree of coherence still persist. For the Rayleigh system the mercury source is quaisi-monochromatic, and so the spatial frequency spectrum of the image intensity will be similar for this as for the laser illumination. However, two phenomena become particularly troublesome when the highly coherent laser illumination is employed. Firstly, there is the " speckle effect" which

is a direct consequence of the optical roughness of the object, and produces a granular effect on the image. The size of the " speckles" are roughly the size of the resolution area on the object. Secondly, highly coherent illumination is particularly sensitive to optical imperfections such as dust particles that may exist along the path to an observer. The pronounced diffraction patterns associated with the imperfections are superimposed on the image - see air/air column of figure 3-7. The latter is present with the mercury source but the effects are not so pronounced. Indeed both of the above effects may be minimized (theoretically) by placing a moving scatterer e.g., ground glass in the illuminating beam.

6. CONCLUSION

In this chapter a modulated laser system for use with the interference optics in the analytical ultracentrifuge has been described. The experimental tests have shown that the interference data obtained using this system are reliable and of a comparable if not greater accuracy than those obtained with the conventional non-modulated mercury system, with which it is compatible. Furthermore, the laser has served as an additional tool in the critical alignment of the Interference/Schlieren optics of the instrument, and has therefore contributed to the reliability of the same. The tests have shown the laser to be superior under conditions of severe concentration and speed, and its potential in multicell usage in the rotor is obvious. The routine and accurate monitoring of the rotor frequency enables accurate transient experiments to be performed, and this is a useful additional facility for the study of macromolecules.

In addition to the above advantages is the increased precision with which the menisci positions may be determined in an experiment using a laser source. This lends promise of employing the interference optics for accurate end of column experiments when appropriate. Naturally, the development and improvement of the instrumentation is a continuing process, and concomitant with the above will be the application of new methods and techniques that were precluded in previous work owing to experimental shortcomings. However, the discussion in this chapter has indicated in some measure the current performance of the modulated laser system described. The system has been operating in the laboratory since early 1969 in more or less its present form and its reliability under normal laboratory conditions has been proven.

CHAPTER 4

DEVELOPMENT AND PRELIMINARY EXPERIMENTS ON A NEW CELL FOR INTERFERENCE STUDIES IN THE ANALYTICAL ULTRACENTRIFUGE.

1. INTRODUCTION

The use of interference optics in the analytical ultracentrifuge has been validated fully both in this thesis and elsewhere[12,19,21,54-56]. It has been shown in chapter 1 that the determination of the concentration distribution of the solute in the centrifuge cell requires the evaluation of $n(x)$ in the interference system. Here n is the difference between the refractive index of the solution and solvent (assumed proportional to the solute concentration), and x is the radial distance from the axis of rotation to a given position in the centrifuge cell. The theory indicates, for the double sector Rayleigh interference cell, that n is characterized by a vertical shift in the overall fringe pattern. In other words the phase advance introduced by the solution cell relative to that of the solvent (reference) cell (which is characteristic of the solute concentration), produces a displacement in the vertical (ξ') direction of the interference fringes that are localised in the focal plane ($\eta'\xi'$) of the upper collimating lens L_2. By means of the camera/cylinder lens combination in the ultracentrifuge, the fringes are focussed in the vertical plane onto the photographic plate together with a magnified version of the radial cell coordinates. From microcomparator measurements obtained from the photographic plate the desired concentration distribution in the centrifuge cell is determined.

In practice the alignment of the photographic plate in the true radial direction under the microcomparator is critical, since besides the obvious small radial error the misalignment would result in a systematic vertical shift in the fringe system as the plate is scanned radially producing an effective error gradient. An idea of the required precision of alignment may be gauged from the fact that fringe displacements can be measured to an accuracy of about 0.02 fringes on the photographic plate. Practical plate alignment is accomplished by use of the fringe system associated with a reference cell that is inserted in the rotor separate from the actual cell during the experiment. The reference cell includes the wire of known distance from the axis of rotation (x_w), and the

interference pattern associated with the reference cell is shown in the experimental plates of chapter 3 of this thesis (e.g. figure 3-7). The problem of plate alignment in the comparator is not new and experimental procedures have been devised to help minimise errors from this source. However, the problem is inherent in the Rayleigh system in which the concentration increments are characterized by vertical fringe displacements.

The cell proposed and designed by the author and discussed here overcomes the above problem, since as will be shown both theoretically and experimentally n is characterized by fringe intensity variation rather than a fringe displacement. The cell is based on a concept first proposed by Zernicke[58] in 1950, in which the two slits of Young's classical experiment are replaced by three slits. The former is the basis of the Rayleigh interference system. Marechal et al[59] have used the concept of the three slits in an interferometer used for the measurement of very small phase differences between liquids and solids, and in particular for the measurement of thin films for which it has proved both sensitive and convenient.

2. THEORETICAL

(a) BASIC THEORY WITH NON ABSORBING SOLUTIONS

Theory and notation proposed and defined in chapter 1 of this thesis will be used in this analysis. The basic system with the triple aperture mask is shown in figure 4-1 and should be compared with figure 1-4 applicable to the double slit Rayleigh system. By analogy with figure 1-5 the aperture mask is a pure intensity object and may be represented by

$$f(y) = \Pi(y) \otimes \left[\delta(y) + \sum_n \delta(y-y_n)\right] \qquad (4\text{-}1)$$

Here $y_n = \pm \frac{b}{2}$, and $\otimes$ and $\delta(y)$ represent convolution and a δ-function respectively. As usual the complex amplitude distribution of the electric field vector in the focal plane of lens L_2 arising from this object is given by

$$E = \mathcal{F}\{f(y)\} = \mathcal{F}\{\Pi(y)\}\,\mathcal{F}\{\delta(y) + \sum_n \delta(y-y_n)\} \qquad (4\text{-}2)$$

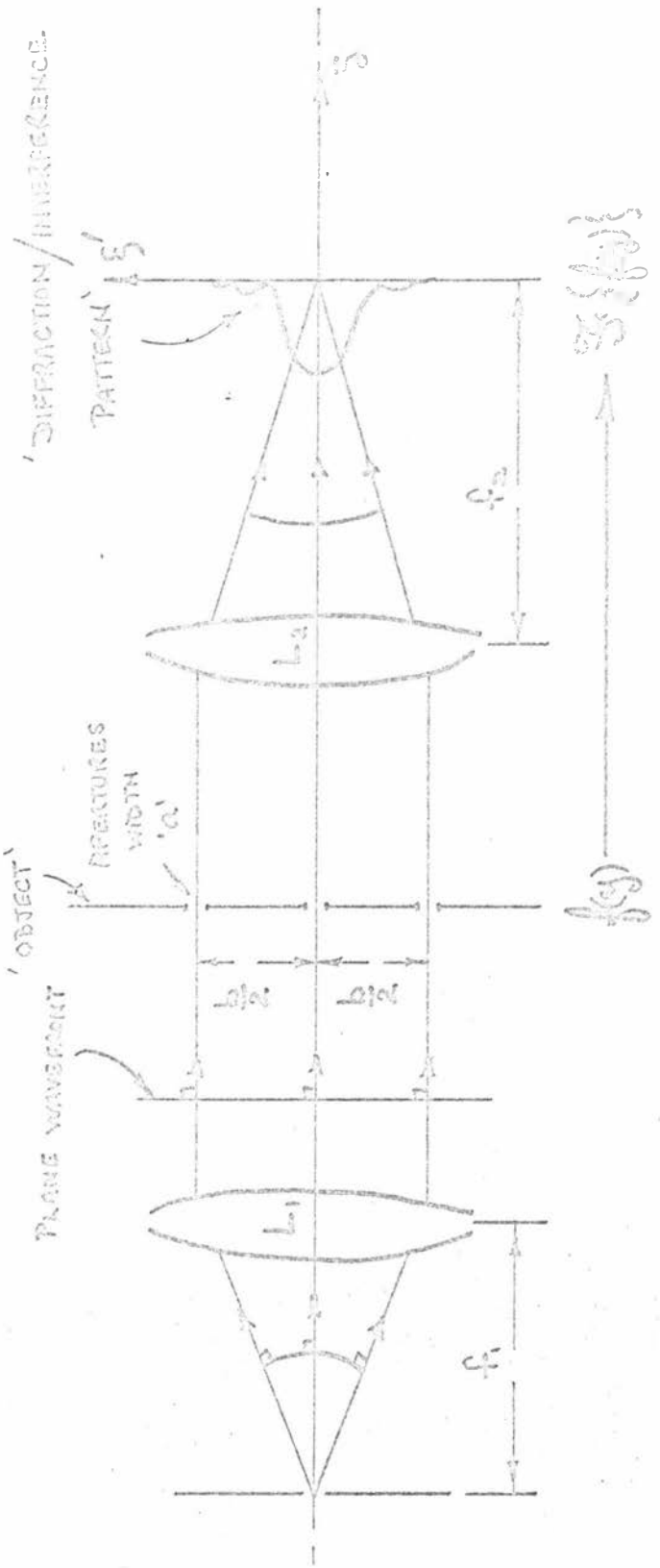

FIGURE 4-1. THE BASIC INTERFERENCE SYSTEM "WITH THE TRUTH AS SEEN BY KANT."

wherein use has been made of equation (4-1) and the convolution integral[26].

If $$\phi_3(y) = \delta(y) + \sum_n \delta_{(y-y_n)} \qquad (4\text{-}3)$$

then $$\mathcal{F}\{\phi_3(y)\} = \mathcal{F}\{\delta(y)\} + \mathcal{F}\left\{\sum_n \delta_{(y-y_n)}\right\} \qquad (4\text{-}4)$$

and for the object dimensions depicted in figure (4-1) it may be shown that

$$\mathcal{F}\{\phi_3(y)\} = 1 + 2\cos\left(\frac{k\,b\sin\alpha}{2}\right) \qquad (4\text{-}5)$$

Using this result in conjunction with equation (4-2) and (1-12) we obtain

$$E = \frac{a\,\sin\left(\frac{k\,a\sin\alpha}{2}\right)}{\left(\frac{k\,a\sin\alpha}{2}\right)}\left[1 + 2\cos\left(\frac{k\,b\sin\alpha}{2}\right)\right] \qquad (4\text{-}6)$$

If α is small as is usual practice $\sin\alpha = \alpha$ and equation (4-6) becomes

$$E = a\,\mathrm{sinc}\left(\frac{k\,a\alpha}{2}\right)\left[1 + 2\cos\left(\frac{k\,b\alpha}{2}\right)\right] \qquad (4\text{-}7)$$

As usual the observed intensity of the diffraction/interference pattern is obtained from equations (2-2) and (4-7) i.e.

$$I = E\,E^* = a^2\mathrm{sinc}^2\left(\frac{k\,a\,\alpha}{2}\right)\left[1 + 4\cos\left(\frac{k\,b\,\alpha}{2}\right) + 4\cos^2\left(\frac{k\,b\,\alpha}{2}\right)\right] \qquad (4\text{-}8)$$

This result should be compared with equation (1-16) which is the equivalent pattern for the double aperture Rayleigh mask. Again the interference term (in square brackets) is intensity modulated by the single slit diffraction pattern, and photographs showing the fringe patterns associated with equations (1-16) and (4-8) are shown in figures 4-11(b) and 4-11(c) for comparison. The phase variations introduced by the centrifuge cell modify these patterns and this enables the concentration distribution within the cell to be determined.

If now a triple sector (Lewis) cell is inserted with the mask into the focal plane of lens L_2 so that the central sector contains solution and the two outer sectors solvent, the combination will constitute a phase/intensity

object. By use of equation (1-23) and (4-4) we may write down directly the equation representing the complex amplitude of the electric field vector in the focal plane of lens L_2 for this arrangement,

i.e.,

$$E' = \exp^{-i\Theta}\mathcal{F}\{\Pi(y)\}\mathcal{F}\{\delta(y)\} + \mathcal{F}\{\delta(y)\}\mathcal{F}\{\sum_n \delta(y-y_n)\} \qquad (y_n = \pm b/2) \qquad (4\text{-}9)$$

whence by mathematical manipulation and analysis

$$E' = a\,\mathrm{sinc}(\frac{k\,a\,\alpha}{2})\left[2\cos\frac{k\,b\,\alpha}{2} + \cos\Theta - i\sin\Theta\right] \qquad (4\text{-}10)$$

Again the observed intensity of the diffraction/interference pattern in the $(\eta'\xi')$ plane is given by

$$I' = E'E'^{*} = a^2\mathrm{sinc}^2(\frac{k\,a\,\alpha}{2})\left[1 + 4\cos(\frac{k\,b\,\alpha}{2})\cos\Theta + 4\cos^2(\frac{k\,b\,\alpha}{2})\right] \qquad (4\text{-}11)$$

By comparison with equation (1-26) for the double sector Rayleigh system it is noted that the phase information with which we are concerned is again located within the interference term. In practice $a \ll b$ and so the diffraction envelope may be ignored for the moment, and we concern ourselves solely with the interference term

i.e., $I = 1 + 4\cos(\frac{k\,b\,\alpha}{2})\cos\Theta + 4\cos^2(\frac{k\,b\,\alpha}{2})$

or $$I = 1 + 4\cos\gamma\cos\Theta + 4\cos^2\gamma \qquad (4\text{-}12)$$

where $\gamma = (\frac{k\,b\,\alpha}{2})$.

We note if $\Theta = 0$, the interference term expressed in equation (4-12) reduces to that given by equation (4-8) for the mask alone as expected.

The fundamental importance of equation (4-12) is that the intensity of <u>any</u> given fringe (i.e. constant γ) in the pattern corresponding to a given position in the cell will depend on the phase advance introduced by the solution relative to that from the solvent at that position. In practice $\Theta = k\,t\,n(x)$ (see equation 1-21) where t is the thickness of the centrifuge cell, $n(x)$ is the refractive increment at radial position x in the

cell and $k = 2\pi/\lambda$. Thus it is possible theoretically to determine the concentration distribution in a centrifuge cell from the intensity variations of any fringe in the observed interference pattern. It is convenient both experimentally and theoretically to consider the central fringe for which $\alpha = 0$. In any pattern this fringe has optimum overall intensity, and lies on a radius on the optic axis in a correctly aligned system. From equation (4-12), $\gamma = 0$ and hence the intensity of this fringe is given by

$$I_o = 5 + 4\cos\theta \qquad (4\text{-}13)$$

It will be noticed that this simple mathematical expression is never zero. A qualitative explanation for this phenomena was given by Zernicke[58] who indicated that the outer slits (reference) contribute twice as much light to the interference pattern as does the central slit (solution) from its single aperture. This may be remedied by making the central slit pertaining to the solution of double the width of the individual outer slits. Naturally, the use of non absorbing solutions and solvents have been assumed throughout the above analysis. By carrying out an analysis similar to the above, but now assuming the central slit to be of width $2a$ and the outer slits of width a, it may be shown that the complex amplitude of the electric field vector in the focal plane of lens L_2 is given by

$$E'_2 = a\,\mathrm{sinc}\,\frac{k a \alpha}{2}\left[2\cos\left(\frac{k a \alpha}{2}\right)\left[\cos\theta - i\sin\theta\right] + 2\cos\left(\frac{k b \alpha}{2}\right)\right] \qquad (4\text{-}14)$$

and the observed intensity is given by

$$I'_2 = 4a^2\,\mathrm{sinc}^2\left(\frac{k a \alpha}{2}\right)\left[\cos^2\left(\frac{k a \alpha}{2}\right) + 2\cos\left(\frac{k a \alpha}{2}\right)\cos\left(\frac{k b \alpha}{2}\right)\cos\theta + \cos^2\left(\frac{k b \alpha}{2}\right)\right] \qquad (4\text{-}15)$$

For the central fringe $\alpha = 0$, and hence

$$I'_o = 8a^2\left[1 + \cos\theta\right] \qquad (4\text{-}16)$$

The diffraction term has been included in equation (4-16) and we note in this case that as Θ varies between 0 and π radians the intensity of the central fringe varies between $16\ a^2$ and zero (see figure 4-7). Physically, when $\Theta = 0$ the intensity of the central maximum is $16\ a^2$ as expected since it arises from an effective aperture width $4a$.

This general theoretical analysis, derived by the author, is applicable to the use of a triple cell in the analytical ultracentrifuge where large phase differences are measured. Zernicke[58] and Marechal et al[59] have been concerned with the application of concept to the measurement of very small phase differences and in particular to very small phase variations when $\Theta = \pi/2$ radians and the sensitivity is maximum. Indeed, the sensitivity $(\frac{dI}{d\Theta})$ is very much a function of Θ as will be appreciated by differentiating equation (4-16), and the published work[58,59] has been either qualitative or specific.

(b) ABSORBING SOLUTIONS IN CENTRAL SECTOR

In view of the above analysis, it is of theoretical interest initially to consider a situation in which the overall light intensity from the solution is reduced whilst light from the outer reference sectors remains constant. This situation is unlikely to occur in practice, since it assumes a solution characterised by an absorption that is independent of both solvent and solute concentration

Let us assume that the solution has an **amplitude** transmission factor 's' for the radiation used in the system such that $0 \leq s \leq 1.0$. Naturally the absorption is given by (1-s). The complex amplitude of the electric field vector in the focal plane of the upper collimating lens L_2 that results from the central sector of the cell is now given by

$$\bar{E}_c'' = s \exp^{-i\Theta} \mathcal{F}_e\left\{\prod^{2}(y)\right\} \qquad (4\text{-}17)$$

Here Π^2 is the limiting central aperture function of width 2a in the pupil of lens L_2 and all other terms have been defined previously.

By analogy with equation (4-9) the overall complex amplitude of the electric field vector in the focal plane of lens L_2 from all apertures is

$$\bar{E}'' = s \exp^{-i\theta} \mathcal{F}\{\Pi^2(y)\}\mathcal{F}\{\delta(y)\} + \mathcal{F}\{\Pi(y)\}\mathcal{F}\{\Sigma\delta(y-y_n)\} \quad (y_n = \pm \tfrac{b}{2}) \quad (4\text{-}18)$$

Whence by mathematical analysis equation (4-18) may be written in terms of previously defined geometrical parameters

i.e.

$$\bar{E}'' = 2a\ \mathrm{sinc}\left(\frac{k\,a\,\alpha}{2}\right)\left[s\cos\left(\frac{k\,a\,\alpha}{2}\right)\left[\cos\theta - i\sin\theta\right] + \cos\left(\frac{k\,b\,\alpha}{2}\right)\right] \quad (4\text{-}19)$$

As usual the observed intensity $I'' = \bar{E}''\bar{E}'^{*}$, which from equation (4-19) may be shown to be adequately represented by

$$I'' = 4a^2\mathrm{sinc}^2\left(\frac{k\,a\,\alpha}{2}\right)\left[\left(s\cos\frac{ka\alpha}{2}\cos\theta + \cos\frac{kb\alpha}{2}\right)^2 + s^2\cos^2\frac{2ka\alpha}{2}\sin^2\theta\right] \quad (4\text{-}20)$$

By analogy with equation (4-12) it has been shown that all the information regarding the solution concentration is contained in the interference term of the expression, and moreover that all information is contained within the intensity variations of any radial (horizontal) fringe within the pattern. As before the central fringe is both theoretically and experimentally convenient, and by use of equation(4-20) the effects of an absorbing solution on the intensity of the central fringe may be evaluated, since obviously for this fringe $\alpha = 0$. This being so,

$$I_c'' = 4a^2\left[1 + s^2 + 2s\cos\theta\right] \quad (4\text{-}21)$$

where I_c'' is the intensity of the central fringe arising from the use of a triple sector cell centrepiece in the

ultracentrifuge with an absorbing solution in the central sector.

When $s = 1.0$ we have a non-absorbing solution and equation (4-21) reduces to $8a^2\left[1 + \cos\theta\right]$, a result identical to that attained in equation (4-16) as expected. On the other hand, when $s = 0$ we have a non-transmitting solution and the intensity formulated in equation (4-21) becomes of magnitude $4a^2$. The latter result is physically reasonable since the central aperture is effectively excluded and the central fringe is the result of two similar apertures of width 'a' symmetrically displaced about the optic axis.

Of interest is the effect when $s = 0.5$, and equation (4-21) becomes $a^2\left[5 + 4\cos\theta\right]$. This result should be compared with equation (4-13) since the physical effect of having a solution with $s = 0.5$ in conjunction with a central aperture of width $2a$, is identical to having a non-absorbing solution with the central aperture of width a.

The above examples have shown that the results predicted by equations (4-18) and 4-21) are physically reasonable and compatible with the previous analysis for the triple sector (Lewis) cell.

The foregoing study is appropriate if the transmission or absorption of the solution is independent of the solute concentration, i.e. s = constant. However, if the absorption is proportional to the solute concentration ie., $s = s(x)$, then (as will be shown) we have at our disposal an additional and independent means of evaluating the concentration distribution in centrifuge cell. To evaluate $s(x)$ one would make measurements of the fringe visibility or contrast at points in the interference pattern corresponding to various positions within the centrifuge cell, as will be appreciated from the following.

It is assumed that the spatial coherence of the light, and other sources of spurious intensity changes in the interference pattern are constant or may be eliminated from the experiment. From equation (2-6) the fringe visibility or contrast ($\emptyset$) is defined by the usual expression.

$$\phi = \frac{I''_{max} - I''_{min}}{I''_{max} + I''_{min}} \qquad (4\text{-}22)$$

in which I''_{max} and I''_{min} are the maximum and minimum intensity of the fringes respectively at a given position. From equation (4-22) it is apparent that ϕ varies in the range $0 \leq \phi \leq 1.0$, and from equation (4-21) we may find analytical expressions for both I''_{max} and I''_{min}.

i.e. $$I''_{max} = 4a^2\left[1 + s^2 + 2s\right] \qquad (4\text{-}23)$$

and $$I''_{min} = 4a^2\left[1 + s^2 - 2s\right] \qquad (4\text{-}24)$$

and these have been plotted in figure (4-2a). By use of equations (4-22) - (4-24) we may determine the fringe visibility (ϕ) in terms of the transmission factor s

i.e., $$\phi = \frac{2s}{1 + s^2} \qquad (4\text{-}25)$$

and this expression is represented graphically in figure (4-2b). This graph could be used in the evaluation of the concentration distribution (c(x)) in the centrifuge cell, since from s(x), c(x) may be determined, and s(x) can be evaluated from measurements of $\phi(x)$ on the photographic record of the fringe pattern.

In practice for interference work the solution has neglible absorption, i.e. $s \simeq 1.0$, and we note from figure (4-2b) that the variations in fringe visibility are very small in this region. Indeed for the range $0.5 \leq s \leq 1.0$ the variation in fringe visibility is only 20% and thus even with absorbing systems in this range the precision of the interference system will be virtually unimpaired. Obviously, the use of the specific absorption in the determination of c(x) from ϕ is of little use in this region as is to be expected.

Figure (4-2b) indicates that the usage of the combined interference/absorption technique for the simultaneous determination of the concentration distribution in the centrifuge cell will involve a compromise. The

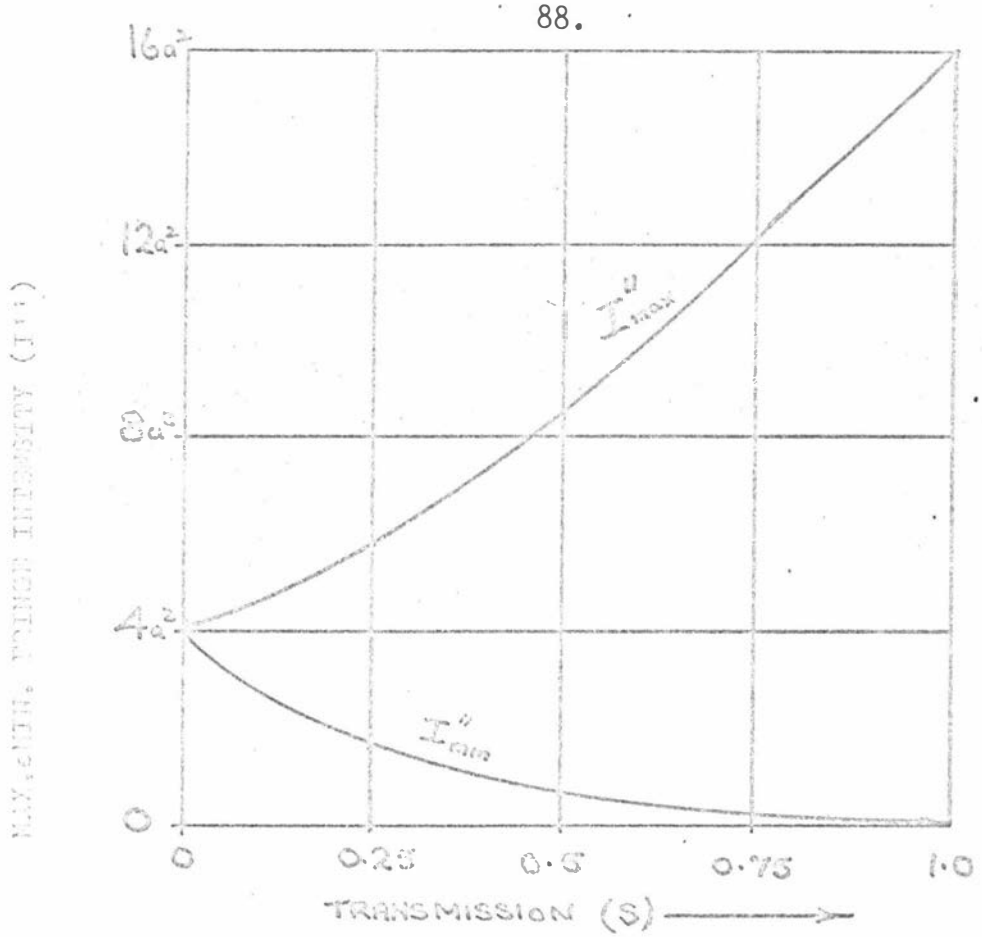

FIGURE 4-2(a). Maximum and Minimum Fringe Intensity versus Transmission Factor (s).

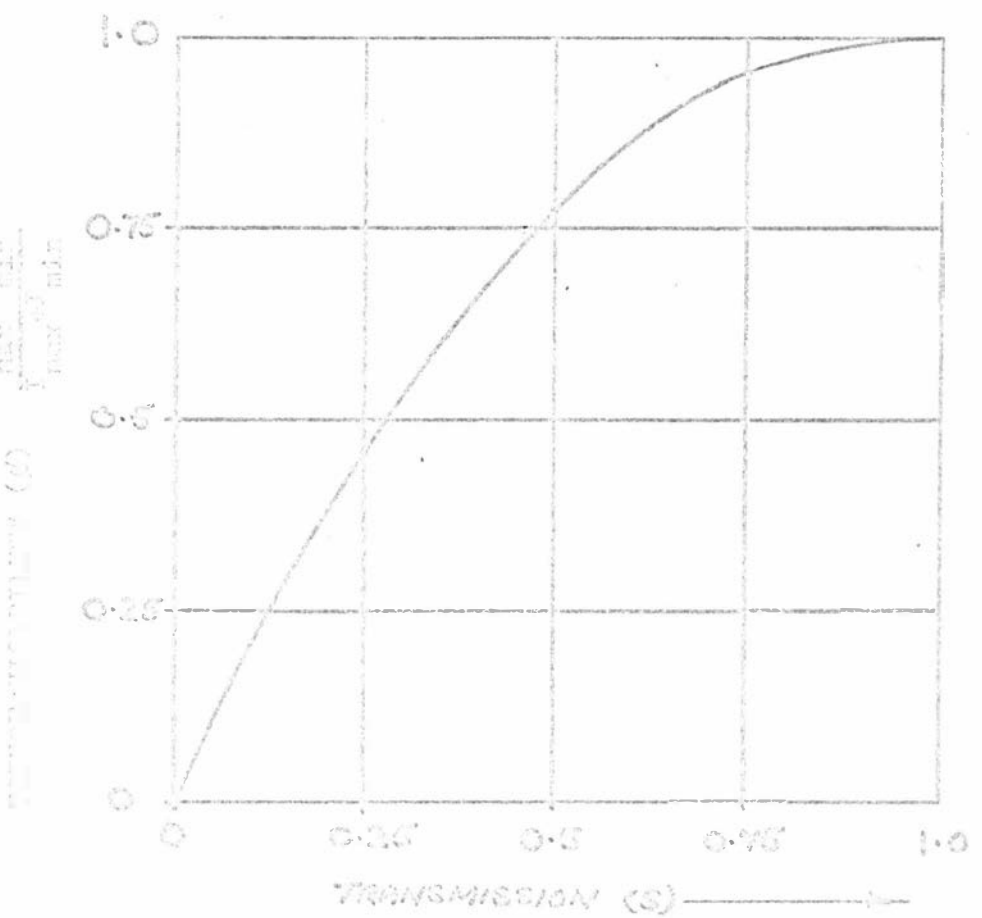

FIGURE 4-2(b). Fringe Visibility versus Transmission Factor (s).

sensitivity ($d\phi/ds$) of the absorption technique obviously increases as s decreases as will be seen from the slope of the $\phi(s)$ curve depicted in figure 4-2(b). On the other hand, a small s value must impair the accuracy of the interference measurements owing to a lack of fringe visibility.

In practice the optical density (O.D.) of the solution is proportional to the solute concentration (c)

$$\text{i.e.,} \quad \text{O.D.} = K'c = \log \frac{1}{T} \tag{4-26}$$

Here K' is a constant and the transmission $T(= s^2)$ is the ratio of the transmitted to incident light intensity. From figure 4-2(b) the useful range of s for a combined interference/absorption system is given by $0.1 \leq s \leq 0.7$, since here the fringes are visible and ϕ varies about 0.25 to 0.9. At equilibrium the solute concentration at the meniscus (c_m) and base (c_b) of the solution column are typically $\frac{c^o}{2}$ and $2c^o$ respectively, where c^o represents the initial solute concentration of the solution. Using this information, together with the useful s range and equation 4-26, it may be shown that if the initial concentration gives a value $s^o = 0.4$, then $s_m = 0.6$ and $s_b = 0.16$, whereas if $s^o = 0.5$, then $s_m = 0.7$ and $s_b = 0.25$. This indicates that if s^o could be adjusted to have a value in the range $0.4 \leq s^o \leq 0.5$ e.g., by varying the wavelength of the illumination, and with c^o fixed by the usual interference requirements then there is a theoretical possibility of using a combined system in a single experiment.

The practical application of the above analysis is two-fold. Primarily, it has shown that the sensitivity of the interference system using the modulated laser will be impaired to a negligible extent for partially absorbing solutions. If $s^o = 0.8$ (say) then for the typical conditions $s_m = 0.9$ and $s_b = 0.6$, for which the fringe visibility ϕ varies between about 1.0 and 0.8 as seen in figure 4-2(b). Secondly, the analysis has indicated that the triple sector (Lewis) cell may have possible applications in a modulated ultraviolet system of the ultracentrifuge wherein the advantages of both the absorption and interference systems may be

utilised in a single experiment. In particular the absorption system is frequently selective owing to the high molar extinction coefficients of the purine and pyrimidine bases of the nucleotides, whereas the interference system lacks this discrimatory effect. Thus a combined system holds promise of permitting new experiments to be performed with certain macromolecules. Instrumental problems are obvious in its direct applicability to the current instrument, but with ingenuity and development these should prove to be temporary.

3. INSTRUMENTATION

The foregoing theoretical analysis has indicated that there may be experimental advantages to be gained by using a triple sector cell in the analytical ultracentrifuge, rather than the conventional double sector Rayleigh cell for interference work. To this end, various cells and associated components were designed and constructed by the author that were compatible with the Beckman/Spinco analytical ultracentrifuge, and have been used successfully in some studies for over a year.

(a) TRIPLE SECTOR CENTREPIECES

The first triple sector centrepiece to be constructed was made from duralumin, since this was relatively easy to machine and proved sufficient for the preliminary feasability studies. However, owing to the inevitable contamination[60] of the solution with aluminium ions, the cell is unsuitable for use with extreme pH or for solutions with high salt concentration. To avoid these a second triple sector centrepiece was constructed from titanium, which has been shown by Hearst and Gray[61] to be admirably suited for ultracentrifuge studies under extreme conditions owing to its chemical and mechanical stability.

The dimensions used in the construction of both triple sector centrepieces were based on the standard 1.2 cm aluminium Spinco centrepieces, and the sectors were 2^{o} with an angular separation of 2^{o} between the centres of individual sectors measured from the axis of rotation. A view of the two centrepieces is shown in figure (4-3), wherein the filler holes and normal cell alignment slot is clearly visible. Naturally, the triple sector centrepieces require a groove between sectors (fig.4-3) to form a seal with the gaskets and prevent transfer of liquid between compartments.

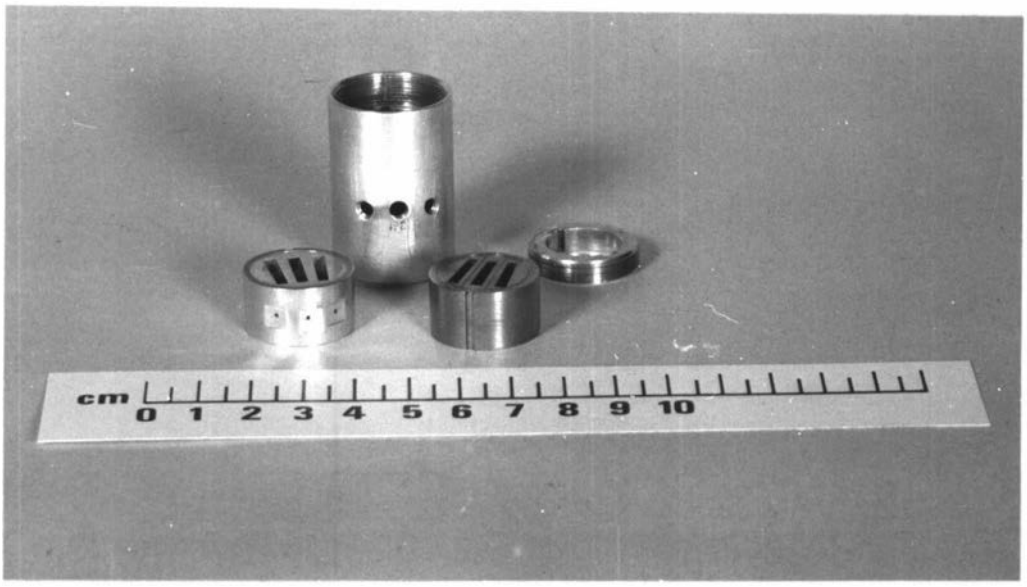

FIGURE 4-3 VIEW OF THE DURALUMIN AND TITANIUM TRIPLE-SECTOR CENTREPIECES AND CELL HOUSING.

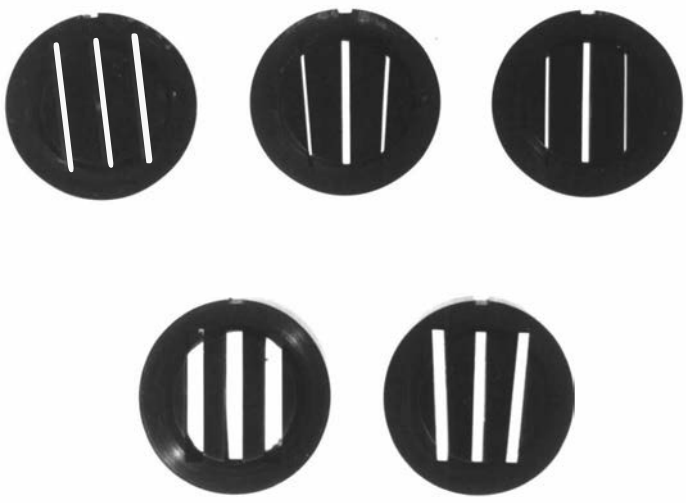

FIGURE 4-4 VIEW OF ASSORTED TRIPLE APERTURE WINDOW HOLDERS FOR USE WITH THE TRIPLE-SECTOR CELL ASSEMBLY.

The sectors were machined at the Physics and Engineering Laboratory, D.S.I.R., Lower Hutt, New Zealand, using an electric discharge machining process[62]. The copper tools were designed by the author to be compatible for use in the aforementioned machine, and consisted of three prongs of the desired sector shape. In the machining process the tool and blank centrepiece were immersed in a liquid dielectric. The tool was brought very close to the centrepiece under automatic conditions with remote sensing and a pulsed current was passed between the tool and blank which enabled the tool to cut the sectors in the centrepiece blank as it passed through.

(b) WINDOW HOLDERS AND APERTURE MASKS

The window holders were constructed from duralumin rod and were anodised on completion. A view of the assorted window holders is shown in figure (4-4) wherein it will be noted that the centre aperture of the lower window holders have twice the width of the outer apertures, as proposed in the theoretical analysis. Naturally, the dimensions of these window holders were based on the standard Spinco window holders so that the conventional sapphire and quartz windows together with their associated gaskets could be employed. However, in the manufacture of the window holders good use was made of the experience of Ansevin et al[49], and the metal rim was made to extend to within 0.2 mm of the face of the window rather than the normal 0.7 mm. The above authors have shown that such a construction gives excellent optical stability for interference studies, particularly at the higher rotor speeds, using the conventional polyvinyl chloride strips around the windows.

Five separate window holders were manufactured, of which three were designed specifically for the upper cell window and two were designed for the lower cell window. In general the slits in the lower window holders constitute the cell diaphragm which could be considered as the optically active element, since these had considerably finer dimensions than those in the corresponding upper window holder. It will be noted (figure 4-4) that a set of window holders were manufactured with radial slits, of which there is not an equivalent in the conventional Rayleigh system. The use

of the latter, together with the parallel slit window holders will be discussed later. Typical working drawings of these window holders and associated components are included in an appendix to this thesis.

In conjunction with the manufacture of the triple-sector cell window holders described above, was the construction of appropriate aperture masks. A view of these masks is included in figure (4-5), and these were made from 1/16" brass plate and machined, together with the window holders, at P.E.L., Lower Hutt, New Zealand using the electric discharge machining process as mentioned previously. Again all copper tool pieces employed in the above manufacturing process were designed and constructed by the author with some machining assistance from a technician (Mr. D.P. O'Brien) at Massey University. Typical technical information is included in an appendix to this thesis.

(c) CENTREPIECE GASKETS AND GASKET PUNCH

All metal centrepieces require gaskets between the cell windows and the centrepiece. The gaskets required for the triple-sector centrepieces are quite complex and since gaskets that were completely dependable were essential, once the problems of cell leakage were overcome, it was decided to design and make a punch that could be used to make uniform gaskets. A view of this punch and associated gaskets is shown in figure (4-6), together with a convenient box/block. The male central punch was machined on the special jig that was made for the manufacture of the copper tool pieces used in the electric discharge machining processes (see appendix), and the radial blades were constructed from safety razor blades.

The gaskets were punched by placing the gasket material on the end cut hard wood block, placing the cutting end of the outer punch (figure 4-6) on the material, and striking the punch a sharp blow with a wooden mallet. The inner punch was then inserted into the outer punch so that its cutting end was on the disc of gasket material within the outer punch, and then this punch too was given a sharp blow with the mallet to produce the required gasket. The punch has worked well with consistent results using the red polyethylene supplied by Spinco. To date all ultracentrifuge runs have been conducted below 40°, but it is anticipated

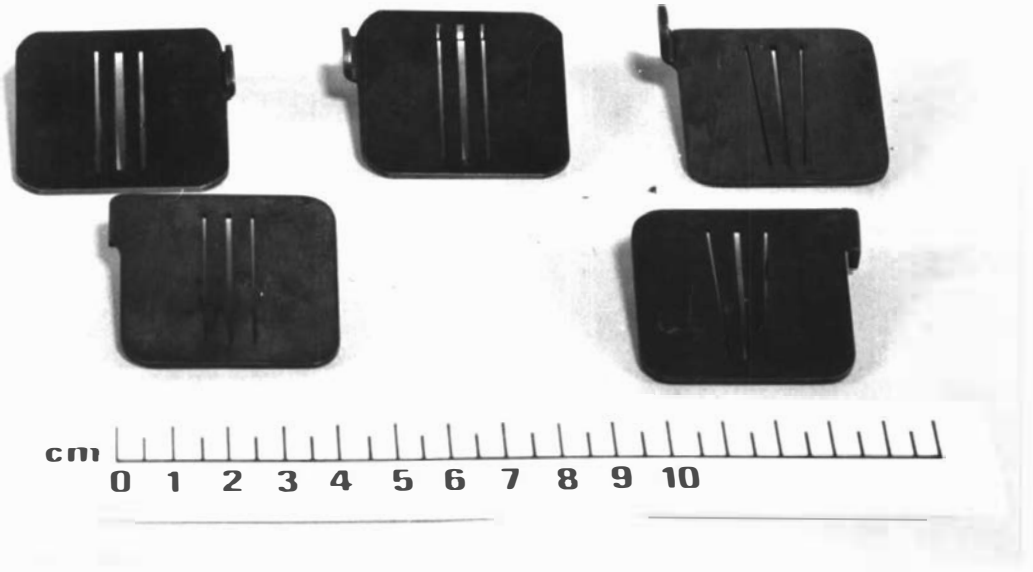

FIGURE 4-5. VIEW OF ASSORTED APERTURE MASKS FOR USE WITH THE TRIPLE-SECTOR CELL IN THE ULTRACENTRIFUGE.

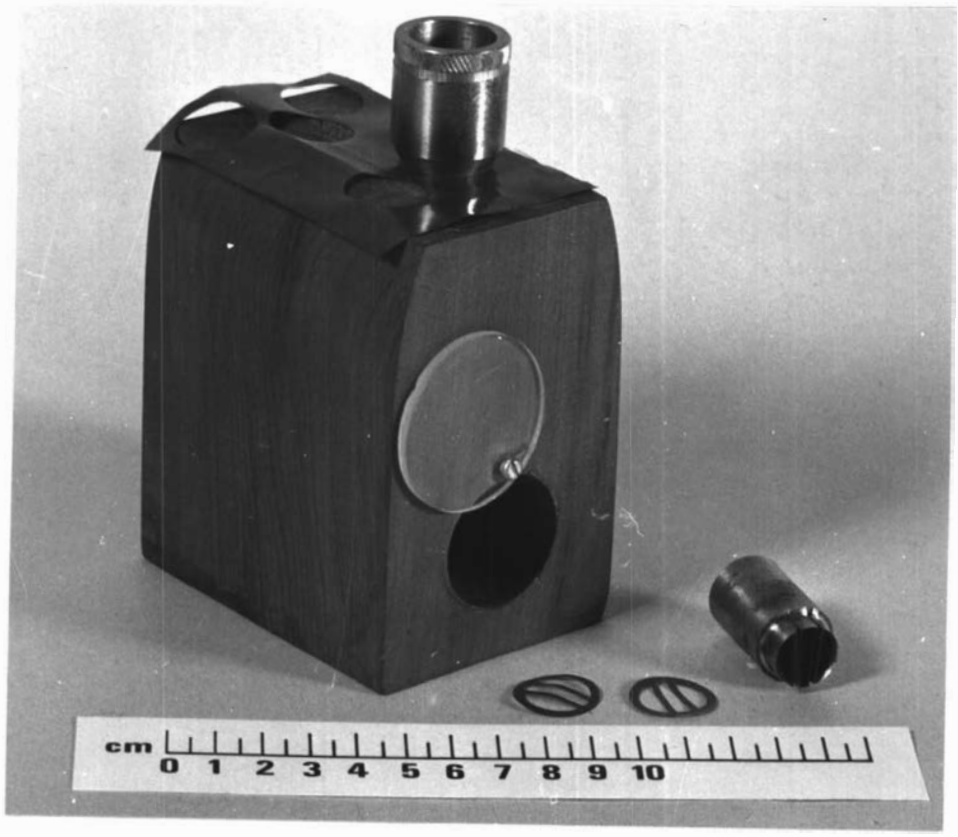

FIGURE 4-6. VIEW OF THE GASKET PUNCH AND GASKETS TOGETHER WITH ITS BOX/BLOCK.

that at higher temperatures where the above material is unsuitable that 0.005" Teflon sheet should be satisfactory as gasket material as indicated by Hearst and Gray[61].

(d) CELL ASSEMBLY

The complete cell was assembled in a manner analogous to a conventional cell with metal centrepieces. The cell housing for the triple-sector centrepiece was adapted from a single-sector cell housing (Beckman parts No. 30192), in which the two additional filler holes and screw plugs were added.

The inevitable leaks were encountered when the new cells were first assembled and subjected to an ultracentrifuge run, but by judicious use of a slurry of very fine carborundum paste (No. 600) on the faces of the centrepieces and a torque of 135 lb-in these were virtually eliminated even at high speed. However, small leaks still arose when the machine was run for long periods and it was found advisable to run the assembled cell up to speed initially and then stop the machine. The assembled cell was then removed from the rotor and re-torqued to 135 lb-in before being inserted into the ultracentrifuge for the actual experiment. The latter action eliminated all leaks and was adopted as a routine procedure for all studies involving the triple-sector cell assembly.

(e) COUNTERBALANCES AND RADIAL REFERENCE

Strictly speaking the triple-sector cell requires a special counterbalance and reference cell for optimum performance but these were not available and use had to be made of the conventional Schlieren and Rayleigh interference counterbalances appropriate to the Spinco An-D rotor that was used in this work. The interference counterbalance/reference cell was suitable for use with the duralumin centrepiece in which most of the current work was undertaken, but could not be used with the titanium centrepiece owing to lack of weight. The necessary more dense tungsten alloy counterbalance weights obtainable from Spinco were not available in our laboratory. However, the additional counterbalance weight was attained by using the Schlieren counterblance with a specially constructed stainless steel, split-ring outer collar replacing the normal duralumin collar.

Both these reference cells provided an interference pattern in conjuction with the fixed aperture mask on the photographic plate, and enabled radial measurements and plate alignments to be made under the microcomparator. Naturally, a special triple aperture interference counterbalance and reference cell would be advantageous as mentioned earlier.

4. EXPERIMENTAL

The experimental triple-sector cell is not yet fully developed as will be apparent from the discussion within this chapter. However, as an initial test of the feasibility of the system a standard sucrose solution was used as described in chapter 3 of this work, together with the various protein solutions used in testing the Rayleigh system with the modulated laser light source. This was experimentally convenient since pertinent data was obviously available in all cases, and at the same time these provided a useful comparative test of the two interference cell types.

(a) METHOD

Sedimentation-diffusion equilibrium experiments were performed with the Beckman-Spinco Model E ultracentrifuge employing the interference optical system, as described in chapters 1 and 3 of this thesis. The optical system was focussed and aligned according to the procedure of chapter 3, wherein the camera lens was focussed on the mid-plane of the cell. Sapphire windows were employed throughout in all experiments to ensure optimum optical stability. The modulated laser system was employed, and proved to be essential for the triple-sector interference work, since otherwise the multiple contributions from the undersirable orientations between the cell diaphragm and fixed aperture mask during cell rotation fogged the desired interference pattern on the photographic plate.

The fringe patterns were photographed with Ilford HP3 (hypersensitive panchromatic backed) photographic plates, which were developed in complete darkness according to the manufacturer's instructions. The sucrose equilibrium experiments were performed at 25°C according to the detailed procedure devised by LaBar[12] and others[19]. Sucrose equilibrium has proved to be a good test for both the interference and Schlieren optical systems in the ultracentrifuge, and is now sufficiently well established both

theoretically and experimentally to considered a standard. However, as will be indicated in chapter 5 of this thesis, the simple sucrose system could lead to a false sense of experimental accuracy in more complex macromolecular studies, unless the effects of the non-linear refractive index gradients are taken into consideration.

The sucrose equilibrium method has been summarized in chapter 3, and it was shown that the results obtained using the interference system with normal double sector cell and laser source were of the anticipated accuracy. As mentioned the test is based on the data obtained by Gosting and Morris[50] on the physical properties of sucrose solutions.

(b) PHOTOGRAPHIC PLATE MEASUREMENTS

Much of this work was undertaken using the Topcon Measuring Projector Model PP-30E with the high precision micrometer stage as described in chapter 3 of this thesis. However, the theory has indicated that the concentration distribution within the cell is characterized by intensity variations in the radially oriented central fringe of the interference pattern (see also figure 4-8). This being so, it was decided to use a microdensitometer in the analysis of the fringe patterns obtained using a triple-sector cell. This was especially convenient in our case since a Joyce Loebl Microdensitometer IIIc suitable for such measurements was available in the laboratory, and had been purchased sometime previously for the analysis of the plates obtained using the ultraviolet system in the analytical ultracentrifuge. The latter must apply to many laboratories in which an ultracentrifuge exists, and should the use of triple-sector cells be adopted for interference work many workers will be familiar with making densimetric measurements. Indeed the main advantage of the triple-sector (Lewis) cell is that all the data may be obtained photoelectrically and hence it is possible theoretically to scan the pattern directly during the course of an experiment and hence perform all the required calculations by an on-line computer.

A qualitative appreciation of the problem may be obtained from figures (4-8). Figure 4-8(a) depicts a

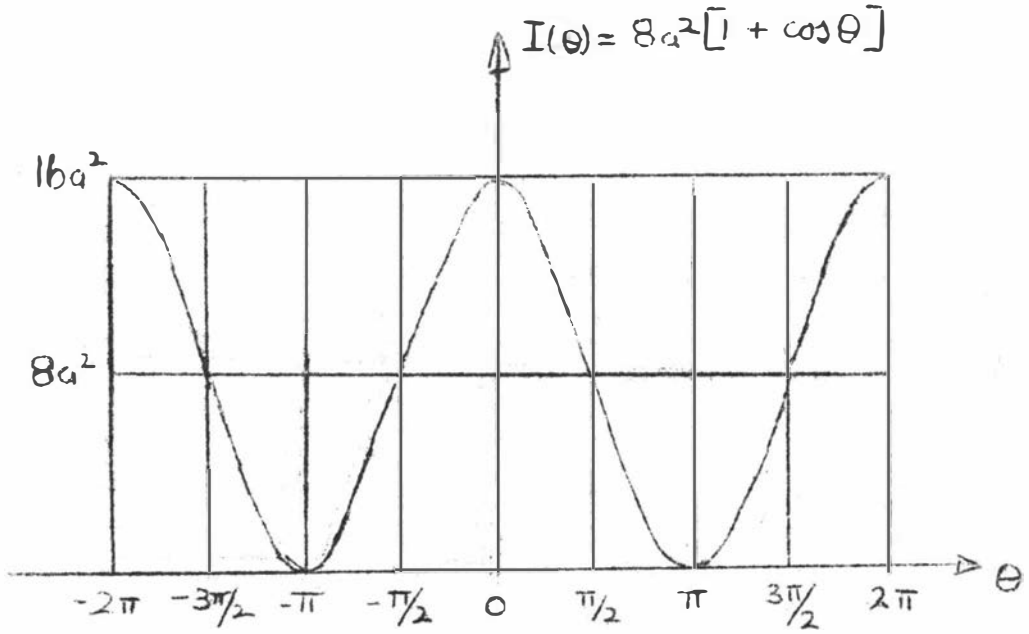

FIGURE 4-7. CENTRAL FRINGE INTENSITY VERSUS PHASE ADVANCE (θ) INTRODUCED INTO THE CENTRAL SECTOR. (Central aperture is double the width of the outer apertures.)

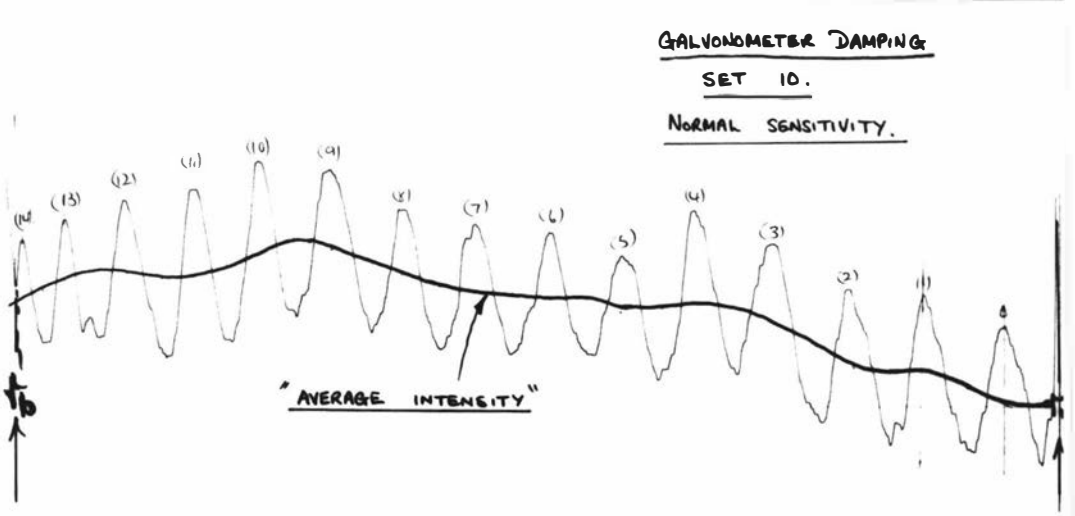

FIGURE 4-9. DENSITOMETER TRACE OF THE CENTRAL FRINGE OF THE PATTERN SHOWN IN FIGURE 4-8(b).

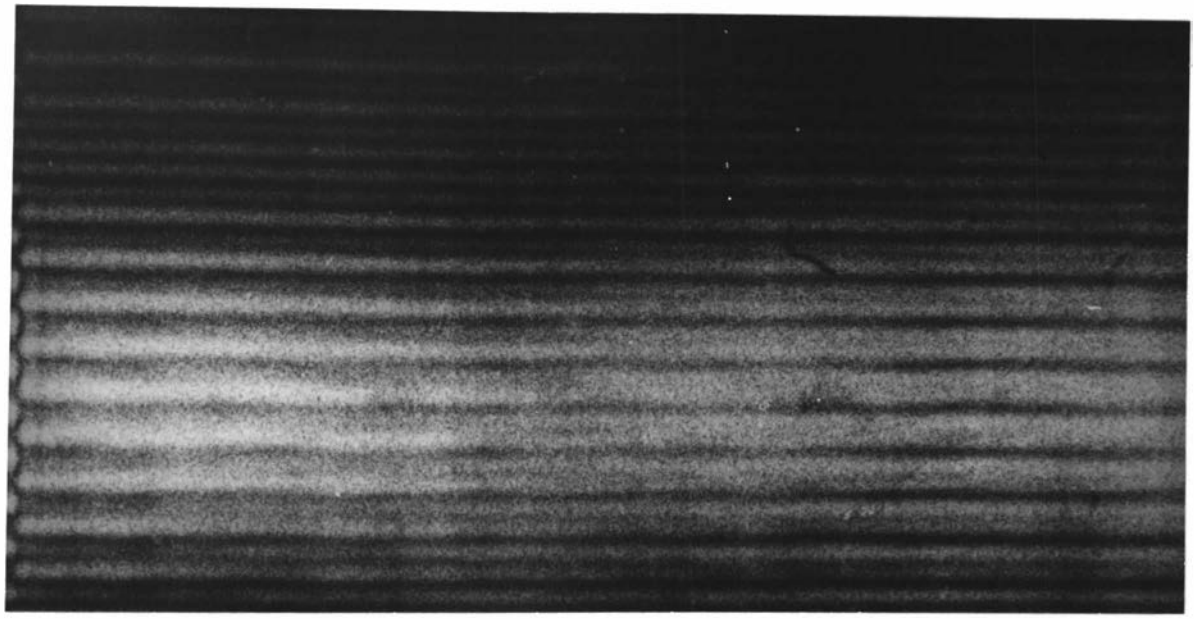

FIGURE 4-8(a). TRIPLE-SECTOR CELL FRINGE PATTERN WITH WATER IN ALL SECTORS.

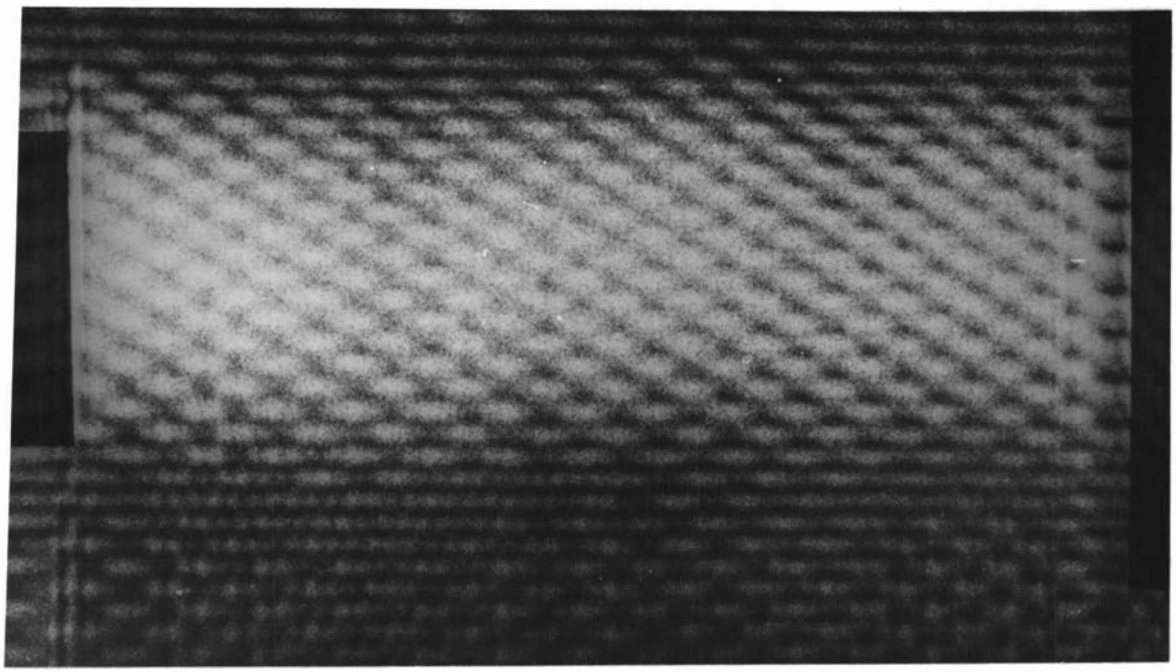

FIGURE 4-8(b). TRIPLE-SECTOR CELL FRINGE PATTERN FOR A SUCROSE IN WATER EQUILIBRIUM EXPERIMENT.

magnified version of the actual fringe pattern for a triple sector cell in which all sectors are filled with solvent (water), whereas Figure 4-8(b) is the fringe pattern obtained for a sucrose equilibrium experiment. In the latter the intensity variations of the horizontal fringes for which the central one is radially inclined are clearly visible, and the microdensitometer trace for the central fringe is depicted in figure (4-9).

The fringe patterns obtained on the 10" x 2" plates used in the ultracentrifuge were unsuitable for direct use with the densitometer, and suitable enlargements had to be made. It was found by using the x20 magnification and the photographic attachment of the profile projector, used in normal plate analysis, that suitably enlarged patterns on $4\frac{3}{4}$" x $6\frac{1}{2}$" plates could be made, and these were used in obtaining the traces shown.

The profile projector was used to obtain the appropriate radial plate dimensions in the normal way, and these were used subsequently in the evaluation of the relevant radial dimensions on the densitometer traces. It was found convenient to mask with black tape the regions immediately prior to the solution meniscus and following the solution base respectively (see figure 4-8) on the enlarged patterns, and these produced sharp recordings of these important and accurately determined positions on the trace when scanned. Furthermore, the taped regions gave the reference zero transmission on the photographic plates.

As with the ultraviolet absorption system, any spurious factors that alter the light intensity across the photographic plate are inconvenient. In the present case the intensity in illumination across the pattern is non-uniform as will be noted by the slow variation in the average height of the densitometer trace of figure (4-9). The primary source of this variation in illumination lies within the electro-optic modulator, which in its optimum modulating position for the plane of polarization required developed a pronounced non-uniform beam. However, it should be appreciated that the un-modulated laser beam is itself non-uniform in this case since the fundamental TEM_{oo} mode in which it operates is characterized by a beam of

Gaussian profile, being a maximum in the centre with circular cross-sectional symmetry. Naturally, any oil or dust on the optical components give rise to spurious diffraction/intensity effects and care was taken to keep components as clean as possible.

The inherent intensity variations across the pattern from the " non-signal" sources mentioned above are not too serious provided they are constant during the course of an experiment and may be corrected should the need arise.

The characteristic cosinusoidal trace (see figure 4-7) indicative of a concentration distribution in the centrifuge cell, is clearly indicated in figure (4-9). From the latter it is possible to evaluate the concentration distribution if desired, but to date the only quantitative measurements have been made using the recorded pattern from the actual instrument on the 10" x 2" plates in conjunction with the profile measuring projector, as is routine practice in conventional interference work.

5. RESULTS AND DISCUSSION

Although the actual technique of plate measurement differs, as indicated above, from that used in the conventional Rayleigh system, the analysis of the data so derived is similar in all respects. This is not surprising since both are interference systems sharing the same optical components and giving the same refractometric information. However, all sedimentation equilibrium experiments in the analytical ultracentrifuge require the evaluation of a constant relating the initial concentration of the solution (c^{o}) to the experimental observable. This requirement still prevails for the triple-sector cell.

In chapter 3 it was assumed that the change in the specific refractive increment of sucrose was very small when the source used was changed from the mercury (λ = 546.1 nm) to the laser (λ = 632.8 nm). The validity of this assumption was substantiated by the experimental results obtained with a synthetic boundary cell, and the use of such a test for the triple-sector cell was undertaken therefore with some confidence. However, the work of Nazarian[55], whereby the interference data is analysed

in terms of finite differences of concentration, has obviated the necessity of determining the initial concentration (c^o) in terms of fringes (j^o), making the assumption above unnecessary. Indeed, the fringe data obtained using the current triple-sector cell is suited ideally for the finite difference analysis. A triple sector capillary type synthetic boundary cell that could be used for the determination of j^o, as is routine practice in equilibrium studies, is not currently available. However, there are no reasons why such a synthetic boundary cell could not be constructed for triple-sector interference work from an epoxy resin centrepiece, based on the design of the equivalent double sector cells. Naturally, owing to the large concentrations employed a synthetic boundary cell is unsuited for the determination of j^o for sucrose equilibrium work, and the procedure outlined previously using the cell dimensions and specific refractive increment of solution was used in a conventional analysis of the sucrose equilibrium data.

As with the conventional Rayleigh interference studies, baseline reference measurements are essential to correct for the spurious refractive index effects introduced owing to distortion of the cell windows in the centrifugal field and in this case spurious intensity effects have to be compensated too. The established techniques described in chapter 3 for obtaining such baseline references are applicable in principle to the current system. However, in general unless the conditions under which the baseline reference plates are analysed are optimum, the precision with which the relevant measurements may be made is not as good as for the Rayleigh system.

If the baseline is obtained by running a cell at the speed of the actual experiment with all sectors filled to appropriate levels with solvent then the central fringe will be an intensity maxima, as indicated in the theory (see figure 4-8(a)). This is unfortunate experimentally for two important reasons. Firstly, the corrections for window distortion can be both positive and negative, but the intensity variations of the central fringe are the same for both positive and negative changes in refractive

index, (they both reduce the intensity), and hence no discrimination is available (see figure 4-7). Secondly, as will be noted from equation (4-16), and figure (4-7), the fringe maxima and minima are the regions of least sensitivity ($\frac{dI}{d\Theta}$) as regards change in intensity to change in refractive index. This is unfortunate since the changes in Θ owing to window distortion are small($\pm$ 12°) in practice. However, both these faults may be overcome if the central sector is optically biased by $\pi/2$ radians (see figure (4-7)). This may be achieved by having one window with a coating strip across the centre in line with the central aperture in one of the window holders that gives a phase advance of $\pi/2$ radians. This would automatically optically bias the central radial fringe to the region of maximum sensitivity, and where good discrimination exists between positive and negative refractive index changes (see figure 4-7). Naturally, this same window would be perfectly satisfactory for use in the normal equilibrium run with solution in the central sector, since it has no effect on the relative position of the fringes. The above procedure for obtaining baseline references would appear to be the most suitable for triple sector interference work and it is anticipated that it will be adopted as routine in this laboratory when a sapphire cell window has been coated. Work is in hand for the coating of a sapphire window and it is confidently anticipated that with the routine use of this window measurements of comparable (if not better) precision to those obtained from Rayleigh type reference plates will be possible.

The theory upon which the baseline measurements will be based is given in an appendix to this chapter.

In the absence of a baseline reference it was decided to make measurements of the uncorrected fringe count between the meniscus and base of the solution column at equilibrium ($\Delta j'_{eq}$). For the plate shown in figure 4-8(b) $\Delta j'_{eq} = 14.95 \pm .04$ fringes, and is of a precision comparable to that achieved with similar double sector experiments. It is reasonable to assume therefore, that when precise baseline references are obtained (with the specially coated window) that the

triple-sector cell will be capable of producing experimental data of an accuracy at least comparable to that obtained in the Rayleigh system, and superior to that obtained with the conventional mercury source. Obviously the molecular weight determination obtained using the uncorrected fringe count were in error and were larger normally than those obtained with the Rayleigh system for which baseline references were possible. However, the discrepancies could be associated with the absent baseline reference measurements.

Of interest was an investigation of the various fringe patterns associated with the triple sector cell in the ultracentrifuge. By judious use of the modulating system in conjunction with the moving cell and fixed aperture mask, it was possible to obtain Rayleigh type double sector patterns during a triple-sector experiment. These are shown in figure (4-10), and were taken at a time before equilibrium was reached. The manner in which they are obtained is shown schematically on the same figure. The desired triple-sector pattern is shown in figure (4-10c), and it should be appreciated that it is not just the superposition on the photographic plate of the two Rayleigh type patterns depicted in figures (4-10b) and (4-10d). The reason for this is fundamental to coherent optics and is expressed in equations (1-4) and (1-5) of this thesis. The " Lewis" pattern in figure (4-10c) is the result of the complex amplitudes of the electric field vectors from the three apertures having added before forming the time averaged intensity pattern (equation 2-2) on the photographic plate. On the other hand, the superpositions of the patterns in figure (4-10b) and (4-10d) would arise from the addition of two separate intensity patterns which have occured from the complex addition of the electric field vectors from two different apertures at different times. Furthermore, although the latter patterns may appear similar to those obtained with the Rayleigh system, they have occurred when the cell is incorrectly aligned within the interferometer as may be appreciated from figure (4-10) which indicates their origin schematically. In a non-modulated interference system, the recorded pattern would

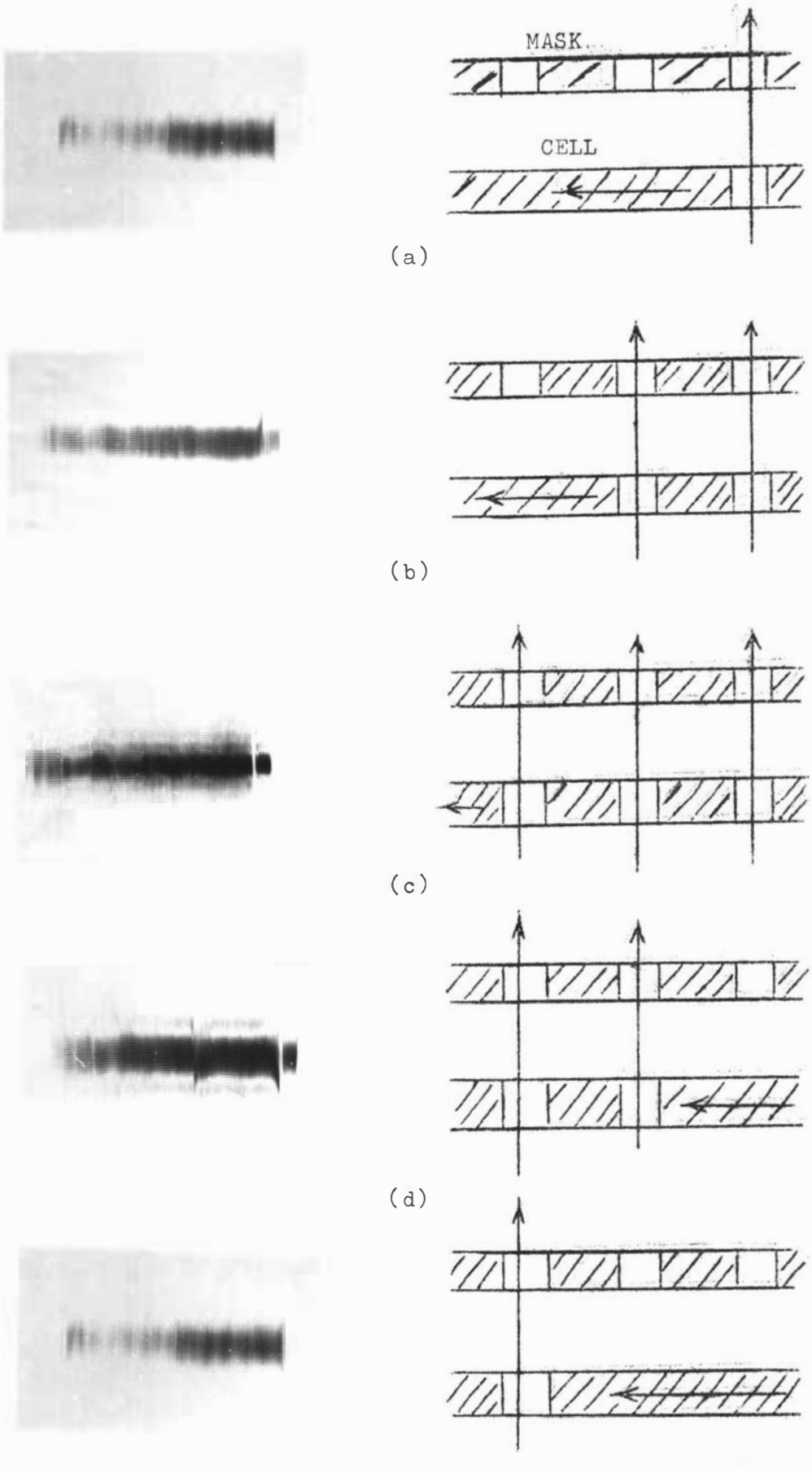

FIGURE 4-10. MISCELLANEOUS TRIPLE-SECTOR CELL PATTERNS OBTAINED IN THE CENTRIFUGE WITH THE MODULATION SYSTEM.

(a). FINE DOUBLE APERTURE (RAYLEIGH) MASK.

Note spurious intensity variations even with mercury source.

(b). WIDE DOUBLE APERTURE (RAYLEIGH) MASK.

(c). TRIPLE APERTURE MASK (PARALLEL).

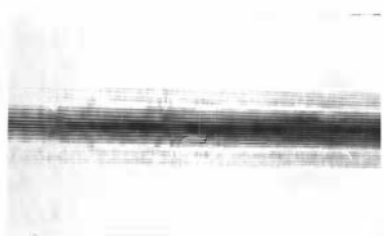

(d). TRIPLE APERTURE MASK (RADIAL).

FIGURE 4-11. BASIC ('CARRIER') FRINGE PATTERNS FOR VARIOUS CENTRIFUGE MASKS USING THE MERCURY SOURCE.

be the result of the superposition of all the patterns resulting from the various orientations of the cell diaphragm and aperture mask, and it will be obvious why a modulated system is essential for triple-sector cell usage in the analytical ultracentrifuge.

The off-axis patterns are useful in that they give a visual indication of the extent of sedimentation during the course of an experiment in a form familiar to those who have had experience with the double-sector Rayleigh system. However, the foregoing discussion has indicated that they may not be used directly for actual quantitative measurements.

It has been mentioned that a complete triple-sector cell assembly and aperture mask were constructed (see figures (4-4) and (4-5)) with radial slots, for use in the interference system. The basic ("carrier") interference pattern of this aperture mask is shown in figure (4-11) together with interference patterns applicable to various other masks used in the instrument; with which it may be compared. It will be noted that the central fringe is radial and on the optic axis of the system for all triple-aperture masks whereas the off-axis fringes do vary according to whether the aperture slots are radial or parallel. The theory has shown that all the desired information lies on the central fringe when a triple sector cell is used and so both radial and parallel masks can be used. The only real advantage of the radial apertures over the parallel variety is that narrower cell sectors could be used if necessary, and this would be the case if a five sector centrepiece were constructed for use in the current instrument. The theoretical analysis of this and other multiple sector centrepieces are relatively straightforward using the transform methods developed in this work.

It should be appreciated that non-conjugate levels are compared between the solvent and solution in both the radial and parallel assemblies. A separate analysis of the effects of this appropriate to triple and double sector cells used in the ultracentrifuge is included in chapter 5 of this thesis. However, the radial assembly

Cell approaching alignment
cf. Fig.4-10(b)

(a).

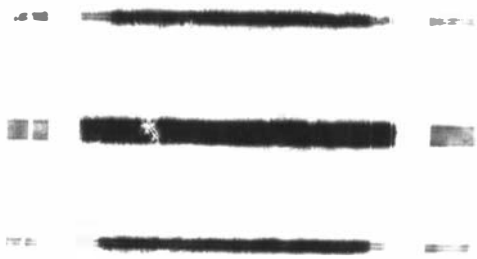

Cell aligned with mask
cf.Fig.4-10(c)

(b).

Cell past alignment
cf.Fig.4-10(d)

(c).

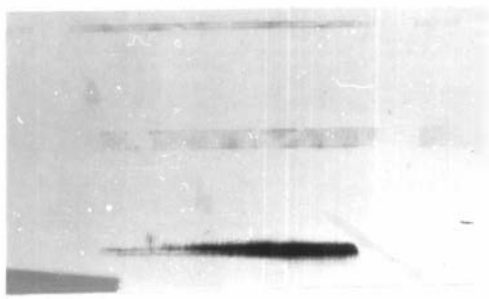

Cell further past alignment
cf.Fig.4-10(e)

(d).

FIGURE 4-12. VIEWS OF VARIOUS ORIENTATIONS BETWEEN THE APERTURES IN THE CELL WINDOW HOLDERS AND THE FIXED APERTURE MASK IN THE ULTRACENTRIFUGE.

was particularly useful (see chapter 3) in the physical alignment of the aperture mask in the instrument when the system was critically focussed and aligned. Here the cylinder lens was removed from the instrument, as proposed by Dyson[46], allowing the cell and aperture mask to be viewed together in the viewing telescope and/or recorded on the photographic plate. Initially, the tranlational position of the aperture mask had been fixed using the undeviated laser beam that defined the optical axis of the interference system. A radial slot cell assembly was loaded into an An-D rotor with a suitable counterbalance and with the normal laser modulation system the cell was stopped effectively in the optimum position in the interferometer as seen through the viewing telescope. The aperture mask slots were made visible by off-setting the modulator E.H.T. so that the interferometer illumination was never zero (see figure 4-12). Thence by trial and error the aperture mask was adjusted rotationally until the radial slots in both lower window holder and aperture mask were accurately aligned as seen through the viewing telescope during a centrifuge run.

The modulation system was essential for this adjustment, but the technique was simple in execution and the precision attained was such that when the system was tested using the Rayleigh system and the boundary cancelling procedure in a single-sector cell as proposed by Gropper[45], it was found that no further mask adjustments were required. Photographs of miscellaneous alignments during a cell rotation between the cell diaphragm in the lower window holder and a fixed parallel slot aperture mask taken for the aligned system with the cylinder lens removed are shown in figure (4-12), and should be compared with the diagrams in figure (4-10), since they are substantive evidence for the same.

6. SUMMARY

In this chapter a new cell for use with the interference optics in the analytical ultracentrifuge has been presented. The theory and preliminary experimental results have indicated that the cell is well suited for use in macromolecular studies involving the interference

system in the ultracentrifuge, and is particularly interesting in that data can be obtained photo-electrically using a microdensitometer. The importance of the latter compared with the Rayleigh system is the possibility of using the triple-sector patterns in on-line analysis using photo-electric measurements and a computer. Furthermore, the theory indicates that the baseline reference corrections for window distortion and other spurious "noise" effects should be correctable to a high precision with the specially coated cell window that is being manufactured. It will be apparent that much work associated with this new cell remains to be done, but all the experimental evidence available to date has been encouraging. The author is continuing with the development of this cell at present in conjunction with the modulated laser system, but as the theory indicated it may have other useful applications in conjunction with the ultraviolet system, and this too is under consideration.

7. APPENDIX

THEORY OF PROPOSED BASELINE CORRECTION MEASUREMENTS

As usual in this type of correction procedure it is assumed that the cell window distortion is generated by small changes in the refractive index of the solution in the central sector. These in turn may be considered to be brought about by changes in solute concentration ($\pm \Delta c$) in this sector. Thus the small phase change ($\delta\theta$) originating from the window distortion may be written as

$$\delta\theta = \pm kt\left(\frac{\partial n}{\partial c}\right)\Delta c \qquad (4\text{-}27)$$

where as usual $k = \frac{2\pi}{\lambda}$, t = cell thickness and $\left(\frac{\partial n}{\partial c}\right)$ is the specific refractive increment for the solute.

From equation (4-16) we know that the intensity of the central maxima in the fringe pattern is given by $I = 8a^2(1 + \cos\theta)$, and assuming the windows coating has biased the central aperture such that $\theta = \pi/2$ radians the intensity of this fringe will be given by

$$I_m = 8a^2(1 + \cos\pi/2) = 8a^2 \qquad (4\text{-}28)$$

This is the fringe intensity without the presence of the window distortion or other spurious amplitude effects. In practice it may be found from a fringe pattern by averaging the maxima and minima about the central fringe.

Window distortion produces intensity variations in the central fringe and these vary about the mean value given in equation (4-28), according to $\delta\theta$ which is expressed in equation (4-27).

i.e.,

$$I_m \pm \delta I = 8a^2(1 + \cos(\pi/2 \mp \delta\theta)) \qquad (4\text{-}29)$$

Now $\cos(\pi/2 \mp \delta\theta) = \mp \sin\delta\theta$, and by inserting this identity into equation (4-29) and manipulating the terms we find that

$$\pm \frac{\delta I}{I_m} = \mp \sin\delta\theta \qquad (4\text{-}30)$$

In practice the effects of window distortion are relatively small as mentioned, i.e., $\delta\theta = \pm 12^\circ$, and for these small changes it may be sufficiently accurate to replace the sine by the angle in radians in equation (4-30)

$$\text{i.e.} \qquad \pm\delta\theta = \mp\frac{\delta I}{I_m} \qquad (4\text{-}31)$$

The signs are such since a decrease in θ gives rise to an increase in intensity for the proposed $\pi/2$ window coating as will be apparent from figure (4-7). A coating giving a $\frac{3\pi}{2}$ phase advance would be equally acceptable as will be obvious from figure (4-7) but in this case the signs would have to be changed on the right hand side of equation (4-31).

Having determined the magnitude and relevant direction of change on the correction i.e., $\pm\delta\theta$, it is relatively straightforward to evaluate the appropriate fringe correction Δj , since one fringe corresponds to a phase change of 2π radians we have

$$\Delta j = \frac{\delta\theta}{2\pi} = \frac{1}{2\pi}\left(\frac{\delta I}{I_m}\right) \qquad (4\text{-}32)$$

Naturally, the corrections to the fringe data are opposite to the distortional changes, in that positive effects are subtracted and vice versa.

Although the above technique has yet to be used in this application in this laboratory, the author is confident of its eventual success owing to the work of Marechal et al[59] who developed a special interferometer for thin film work based on the same principle as mentioned previously.

CHAPTER 5.

'THE EFFECTS OF REFRACTIVE INDEX GRADIENTS ON EXPERIMENTAL DATA OBTAINED USING INTERFERENCE OPTICS IN THE ANALYTICAL ULTRACENTRIFUGE' .

1. INTRODUCTION

Much emphasis has been placed both in this thesis and elsewhere on the accuracy of data obtainable using the interference system in the analytical ultracentrifuge, and recently detailed alignment and focussing procedures have been devised[47,48] for the instrument to ensure that these may be attained. Experimental evidence has validated fully the theoretical predictions to date, and a measure of the interest shown in this area of research is indicated within the report[7] of the proceedings of the second conference on advances in ultracentrifugal analysis. However, as the theoretical understanding of macromolecular systems improves so also will there be a corresponding demand for increased precision in centrifgue techniques and instrumentation. The latter will necessitate the inclusion of correction procedures neglected previously, and in this chapter a study of the effects of the concentration (refractive index) gradients for the interference optical system is undertaken to establish their significance and to devise suitable correction procedures should they prove necessary.

2. DEFINITION OF PROBLEM

The fundamental problem associated with a sedimentation equilibrium experiment in the analytical ultracentrifuge, wherein the interference optics are being employed, is the evaluation of $n(x)$, the difference between the refractive index of the solution and that of the solvent at a distance x from the axis of rotation in a centrifuge cell. It has been shown in chapter 1 that the dependent variable n, which is assumed to be proportional to the solute concentration, is determined experimentally from the interference/diffraction pattern that is located in the focal plane (η', ξ') of the collimating lens L_2 of the centrifuge. On the other hand, the independent variable x is located within the cell in the plane (x,y) parallel to $(\eta'\xi')$ in the pupil lens L_2 as will be seen from figure 5-1 which depicts a schematic representation of the interference optical system in the ultracentrifuge. The problem of having the dependent and independent variables located in separate but parallel planes on the optic axis is overcome by using the camera and cylinder lens as an astigmatic doublet that focusses onto the mid-plane of the cell in the horizontal radial x direction and onto the

fringe pattern (ξ') in the vertical direction. The latter arrangement ensures that vertical fringe displacements characteristic of n in the Rayleigh system are in focus simultaneously with the cell from which they originate.

However, it is permissible to treat the solution cell as a simple phase object, and initially for simplicity we consider the cell to have a linear gradient in the radial x direction. We assume that the latter may be simulated by a thin prism of angle α as shown in figure 5-2. In compliance with our notation the refractive increment between the solution and solvent cells is given by n , and it is shown[65] that the light from the solution cell containing this linear gradient will be deviated from the light passing through the solvent cell by an angle Θ in the direction of increasing gradient, given by,

$$\Theta = n\alpha \qquad (5\text{-}1)$$

Hence the diffraction pattern originating from a linear gradient will be displaced radially on the photographic plate relative to the meniscus (x_m) and base (x_b) positions that are defined precisely, provided the camera lens is focussed on the mid-plane of the cell[43]. The problem for the Schlieren system where the exact location of a boundary is important has been investigated by Svensson[66,67] and others[68,69] who indicated that the camera lens should be focussed on the 2/3 plane of the cell for these studies. However, with interference work the exact location of the meniscus and base are frequently important, and so the camera lens is focussed routine-ly on the mid-plane of the cell in this work. The recent analysis and focussing procedure of Richards et al[47,48] are pertinent to the interference system and indicate a method by which the camera/cylinder lens combination may be focussed accurately on any desired plane in a centrifuge cell.

From figure 5-2, depicting the diffraction pattern and cell for a linear gradient, it will be apparent that although the fringe pattern is displaced relative to the

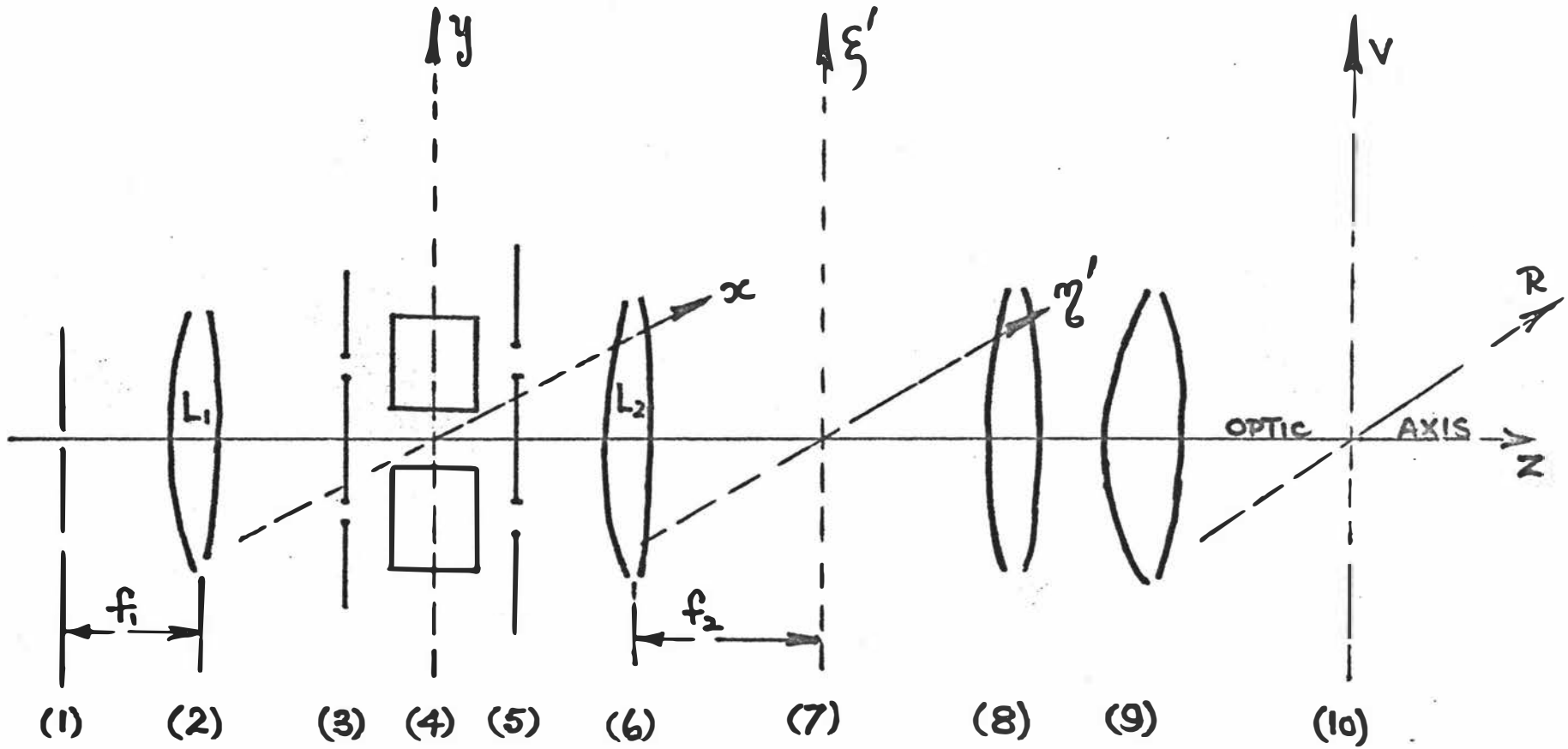

FIGURE 5-1. INTERFERENCE OPTICAL SYSTEM IN THE ANALYTICAL ULTRACENTRIFUGE.

(1) SOURCE (2) LOWER COLLIMATING LENS L_1 (3) CELL DIAPHRAGM (4) CENTRIFUGE CELL CENTER (5) APERTURE MASK (6) UPPER COLLIMATING LENS L_2 (7) FOCAL PLANE OF LENS L_2 (8) CAMERA LENS (9) CYLINDER LENS (10) PHOTOGRAPHIC PLATE

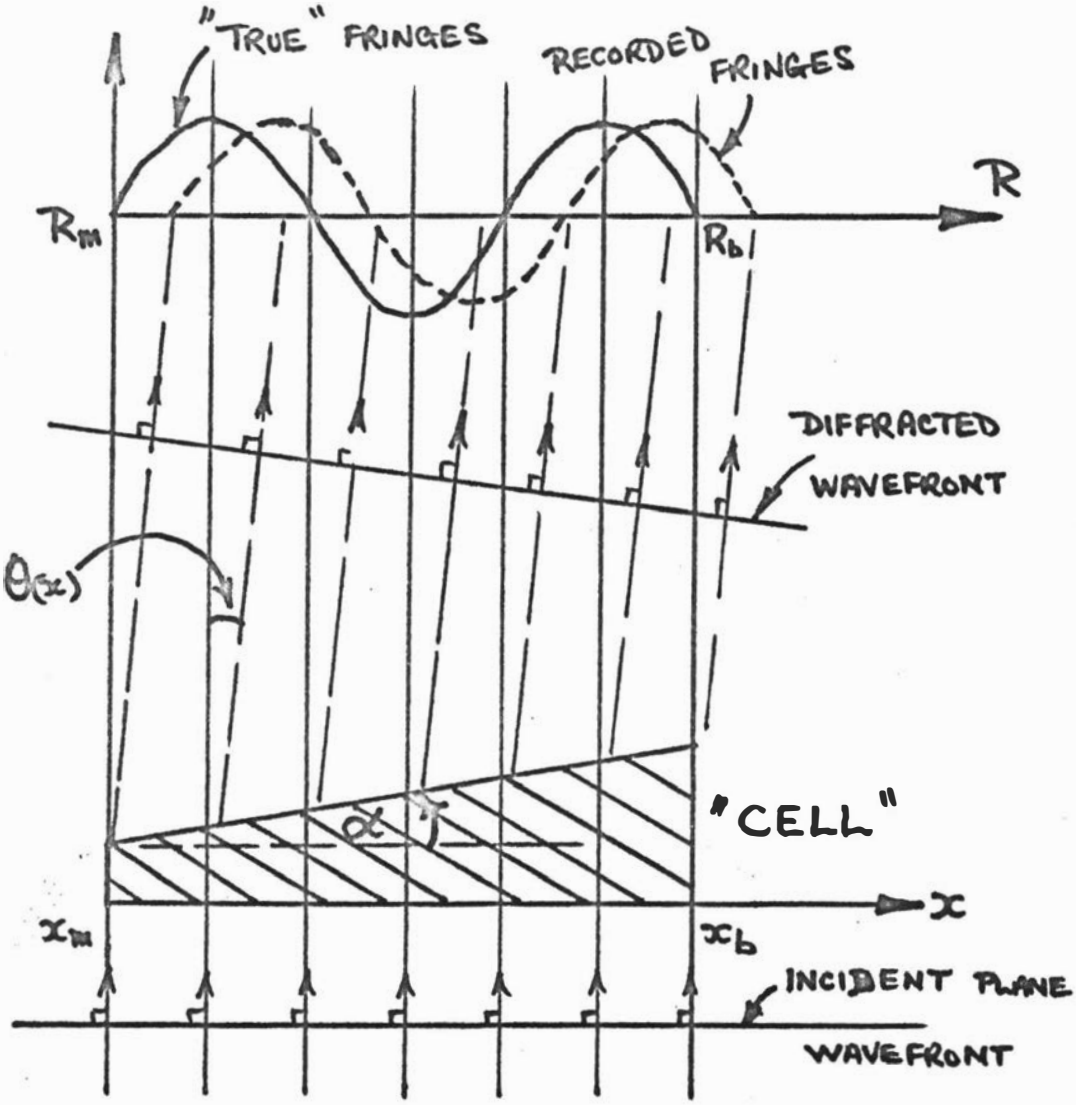

FIGURE 5-2.

SCHEMATIC REPRESENTATION OF A CENTRIFUGE CELL CONTAINING A LINEAR GRADIENT, AND THE RELEVANT FRINGE PATTERN ON THE PHOTOGRAPHIC PLATE. (RADIAL MAGNIFICATION OF THE CELL TO PLATE COORDINATES TAKEN AS UNITY).

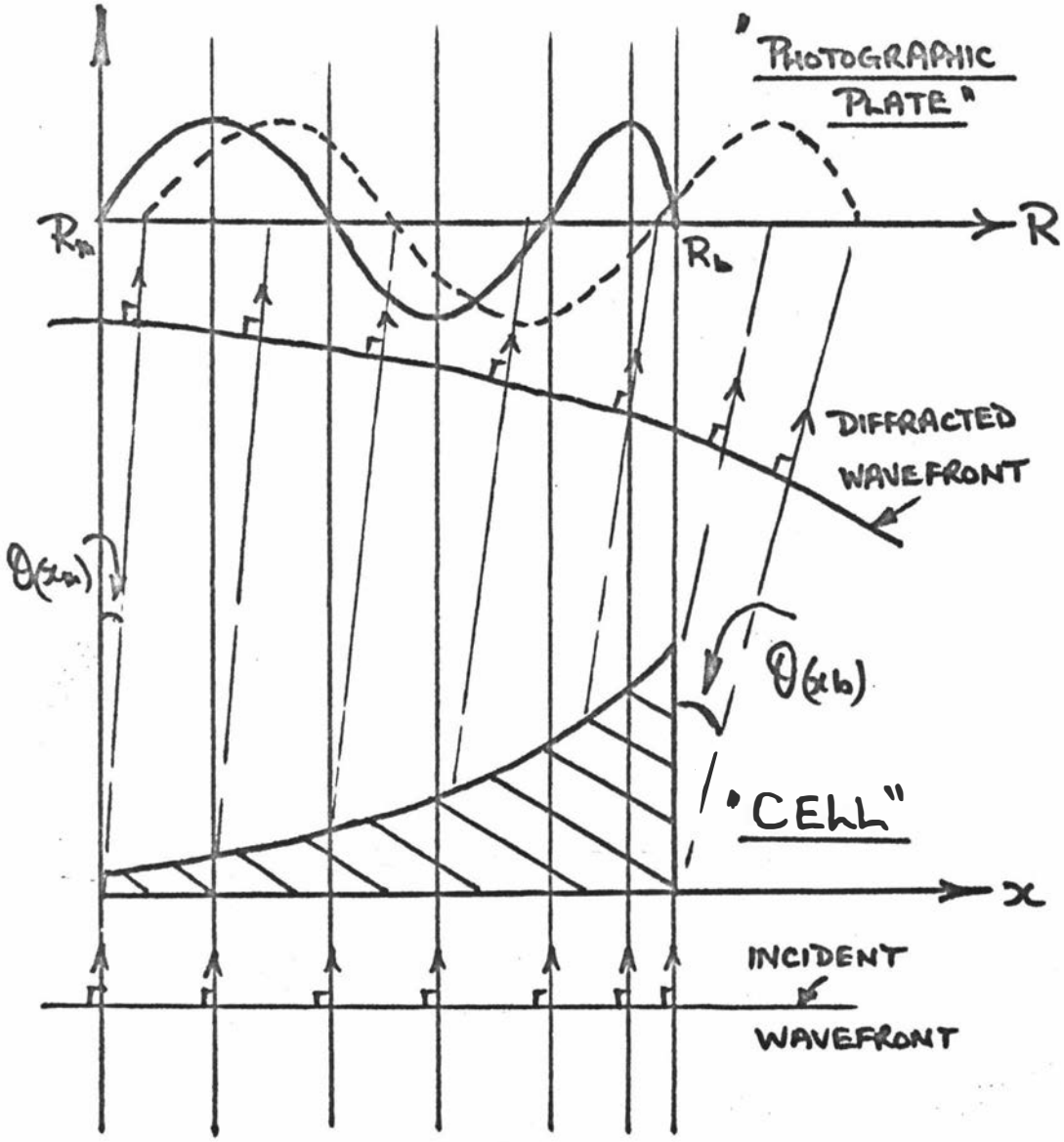

FIGURE 5-3.

SCHEMATIC REPRESENTATION OF A CENTRIFUGE CELL CONTAINING A NON-LINEAR GRADIENT, AND THE RELEVANT FRINGE PATTERN ON THE PHOTOGRAPHIC PLATE. (RADIAL MAGNIFICATION OF THE CELL TO PLATE COORDINATES TAKEN AS UNITY).

cell coordinates there would in this case be no error in determining the concentration gradient from the pattern, since one always extrapolates the fringe data to the meniscus and base in practice, and for the linear gradient this will be exact. However, in a normal sedimentation equilibrium experiment the gradient is non-linear and the effects are illustrated in figure 5-3. This could lead to errors, and the figure also indicates why fringe data, together with the diffraction effects at the optical discontinuity, are observed sometimes in the region on the photographic plate corresponding to the fluoro-carbon oil used in the cell to provide a base for the liquid column. Naturally figure 5-3 grossly exaggerates the true conditions, although with the high speed meniscus depletion methods[70] very steep gradients are now being employed routinely using interference optics.

Figure 5-3 depicts the problem of the radial gradient explicitly as it applies to the interference optics in the analytical ultracentrifuge - i.e., we require to know the radial displacement at any point on the fringe pattern as recorded on the photographic plate, relative to true cell radial dimensions x. From the latter we may ascertain the true radial solute concentration distribution within the cell as depicted schematically in figures 5-2 and 5-3 remembering that the meniscus (x_m) and base (x_b) positions are defined exactly on the photographic plate.

3. THEORY

Here we are concerned primarily with the effects of the radial gradient in the cell as exemplified in figures 5-2 and 5-3. It is assumed that equilibrium has been attained in an ideal two component system, and as usual n, the difference between the refractive index of the solution and solvent, is proportional to the solute concentration.

Hence

$$\frac{d(\ell n\ n)}{d(x^2)} = p = \frac{M_{app}\ \omega^2(1-\bar{v}\ \rho)}{2RT} \qquad (5\text{-}2)$$

Where M_{app} = apparent molecular weight of solute, ω = angular frequency of rotor, $\bar{v}$ = partial specific volume of solute, ρ = density of solution, R = the universal gas constant and T = the absolute temperature.

Equation (5-2) forms the basis for molecular weight determinations in sedimentation equilibrium studies. In practice n, which is obviously a function of the radial coordinate x, may be determined by integration from equation (5-2) whence

$$n(x) = n_m \exp^{p(x^2 - x_m^2)} \qquad (5\text{-}3)$$

where n_m is the refractive increment at the solution meniscus (x_m). At a position x in the cell the path difference Δ introduced between a wave travelling through the solution to one travelling through an equivalent radial position in the solvent is given by

$$\Delta(x) = n(x).t \qquad (5\text{-}4)$$

where t is the thickness of the cell. Hence by comparison with equation (5-1) we note that the angular deflection in the radial direction $\Theta(x)$ to which this wave is subjected is given by

$$\Theta(x) = \frac{d(\Delta(x))}{d(x)} \qquad (5\text{-}5)$$

Thus from equations (5-3) to (5-5) we determine that

$$\Theta(x) = 2pt \times n(x) \qquad (5\text{-}6)$$

Now in the ultracentrifuge $n(x)$ is determined from its equivalent fringe number $j(x)$ defined by

$$j(x) = \frac{t\ n(x)}{\lambda} \qquad (5\text{-}7)$$

and substituting (5-7) in (5-6) we can obtain $\Theta(x)$ to a close approximation in terms of the experimental observable $j(x)$ i.e.,

$$\Theta(x) = 2p\lambda \times j(x) \qquad (5\text{-}8)$$

where as usual λ is the wavelength of the radiation employed.

Equation (5-8) enables one to determine the approximate angular radial displacement of waves for each position in the cell. Now if $\theta(x)$ is small as is the case in normal ultracentrifuge studies, the equivalent radial displacement ($\Delta\eta'$) of the fringe pattern which exists in the focal plane of lens L_2 is given by

$$\Delta\eta'(x) = f_2.\theta(x) = 2p\,\lambda\, f_2\, x\, j(x) \qquad (5\text{-}9)$$

where f_2 is the focal length of the upper collimating lens L_2.

In turn $\Delta\eta'$ gives rise to a displacement in the radial direction (R) on the photographic plate given by $\Delta R(x)$, whence if we can determine the optical magnification (G) between the effective radial displacements ($\Delta\eta'$) in the focal plane of lens L_2 and the corresponding displacements (ΔR) on the photographic plate the problem will be solved since from (5-9)

$$\Delta R(x) = G\, f_2\, \theta(x) \qquad (5\text{-}10)$$

or

$$\Delta R(x) = Q\, \theta(x) \qquad (5\text{-}11)$$

in which $Q = G\, f_2$ and is the radial magnification of the interference optical system in the ultracentrifuge relating angular displacement at the cell with effective radial displacement on the photographic plate.

However, as mentioned earlier the fringe pattern is only focussed in the vertical (ξ') plane on the photographic plate, and this precludes the evaluation of Q directly in terms of known optical constants for a specific instrument. Fortunately, as will be appreciated from the following reasoning it should be possible to evaluate Q to sufficient accuracy for the current purpose by taking new measurements from the photographic plates obtained using the Rayleigh interference system of the centrifuge.

Firstly, from the slope of $\ln(c)$ versus x^2 (see equation (5-2)) one evaluates p' which one assumes approximates the true slope p. Thence in the cell the

gradient of the solute concentration versus x curve will be given to a close approximation by

$$\tan \gamma = 2p' \times n(x) = \frac{2p'\lambda}{t} \times j(x) \qquad (5\text{-}12)$$

where use has been made of equation (5-3). Now the upper collimating lens L_2 is not astigmatic and therefore the slope of the fringe located in the focal plane (η', ξ') of this lens must approximate closely $\tan \gamma$ given in equation (5-12). The radial fringe displacement $(\Delta\eta')$ in this focal plane of lens L_2 is given by equation (5-9), and this may be considered to give rise to an equivalent vertical shift $(\Delta\xi')$ in the same plane for any individual fringe in the fringe pattern at a specific value of η', given by

$$\Delta\xi' = \Delta\eta' \tan \gamma = \frac{2p' f_2 \lambda}{t} x.j(x) . \theta(x) \qquad (5\text{-}13)$$

Now the relationship within the instrument between vertical displacements in the focal plane of lens L_2 $(\Delta\xi')$ and vertical displacements on the photographic plate (Δv) is a known constant for a centrifuge and may be designated F'.

Hence

$$\Delta v = F' \Delta\xi' \qquad (5\text{-}14)$$

However it is possible to measure the slope of fringes recorded at the photographic plate at the position corresponding to position x in the cell which equals $\tan \gamma'$ (say).

Hence the equivalent radial displacement (ΔR) on the photographic plate corresponding to Δv given by equation (5-14) is

$$\Delta R(x) = \Delta v \cot \gamma' \qquad (5\text{-}15)$$

and from equations (5-13) and (5-14) we obtain

$$\Delta R(x) = \frac{F' f_2 \, 2p' \, \lambda \times j(x)}{t \tan \gamma'} \theta(x) \qquad (5\text{-}16)$$

from which by comparison with (5-11) we get

$$Q = \frac{F' f_2 \, 2p' \, \lambda \, x \, j(x)}{t \tan \gamma'} \qquad (5\text{-}17)$$

Q^* may be evaluated from equation (5-17) using instrumental constants and data obtained from any sedimentation equilibrium experiment in which the interference optics were used.

4. EXPERIMENTAL APPLICATION

The above analysis has indicated that the non-linear gradient gives rise to a non-linear magnification of the radial coordinates of the fringe data as recorded on the photographic plate, i.e., $\Delta R(x)$. Since the true radial coordinates for the cell are focussed onto the photographic plate it is convenient both theoretically and practically to transfer them back to the cell itself located in the pupil (x,y) of the lens L_2.

i.e.,

$$\Delta x = F.\Delta R(x) \qquad (5\text{-}18)$$

where F is the usual radial photographic plate to cell magnification factor.

Let the radial displacement of a fringe at true cell position x be Δx, and hence the recorded cell fringe position x' is given by

$$x' = x + \Delta x \qquad (5\text{-}19)$$

*Footnote:

In the evaluation of Q care must be taken to ensure that the dimensions are correct i.e., cm radian^{-1}. This entails determining the "true" refractive index gradient in the cell ($\tan\gamma$ in equation 5-12) in the same units as the recorded gradient on the photographic plate ($\tan\gamma'$). Fringes per cm are convenient units experimentally since the recorded gradient is then merely the reciprocal of the fringe spacing at the point on the photographic plate corresponding to the selected radial position x in the cell.

If Δx is small the square of the radial position is represented adequately by

$$x'^2 = x^2 + 2x\,\Delta x \qquad (5\text{-}20)$$

Using equations (5-11) and (5-18) we note that

$$\Delta x = F.Q.\theta(x) = K\,\theta(x) \qquad (5\text{-}21)$$

Substituting for $\theta(x)$ from equation (5-8) into (5-21) one obtains

$$\Delta x = 2K\lambda p \times j(x) \qquad (5\text{-}22)$$

Letting the fractional change in x^2 be q, we note from equation (5-20) and (5-22) that

$$q = \frac{2\Delta x}{x} = 4K\lambda\, p\, j(x) \qquad (5\text{-}23)$$

Which is obviously a function of the radial coordinate x, and in which we have assumed that the measured slope p' of the $\ell n(n)$ versus x^2 graph to be a close enough approximation to the true slope p.

Now

$$p' = \frac{\ell n(\frac{n_2}{n_1})}{(x_2'^2 - x_1'^2)} = \frac{A}{(X_2' - X_1')} \qquad (5\text{-}24)$$

in which it is assumed that the recorded fringe data is correct but displaced radially; x^2 has been replaced by X; the subscript indicates specific values and the prime indicates the value inferred from the photographic plate.

Letting

$$p' = p(1 - w) \qquad (5\text{-}25)$$

where w is the fractional change in p' owing to the radial displacements of the fringe, it may be shown that

$$w = \frac{X_2 q_2 - X_1 q_1}{X_2 - X_1} \qquad (5\text{-}26)$$

since from equation (5-20), $X' = X(1 + q)$.
Substituting specific values for q from equation (5-23) into equation (5-26), we obtain

$$w = 4K\lambda p \frac{x_2^2 j(x_2) - x_1^2 j(x_1)}{x_2^2 - x_1^2} \qquad (5\text{-}27)$$

In practice it would be convenient to allow $x_2 = x_b$ and $x_1 = x_m$ since these data are readily available, i.e.,

$$w = B p \frac{x_b^2 j_b - x_m^2 j_m}{x_b^2 - x_m^2} \qquad (5\text{-}28)$$

Here B is a constant $(4K\lambda)$ for a given ultracentrifuge and source wavelength, and j_m and j_b are the absolute fringe numbers corresponding to the solute concentrations at the meniscus (x_m) and base (x_b) respectively for the solution in the centrifuge cell.

It should be noted from equation (5-2) that w expressed in equation (5-27) is a measure of the fractional error in the apparent molecular weight of the solute for the ideal two-component system considered herein, and that w is in fact proportional to the molecular weight if other factors (ω^2 etc) remain constant. Again, for the Yphantis[70] type high speed equilibrium runs employing interference optics $j_m = 0$, and hence from equations (5-27) or (5-28)

$$w = B p \frac{x^2 j(x)}{x^2 - x_m^2} \qquad (5\text{-}29)$$

5. RESULTS AND DISCUSSION

Having analysed the effect of the radial gradient in the centrifuge cell for the interference optics, it is of interest to apply the results of the analysis to data applicable to an actual experiment to determine the orders of magnitude of the errors arising from this effect. Naturally, the analysis has been sufficiently general to apply to any ultracentrifuge employing interference optics with few modifications. However the author is familiar with a Beckman-Spinco Model 'E' analytical ultracentrifuge and

therefore data applicable to this instrument have been employed. Typical data are listed below for the instrument, and these were used in conjunction with data obtained from low speed equilibrium experiments (described in chapter 3) for the enzyme protein and a standard sucrose solution

λ(mercury) = 5.461×10^{-5} cm. λ(laser) = 6.328×10^{-5}cm.
t = 1.2 cm. F' = 3.4; F = 0.4564;
p'(sucrose) = 0.0257cm^{-2} p'(protein) = 0.6cm^{-2}

From measurements taken from the data derived from the equilibrium patterns the ratio $(\frac{x\ j(x)}{\tan \gamma'})$ was derived for the enzyme protein at various positions x between the meniscus and base. In all cases the ratio was found to be constant within the limits of experimental error with values of $1.86 \pm .03$ for the mercury source and $1.87 \pm .02$ for the laser source. For the sucrose equilibrium study with the laser source the ratio $(\frac{x\ j(x)}{\tan \gamma'})$ was found to be 41.4 ± 0.4, and as above the variations about the mean value was distributed randomly with radial position. From these results and the listed pertinent data, the value of Q for the laser source was found to be the same for both the protein and sucrose studies within experimental error i.e., Q = $0.024 \pm .001$, and this indicates that the differing solution refractivities encountered in ultracentrifuge interference work have little effect on this magnification factor. This is significant since it shows that Q remains constant for all radial positions in high speed experiments in which steep gradients are encountered. For the mercury source Q = $0.020 \pm .001$ for our instrument, indicating that there is a wavelength dependence.

It was found for the enzyme protein using equation (5-28) that W = 0.0003, or for this low speed equilibrium study the measured molecular weight was too small by only 0.03% owing to the above aberrations. Furthermore, for the sucrose study the calculated molecular weight would be too small by only 0.002% (which is negligible) since W is proportional to p' and the data shows that p' is a factor of 10 smaller for sucrose than for the protein. In addition, the linearity of the sucrose gradient

and the end of column extrapolations of fringe data (as is routine practice) would further diminish this effect if observable as mentioned previously in considering the linear gradient shown in figure 5-2.

The systematic error in the measurement of p would be hidden in practice since we note from equation (5-3) that the concentration distribution at equilibrium is exponential, and with the necessary correction being proportional to the gradient of the distribution, they are in fact proportional to the distribution itself, as will be apparent from the analysis. This means that the graph of $\ell n(n)$ versus x^2 will be a straight line both for the non-corrected and corrected data.

Naturally, the aberrations will be more serious for high speed meniscus depletion experiments, but for the typical experimental data of Chervenka[52] the error was estimated to be about 0.04%, which is again very small.

So far only the simple ideal two-component system has been considered, but it is known that the slope of the $\ell n(c)$ versus x^2 graph is proportional to the apparent weight average molecular weight of a mixture of ideal solutes at the position at which it is measured, and thus may be utilised in the determination of molecular weight distributions. Naturally, the simple correction procedure stated above is not applicable directly in this case, since p will vary with radial location and this necessitates a point by point radial correction for the fringe data. This problem is relatively straightforward, especially with the increasing use of computers[7] in the analysis of ultracentrifuge data. A mathematical appendix applicable to this problem is at the end of this chapter in which the non-linear curve $\ell n(n)$ versus x^2 is considered to be comprised of small sequential linear sections.

6. GRADIENTS FROM OFF-AXIS (REFERENCE) SECTORS

(a) Introduction:

In the ultracentrifuge cell, the surfaces of equal solute concentration are cylindrical rather than planes perpendicular to the slits of the Rayleigh aperture mask in

the machine. Hence a concentration gradient exists which is perpendicular to the aperture slits in the cell, i.e., in a direction y, perpendicular to the radial coordinate x in the pupil of the upper collimating lens L_2. This effect, depicted schematically in figure 5-4, was recognised from early times[71] and has been the subject of independent study undertaken by Charlwood and Mussett[72]. The latter's work indicated the effects to be small, but in the light of the author's analysis above it is appropriate to re-examine the problem, and attempt to devise suitable correction procedures that could be applied in practice if and when appropriate.

A schematic diagram illustrating the interference optical system in the analytical ultracentrifuge is shown in figure 5-1 and a schematic representation of the aperture mask and cell are shown in figure 5-5. The problem specific to the current work may be appreciated pictorially from figures 5-4 and 5-5 which are used in the subsequent analysis.

Since the effects of the non-radial gradients are small[72] it is convenient in the current work to analyse the system for the asymmetrical mask[4] (as is depicted in figure 5-5) in which the effects are more pronounced. The mask comprises two parallel slots of greater width than those in the cell diaphragm (see figure 5-1). The " solution" slot (slot 1) is centered in the optical system along a radius from the axis of rotation whilst the reference slot (slot 2) is displaced laterally a distance $y = b$.

(b) Theory

The theory and notation in this analysis are based on that developed above by the author. To exemplify the effects of the non-radial refractive index gradients, it is assumed in the analysis that both sectors of a centrifuge cell are filled with an identical two-component system in which equilibrium has been attained. Neglecting for the moment the effects of comparing non-conjugate levels and the non-radial gradients, the above system in the centrifuge would result in a fringe pattern consisting of perfectly horizontal fringes owing to the solution and reference being identical. However, for the actual system the above assumptions are unwarranted and so the fringe pattern observed will be modified owing to the foregoing effects.

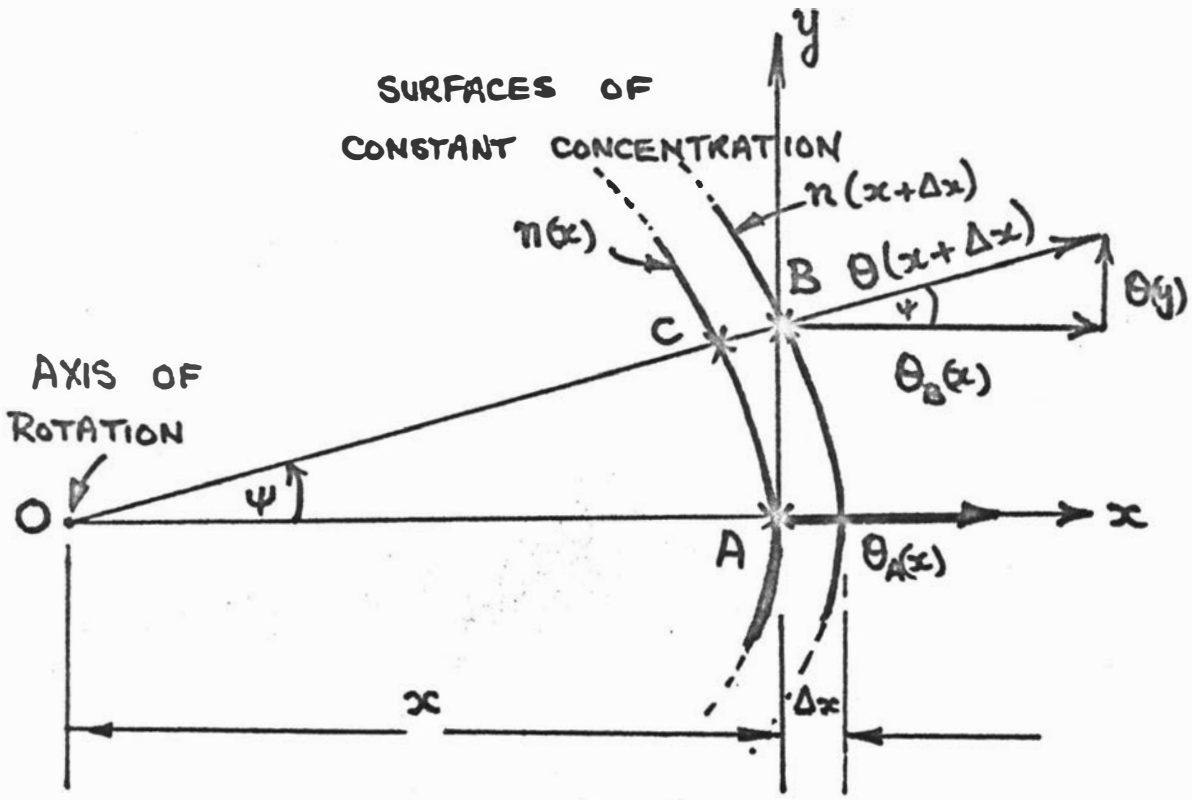

FIGURE 5-4. SCHEMATIC DIAGRAM OF REFRACTIVE INDEX GRADIENTS IN A CENTRIFUGE CELL.

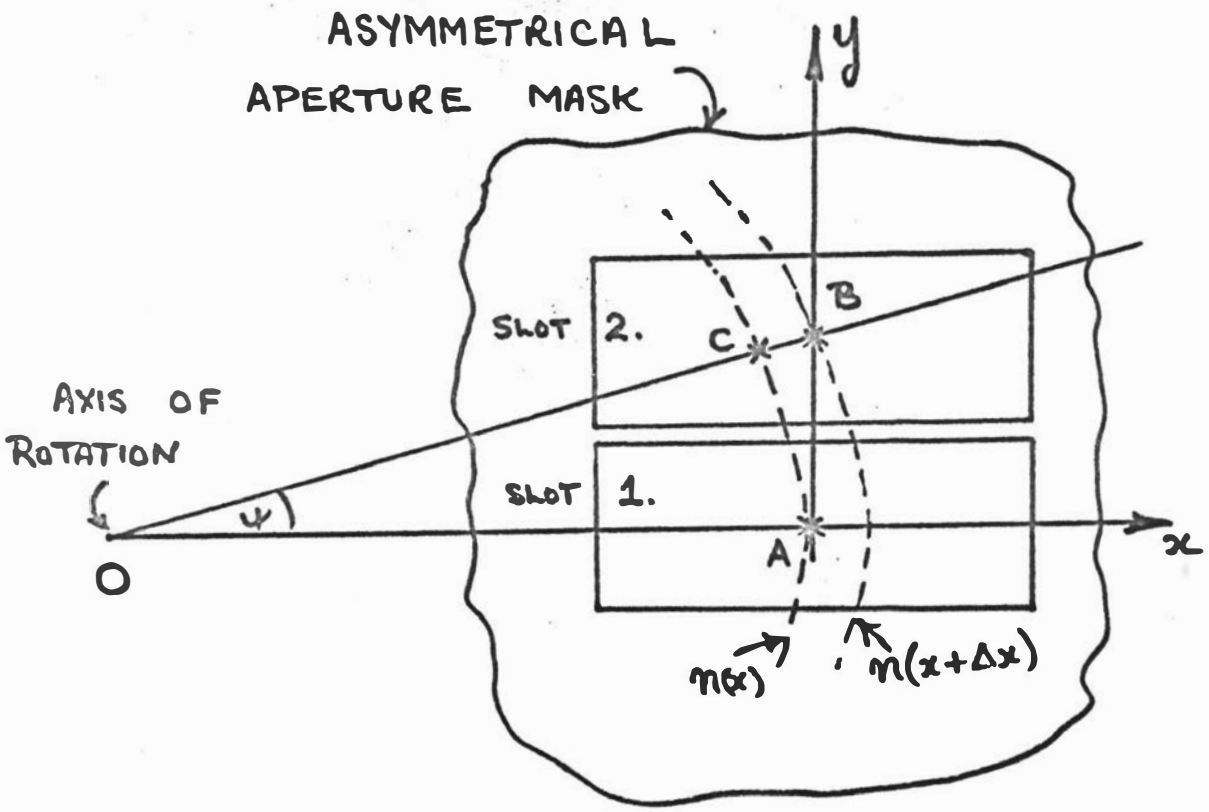

FIGURE 5-5. DIAGRAM SHOWING THE SURFACES OF CONSTANT CONCENTRATION IN A CENTRIFUGE CELL IN RELATION TO AN ASYMMETRICAL APERTURE MASK.

For the above system in equilibrium it may shown from equation (5-2) that

$$\frac{d(\ell n\ n)}{d(x^2)} = p = \frac{M_{app}\,\omega^2(1-\bar{v}\rho)}{2RT} \qquad (5\text{-}30)$$

where n is the difference between the refractive index of the solution in both sectors of the cell and that of the solvent alone. As usual n is assumed to be proportional to the solute concentration at a given radial position x. For the given ideal system p is a constant, and the parameters on the right hand side of equation 1 have their usual meaning.

The cell is assumed to be aligned instantaneously with the aperture mask within the centrifuge. A cylindrical surface of constant solute concentration $n(x)$ is shown in figure 5-5, and cuts the two aperture slits (1 and 2) at points A and C respectively. However, the interference system compares the concentration at point A in slit 1 with B in slit 2, rather than with the conjugate position C in slit 2. Writing $n(y)$ as the refractive index difference between solution and solvent alone at B, it may be shown[72] by Pythagoras' theorem and equation 1 that

$$\ell n\ \left(\frac{n(y)}{n(x)}\right) = py^2$$

or
$$n(y) = n(x)\ \exp^{py^2} = n(x)\ (1 + py^2 + \ldots\ldots) \qquad (5\text{-}31)$$

The latter expansion is valid in practice since even for solutions of macromolecules such as proteins (which are unlikely to be constituents of solvent solutions) the value of py^2 is ~ 0.1.

It is assumed in the analysis that the cell diaphragm, aperture mask and lens L_2 are very close to the plane OAB on the optic axis (see figures 5-1 and 5-5), and that the effects of the finite widths (Δy) of the slits in the aperture mask and cell diaphragm are negligible[72].

At a given radial position (x), $n(x)$ is a

constant given by

$$n(x) = n_m \exp^{p(x^2 - x_m^2)} \qquad (5\text{-}32)$$

Here n_m is the refractive increment at the solution meniscus (x_m) and is proportional to the solute concentration at this position.

Now the optical path difference (Δ) between a light wave travelling through the solution at position B in figure 5-5 to that travelling through the solvent alone at the same position is given by

$$\Delta(y) = n(y)\, t \qquad (5\text{-}33)$$

where t is the thickness of the centrifuge cell. In addition it is shown (equation (5-5)) that the angular deflection experienced by the wave travelling through the solution compared to that travelling through solvent is given by the gradient of this path difference in the relevant direction,
i.e.,

$$\Theta(x_k) = \frac{d(\Delta)}{d(x_k)} \qquad (5\text{-}34)$$

in which Δ and x_k are the generalised optical path difference and coordinate respectively. Hence from equations (5-31, 5-33 and 5-34) it may be shown that

$$\Theta(y) = \frac{d(\Delta(y))}{dy} = 2p\, ty\, n(x) \qquad (5\text{-}35)$$

Here $\Theta(y)$ represents the angular deflection in the y direction of a wave passing through the solution at a position y (B in figure 5-5) relative to an undeflected wave that would pass through the solvent alone at that point.

On the other hand, we notice from equation (5-35) that when $y = 0$, (solution cell slit 1) $\Theta(y) = 0$, and thus with the identical two component systems in both sectors of the centrifuge cell as arranged above, $\Theta(y)$ will be relative to the solution cell (slit 1). The latter effect is systematic to the instrument, and occurs because non-conjugate levels are being compared

between the two sectors of the cell.

Following a similar line of analysis to that undertaken by the author above it is possible to write equation (5-35) in terms of fringe numbers by use of the identity

$$j(x) = \frac{t\, n(x)}{\lambda} \qquad (5\text{-}36)$$

Here $j(x)$ is the absolute number of fringes corresponding to a solute concentration represented by $n(x)$, and λ is the wavelength of the light used.

Whence from equations (5-35) and (5-36)

$$\Theta(y) = 2p\,\lambda\, y\, j(x) \qquad (5\text{-}37)$$

Equations (5-35) and (5-37) enable the magnitude of the effects introduced by using the assymmetrical mask to be evaluated in specific cases, since the negative vertical displacement of the fringes in the focal plane of lens L_2 is given by

$$\delta\xi' = f_2\, \Theta(y) = 2\, f_2\, \lambda\, y\, j(x) \qquad (5\text{-}38)$$

where f_2 is the focal length of the upper collimating lens L_2.

On the photographic plate the corresponding vertical displacement of the fringes (δv) is given by

$$\delta v = F'\, f_2\, \Theta(y) = 2F'\, f_2\, \lambda\, p\, y\, j(x) \qquad (5\text{-}39)$$

in which F' is the vertical magnification factor of the instrument between the photographic plate and the fringe system located in the focal plane of lens L_2.

Further to the above, it will be apparent from equations (5-31) and (5-33) that $\Delta(y)$ is infact a function of the radial coordinate x. The physical significance of this mathematical observation will be appreciated from (5-34) and figure (5-5), since for the assumed experimental conditions the radial deflection for waves emanating from B in slit 2 is greater than the radial

deflection of the waves from the compared position A in slit 1.

From equations (5-31) and (5-33) the relative path difference $(\Delta_B - \Delta_A)$ between the two compared positions A and B in figure 5-5 is given by

$$\Delta_B - \Delta_A = t\ p\ y^2\ n(x) \tag{5-40}$$

which is obviously a function of x and y. By use of equations (5-34) and (5-40) the relative angular radial deflection may be found

i.e.

$$\delta\theta(x) = \frac{d(A_B - \Delta_A)}{dx} = 2t\ p^2 y^2\ x\ n(x) \tag{5-41}$$

This is very small and again n(x) may be written in terms of the fringe numbers (j(x)) if convenient by use of equation (5-36).

(c) Discussion and Results

It is appropriate to remind ourselves of the physical significance to the actual analytical ultra-centrifuge of the analysis developed above. Firstly, the non-radial gradient gives rise to a vertical shift in the fringes on the photographic plate owing to $\theta(y)$, and this would be interpreted as a change in concentration within the cell. Secondly, the radial gradient will give rise to a horizontal shift in the fringes on the photographic plate, and this effect would be interpreted as a change in the radial position in the centrifuge cell at which the recorded concentration occurred.

In addition to the above, it should be appreciated that the deflection phenomena just referred to occurs within the offset sector of the centrifuge cell (slot 2 in figure 5-5) relative to the radial sector. This former sector normally contains the reference solution in an actual experiment, and hence positive effects in this cell will have a negative interpretation where evaluated from plate measurements. In other words, a positive gradient in the reference cell 2 would give the same record on the photographic plate as an identical negative gradient in the solution cell 1. In practice one always interprets the data

as if it arose for the solution cell (slot 1 in figure 5-5) relative to the reference cell 2.

We are now in a position to evaluate the aberrations analysed above as they will apply in practice. The magnitudes of the effect of the non-radial gradient $\Theta(y)$ have been evaluated in the independent and different analysis of Charlwood and Mussett[72]. Their work indicated that the concentration changes owing to $\Theta(y)$ inferred from photographic plates were of the same order of magnitude as the experimental errors involved in making the plate measurements using current procedures. However, the analysis has shown that concomitant with the non-radial deflection of the waves ($\Theta(y)$) from the reference sector there exists an additional radial deflection ($\delta\Theta(x)$) relative to the solution sector given by equation (5-41). The effect of this additional and inherent radial gradient will be small, but from the above discussion its effect on the plate measurements will be such as to reduce the overall effect of $\Theta(y)$. Thus numerical results evaluated for $\Theta(y)$, which were computed by Charlwood and Mussett[72] using typical data, are larger than would be observed should the precision of experimental plate measurements be increased.

The importance of the current analysis is that it has indicated procedures whereby the effects of the above extraneous gradients may be corrected should the need arise. Under normal conditions the effects will be small since the ideal solution in the reference arm is the solvent normally used in macromolecular studies e.g., buffer or salt solutions. Much of the physical data applicable to standard solvents are available from reference tables or may be determined for specific cases in the laboratory. From these and the above work appropriate procedures may be developed that could be used routinely in the computer analysis of sedimentation equilibrium data along with the corrections for other inherent effects, e.g., rotor stretch etc. .

7. SUMMARY

A theoretical analysis of the effects of the radial concentration gradient on the observed experimental data obtained by using the interference optics in the

analytical ultracentrifuge has been made. The analysis, which is applicable to both double and triple sector cell interference work, has shown that the gradients produce systematic errors in the apparent molecular weights of molecules, if the actual observed data from equilibrium studies is used directly. The errors have been shown to be small for the assumptions made in this analysis and if valid (see below) can be safely ignored in comparison with current instrumental accuracy. However, should the need arise the correction procedures outlined are simple and amenable to routine laboratory practice. This is especially so with the increasing use of computers for data analysis, since the procedures are based on the normal input data.

The small apparent effects are disappointing, but the novel approach to the gradient problem developed in the above analysis has been worthwhile, since it has given new insight into the interference optics of the analytical ultracentrifuge. However, the analysis was based on the premise that the cell containing the sedimenting solution could be simulated by an optically homogeneous prism. In retrospect, and in the light of the work of Ford and Ford[68], the author feels that this initial assumption may have been an oversimplification of the actual conditions. The sedimenting solution is obviously optically non-homogeneous and so the exit angle $\Theta(x)$ of the light waves could well be larger in practice than supposed in the analysis.

A re-investigation of the problem is in hand, based on the procedures developed in this chapter and the theory of light rays in non-homogeneous media given by Born and Wolf[24]. It is hoped to include the preliminary results of the analysis in a supplementary appendix to this thesis.

8. APPENDIX

MATHEMATICAL FORMULATION OF RADIAL FRINGE DATA CORRECTION PROCEDURE FOR IDEAL MIXED SOLUTE SYSTEMS

Here it is assumed that the slope ($p(x)$) of the $\ell n(n)$ versus x^2 graph for an ideal mixed-solute system in equilibrium is proportional to the weight-average molecular

weight of the solute at the given radial position x. We see from equation (5-6) that the angular radial displacement of fringe data at x_j will be given by

$$\Theta(x_j) = 2p(x_j)t\, x_j\, n(x_j) \qquad (5\text{-}A1)$$

in which the parameters have been defined previously. Assume that the graph of $\ell n(n)$ versus x^2 is considered sufficiently linear from position x_j to $(x_j + h)$. Obviously, h may vary from position to position on the graph as experimental conditions dictate. If we take a Taylor's expansion of equation (5-A1) we find that

$$\Theta(x_j + h) = \Theta(x_j) + h\, D_x^1\, \Theta(x_j) + \frac{h^2}{2!}\, D_x^2\, \Theta(x_j)$$

$$+ \ldots\ldots\ldots\ldots\ldots\ldots\ldots$$

or
$$\Theta(x_j + h) = \sum_{m=0}^{\infty} \frac{h^m}{m!}\, D_x^m\, \Theta(x_j) \qquad (5\text{-}A2)$$

where $D_x^m\, \Theta(x_j) = \dfrac{d^m \Theta(x)}{dx^m}$ evaluated at $x = x_j$

Fortunately, for small h the series represented by equation (5-A2) converges rapidly under normal experimental conditions, and the number of terms required to achieve a given accuracy will be dictated by specific data, but one would expect the first few terms to suffice. From equations (5-A1) and (5-3) the first few differential terms have been evaluated, and are listed below, together with a reduction formula from which all the differentials may be derived.

$$D_x^0 = \Theta(x) = 2pt\, x\, n(x)$$

$$D_x^1 = 2pt \left[2p\, x\, n(x) \right]$$

$$D_x^2 = 2pt \left[2p\, n(x) + 2p\, x\, D_x^1\, n(x) \right]$$

$$D_x^3 = 2pt \left[4p\, D_x^1\, n(x) + 2p\, x\, D_x^2\, n(x) \right]$$

$$D_x^m = 2pt \left[(2m-2)p\, D_x^{m-2} n(x) + 2p\, x\, D_x^{m-1} n(x) \right]$$

whence substituting this result into equation (A2) we obtain

$$\Theta(x_j + h) = \Theta(x_j) + 2pt \sum_{m=1}^{\infty} \frac{h^m}{m!} \left[(2m-2)\, D_x^{m-2} n(x_j) + 2p\, x_j D_x^{m-1} n(x_j) \right] \tag{5-A4}$$

where $D_x^m n(x_j) = D_x^m n(x)$ evaluated at $x = x_j$.

Obviously, one repeats the above procedure across the cell from x_m to x_b making point by point radial corrections to the fringe data by use of equations (5-11) and/or (5-18).

CHAPTER 6.

'MATHEMATICAL FORMULATIONS OF THE EFFECTS OF CELL DISTORTION AND LIQUID COLUMN HEIGHT COMPRESSION IN ANALYTICAL ULTRACENTRIFUGATION

1. INTRODUCTION

The advent of high speed analytical ultracentrifugation methods such as those of Yphantis[70], together with the enhanced accuracy in the optical analysis as shown in this thesis and elsewhere[11,12,21] has led to an increasing demand for precision in techniques involving the analytical ultracentrifuge, and this has made it necessary to take into account effects heretofore neglected. Furthermore, improvements in rotor speed mechanisms such as that of Smiriga and Hearst[73] and others[74], have reduced the instantaneous deviations of rotor speed to less than 0.01% in the Beckman Model E instrument. In addition the instrument is equipped with a standard RTIC (Rotor Temperature Indicator and Control) unit[75] which maintains the rotor temperature constant to within 0.1 ^{o}C during operation. Thus the rotor and cell are effectively isothermal during operation and the centrifugal field terms $\omega^2 r$, where ω is the angular velocity and r the radius, can be calculated to 0.02%. This implies that for the true precision to be realised, account has to be taken of rotor stretch, and cell deformation in the centrifugal field. The former has been investigated experimentally by Kegeles and Galter[76], Schachman[4], and Baghurst and Stanley[77], from whose work data are available for both aluminium and titanium rotors. In addition mathematical analyses of rotor stretch for variable geometry rotors have been formulated by Timoshenko[78] and by Biezeno and Grammel[79]. For the Beckman Model 'E' ultracentrifuge it has been shown experimentally by Schachman[4] that the radial coordinates r can increase by 0.5% at 59,780 rpm for an aluminium rotor, and Baghurst and Stanley[77] have shown that r increases by as much as 0.75% at 67,770 rpm for an An-H Titanium rotor. Hence as the above authors have intimated it is essential to correct for the effects of rotor stretch for precise work. However, owing to body forces in the centrifugal field the cell itself undergoes distortion (compression), and experimentally in the past this effect has been masked partially by the rotor stretch. It is the purpose of this chapter to investigate cell distortion theoretically as distinct from rotor stretch, so that these effects may be assessed

and their significance appreciated.

2. THE MODEL AND THEORY

The model that has been developed is the result of various attempts to simulate the conditions of the cell centrepiece in the rotor. I have analysed this model according to the theory and notation of Landau and Lifshitz[80], and for simplicity have assumed rectangular symmetry for the cell and centrifugal field as indicated in the diagram of the cell centrepiece in figure 6-1. To separate the effects of rotor stretch from those of cell distortion a symmetrical position has been selected, distance 'R' from the axis of rotation as the origin of the coordinate system. Naturally, R will vary with rotor speed owing to rotor stretch. The cell is located in the xy plane and the positive z-axis of our system is in the negative radial direction of the rotor. The undeformed cell centrepiece considered is a rectangular block of square cross-section a^2 in the xz plane and of length 'b' in the y direction, (the direction of the optical axis in the ultracentrifuge). Physically the field is that which applies for $R \gg a$. Hence the problem was to determine the deformation of the centrepiece resting in the rotor at $z = o$ subjected to a gravitational field $g_z = -\omega^2(R-z)$; $g_y = g_x = o$, since the earth's field in the y direction is neglected. Furthermore, one boundary condition imposed was that the displacement vector u_z was zero when $z = o$, since the centrepiece was assumed to be supported by the rotor in this plane.

It is shown by Landau and Lifshitz[80] that if a body is in equilibrium and is located in a gravitational field, then the internal stresses and the force of gravity per unit volume must vanish, and this result is expressed in their equation (2-7)

i.e.,

$$\frac{\partial \sigma_{ik}}{\partial x_k} + \rho g_i = 0 \qquad (6\text{-}1)$$

Where σ_{ik} is a general stress tensor element, x_k is a generalised coordinate, ρ is the density of the centrepiece material and g_i is the component of the gravitational field in the i th direction.

From (6-1) the equations of equilibrium for the body become

$$\frac{\partial \sigma_{yk}}{\partial x_k} = \frac{\partial \sigma_{xk}}{\partial x_k} = 0 \qquad (6\text{-}2)$$

and

$$\frac{\partial \sigma_{zk}}{\partial x_k} = \rho\omega^2(R-z) \qquad (6\text{-}3)$$

Now the boundary conditions that must be satisfied for the model are as follows:

(a) On the sides of the centrepiece all components σ_{ik} vanish except σ_{zz}.

(b) When $z = a$, $\sigma_{xy} = \sigma_{yz} = \sigma_{zz} = 0$.

The solution of the equilibrium equations satisfying the boundary condition is

$$\sigma_{zz} = -\rho\omega^2 \left[R(a-z) - \tfrac{1}{2}(a^2 - z^2) \right] \qquad (6\text{-}4)$$

with all other

$$\sigma_{ik} = 0 \qquad (6\text{-}5)$$

Knowing the stress elements σ_{ik} we can find the strain tensor elements u_{ik} by use of Landau and Lifshitz's[80] equation (5-12)

i.e.,

$$u_{ik} = \left[(1+\sigma)\sigma_{ik} - \sigma\sigma_{\ell\ell}\,\delta_{ik} \right] / E \qquad (6\text{-}6)$$

Where σ is Poisson's ratio and E is Young's modulus for the centrepiece material, δ_{ik} is a unit matrix, and the double subscript for the stress tensor indicates summation in accordance with standard tensor notation.

Whence

$$u_{xx} = \frac{\rho\omega^2}{E}\sigma \left[R(a-z) - \tfrac{1}{2}(a^2 - z^2) \right] \qquad (6\text{-}7)$$

$$u_{yy} = \frac{\rho\omega^2}{E}\sigma \left[R(a-z) - \tfrac{1}{2}(a^2 - z^2) \right] \qquad (6\text{-}8)$$

$$u_{zz} = \frac{\rho\omega^2}{E} \left[R(a-z) - \tfrac{1}{2}(a^2 - z^2) \right] \qquad (6\text{-}9)$$

and

$$u_{xy} = u_{xz} = u_{zy} = 0 \qquad (6\text{-}10)$$

- the strain tensor being symmetrical of course as shown by Landau and Lifshitz's[80] equation (1-4). The object of this analysis is to determine the displacement vector $\bar{u}$ at any point in the centrepiece, since this is the quantitative measure of deformation. This is found from the relationship between the strain tensor elements and the displacement vector formulated in Landau and Lifshitz's[80] equation (1-5)

i.e., $$u_{ik} = \frac{1}{2}\left[\frac{\partial u_i}{\partial x_k} + \frac{\partial u_k}{\partial x_i}\right] \qquad (6\text{-}11)$$

Where the double subscript indicates strain tensor elements, and the single subscript the relevant displacement vector component. Thus by integration we obtain the components of the displacement vector,

$$u_x = \frac{\rho\omega^2}{E}\sigma\left[R(a-z) - \tfrac{1}{2}(a^2 - z^2)\right]x \qquad (6\text{-}12)$$

$$u_y = \frac{\rho\omega^2}{E}\sigma\left[R(a-z) - \tfrac{1}{2}(a^2 - z^2)\right]y \qquad (6\text{-}13)$$

$$u_z = -\frac{\rho\omega^2}{2E}\left[R\,z(2a-z) - z\left(a^2 - \frac{z^2}{3}\right) + \sigma(R-z)(x^2+y^2)\right] \qquad (6\text{-}14)$$

It should be noted at this stage that the expression for u_z satisfies the boundary condition $u_z = 0$ only at the point of origin of the coordinate system, and hence the solution is not valid near this plane. However, the solution near this latter plane is not required in the subsequent analysis.

A cell cavity in the model has rectangular geometry and initally it is assumed that it is positioned symmetrically as shown in figure 6-2. In practice the liquid under investigation is placed in the cavity in the cell centrepiece, and it is of interest to determine the cavity deformation in the centrifugal field. In stress analysis this problem frequently introduces complexity owing to new boundary conditions, but in the present model the problem is relatively simple, since we note from equations (6-4) and (6-5) that only σ_{zz} is finite and all other σ_{ik} are zero. Physically, this means that a cavity and body material in our cell

centrepiece behave identically.

It can be shown by the use of equation (6-14) that the fractional change in the overall length of side z_2z_1 owing to cell deformation is given by

$$p_z = \frac{\rho\omega^2}{2E}\left[2Ra - R(z_2+z_1) - a^2 + \frac{z_2^2+z_2z_1+z_1^2}{3} - \sigma(x^2+y^2)\right] \qquad (6\text{-}15)$$

whereas by use of equations (6-12) and (6-13) the fractional changes in overall lengths of the sides parallel to the x and y axes located at z_1 and z_2 respectively are given by

$$p_{x1} = p_{y1} = \frac{\rho\omega^2\sigma}{2E}(a-z_1)(2R-a-z_1) \qquad (6\text{-}16)$$

$$p_{x2} = p_{y2} = \frac{\rho\omega^2\sigma}{2E}(a-z_2)(2R-a-z_2) \qquad (6\text{-}17)$$

Where p_{x1} is the overall fractional change in the side parallel to the x-axis located at z_1 etc.

Thus from equations (6-15) - (6-17), and a knowledge of the undeformed cavity dimensions, the deformation of the cavity may be calculated.

By inspection of equations (6-16) and (6-17) it will be noted that the R.H.S.'s are always positive and hence the dimensions in the xy plane are always increased owing to cell deformation, whereas the R.H.S. of equation (6-15) could be positive, negative or zero. A diagrammatic picture of the deformed rectangular cavity is shown in figure 6-3.

Consider a rectangular cavity of initial volume

$$V = (z_2-z_1)x_1y_1 \qquad (6\text{-}18)$$

where (z_2-z_1), x_1 and y_1 are the undeformed lengths of the sides. It can be shown that the volume V' of the deformed cell depicted in figure 6-3 is given to a close approximation by

$$V' = \frac{(z_2-z_1)'_o}{2}\left[y'_{12}(x'_{11}+x'_{12}) + x'_{11}(y'_{11}-y'_{12})\right] \qquad (6\text{-}19)$$

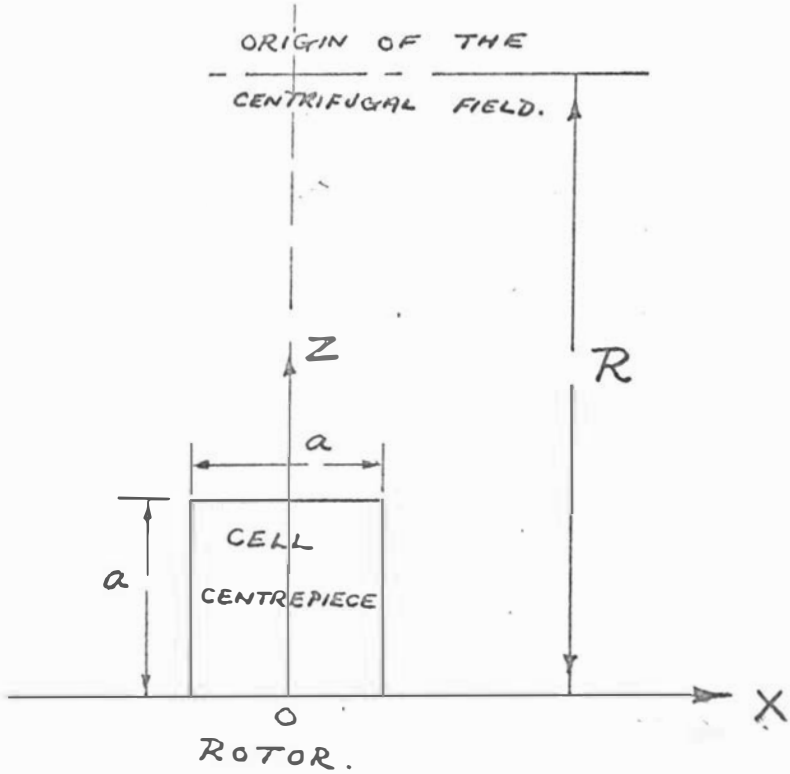

FIGURE 6-1. DIAGRAM OF THE RECTANGULAR CELL CENTREPIECE AND ITS COORDINATE AXIS SYSTEM. THE y-AXIS IS PERPENDICULAR TO THE PLANE OF THE PAPER.

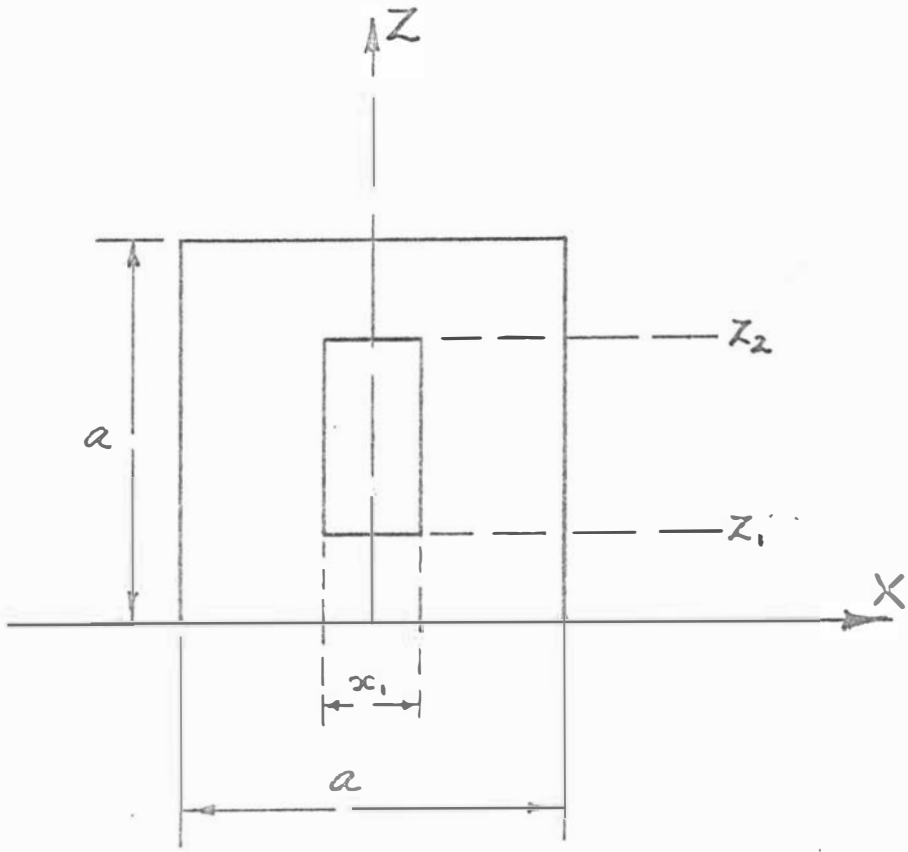

FIGURE 6-2. DIAGRAM OF THE SYMMETRICAL RECTANGULAR CAVITY IN THE MODEL CELL CENTREPIECE. THE CAVITY HAS DIMENSIONS y_1 PERPENDICULAR TO THE PLANE OF THE PAPER.

where $(z_2-z_1)'_o$ * is the deformed length of the side (z_2-z_1) evaluated at $x = o$, $y = o$; and y'_{12} is the deformed length of side y_1 evaluated at z_2 etc.

*[Note the variation in $(z_2-z_1)'$ over the range of values of x and y used for the cavities within the model is negligible.]

Using equations (6-18) and (6-19) it can be shown that fractional volume change (δ) of the cavity is

$$\delta = \frac{\rho\omega^2}{2E}\left[(2\sigma+1)\left\{a(2R-a)-R(z_2+z_1)\right\} + \frac{z_2z_1}{3} + \frac{1}{3}(3\sigma+1)(z_2^2+z_1^2)\right] \tag{6-20}$$

The practical significance of equation (6-20) insofar as the ultracentrifuge is concerned, is that the height of the liquid column in the cell varies with the rotor speed, and this effect if observed may be misinterpreted as additional liquid compression. A separate analysis of this latter effect together with an appropriate discussion of the effects and magnitudes to be expected from this source are included in an appendix to this chapter. However, assuming that a liquid in the cell under investigation is incompressible we can determine the change in liquid column height in terms of the known parameters using equation (6-20). Doing this we find that in the deformed cell the liquid column height h' is given by

$$h' = h(1-q) \tag{6-21}$$

where $$q = \frac{\rho\omega^2}{2E}\,\sigma\left[2a(2R-a) - 2R(z_b + z_m) + z_b^2 + z_m^2\right] \tag{6-22}$$

and in which z_b and z_m are the locations of the liquid base and meniscus respectively. From equation (6-22) we note that q can be positive, negative or zero, and that the sign depends only on the rotor and cell coordinates, and is independent of materials and rotor speed. Thus it should be possible (theoretically) to design a centrifuge system partially to eliminate this effect.

We also see from equation (6-22) that the fractional change in liquid column height q is itself a

function of the column height $h = (z_m - z_b)$ and of its location z_b in the cell. Rewriting equation (6-22) in terms of these latter two observable parameters we obtain

$$q = \frac{\rho\omega^2}{2E}\sigma\left[2a(2R-a) - 2R(2z_b + h) + z_b^2 + (z_b + h)^2\right] \qquad (6\text{-}23)$$

3. APPLICATION OF THEORY AND DISCUSSION

Having derived equations relevant to a cell in an ultracentrifuge it is important to determine an estimate of the order of magnitude of the aforementioned effects. To this end, data relevant to the Beckman Model 'E' instrument were inserted into the equations, under the assumption that the cell was constructed of duralumin but the results may be applied readily to centrepieces constructed from other materials. The data used are as follows, assuming the symmetrical cavity of figure 6-2.

$R = 7.5$ cm ; $a = 2.2$ cm ; $z_1 = 0.6$ cm ;

$z_2 = 1.6$ cm ; $x_1 = 0.25$cm ; $y_1 = 1.2$ cm.

From Kaye and Laby[81] for duralumin

$\rho = 2.8$ g/ml ; $\sigma = 0.33$; $E = 7.3 \times 10^{11}$ dynes cm^{-2}

and the rotor speed varies in the range 0 - 75,000 rpm. The above data are applicable to a typical cell used for long column experiments.

Since z_b is fixed by the above data to about 0.6 cm (i.e. $r_b \simeq 6.9$ cms from axis of rotation), it was of interest to use equation (6-23) to find the column height for which q the fractional change in column height was zero. The resulting calculation gave column heights $h = 4.0$ cm and 9.8 cm which are physically impossible with the cells used. For a typical cell $0 \leq h \leq 1.0$ cm and therefore a change in liquid column height should be present in practice. Furthermore, by differentiating equation (6-23) with respect to h and inserting values of h in the range $0 \leq h \leq 1.0$ cm, we find that $\frac{dq}{dh}$ is always negative, indicating that the shorter the column

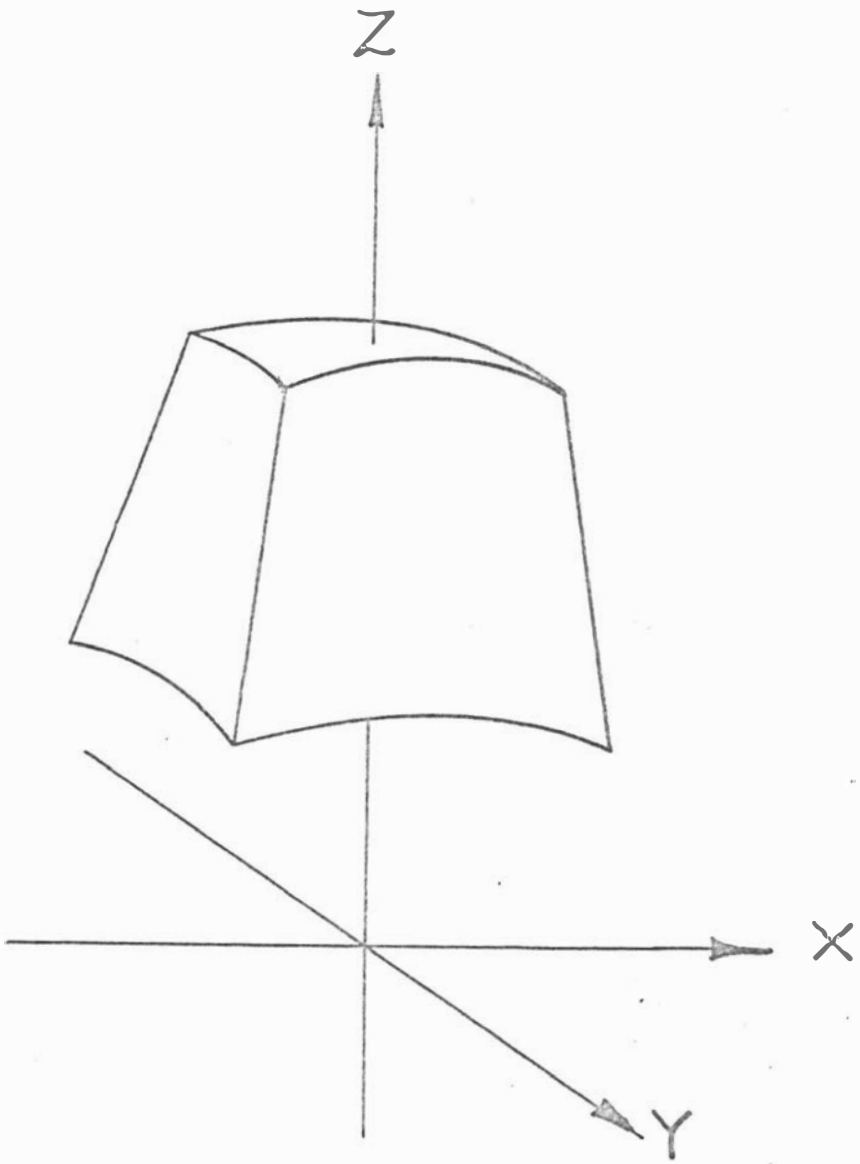

FIGURE 6-3. DIAGRAMATIC REPRESENTATION OF THE CAVITY SHOWN IN FIGURE 6-2 AFTER DEFORMATION OWING TO THE CENTRIFUGAL BODY FORCES.

the greater the effect. The latter result is important owing to recent emphasis on high speed, short column methods[70], and contrasts with the effect associated with finite liquid compressibilities (see appendix). Again from equation (6-23) for h in our experimental range, we find that q is always positive, and hence from equation (6-21) we see that liquid column heights should always contract owing to cell distortion under the applied experimental conditions. Figures 6-4 and 6-5 show graphically the percentage contraction for liquid column heights in the range of interest for the duralumin cell model under consideration. Data are plotted over the typical rotor speed range 0-75,000 rpm of the Beckman Model 'E' instrument. From graphs we note that at 70,000 rpm for a short column experiment of 3 mm the percentage contraction is in the region of 0.12%. This gives an actual change in column height of about 0.0004cm. Since the Interference/Schlieren optical system of the ultracentrifuge magnifies the radial dimensions by about x2 this would result in a change of about 0.001 cm on the photographic plate. This should be observable since the microcomparators employed in plate analysis for interference work have least count of 0.0001 cm. In practice cell distortion is coupled with window distortion, since the above stress analysis could apply equally to isotropic cell windows, and such a simple extrapolation is not really relevant at these speeds owing to uncertainties associated with locating the exact positions of the meniscus and base on the photographic plates. However, with the introduction of laser sources as shown in this thesis and elsewhere[82], coupled with improved window holder design[57], the menisci will be more clearly defined, and it should be possible to measure the above effect in practice and make any necessary corrections when precise work (particularly interference) is being undertaken. Obviously for cells with an improved density to strength ratio ($\frac{\rho}{E}$) this effect will be diminished as expected, and this is indicated in the theoretical equations.

For an interference cell model in which there are two cavities symmetrically located about the z-axis

we find the results for each cavity similar to those for the single cavity described above.

A cell that is becoming increasingly popular in experimental work and to which cell distortion could be of major importance is the high speed Yphantis type cell - of which a recently improved side access version has been described by Ausevin, Roark and Yphantis[57]. This latter cell is specifically designed for rotor speeds in excess of 40,000 rpm. Now this cell is fabricated to improve amongst other things its density to strength ratio, and to consider a duralumin version as an example of the effects of cell distortion is unduly pessimistic. However the results obtained by the analysis of a duralumin cell will emphasise the effects cell distortion could have in such a cell, and indicate relevant correction procedures should these be found necessary. A diagram of a three channel Yphantis cell applicable to our model is shown in figure 6-6. Cell distortion could be of primary importance in a cell of this type owing to its discrimatory effects amongst the channels. This is in contrast to rotor stretch which effects all channels equally. Fundamentally, the cell distortion effects are twofold: (a) the displacement of the cell base position (u_{zb}) will be different for each channel, and (b) the variation in liquid column height (q) for similar levels (h) in the channels will be different.

An estimate of the effect of cell base positions displacement can be found from equation (6-14) where z is replaced by the appropriate z_b and other parameters have the same numerical values as defined previously. However, the last term in the brackets indicating the effect of the cell position in the xy plane is small and hence equation (6-14) may be rewritten as

$$u_{zb} = -\frac{\rho\omega^2}{2E}\left[Rz_b\,(2a-z_b) - z_b\left(a^2 - \frac{z_b}{3}\right)^2\right] \qquad (6\text{-}24)$$

Note the negative sign indicates that the displacement is in the negative z-direction i.e., in the radial direction of the rotor as expected. We see that the displacement is proportional to (i) the square of the rotor speed, (ii) the density to strength ratio of the cell material,

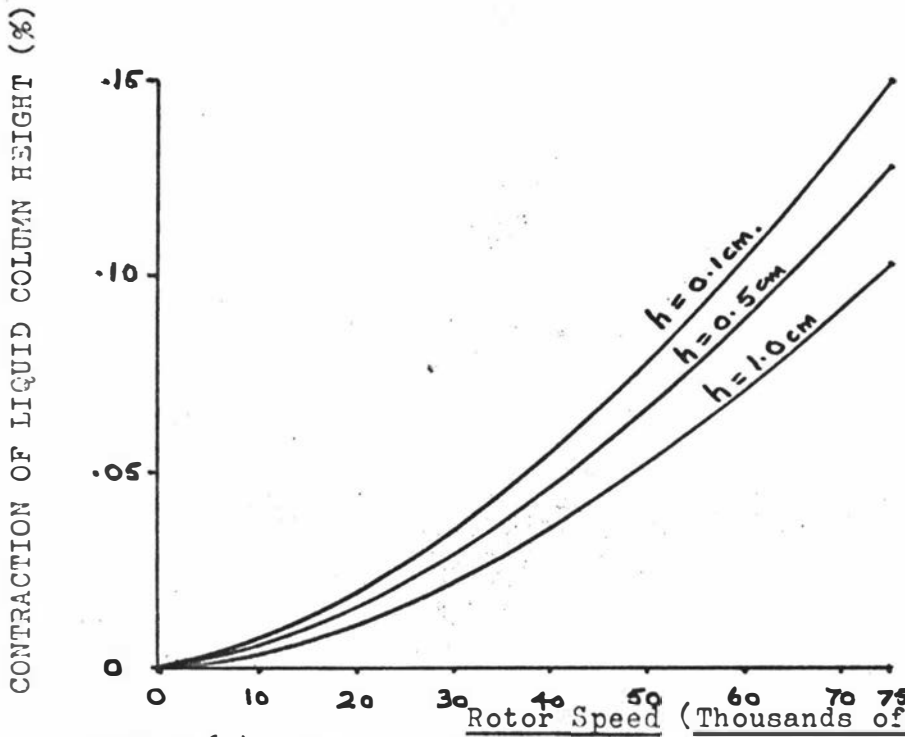

FIGURE 6-4. Graph Showing the Percentage Contraction of the Liquid Column Height with Rotor Speed for Three Different Column Heights in the Duralumin Model.

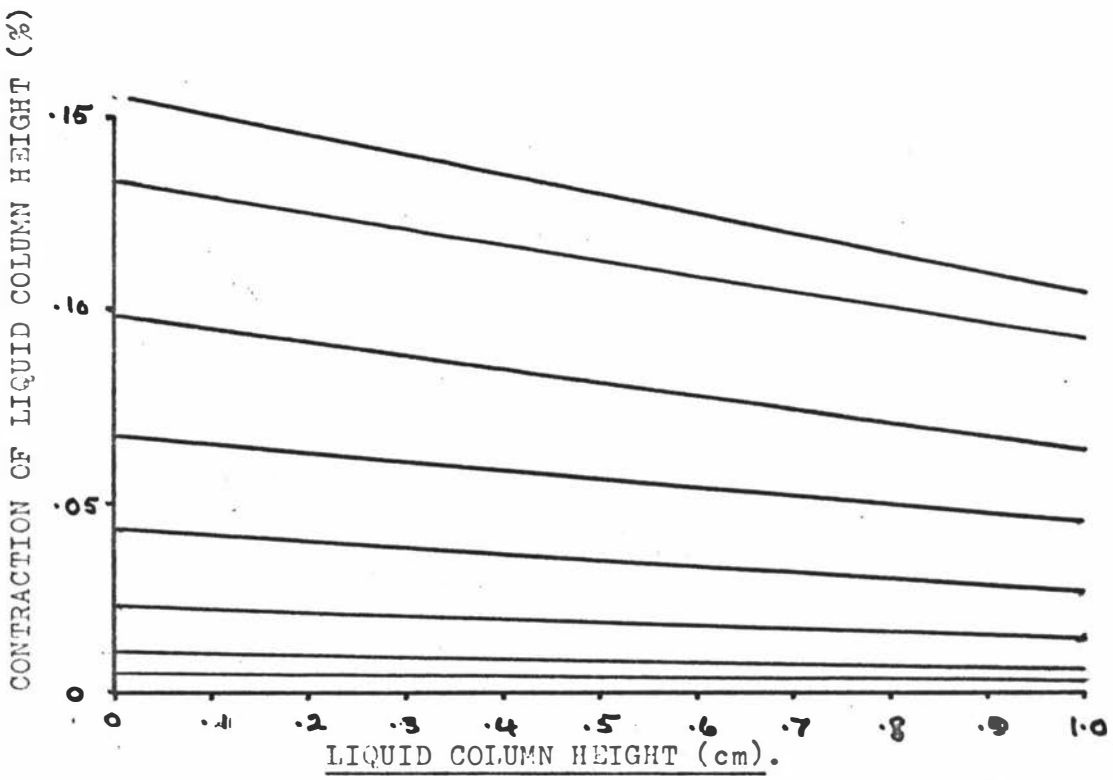

FIGURE 6-5. Graph Showing the percentage contraction of Liquid Column Height with Liquid Column Height at Constant Rotor Speeds for the Model.

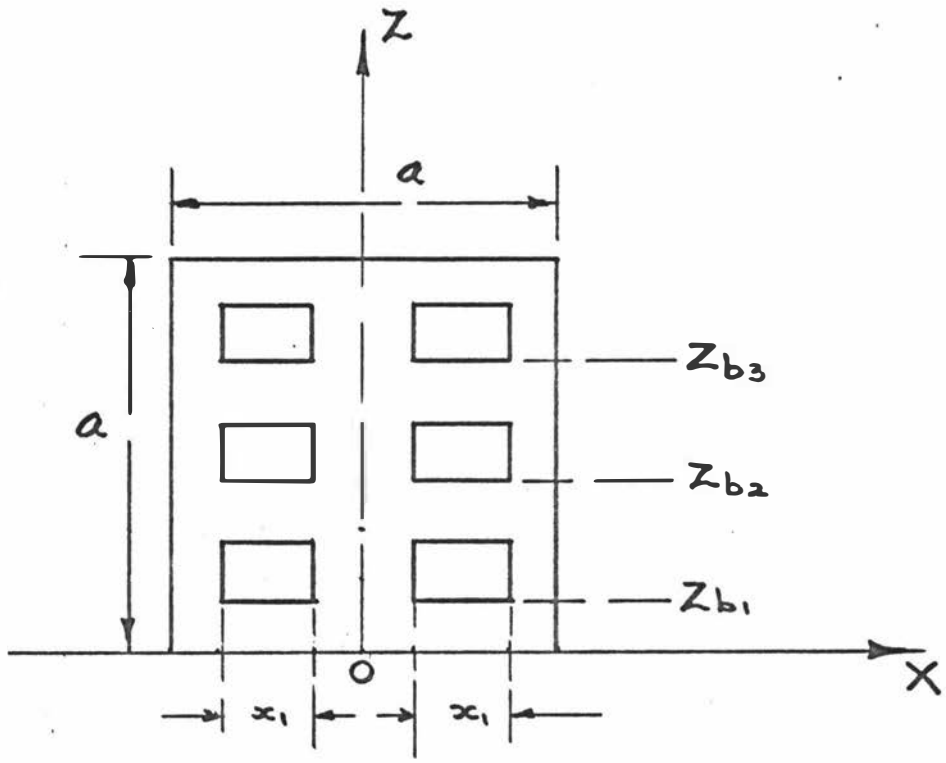

FIGURE 6-6. Diagram of the Three Channel Yphantis - type Cell Centrepiece applicable to our model.

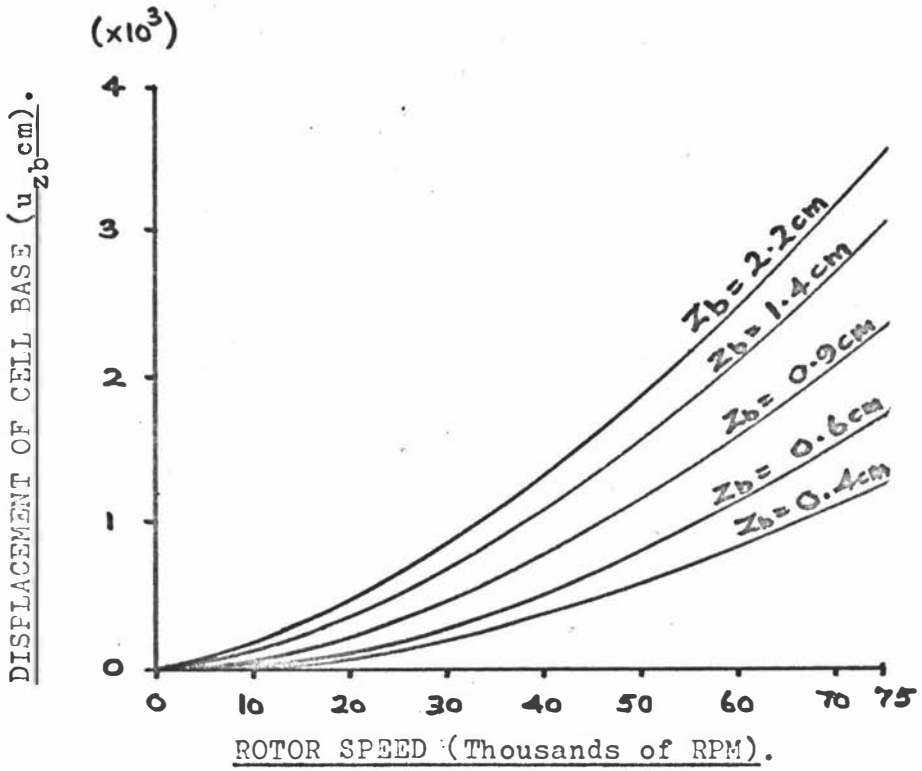

FIGURE 6-7. Graph showing Cell Base Displacement versus Rotor Speed for various initially fixed positions of the Cell Base within the Duralumin Model.

and (iii) the location of the base in the cell centrepiece (assuming that the cell centrepiece dimensions and positions within the rotor are fixed). The base positions selected for our model Yphantis cell were z_{b1} = 0.4 cm, z_{b2} = 0.9 cm and z_{b3} = 1.4 cm, where the subscripts 1,2, and 3 indicate the three channels numbered from bottom to top of the cell. The cell base displacement (u_{zb}) is plotted against rotor speed in figure 6-7 for the position of the three channels above as well as for the top of the centrepiece, z_b = 2.2 cm, and for z_b = 0.6 cm, the latter being typical for the cells used for long column experiments and Schlieren work. Figure 6-8 depicts the variations in base displacement (u_{zb}) as a function of the position within the centrepiece, whilst rotor speed is maintained constant. It should be appreciated that the origin relative to the axis of rotation of the rotor will itself vary with rotor speed owing to rotor stretch and moreover the displacement at the top of the centrepiece gives rise to a widening of the gap between the rotor and cell already present owing to rotor stretch. By extrapolation one can determine the relative base displacements for any base position with respect to a reference position (channel) since these depend on their relative positions. Thus at 70,000 rpm we note that the base position in channel 2 has a radial displacement of about 2x that of channel 1 whereas the base position in channel 3 has a radial displacement of just over 2.5x that of channel 1. Naturally as noted previously from equation (6-24) the order of magnitude depends on ω^2 and $\frac{\rho}{E}$, but for our duralumin model the radial displacement of channel 1 at 70,000 rpm is about 0.001 cm which would be measureable in such a cell. However the radial displacement of a single channel base position is masked by rotor stretch in practice owing to the practical origin of coordinates being the axis of rotation and not the centrepiece base. In contrast, the relative displacements indicative of cell distortion are not masked and experimental evidence of this as regards the inner and outer reference positions of a cell counterbalance is intimated by Baghurst and Stanley[77].

The channel discrimination exhibited by change

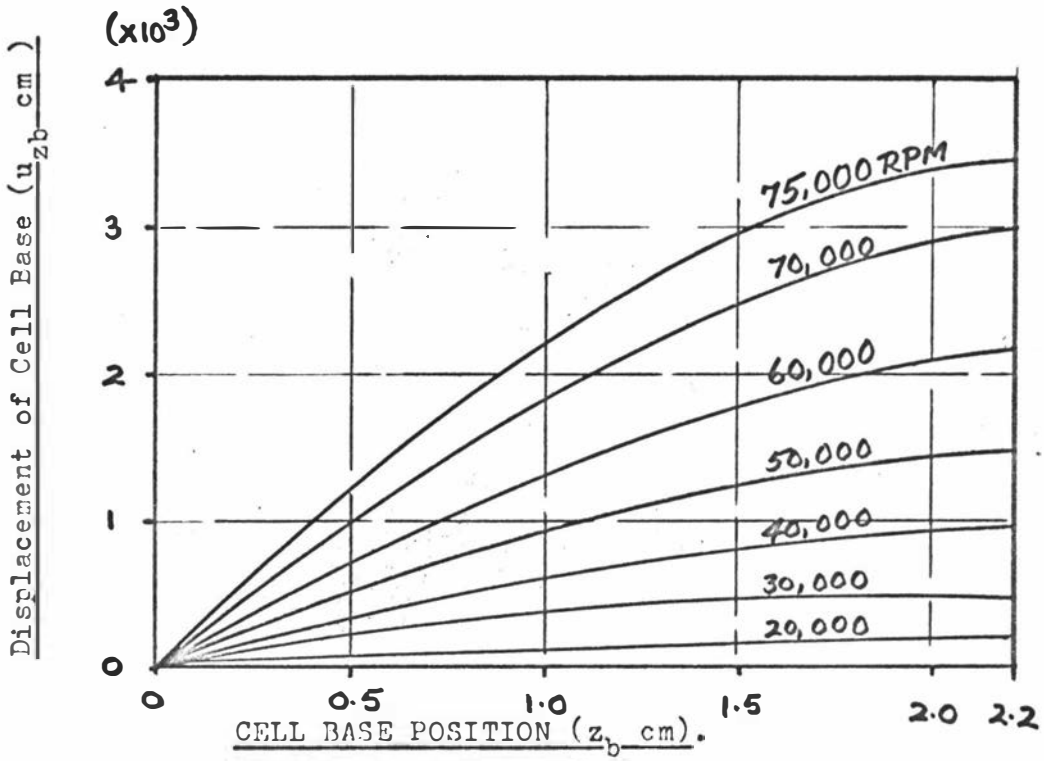

FIGURE 6-8. Graph showing the variation of Cell Base Displacement versus Cell Base Position at constant Rotor Speeds for the Duralumin Model.

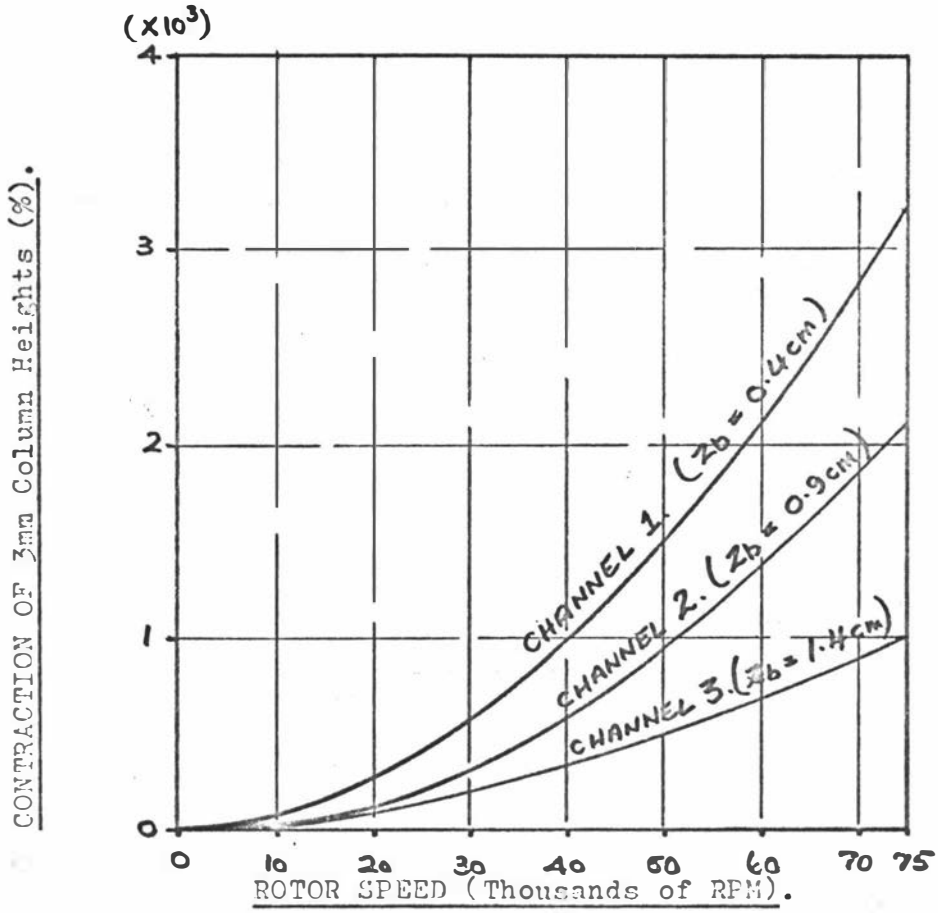

FIGURE 6-9. Graph showing the Percentage Contraction of 3mm Liquid column heights in the Channels of the Yphantis - type cell model of Figure 6-6, versus Rotor speed.

in liquid column heights is depicted in figure 6-9. Here the percentage decrease in liquid column height for a fixed initial column height of $h = 0.3$ cm in each channel is plotted against rotor speed (rpm). The data for this graph were obtained from equation (6-23). From equation (6-23) we make a general observation that the magnitude of the fractional decrease in liquid column height (q) is the product of two distinct functions, this observation applying equally to the radial displacement u_z in equation (6-14). Firstly as expected it depends on the centrifugal field and the cell material ($\frac{\rho\omega^2\sigma}{2E}$), and secondly on relevant cell dimensions and positions $\left[2a(2R-a) - 2R(2z_b + h) + z_b^2 + (z_b + h)^2\right]$. If the first is plotted against rotor speed and the second is plotted against liquid column height (h) over the range of interest for various relevent positions (z_b) in a centrepiece, it is possible by normal extrapolation procedures to determine the effective value of 'q' for any rotor speed, column height and base position of interest, and in theory for a practical case such plots could form the basis for experimental correction procedures. The plots applicable to the model duralumin cell are shown in figures 6-10 and 6-11 for illustration - from which figure 6-9 could be derived. Obviously, a similar procedure could be used to evaluate the radial displacement - u_z from equation (6-14). Finally, it is appropriate to mention the experimental work of Schachman[4] and Cheng and Schachman[83], who investigated the compressibility of liquids from ultracentrifuge measurements. This is because the observable decrease in liquid column heights arising from finite liquid compressions, that is discussed in the appendix to this chapter, could be exaggerated by cell centrepiece deformation if precautions are not taken. Furthermore, as indicated by Schachman[4], the experimental conditions are complicated by window bulging and distortion owing to liquid pressure effects. In practice the effects of cell distortion as regards decrease in liquid column height with increase of the rotor speed are accentuated by the above effects. However, our model indicates that the effects

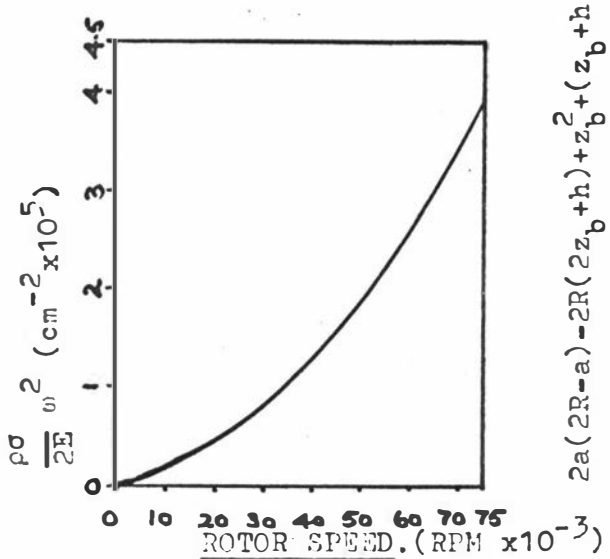

FIGURE 6-10.

$\frac{\rho\sigma}{2E}\omega^2$ versus Rotor Speed.

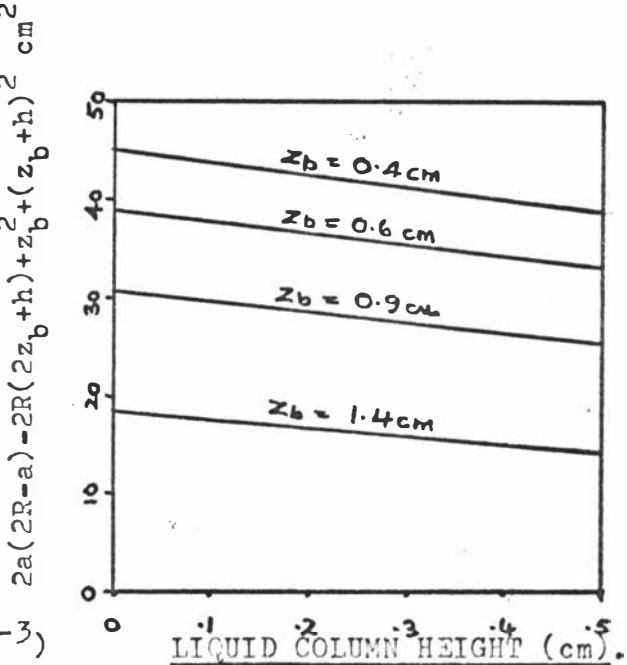

FIGURE 6-11.

$2a(2R-a)-2R(2z_b+h)+z_b^2+(z_b+h)^2$ versus column height h.

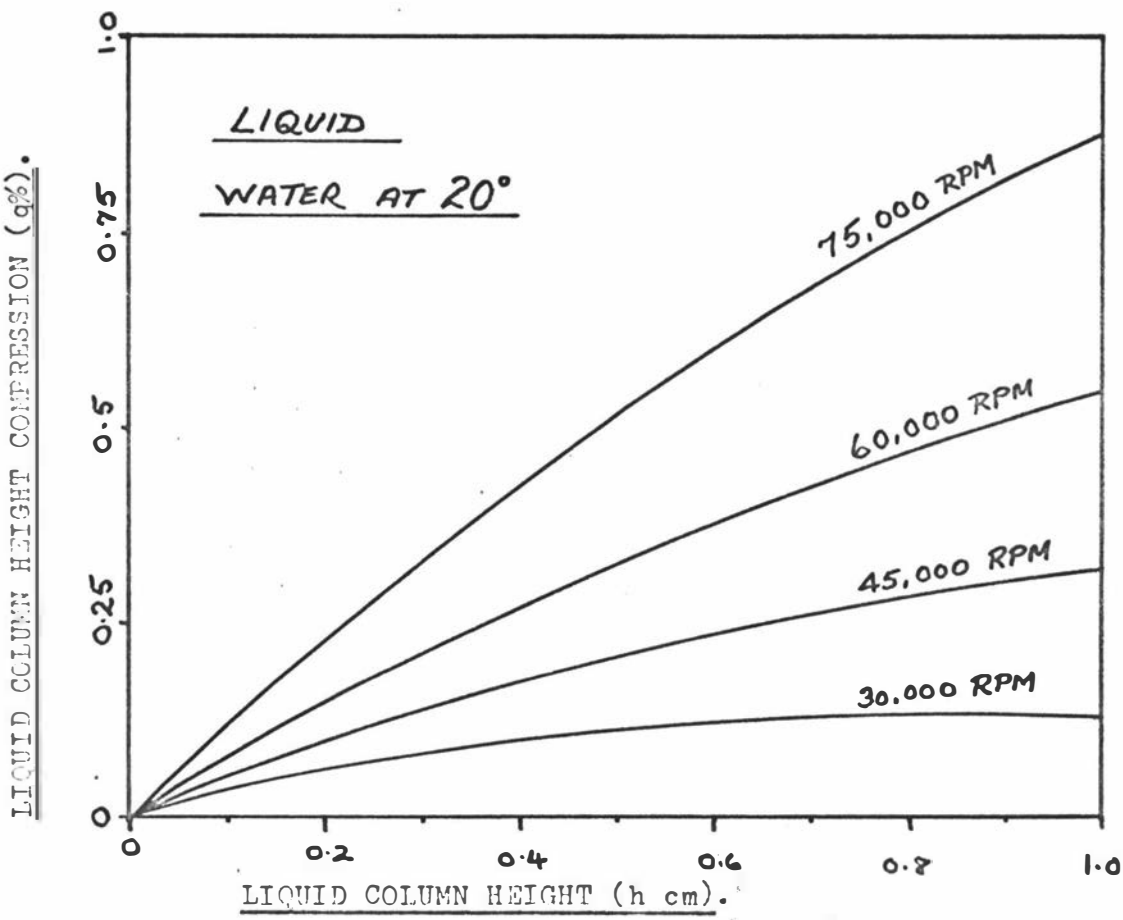

FIGURE 6-12. Percentage Compression versus Liquid Column Height in a Centrifuge Cell at constant Rotor Speeds owing to Finite Liquid Compressibilty.

of cell distortion may be evaluated devoid of the complications of window bulging and finite liquid compressibility. This is achieved experimentally by using a Yphantis type cell centrepiece and making simultaneous measurements of liquid column height contraction, together with relative base position displacements, the latter being independent of the aforementioned complications.

4. SUMMARY

A model of a cell has been introduced into an analytical ultracentrifuge, and mathematical expressions have been formulated specific for the effects of cell centrepiece deformation under the centrifugal body forces. Data relevant to standard cells used with the Beckman Model 'E' instrument have been evaluated and have indicated effects to be of an order of magnitude relevant for correction in present day high precision methods. The orders of magnitude established are similar to those intimated by experimentally derived raw data results of Baghurst and Stanley[77] applicable to the inner and outer reference holes in a counter-balance cell. However, these authors stressed that an analysis of co-variance failed to confirm the effect at the 5% probability level, but a suggestion of cell compression was made. The model has highlighted the specific effects of cell distortion, as distinct from rotor stretch, and has indicated correction procedures that could be relevant for high precision, sedimentation equilibrium Rayleigh interference work. The analysis of experimental data for the latter sometimes assumes the conservation of mass to evaluate a constant of integration, when use is made of the initial concentration of solute in the cell. The variation in liquid column height owing to cell distortion and finite liquid compressibility could influence the result of this calculation if precautions are not taken. Furthermore the radial displacement of the base region owing to cell distortion, should be considered along with the corrections for rotor stretch. For the less precise Schlieren work the effects will be relatively minor, although theoretically they would exaggerate effects of radial dilution. In particular the model has warned of possible complications associated with the use of Yphantis type cells and has

indicated appropriate correction procedures for precise work.

Finally, it must be emphasised that the theory is based on a model, and that the exact results evaluated are really only applicable to this model. However the model does approximate the experimental conditions experienced; the results it predicts are intuitively correct, and these are of the orders of magnitude expected from experimental evidence to date. Therefore it is felt within the limitations imposed, that the model is useful and applicable to the task in hand.

5. APPENDIX

A MATHEMATICAL FORMULATION OF LIQUID COLUMN HEIGHT COMPRESSION OWING TO FINITE LIQUID COMPRESSIBILITY IN THE ANALYTICAL ULTRACENTRIFUGE

At the higher rotor speeds (about 60,000 rpm) a large pressure difference exists between the air-liquid meniscus (where the pressure is one atmosphere) and the bottom of a centrifuge cell. Svedberg and Pedersen[2], Fujita[5], and Schachman[4] have discussed the effects of this pressure variation and give appropriate references to both experimental and theoretical work undertaken in this area. However, the analysis above has indicated that one of the observable effects of cell deformation in these large centrifugal fields is an effective compression of the liquid column, and hence in the context of this paper it is appropriate to determine the relative contributions that these two independent sources make to the experimentally observable compression.

Using the notation of Fujita[5] the pressure distribution in a sector shaped centrifuge cell may be determined from

$$\frac{\partial p}{\partial r} = \rho\omega^2 r \qquad (6\text{-}A1)$$

where ρ = density of the solution at the radial position r, ω is the rotor's angular velocity and p is the pressure.

For dilute solutions ρ may be replaced by the density of the solvent ρ_o at the same point. Denoting the compressibility by β we obtain,

$$\rho_o = \frac{\rho_o^o}{1-\beta p} = \rho_o^o (1 + \beta p) \qquad (6\text{-A2})$$

i.e.,

$$\rho_o = \rho_o^o + \lambda p \qquad (6\text{-A3})$$

where $\lambda = \rho_o^o \beta$ with ρ_o^o being the value of ρ_o at $p = o$, and this approximates the value at the meniscus (r_m).

Whence by substitution and integration the solvent density is given by

$$\rho_o(r) = \rho_o^o \exp \left[\tfrac{1}{2} \beta \rho_o^o \omega^2 (r^2 - r_m^2) \right] \qquad (6\text{-A4})$$

Defining $$x = \left(\frac{r}{r_m}\right)^2 \qquad (6\text{-A5})$$

and $$\nu = (\tfrac{1}{2}) \beta \rho_o^o \omega^2 r_m^2 \qquad (6\text{-A6})$$

We get $$\rho_o(x) = \rho_o^o \exp \nu (x - 1) \qquad (6\text{-A7})$$

The fractional decrease in liquid column height (q) is defined by

$$h' = h(1 - q) \qquad (6\text{-A8})$$

where h' is the liquid column height at rotor frequency ω and h its value when $\omega = o$. It is easy to show that

$$\frac{\bar{\rho}_o(x)}{\rho_o^o} = \frac{1}{1-q} \left[1 - \frac{hq}{2r_b} \right] \qquad (6\text{-A9})$$

Where r_b is the radial position of the liquid column base and $\bar{\rho}(x)$ is the average density of the liquid at angular frequency ω.

In practice $\frac{hq}{2r_b} \ll 1$ and hence from equation (6-A9) the fractional liquid column height compressions (q) is given by

$$q = \frac{\bar{\rho}_o(x)}{\rho_o^o} - 1 \qquad (6\text{-A10})$$

Defining a function f(x) by

$$f(x) = \frac{\rho_o(x)}{\rho_o^o} - 1 \qquad (6\text{-A11})$$

we see from equation (6-A10) that the mean value of $f(x)$ is q. Substituting $\rho_o(x)$ from equation (6-A7) into equation (6-A11) we obtain

$$f(x) = \exp^{\nu(x-1)} - 1 \qquad (6\text{-A12})$$

and since in practice $\nu(x-1) \ll 1$ equation (6-A12) becomes to a close approximation

$$f(x) = \nu(x-1) \qquad (6\text{-A13})$$

Thus the required fractional liquid column height compression is given by

$$q = \nu(\bar{x} - 1) \qquad (6\text{-A14})$$

Where $\bar{x}$ is the mean value of x for the centrifuge cell. Writing x_b as the value for x at the cell base we find that

$$q = \frac{\nu}{2}(x_b - 1) \qquad (6\text{-A15})$$

By the reinsertion of previously defined terms we can re-write equation (6-A15) as

$$q = \frac{\rho_o^o \omega^2 \beta}{4} h(2r_b - h) \qquad (6\text{-A16})$$

Differentiating equation (6-A16) with respect to h we note that $\frac{dq}{dh}$ is positive for all values of h used experimentally, and hence the larger the column (h) the greater q, this latter effect contrasting with the effective compression produced by cell centrepiece deformation. Figure 6-12 shows the variation in q with h at constant rotor speeds, calculated from equation (6-A16) with

$$r_b = 7.1 \text{ cm} \; ; \; \rho_o^o = 0.998 \text{ g cm}^{-3} \; ; \; \beta = 40 \times 10^{-6} \text{ atm}^{-1} .$$

These data are applicable to water at $20\ ^{o}C$ in a typical ultracentrifuge cell. By comparison of figures 6-12 and 6-5 the relative effects of cell distortion and finite compressibility may be estimated.

As with cell distortion it is of interest to determine the discrimatory effects of finite liquid compressibility amongst the channels of high speed Yphantis type centrifuge cell.

The percentage compression (q) of a fixed water column height of 0.3 cm at 20 °C in each of the three channels were determined using the following pertinent data.

$\omega^2 = 4 \times 10^7 \ (\text{rad s}^{-1})^2$; $r_{b1} = 7.1$ cm ;

$r_{b2} = 6.6$ cm ; $r_{b3} = 6.1$ cm

The numerical subscript indicates the channel numbered from bottom to top of the cell.
The calculations gave

$q_1 = 0.35\%$; $q_2 = 0.32\%$ and $q_3 = 0.30\%$.

These imply that the overall radial movement of the menisci for the above conditions as recorded photographically in the ultracentrifuge, would be in the region of 0.002 cm, account being taken of the x2 magnification of the radial cell coordinates by the Interference/Schlieren optical system of the ultracentrifuge. The variations amongst the channels is shown to be small, but they do lie within the precision of the instrument. Naturally, should the liquid employed have a larger compressibility and/or density then the observable effect from this source will be increased accordingly, as indicated by equation (6-A16). Again, as for cell deformation, it is anticipated that appropriate precautions for the aforementioned physical effects should be made in accurate sedimentation equilibrium studies employing Rayleigh interference optics.

REFERENCES.

REFERENCES:

1. T. Svedberg and J.B. Nicols, J.Am.Chem.Soc., 45,2910 (1923).

2. T. Svedberg and K.O. Pederson, 'The Ultracentrifuge', Oxford Univ. Press, London and New York, (1940).

3. J.W. Williams, K.E. Van Holde, R.L. Baldwin and H. Fujita, Chem. Revs., 58,715 (1958).

4. H.K. Schachman, 'Ultracentrifugation in Biochemistry', Academic Press, New York and London, 1959.

5. H. Fujita,'Mathematical Theory of Sedimentation Analysis', Academic Press, New York and London, 1962.

6. J.M. Creeth and R.H. Pain, Progr. Biophys. and Mol. Biol., 17, 217 (1967).

7. D.A. Yphantis, Ann. N.Y. Acad. Sci., 164, 1-305(1969).

8. S. Claesson and I. Moring-Claesson, 'Analytical Methods of Protein Chemistry', p.121 Pergamon Press, New York, Oxford, Paris 1961.

9. O.Lamm, Z. Physik. Chem. (Leipzig), A143, 177; Arkiv. Mat. Astron, Fysik 21B(2) (1929).

10. R.J. Goldberg, J.Phys. Chem., 57, 194 (1953).

11. H. K. Schachman, Biochemistry, 2, 887 (1963)

12. F.E. LaBar, 'Ultracentrifugation using Rayleigh Interference Optics', Thesis in Biochemistry, Stanford University, 1963.

13. A. Javan, W.R. Bennett Jnr., and D.R. Herriott, Phys. Rev. Letters, 6, 106 (1961).

14. J.A. Lewis and N.F. Barber, J. Phys. Chem., 75,2507 (1971).

15. Lord Rayleigh, Proc. Roy. Soc., 59, 203 (1896).

16. J.St.L. Philpot and G. H. Cook, Research, 1, 234 (1948).

17. H. Svensson, Acta Chem. Scand., 3, 1170 (1949).

18. H. Svensson, ibid., 4, 339 (1951).

19. J.S. Johnson and K.A. Kraus, J. Am. Chem. Soc., 81, 1569 (1959)

20. J.S. Johnson, G. Scatchard, and K.A. Kraus, J. Phys. Chem., 63, 787 (1959).

21. E.G. Richards and H.K. Schachman, ibid., 63, 1578 (1959).

22. K.E. Van Holde and R.L. Baldwin, ibid., 62, 734 (1958).

23. H.K. Schachman, 'Ultra centrifugal Analysis in Theory and Experiment' p.171 Ed. J.W. Williams, Academic Press New York and London,(1963).

24. M. Born and E. Wolf, 'Principles of Optics', Pergamon Press, Oxford, London, New York, Paris, Frankfurt. (1964).

25. G.W. Stroke, 'An Introduction to Coherent Optics and Holography', Academic Press, New York - London (1966).

26. J. Mathews and R. L. Walker, 'Mathematical Methods of Physics', 2nd Ed., p.113, W.A. Benjamin, Inc., New York, (1970).

27. H. Kuhn, Rep. Progr. Phys., 14, 89 (1951).

28. W.H. Steel,'Interferometry', Cambridge University Press (1967).

29. K.D. Miclenz, 'Electron Beam and Laser Beam Technology', Edited by L. Martin and A.B. El-Kareh, Academic Press, New York and London, (1968).

30. E. Verdet, Lecons d'Optique Physique, 5, 108 (1896).

31. R. Rempel, 'Optical Properties of Lasers as compared to Conventional Radiators', Spectra-Physics, Mountain View, California,(1963).

32. A.G. Fox and T. Li, Bell Syst. Tech. J., 40, 453 (1961).

33. G.D. Boyd and J.P. Gordon, ibid., 40, 489 (1961).

34. A.A. Michelson, Phil. Mag., 31, 338 (1891).

35. C. Candler, 'Modern Interferometers', Hilger and Watts, (1951).

36. J.P. Gordon, H.J. Zeiger and C.H. Townes, Phys. Rev., 99, 1264 (1955).

37. T.S. Jaseja, A. Janan and C.H. Townes, Phys. Rev. Letters, 10, 165 (1963).

38. R. Goldstein, 'Laser Focus Magazine', Advanced Technology Publications Inc., Massachusetts, February 1968.

39. F. Pockels, 'Lehrfuch der Kristalloptik',Leipzig: Teubner, (1906).

40. R. Rempel, 'Optical Properties of Lasers as Compared to Conventional Radiators', Spectra-Physics, Mountain View, California, (1963).

41 W.H. Steel, Progr, in Optics, ed. E. Wolf, 5, 145 (1965).

42. L.G. Longsworth, Anal. Chem., 18,219 (1946).

43. R. Trautman, Biochem. Biophys. Acta, 28,417 (1958)

44. F.E. LaBar and R.L. Baldwin, J. Phys. Chem., 66, 1953 (1962).

45. L. Gropper, Anal. Biochem., 7, 401, (1964).

46. R.D. Dyson, ibid., 33,193 (1970)

47. E.G. Richards, D.C. Teller and H.K. Schachman, ibid., 41, 189 (1971)

48. E.G. Richards, D.C. Teller, V.D. Hoagland, R.H. Haschemeyer and H. K. Schachman, ibid., 41,215 (1971)

49. A.T. Ansevin, D.E. Roark and D.A. Yphantis, ibid., 34, 237 (1970)

50. L.J. Gosting and M.S. Morris, J. Am. Chem. Soc., 71, 1998 (1949).

51. K.E. Van Holde, 'Fractions' 1, Beckman Instruments Inc., Palo Alto, California, 1967.

52. C.H. Chervenka, 'A Manual of Methods for the Analytical Ultracentrifuge', Beckman Instruments Inc., Palo Alto, California, 1969.

53. Amalgamated Wireless (Australasia) N.Z. Ltd., 'RCA Future Product Information', 1971.

54. H. Svensson, Acta. Chem. Scand., 4, 399 (1950).

55. G.M. Nazarian, Anal. Chem., 40, 1766 (1968).

56. E.G. Richards, D.C. Teller and H.K. Schachman, Biochem., 7, 1054 (1968).

57. A.T. Ansevin, D.E. Roark and D.A. Yphantis, Anal. Biochem., 34, 237 (1970).

58. F. Zernike, J. Opt. Soc. Am., 40, 326 (1950).

59. A. Marechal, P. Lostis and J. Simon, 'Advanced Optical Techniques', Ed. Van Heel p. 437, North-Holland Publishing Co., Amsterdam, 1967.

60. V.N. Schumaker, and B. Marano, Arch. Biochem. Biophys., 94, 532 (1961).

61. J.E. Hearst and H.B. Gray, Jr., Anal. Biochem., 24,70 (1968)

62. J. Sandford, Amer. Machinist, July 4, 77 (1966).

63. E.G. Richards, D.C. Teller and H.K. Schachman, Biochemistry, 7, 1054 (1968)

64. D.C. Teller, T.A. Horbett, E.G. Richards, and H.K. Schachman, Ann. N.Y. Acad. Sci., 164, 66 (1969).

65. F.A. Jenkins and H.E. White, 'Fundamentals of Optics', McGraw-Hill Book Co., Inc. New York, Toronto, London, (1957).

66. Svensson H., Optics Acta. 1,25 (1954).

67. Svensson, ibid., 3, 164 (1956).

68. T.F. Ford and E.F. Ford, J. Phys. Chem., 68,2849 (1964).

69. J.C. Swann and J.H. Coates, Anal. Biochem., 33,1 (1970).

70. D.A. Yphantis, Biochemistry, 3, 297 (1964).

71. E.G. Richards and H. K. Schachman, J. Am. Chem. Soc., 79, 5324 (1957).

72. P.A. Charlwood, and M.V. Mussett, J. Phys. Chem., 70,10 (1966).

73. S.R. Smiriga, and J.E. Hearst, Rev. Sci. Instr., 40, 233 (1969).

74. A.A. Windsor, T.H. Rich, R.E. Doyle and F.T. Lindgren, Rev. Sci. Inst., 38, 949 (1968).

75. Beckman Instruments Inc., Tech. Bull. No. TB60003B (1957).

76. G. Kegeles and F.J. Gutter, J. Am. Chem. Soc., 73, 3370 (1951).

77. P.A. Baghurst and P.E. Stanley, Anal. Biochem., 33, 168 (1970).

78. S. Timoshenko, 'Strength of Materials', Part II, 3rd. Ed., p.233. D. VanNostrand Company Inc., Princeton, New Jersey (1956).

79. C.B. Bienzeno and R. Grammel, Technishe Dynamic, 2nd., ed., Vol. II, p.25. Berlin-Gottingen-Heidelberg. (1953).

80. L.D. Landau and E.M. Lifshitz, Theory of Elasticity-Vol 7, of Course of Theoretical Physics, Pergamon Press, London-New York-Paris-Los Angles. (1959).

81. G.W.C. Kaye and T.H. Laby, Tables of Physical and Chemical Constants, 11th. Ed., Longmans, Green & Co., Ltd., London- New York-Toronto (1957).

82. Beckman Instruments Inc., Future Product Information (1969).

83. P.Y. Cheng and H.K. Schachman, J. Am. Chem. Soc., 77, 1498 (1955).

APPENDICES

APPENDIX I.

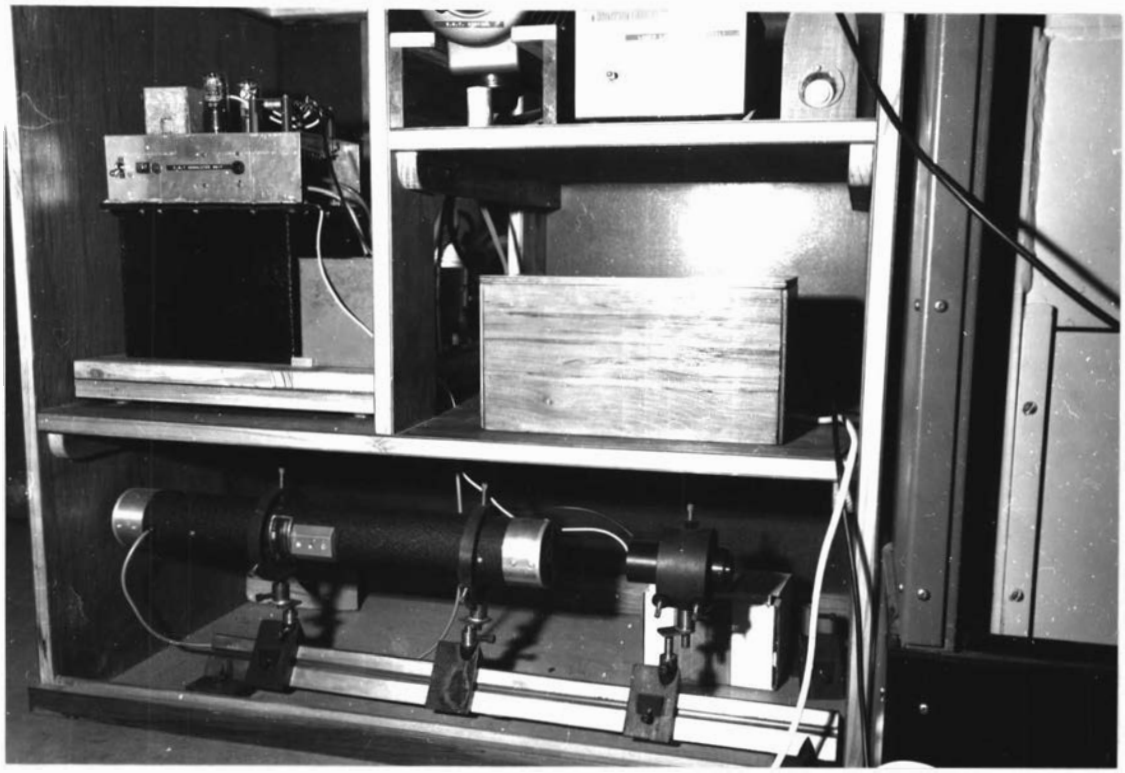

FIGURE A-1(a). VIEW OF THE LASER CUPBOARD SHOWING THE LASER AND OPTICAL MODULATOR MOUNTED ON THE OPTICAL BENCH, TOGETHER WITH THE E.H.T. UNIT ON THE SHELF ABOVE.

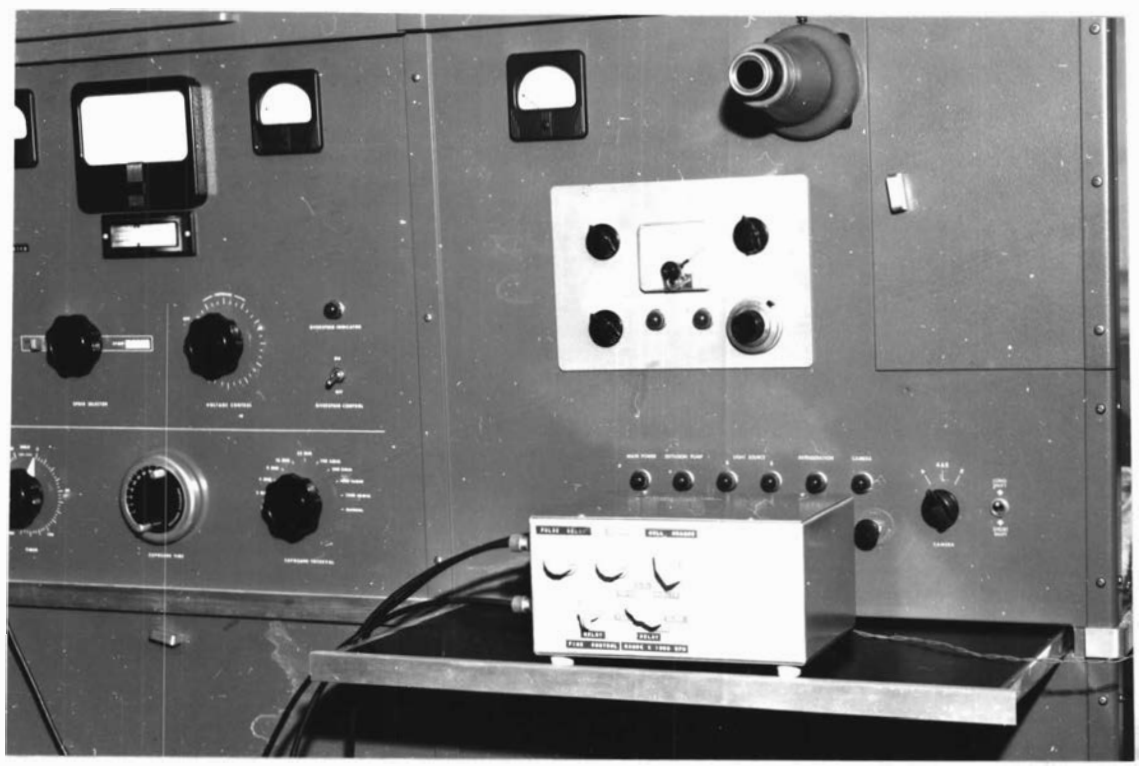

FIGURE A-1(b). VIEW OF THE ELECTRONIC CONTROL UNIT IN ITS NORMAL OPERATING POSITION ON THE ULTRACENTRIFUGE.

APPENDIX II.

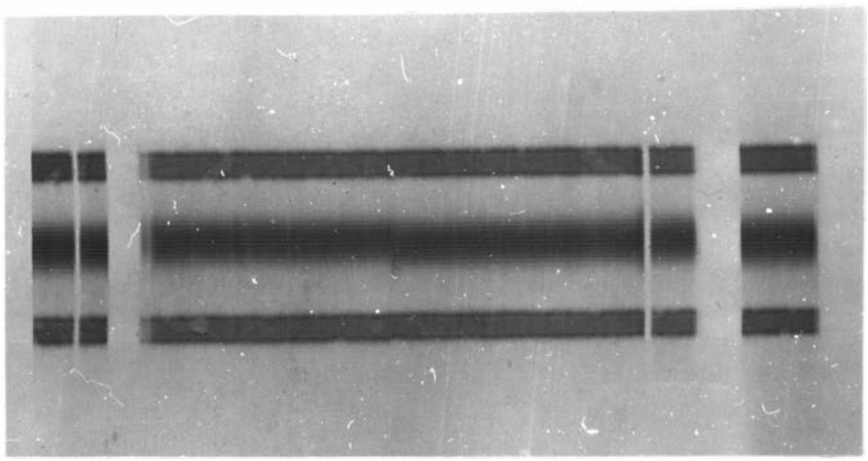

FIGURE A-2(a). PHOTOGRAPH OF THE BOUNDARY CANCELLING TEST FOR THE ALIGNED OPTICAL SYSTEM USING THE MERCURY SOURCE WITHOUT FILTER. (AFTER THE PROCEDURE OF DYSON[46]).

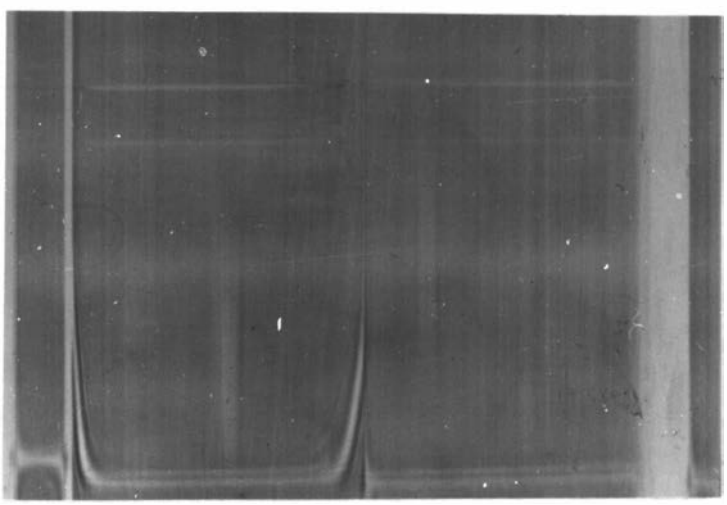

FIGURE A-2(b). SCHLIEREN PATTERN OF THE SYSTEM DEPICTED ABOVE INDICATING THE STEEP GRADIENTS AT THE MENISCUS AND BASE OF THE SOLUTION COLUMN. (SOLUTION 0.5% B.S.A. AT 12,000 rpm PHASE PLATE ANGLE 70°). Note pattern is reversed owing to a photographic reproduction error.

APPENDIX III.

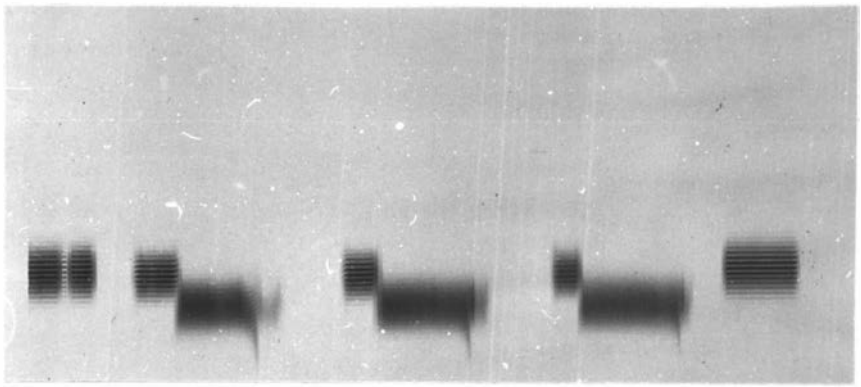

FIGURE A-3(a). HIGH SPEED EQUILIBRIUM PATTERNS USING A THREE CHANNEL YPHANTIS CELL AND NON-MODULATED MERCURY SOURCE. Note absence of fringes owing to the severity of the conditions.

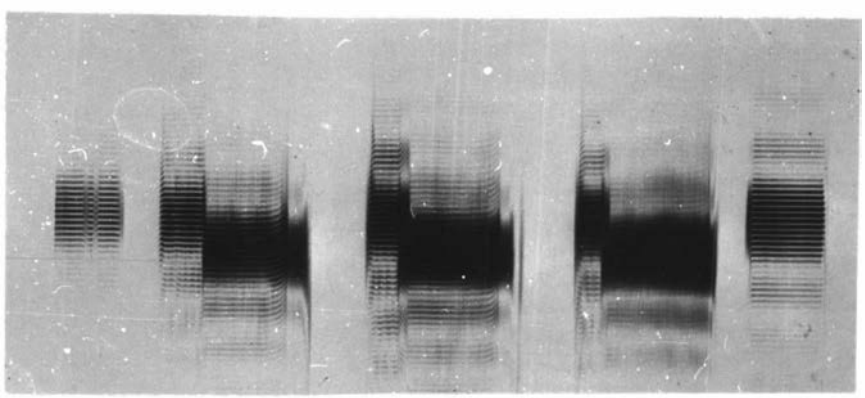

FIGURE A-3(b). SAME EXPERIMENT AS ABOVE BUT WITH THE MODULATED LASER SOURCE. Fringes are now clearly visible and indicate that the rotor speed is too high. THE INITIAL CONCENTRATIONS OF THE SOLUTION (CRAYFISH HAEMOCYANIN) INCREASED WITH THE CHANNELS RADIALLY.

APPENDIX IV.

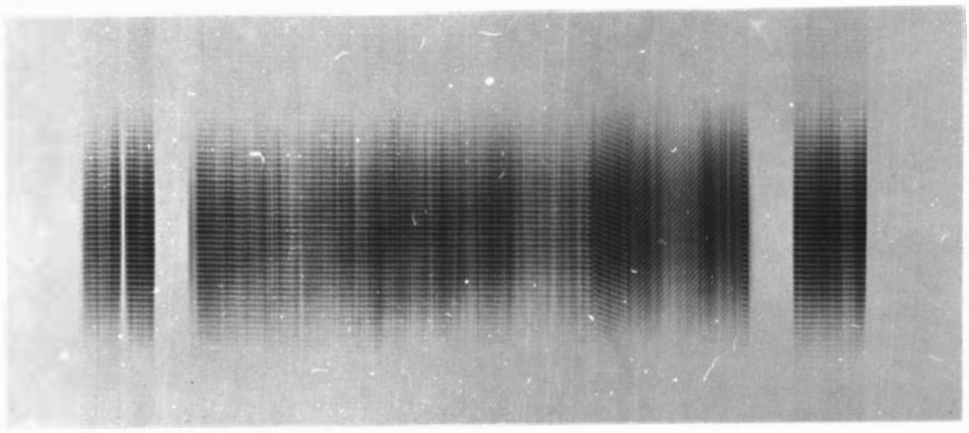

FIGURE A-4 PLATE SHOWING A SUCROSE IN WATER EQUILIBRIUM FRINGE PATTERN FOR THE LASER SYSTEM EMPLOYING THE LINE SOURCE OPTICS.

APPENDIX V.

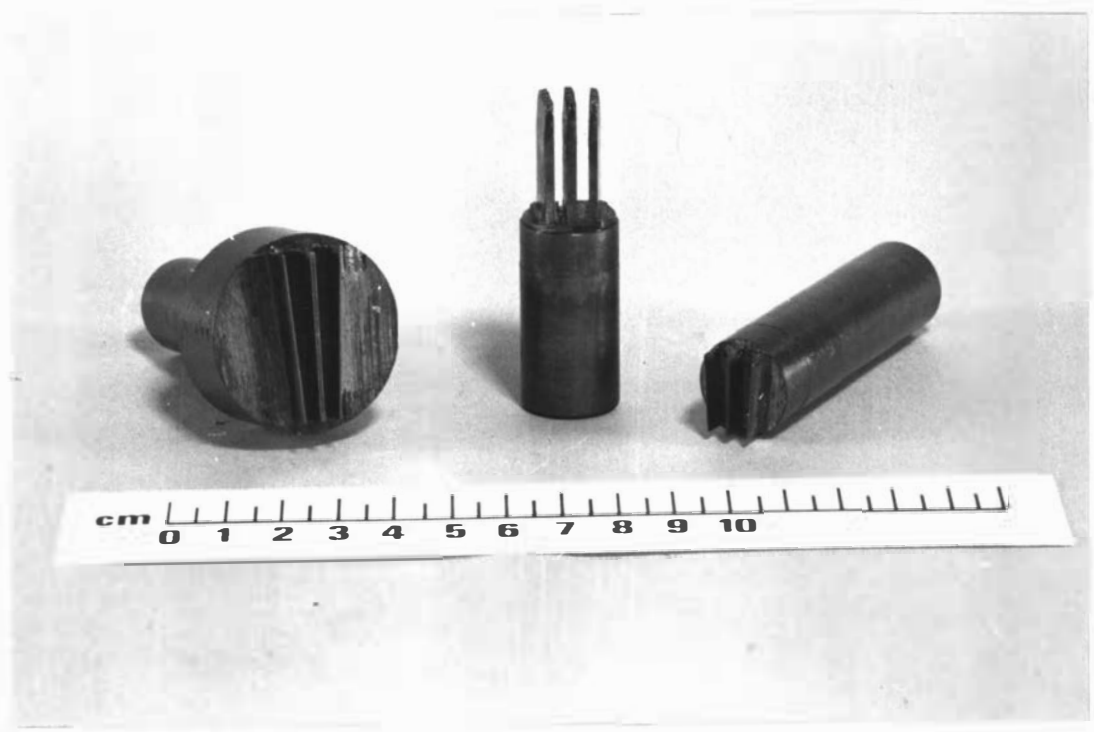

FIGURE A-5. PLATE SHOWING ASSORTED TOOL PIECES USED IN THE ELECTRIC DISCHARGE MACHINING OF THE TRIPLE-SECTOR CELL COMPONENTS.

APPENDIX VII

Supplement to Chapter 5

In chapter 5 of this thesis it was assumed that the cell containing the sedimenting solution could be simulated by an optically homogeneous prism. This assumption is theoretically convenient since it allows the problem of the gradients to be presented devoid of the complications of wave propagation in non-homogeneous media. However, the analysis was based on a model for the cell, and it was felt that the magnitude of the effects so derived could well be smaller than those encountered in practice. A brief formulation of the problem using a non-homogeneous solution in the centrifuge cell is presented, but to date no firm conclusions as to the model's applicability can be made.

It is shown by Born and Wolf[24] that the general equation for a light path in an optically non-homogeneous medium is given by

$$\frac{d}{ds}\left(n \frac{d\bar{r}}{ds}\right) = \text{grad } n \qquad \text{(A7-1)}$$

In the rectangular Cartesian co-ordinate system, relevant to the cell and the analysis of chapter 5, equation (A7-1) may be written[68],

$$\frac{\partial n}{\partial z}\frac{dx}{dz} - \frac{\partial n}{\partial x} + \left[\frac{n}{1 + \left(\frac{dx}{dz}\right)^2}\right]\frac{d^2x}{dz^2} = 0 \qquad \text{(A7-2)}$$

where x is the radial co-ordinate and z is the direction of the optical axis.

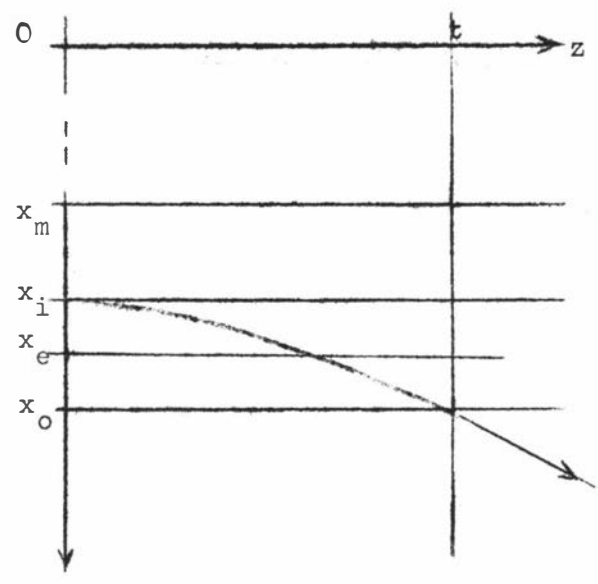

Fig. A7-1

At sedimentation diffusion equilibrium the refractive index distribution in the cell is given by equation (5-3)

ie., $n(x) = n_m \exp^{p(x^2 - x_m^2)}$ (A7-3)

Using this relationship in equation (A7-2) we obtain

$$\frac{d^2x}{dz^2} - 2px\left(\frac{dx}{dz}\right)^2 - 2px = 0 \qquad \text{(A7-4)}$$

The differential equation (A7-4) describes the light paths for rays in the centrifuge cell at equilibrium. An analytical solution for equation (A7-4) is given by

$$\left(\frac{dx}{dz}\right)^2 = C \exp^{2px^2} - 1 \qquad \text{(A7-5)}$$

where C is a constant that depends on the inclination and radial position of entry of a ray into the cell. For our situation the incident light for the cell is collimated

hence $\frac{dx}{dz} = 0$ when $z = 0$, and using this condition in conjunction with an assumed radial position of entry $x = x_i$ (see figure A7-1) we find that

$$C = \exp^{-2px_i^2} \qquad \text{(A7-6)}$$

Thus an exact solution to equation (A7-4) is

$$\left(\frac{dx}{dz}\right)^2 = \exp^{2p(x^2-x_i^2)} - 1 \qquad \text{(A7-7)}$$

Now to determine x in terms of z requires integration of equation (A7-7) which is complex. However equation (A7-7) may be written in expanded form thus

$$\frac{dx}{dz} = \left[\exp^{2p(x^2-x_i^2)} - 1\right]^{\frac{1}{2}}$$

$$= \left[2p(x^2-x_i^2) + \frac{4p^2(x^2-x_i^2)^2}{2!} + \ldots\right]^{\frac{1}{2}} \qquad \text{(A7-8)}$$

Assuming that $(x^2 - x_i^2)$ is sufficiently small that the second term in the brackets may be ignored we can make a first approximation.

i.e. $$\frac{dx}{dz} = \sqrt{2p}\,(x^2 - x_i^2)^{\frac{1}{2}} \qquad \text{(A7-9)}$$

Whence by integration of equation (A7-9) it may be shown that

$$x = x_i \cosh \sqrt{2p}\, z \qquad \text{(A7-10)}$$

Thus to a first approximation the path of a light ray through a centrifuge cell at sedimentation diffusion equilibrium is a catenary.

Unfortunately the cell is too thick for the above first approximation to apply to the whole cell, but obviously by numerical methods it is possible to divide the cell into stratified layers for which the approximation is valid and then trace a ray through the complete cell with the exit angle of one layer being the entrance angle of the following

layer. This analysis is in agreement with the general conclusions of Ford and Ford[68] who were involved with the position of a diffusing boundary with Schlieren optics.

However, although the exit angle is obviously greater for the non-homogeneous solution than for the model, its actual effect is not necessarily as great since the information carried by the emergent ray is applicable to an equivalent level (x_e) somewhere between the radial entrance and exit levels (see figure A7-1) given by

$$n(x_e).t = \int_0^s n(s)\, ds \qquad \text{(A7-11)}$$

Obviously the effective level (x_e) is displaced radially from the entrance level (x_i), and this must compensate somewhat the effect of the radial deflection. In addition there will be refraction at the exit window of the cell that will complicate the situation in practice since this effect too will be dependent on the exit angle from the solution and so on the refractive index distribution within the cell.

Thus until a ray tracing analysis (based on the above procedure) is undertaken for the system one is unable to draw firm conclusions as to the exact extent of the model's application.

[Reprinted from the Journal of Physical Chemistry, 75, 2507 (1971).]

Mathematical Formulations of the Effects of Cell Distortion and Liquid Column Height Compression in Analytical Ultracentrifugation

by James A. Lewis*

Department of Physics and Engineering, Massey University, Palmerston North, New Zealand

and Norman F. Barber

Department of Physics, Victoria University of Wellington, Wellington, New Zealand *(Received December 4, 1970)*

Publication costs borne completely by The Journal of Physical Chemistry

The increase in demands for precision in current analytical ultracentrifuge techniques has necessitated the inclusion of correction terms previously neglected. The effect of cell distortion as distinct from rotor stretch is considered in this paper, where use is made of a theoretical model. The equations for the deformation of the model cell body under a centrifugal gravitational field are derived and the results are applied to cells used in current practice. The numerical calculations indicate that the correction terms are significant at the higher rotor speeds for high-precision Rayleigh interference work, and are particularly relevant in view of the increasing popularity of short-column high-speed methods. The experimental observables specific to cell distortion are shown to be a differential displacement of the liquid cell base, this being relevant to Yphantis-type cells, coupled with a decrease in the liquid column height. The latter observable could be confused with finite liquid compressibility and an analysis of this separate effect is included in an appendix to the paper. It is expected that the correction procedures indicated for the model can be extended to all practical cases where appropriate.

Introduction

The advent of high-speed analytical ultracentrifugation methods such as those of Yphantis,[1] together with the enhanced accuracy in the optical analysis as shown by LaBar[2] and others,[3–5] has led to an increasing demand for precision in techniques involving the analytical ultracentrifuge, and this has made it necessary to take into account effects heretofore neglected. Furthermore, improvements in rotor speed mechanisms such as that of Smiriga and Hearst[6] and elsewhere[7,8] have reduced the instantaneous deviations of rotor speed to less than 0.01% in the Beckman Model E instrument. In addition the instrument is equipped with a standard RTIC (Rotor Temperature Indicator and Control) unit[9] which maintains the rotor temperature constant to within 0.1° during operation. Thus the rotor and cell are effectively isothermal during operation and the centrifugal field terms $\omega^2 r$, where ω is the angular velocity and r the radius, can be calculated to 0.02%. This implies that for the true precision to be realized, account has to be taken of rotor stretch, and cell deformation in the centrifugal field. The former has been investigated experimentally by Kegeles and Gutter,[10] Schachman,[11] and Baghurst and Stanley,[12] from whose work data are available for both aluminum and titanium rotors. In addition, mathematical analyses of rotor stretch for variable geometry rotors have been formulated by Timoshenko[13] and by Biezeno and Grammel.[14] For the Beckman Model "E" ultracentrifuge it has been shown experimentally by Schachman[11] that the radial coordinates r can increase by 0.5% at 59,780 rpm for an aluminum rotor, and Baghurst and Stanley[12] have shown that r increases by as much as 0.75% at 67,770 rpm for an An–H titanium rotor. Hence as the above authors have intimated it is essential to correct for the effects of rotor stretch for precise work. However, owing to body forces in the centrifugal field the cell itself undergoes distortion (compression), and experimentally in the past this effect has been masked partially by the rotor stretch. It is the purpose

(1) D. A. Yphantis, *Biochemistry*, **3**, 297 (1964).

(2) F. E. LaBar, "Ultracentrifugation Using Rayleigh Interference Optics," Thesis in Biochemistry, Stanford University, 1963.

(3) J. W. Beams, N. Snidown, A. Robeson, and H. M. Dixon, *Rev. Sci. Instrum.*, **25**, 295 (1954).

(4) E. Richards and H. K. Schachman, *J. Phys. Chem.*, **63**, 1578 (1959).

(5) H. K. Schachman, *Biochemistry*, **2**, 887 (1963).

(6) S. R. Smiriga and J. E. Hearst, *Rev. Sci. Instrum.*, **40**, 233 (1969).

(7) Beckman Instruments, Inc., Technical Bulletin E-TB-013, Feb 1965.

(8) A. A. Windsor, T. H. Rich, R. E. Doyle, and F. T. Lindgren, *Rev. Sci. Instrum.*, **38**, 949 (1968).

(9) Beckman Instruments Inc., Technical Bulletin No. TB60003B, 1957.

(10) G. Kegeles and F. J. Gutter, *J. Amer. Chem. Soc.*, **73**, 3770 (1951).

(11) H. K. Schachman, "Ultracentrifugation in Biochemistry," Academic Press, New York, N. Y., and London, 1959, p 19.

(12) P. A. Baghurst and P. E. Stanley, *Anal. Biochem.*, **33**, 168 (1970).

(13) S. Timoshenko, "Strength of Materials," 3rd ed, Van Nostrand, Princeton, N. J., 1956, p 223, Part II.

(14) C. B. Biezeno and R. Grammel, "Technishe Dynamic," 2nd ed, Vol. II, Berlin-Gottingen-Heidelberg, 1953, p 25.

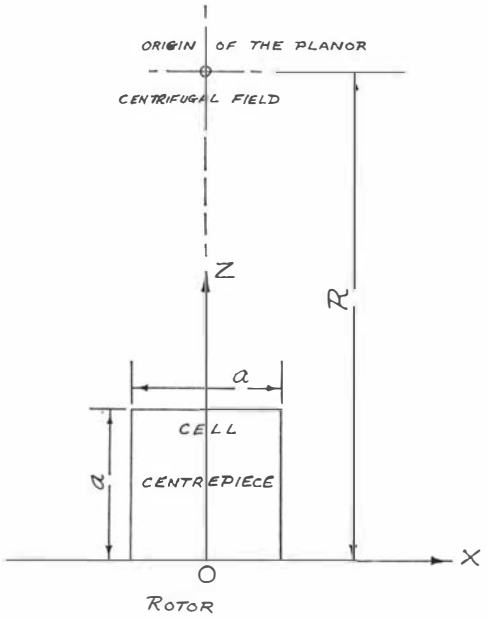

Figure 1. Diagram of the rectangular cell centerpiece within its coordinate axis system. The y axis is perpendicular to the plane of the paper.

of this paper to investigate cell distortion theoretically as distinct from rotor stretch, so that these effects may be assessed and their significance appreciated.

The Model and Theory

The model we have developed is the result of various attempts to simulate the conditions of the cell centerpiece in the rotor. We have analyzed this model according to the theory and notation of Landau and Lifshitz,[15] and for simplicity we have assumed rectangular symmetry for the cell and centrifugal field as indicated in the diagram of our cell centerpiece in Figure 1. To separate the effects of rotor stretch from those of cell distortion we have selected a symmetrical position, distance R from the axis of rotation, as the origin of our coordinate system. Naturally, R will vary with rotor speed owing to rotor stretch. The cell is located in the xy plane and the positive z axis of our system is in the negative radial direction of the rotor. The undeformed cell centerpiece considered is a rectangular block of square cross section a^2 in the xz plane and of length b in the y direction (the direction of the optical axis in the ultracentrifuge). Physically the field is that which applies for $R \gg a$. Hence the problem was to determine the deformation of the centerpiece resting in the rotor at z = zero subjected to a gravitational field $g_z = -\omega^2(R - z)$; $g_y = g_x = 0$, since the earth's field in the y direction is neglected. Furthermore, one boundary condition imposed was that the displacement vector u_z was zero when $z = 0$, since the centerpiece was assumed to be supported by the rotor in this plane.

It is shown by Landau and Lifshitz[15] that if a body is in equilibrium and is located in a gravitational field, then the internal stresses and the force of gravity per unit volume must vanish, and this result is expressed in their eq 2–7, *i.e.*

$$\frac{\partial \sigma_{ik}}{\partial x_k} + \rho g_i = 0 \tag{1}$$

where σ_{ik} is a general stress tensor element, x_k is a generalized coordinate, ρ is the density of the centerpiece material, and g_i is the component of the gravitational field in the ith direction.

From (1) the equations of equilibrium for our body become

$$\frac{\partial \sigma_{yk}}{\partial x_k} = \frac{\partial \sigma_{xk}}{\partial x_k} = 0 \tag{2}$$

and

$$\frac{\partial \sigma_{zk}}{\partial x_k} = \rho\omega^2(R - z) \tag{3}$$

Now, the boundary conditions that must be satisfied for our model are as follows: (a) on the sides of the centerpiece all components σ_{ik} vanish except σ_{zz}; (b) when $z = a$, $\sigma_{xy} = \sigma_{yz} = \sigma_{zz} = 0$. The solution of the equilibrium equations satisfying the boundary condition is

$$\sigma_{zz} = -\rho\omega^2[R(a - z) - \frac{1}{2}(a^2 - z^2)] \tag{4}$$

with all other

$$\sigma_{ik} = 0 \tag{5}$$

Knowing the stress tensor elements σ_{ik} we can find the strain tensor elements u_{ik} by use of Landau and Lifshitz's[15] eq 5-12, *i.e.*

$$u_{ik} = [(1 + \sigma)\sigma_{ik} - \sigma_{ll}\delta_{ik}]/E \tag{6}$$

Where σ is Poisson's ratio and E is Young's modulus for the centerpiece material, δ_{ik} is a unit matrix, and the double subscript for the stress tensor indicates summation in accordance with standard tensor notation. Whence

$$u_{xx} = \frac{\rho\omega^2}{E}\sigma[R(a - z) - \frac{1}{2}(a^2 - z^2)] \tag{7}$$

$$u_{yy} = \frac{\rho\omega^2}{E}\sigma[R(a - z) - \frac{1}{2}(a^2 - z^2)] \tag{8}$$

$$u_{zz} = -\frac{\rho\omega^2}{E}[R(a - z) - \frac{1}{2}(a^2 - z^2)] \tag{9}$$

and

$$u_{xy} = u_{xz} = u_{zy} = 0 \tag{10}$$

the strain tensor being symmetrical of course as shown by Landau and Lifshitz's[15] eq 1-4. The object of

(15) L. D. Landau and E. M. Lifshitz, "Theory of Elasticity of Course of Theoretical Physics," Vol. 7, Pergamon Press, London, New York, Paris, and Los Angeles, 1959.

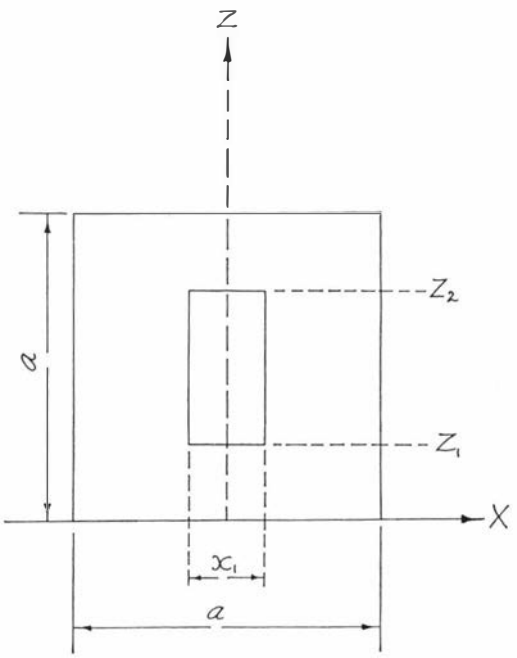

Figure 2. Diagram of the symmetrical rectangular cavity within the model centerpiece. The cavity has dimension y_1 perpendicular to the plane of the paper.

our analysis is to determine the displacement vector $\bar{u}$ at any point in the centerpiece, since this is the quantitative measure of deformation. This is found from the relationship between the strain tensor elements and the displacement vector formulated in Landau and Lifshitz's[15] eq 1-5

$$u_{ik} = \frac{1}{2}\left(\frac{\partial u_i}{\partial x_k} + \frac{\partial u_k}{\partial x_i}\right) \tag{11}$$

Where the double subscript indicates strain tensor elements, and the single subscript the relevant displacement vector component. Thus by integration we obtain the components of the displacement vector

$$u_x = \frac{\rho\omega^2}{E}\sigma[R(a - z) - \frac{1}{2}(a^2 - z^2)]x \tag{12}$$

$$u_y = \frac{\rho\omega^2}{E}\sigma[R(a - z) - \frac{1}{2}(a^2 - z^2)]y \tag{13}$$

$$u_z = -\frac{\rho\omega^2}{2E}\left[Rz(2a - z) - z\left(a^2 - \frac{z^2}{3}\right) + \sigma(R - z)(x^2 + y^2)\right] \tag{14}$$

It should be noted at this stage that the expression for u_z satisfies the boundary condition $u_z = 0$ only at the point of origin of our coordinate system, and hence the solution is not valid near this plane. However, the solution near this latter plane is not required in the subsequent analysis.

A cell cavity in our model has rectangular geometry and initially we shall assume that it is positioned symmetrically as shown in Figure 2. In practice the liquid under investigation is placed in the cavity in the cell centerpiece, and it is of interest to determine the cavity deformation in the centrifugal field. In stress analysis this problem frequently introduces complexity owing to new boundary conditions, but in the present model the problem is relatively simple, since we note from eq 4 and 5 that only σ_{zz} is finite and all other σ_{ik} are zero. Physically, this means that a cavity and body material in our cell centerpiece behave identically.

It can be shown by the use of eq 14 that the fractional change in the overall length of side z_2z_1 owing to cell deformation is given by

$$p_z = \frac{\rho\omega^2}{2E}\left[2Ra - R(z_2 + z_1) - a^2 + \frac{z_2^2 + z_2z_1 + z_1^2}{3} - \sigma(x^2 + y^2)\right] \tag{15}$$

whereas by use of eq 12 and 13 the fractional changes in the overall lengths of the sides parallel to the x and y axes located at z_1 and z_2, respectively, are given by

$$p_{x1} = p_{y1} = \frac{\rho\omega^2\sigma}{2E}(a - z_1)(2R - a - z_1) \tag{16}$$

$$p_{x2} = p_{y2} = \frac{\rho\omega^2\sigma}{2E}(a - z_2)(2R - a - z_2) \tag{17}$$

where p_{x1} is the overall fractional change in the side parallel to the x axis located at z_1, etc.

Thus from eq 15, 16, and 17, and a knowledge of the undeformed cavity dimensions, the deformation of the cavity may be calculated.

By inspection of eq 16 and 17 we note that the right-hand sides are always positive and hence the dimensions in the xy plane are always increased owing to cell deformation, whereas the right-hand side of eq 15 could be positive, negative, or zero. A diagrammatic picture of the deformed rectangular cavity is shown in Figure 3.

Consider a rectangular cavity of initial volume

$$V = (z_2 - z_1)x_1y_1 \tag{18}$$

where $(z_2 - z_1)$, x_1, and y_1 are the undeformed lengths of the sides. It can be shown that the volume V' of the deformed cell depicted in Figure 3 is given to a close approximation by

$$V' = \frac{(z_2 - z_1)'_0}{2}[y'_{12}(x'_{11} + x'_{12}) + x'_{11}(y'_{11} - y'_{12})] \tag{19}$$

where $(z_2 - z_1)'_0$[16] is the deformed length of the side $(z_2 - z_1)$ evaluated at $x = 0$, $y = 0$; and y'_{12} is the deformed length of the side y_1 evaluated at z_2, etc.

(16) Note the variation in $(z_2 - z_1)'$ over the range of values of x and y used for the cavities within our model is negligible.

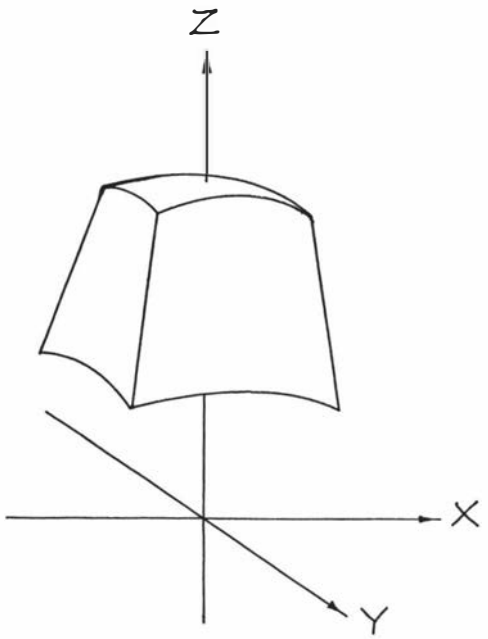

Figure 3. Diagrammatic representation of the cavity shown in Figure 2 after deformation owing to the centrifugal body forces.

Using eq 18 and 19 it can be shown that fractional volume change (δ) of the cavity is

$$\delta = \frac{\rho\omega^2}{2E}\left[(2\sigma + 1)\{a(2R - a) - R(z_2 + z_1)\} + \frac{z_2 z_1}{3} + \frac{1}{3}(3\sigma + 1)(z_2^2 + z_1^2)\right] \quad (20)$$

The practical significance of eq 20 insofar as the ultracentrifuge is concerned is that the height of the liquid column in the cell varies with the rotor speed, and this effect if observed may be misinterpreted as additional liquid compression. A separate analysis of this latter effect together with an appropriate discussion of the effects and magnitudes to be expected from this source are included in an Appendix to this paper. However, assuming that a liquid in the cell under investigation is incompressible we can determine the change in liquid column height in terms of the known parameters using eq 20. Doing this we find that in the deformed cell the liquid column height h' is given by

$$h' = h(1 - q) \quad (21)$$

where

$$q = \frac{\rho\omega^2}{2E}\sigma[2a(2R - a) - 2R(z_b + z_m) + z_b^2 + z_m^2] \quad (22)$$

and in which z_b and z_m are the locations of the liquid base and meniscus, respectively. From eq 22 we note that q can be positive, negative, or zero, and that the sign depends only on the rotor and cell coordinates, and is independent of materials and rotor speed. Thus it should be possible (theoretically) to design a centrifuge system partially to eliminate this effect.

We also see from eq 22 that the fractional change in liquid column height q is itself a function of the column height $h = (z_m - z_b)$ and of its location z_b in the cell. Rewriting eq 22 in terms of these latter two observable parameters we obtain

$$q = \frac{\rho\omega^2}{2E}\sigma[2a(2R - a) - 2R(2z_b + h) + z_b^2 + (z_b + h)^2] \quad (23)$$

Application of Theory and Discussion

Having derived equations relevant to a cell in an ultracentrifuge it is important to determine an estimate of the order of magnitude of the aforementioned effects. To this end, data relevant to the Beckman Model "E" instruments were inserted into the equations, under the assumption that the cell was constructed of duralumin, but the results may be applied readily to centerpieces constructed from other materials. The data used are as follows, assuming the symmetrical cavity of Figure 2: $R = 7.5$ cm; $a = 2.2$ cm; $z_1 = 0.6$ cm; $z_2 = 1.6$ cm; $x_1 = 0.25$; $y_1 = 1.2$ cm. From Kaye and Laby[17] for duralumin: $\rho = 2.8$ g/ml; $\sigma = 0.33$; $E = 7.3 \times 10^{11}$ dyn cm^{-2}; and the rotor speed varies in the range zero–75,000 rpm. The above data are applicable to a typical cell used for long column experiments.

Since z_b is fixed by the above data to about 0.6 cm (*i.e.*, $r_b \cong 6.9$ cm from axis of rotation), it was of interest to use eq 23 to find the column height for which q, the fractional change in column height, was zero. The resulting calculation gave column heights $h = 4.0$ cm and 9.8 cm which are physically impossible with the cells used. For a typical cell $0 \leq h \leq 1.0$ cm and therefore a change in liquid column height should be present in practice. Furthermore, by differentiating eq 23 with respect to h and inserting values of h in the range $0 \leq h \leq 1.0$ cm, we find that dq/dh is always negative, indicating that the shorter the column the greater the effect. The latter result is important owing to recent emphasis on high-speed, short-column methods,[1] and contrasts with the effect associated with finite liquid compressibilities (see Appendix). Again from eq 23 for h in our experimental range, we find that q is always positive, and hence from eq 21 we see that liquid column heights should always contract owing to cell distortion under the applied experimental conditions. Figures 4 and 5 show graphically the percentage contraction for liquid column heights in the range of interest for the duralumin cell model under consideration. Data are plotted over the typical rotor speed range 0–75,000 rpm of the Beckman Model "E"

(17) G. W. C. Kaye and T. H. Laby, "Tables of Physical and Chemical Constants," 11th ed, Longmans, Green and Co., London, New York, and Toronto, 1957.

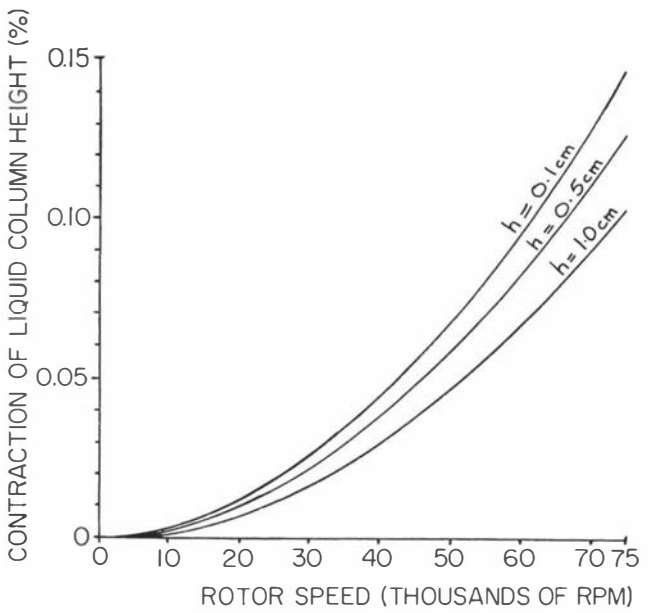

Figure 4. Graph showing the percentage contraction of liquid height with rotor speed for three different column heights in the duralumin model.

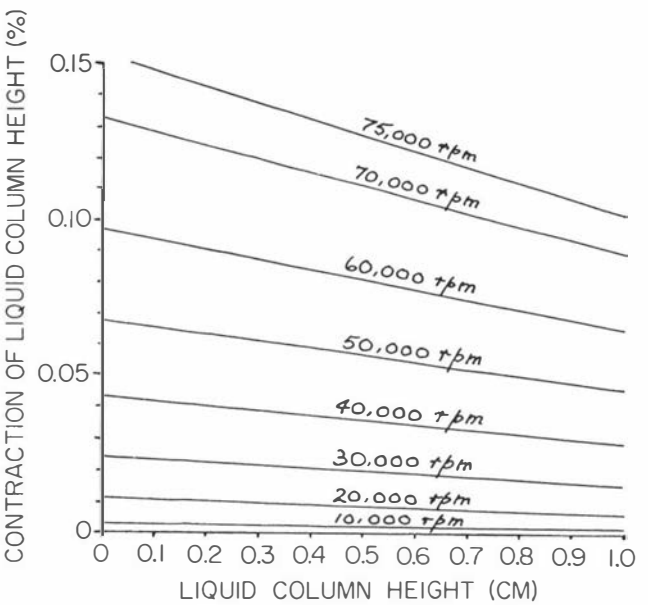

Figure 5. Graph showing the percentage contraction of liquid column height with liquid column height at constant rotor speeds for the duralumin model.

instrument. From graphs we note that at 70,000 rpm for a short-column experiment of 3 mm the percentage contraction is in the region of 0.12%. This gives an actual change in column height of about 0.0004 cm. Since the interference–schlieren optical system of the ultracentrifuge magnifies the radial dimensions by about 2 times this would result in a change of about 0.001 cm on the photographic plate. This should be observable since the microcomparators employed in plate analysis for interference work have a least count of 0.0001 cm. In practice cell distortion is coupled with window distortion, since the above stress analysis could apply equally to isotropic cell windows, and such a simple extrapolation is not really relevant at these speeds owing to uncertainties associated with locating the exact positions of the meniscus and base on the photographic plates. However, with the introduction of laser sources[18,19] coupled with improved window holder design[20] the menisci will be more clearly defined and it should be possible to measure the above effect in practice and make any necessary corrections when precise work (particularly interference) is being undertaken. Obviously for cells with an improved density to strength ratio (ρ/E) this effect will be diminished as expected, and this is indicated in the theoretical equations.

For an interference cell model in which there are two cavities symmetrically located about the z axis we find the results for each cavity similar to those for the single cavity described above.

A cell that is becoming increasingly popular in experimental work and to which cell distortion could be of major importance is the high-speed Yphantis-type cell—of which a recently improved side-access version has been described by Ansevin, Roark, and Yphantis.[20] This latter cell is specifically designed for rotor speeds in excess of 40,000 rpm. Now this cell is fabricated to improve among other things its density to strength ratio, and to consider a duralumin version as an example of the effects of cell distortion is unduly pessimistic. However the results obtained by the analysis of a duralumin cell will emphasize the effects cell distortion could have in such a cell, and indicate relevant correction procedures should these be found necessary. A diagram of a three channel Yphantis cell applicable to our model is shown in Figure 6. Cell distortion could be of primary importance in a cell of this type owing to its discriminatory effects among the channels. This is in contrast to rotor stretch which affects all channels equally. Fundamentally, the cell distortion effects are twofold: (a) the displacement of the cell base position (u_{z_b}) will be different for each channel, and (b) the variation in liquid column height (q) for similar levels (h) in the channels will be different.

An estimate of the effect of cell base position displacement can be found from eq 14 where z is replaced by the appropriate z_b and the other parameters have the same numerical values as defined previously However, the last term in the brackets indicating the effect of the cell position in the xy plane is small and hence eq 14 may be rewritten as

$$u_{z_b} = -\frac{\rho\omega^2}{2E}\left[Rz_b(2a - z_b) - z_b\left(a^2 - \frac{z_b}{3}\right)^2\right] \quad (24)$$

(18) Beckman Instruments Inc., "Future Product Information, 1969".

(19) J. A. Lewis and J. W. Lyttleton, unpublished work.

(20) A. T. Ansevin, D. E. Roark, and D. A. Yphantis, *Anal. Biochem.*, 34, 237 (1970).

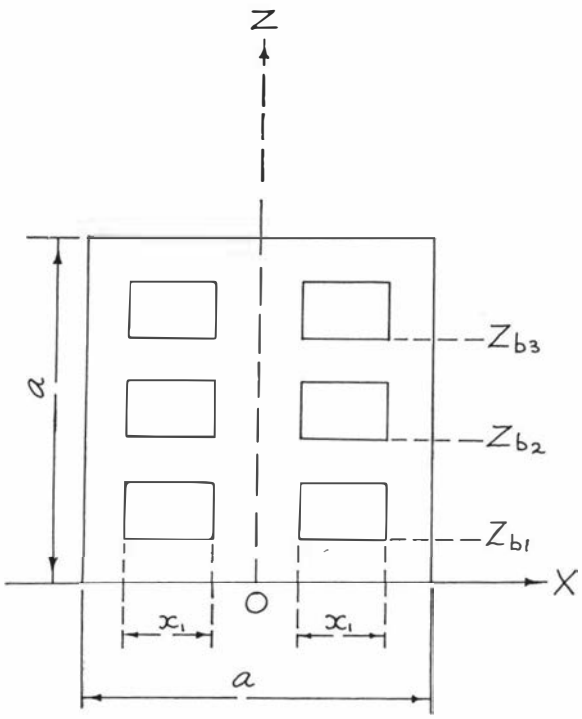

Figure 6. Diagram of the three channel Yphantis-type cell centerpiece applicable to our model.

Note the negative sign indicates that the displacement is in the negative z direction, *i.e.*, in the radial direction of the rotor as expected. We see that the displacement is proportional to (i) the square of the rotor speed, (ii) the density to strength ratio of the cell material, and (iii) the location of the base in the cell centerpiece (assuming that the cell centerpiece dimensions and positions within the rotor are fixed). The base positions selected for our model Yphantis cell were $z_{b1} = 0.4$ cm, $z_{b2} = 0.9$ cm, and $z_{b3} = 1.4$ cm, where the subscripts 1, 2, and 3 indicate the three channels numbered from bottom to top of the cell. The cell base displacement (u_{zb}) is plotted against rotor speed in Figure 7 for the position of the three channels above as well as for the top of the centerpiece $z_b = 2.2$ cm and for $z_b = 0.6$ cm, the latter being typical for the cells used for long-column experiments and schlieren work. Figure 8 depicts the variation in base displacement (u_{zb}) as a function of the position within the centerpiece, while rotor speed is maintained constant. It should be appreciated that the origin relative to the axis of rotation of the rotor will itself vary with rotor speed owing to rotor stretch and moreover the displacement at the top of the centerpiece gives rise to a widening of the gap between the rotor and cell already present owing to rotor stretch. By extrapolation one can determine the relative base displacements for any base position with respect to a reference position (channel) since these depend on their relative positions. Thus at 70,000 rpm we note that the base position in channel 2 has a radial displacement of about 2 times that of channel 1, whereas the

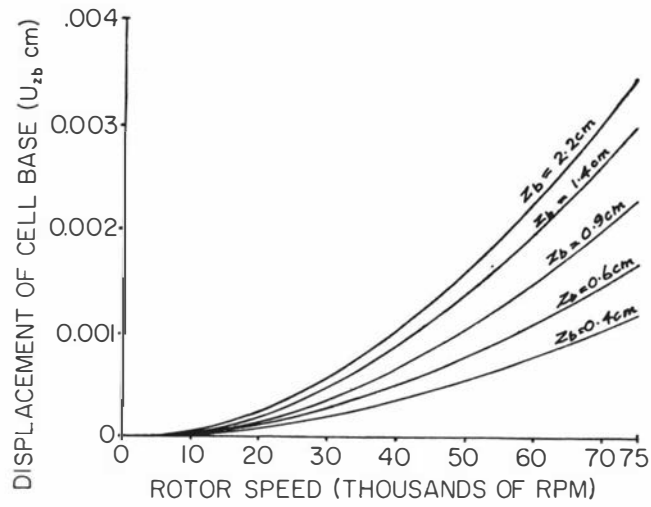

Figure 7. Graph showing cell base displacement *vs.* rotor speed for various initially fixed positions of the cell base within the duralumin model.

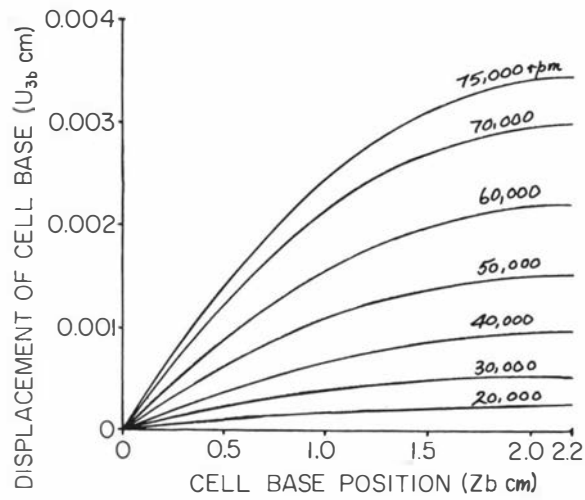

Figure 8. Graph showing the variation of cell base displacement *vs.* cell base position at constant rotor speeds for duralumin model.

base position in channel 3 has a radial displacement of just over 2.5 times that of channel 1. Naturally as noted previously from eq 24 the order of magnitude depends on ω^2 and ρ/E, but for our duralumin model the radial displacement of channel 1 at 70,000 rpm is about 0.001 cm which would be measurable in such a cell. However the radial displacement of a single channel base position is masked by rotor stretch in practice owing to the practical origin of coordinates being the axis of rotation and not the centerpiece base. In contrast, the relative displacements indicative of cell distortion are not masked and experimental evidence of this as regards the inner and outer reference positions of a cell counterbalance is intimated by Baghurst and Stanley.[12]

The channel discrimation exhibited by change in liquid column heights is depicted in Figure 9. Here the percentage decrease in liquid column height for a fixed

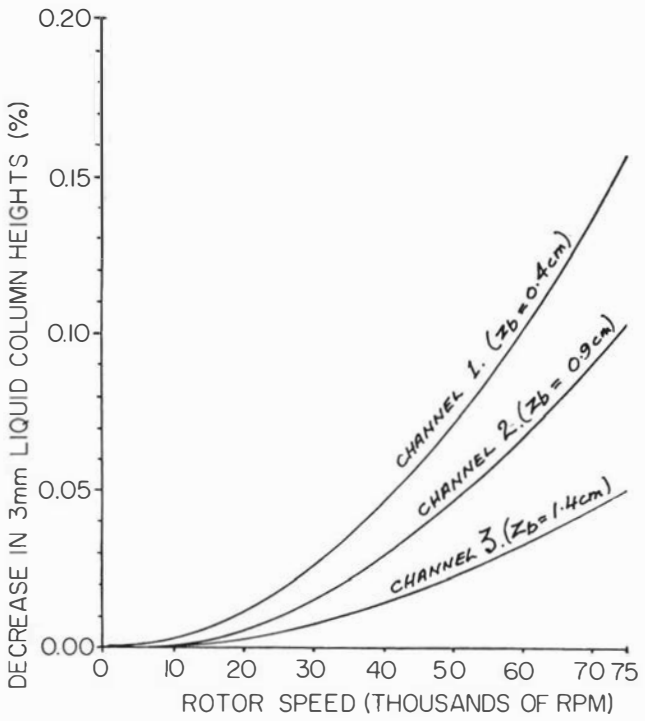

Figure 9. Graph showing the percentage contraction of 3-mm liquid column heights in the channels of the Yphantis type model of Figure 6 *vs.* rotor speed.

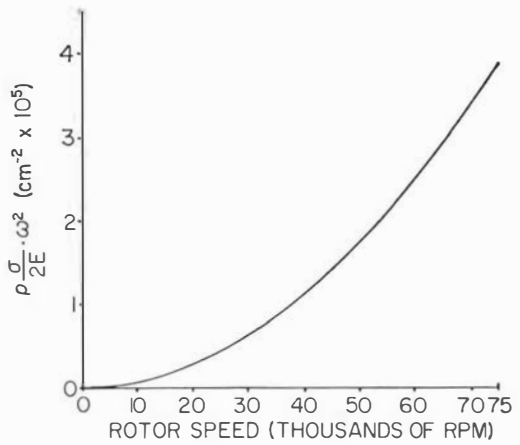

Figure 10. Graph of $(\rho\sigma/2E)\omega^2$ *vs.* rotor speed for a duralumin cell model.

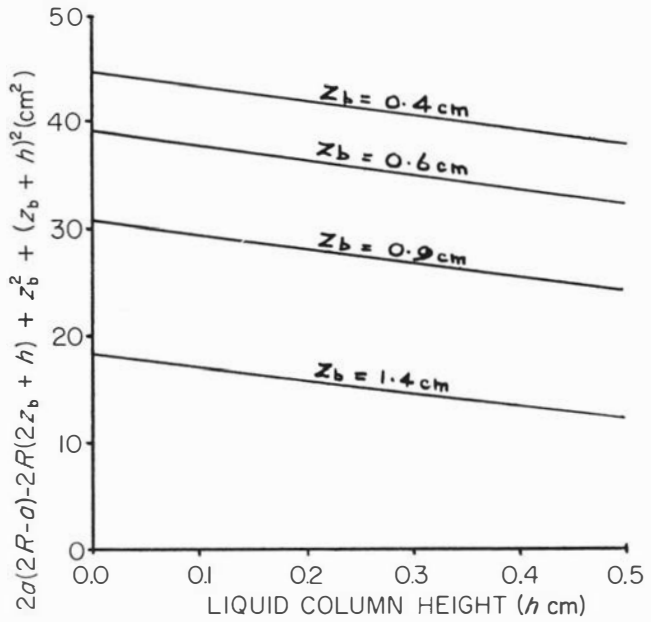

Figure 11. Graph of $2a(2R - a) - 2R(2z_b + h) + z_b^2 + (z_b + h)^2$ *vs.* liquid column height (h) for various base positions within a model cell centerpiece.

initial column height of $h = 0.3$ cm in each channel is plotted against rotor speed (rpm). The data for this graph were obtained from eq 23. From eq 23 we make a general observation that the magnitude of the fractional decrease in liquid column height (q) is the product of two distinct functions, this observation applying equally to the radial displacement u_z in eq 15. Firstly as expected it depends on the centrifugal field and the cell material $[(\rho\omega^2\sigma)/(2E)]$, and secondly on relevant cell dimensions and positions $[2a(2R - a) - 2R(2z_b + h) + z_b^2 + (z_b + h)^2]$. If the first is plotted against rotor speed and the second is plotted against liquid column height (h) over the range of interest for various relevant positions (z_b) in a centerpiece, it is possible by normal extrapolation procedures to determine the effective value of "q" for any rotor speed, column height, and base position of interest, and in theory for a practical case such plots could form the basis for experimental correction procedures. The plots applicable to our model duralumin cell are shown in Figures 10 and 11 for illustration—from which Figure 9 could be derived. Obviously, a similar procedure could be used to evaluate the radial displacement—u_z from eq 15. Finally, it is appropriate to mention the experimental work of Schachman[21] and Cheng and Schachman,[22] who investigated the compressibility of liquids from ultracentrifuge measurements. This is because the observable decrease in liquid column heights arising from finite liquid compressions, that is discussed in the Appendix to this paper, could be exaggerated by cell centerpiece deformation if precautions are not taken. Furthermore, as indicated by Schachman[21] the experimental conditions are complicated by window bulging and distortion owing to liquid pressure effects. In practice the effects of cell distortion as regards decrease in liquid column height with increase of the rotor speed are accentuated by the above effects. However, our model indicates that the effects of cell distortion may be evaluated devoid of the complications of window bulging and finite liquid compressibility. This is acheived experimentally by using a Yphantis-

(21) H. K. Schachman, "Ultracentrifugation in Biochemistry," Academic Press, New York, N. Y., and London, 1959, pp 32, 177–180.

(22) P. Y. Cheng and H. K. Schachman, *J. Amer. Chem. Soc.*, **77**, 1498 (1955).

type cell centerpiece and making simultaneous measurements of liquid column height contraction, together with relative base position displacements, the latter being independent of the aforementioned complications.

Conclusion

We have introduced a model of a cell in an analytical ultracentrifuge and have formulated mathematical expressions specific for the effects of cell centerpiece deformation under the centrifugal body forces. Data relevant to standard cells used with the Beckman Model "E" instrument have been evaluated and have indicated effects to be of an order of magnitude relevant for correction in present day high-precision methods. The orders of magnitude established are similar to those intimated by experimentally derived raw data results of Baghurst and Stanley[12] applicable to the inner and outer reference holes in a counterbalance cell. However, these authors stressed that an analysis of covariance failed to confirm the effect at the 5% probability level, but a suggestion of cell compression was made. The model has highlighted the specific effects of cell distortion, as distinct from rotor stretch, and has indicated correction procedures that could be relevant for high-precision sedimentation equilibrium Rayleigh interference work. The analysis of experimental data for the latter sometimes assumes the conservation of mass to evaluate a constant of integration, when use is made of the initial concentration of solute in the cell. The variation in liquid column height owing to cell distortion and finite liquid compressibility could influence the result of this calculation if precautions are not taken. Furthermore the radial displacement of the base region owing to cell distortion should be considered along with the corrections for rotor stretch. For the less precise schlieren work the effects will be relatively minor, although theoretically they would exaggerate effects of radial dilution. In particular the model has warned of possible complications associated with the use of Yphantis-type cells and has indicated appropriate correction procedures for precise work.

Finally, it must be emphasized that the theory is based on a model, and that the exact results evaluated are really only applicable to this model. However the model does approximate the experimental conditions experienced; the results it predicts are intuitively correct, and these are of the orders of magnitude expected from experimental evidence to date. Therefore we feel within the limitations imposed that the model is useful and applicable to the task in hand.

Appendix

A Mathematical Formulation of Liquid Column Height Compression Owing to Finite Liquid Compressibility in the Analytical Ultracentrifuge. At the higher rotor speeds (about 60,000 rpm) a large pressure difference exists between the air–liquid meniscus (where the pressure is 1 atm) and the bottom of a centrifuge cell. Svedberg and Pedersen,[23] Fujita,[24] and Schachman[21] have discussed the effects of this pressure variation and give appropriate references to both experimental and theoretical work undertaken in this area. However, the analysis above has indicated that one of the observable effects of cell deformation in these large centrifugal fields is an effective compression of the liquid column, and hence in the context of this paper it is appropriate to determine the relative contributions that these two independent sources make to the experimentally observable compression.

Using the notation of Fujita[24] the pressure distribution in a sector-shaped centrifuge cell may be determined from

$$\frac{\partial p}{\partial r} = \rho\omega r^2 \tag{A1}$$

where ρ = density of the solution at the radical position r, ω is the rotors' angular velocity, and p is the pressure.

For dilute solutions ρ may be replaced by the density of the solvent ρ_0 at the same point. Denoting the compressibility by β we obtain

$$\rho_0 = \frac{\rho_0^0}{1 - \beta p} \cong \rho_0^0(1 + \beta p) \tag{A2}$$

i.e.

$$\rho_0 = \rho_0^0 + \lambda p \tag{A3}$$

where $\lambda = \rho_0^0\beta$ with ρ_0^0 being the value of ρ_0 at $p = 0$, and this approximates the value at the meniscus (r_m).

Whence by substitution and integration the solvent density is given by

$$\rho_0(r) = \rho_0^0 \exp[{}^1/_2\beta\rho_0^0\omega^2(r^2 - r_m^2)] \tag{A4}$$

Defining

$$x = \left(\frac{r}{r_m}\right)^2 \tag{A5}$$

and

$$\nu = ({}^1/_2)\beta\rho_0^0\omega^2 r_m^2 \tag{A6}$$

We get

$$\rho_0(x) = \rho_0^0 \exp[\nu(x - 1)] \tag{A7}$$

The fractional decrease in liquid column height (q) is defined by

$$h' = h(1 - q) \tag{A8}$$

where h' is the liquid column height at rotor frequency ω and h its value when $\omega = 0$. It is easy to show that

(23) T. Svedberg and K. O. Pedersen, "The Ultracentrifuge," Clarendon Press, Oxford, 1940, pp 37, 267, 447.

(24) H. Fujita, "Mathematical Theory of Sedimentation Analysis," Academic Press, New York, N. Y., and London, 1962, pp 130–139.

$$\frac{\bar{\rho}_0(x)}{\rho_0^0} = \frac{1}{1 - q}\left(1 - \frac{hq}{2r_b}\right) \tag{A9}$$

where r_b is the radial position of the liquid column base and $\bar{\rho}(x)$ is the average density of the liquid at angular frequency ω.

In practice $hq/2r_b \ll 1$ and hence from eq A9 the fractional liquid column height compression (q) is given by

$$q = \frac{\bar{\rho}_0(x)}{\rho_0^0} - 1 \tag{A10}$$

Defining a function f(x) by

$$f(x) = \frac{\rho_0(x)}{\rho_0^0} - 1 \tag{A11}$$

we see from eq A10 that the mean value of f(x) is q. Substituting $\rho_0(x)$ from eq A7 into eq A11 we obtain

$$f(x) = \exp[\nu(x - 1)] - 1 \tag{A12}$$

and since in practice $\nu(x - 1) \ll 1$ eq A12 becomes to a close approximation

$$f(x) = \nu(x - 1) \tag{A13}$$

Thus the required fractional liquid column height compression is given by

$$q = \nu(\bar{x} - 1) \tag{A14}$$

where $\bar{x}$ is the mean value of x for the centrifuge cell. Writing x_b as the value for x at the cell base we find that

$$q = \frac{\nu}{2}(x_b - 1) \tag{A15}$$

By the reinsertion of previously defined terms we can rewrite eq A15 as

$$q = \frac{\rho_0^0\omega^2\beta}{4}[h(2r_b - h)] \tag{A16}$$

Differentiating eq A16 with respect to h we note that (dq/dh) is positive for all values of h used experimentally, and hence the larger the column (h) the greater q, this latter effect contrasting with the effective compression produced by cell centerpiece deformation. Figure 12 shows the variation in q and h at constant rotor speeds, calculated from eq 16 with: $r_b = 7.1$ cm; $\rho_0^0 = 0.998$ g cm^{-3}; and $\beta = 40 \times 10^{-6}$ atm^{-1}. These data are applicable to water at 20° in a typical ultracentrifuge cell. By comparison of Figures 12 and 5 the relative effects of cell distortion and finite compressibility may be estimated.

As with cell distortion it is of interest to determine the discrimatory effects of finite liquid compressibility among the channels of a high speed Yphantis-type centrifuge cell.

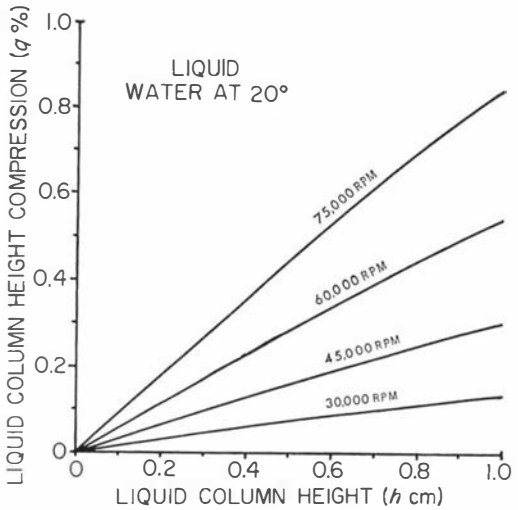

Figure 12. The variation in liquid column height compression (q) *vs.* liquid column height (h) in a centrifuge cell at constant rotor speeds, owing to finite liquid compressibility.

The percentage compression (q) of a fixed water column height of 0.3 cm at 20° in each of the three channels was determined using the following pertinent data: $\omega^2 = 4 \times 10^7$ (rad sec^{-1})^2; $r_{b1} = 7.1$ cm; $r_{b2} = 6.6$ cm; and $r_{b3} = 6.1$ cm.

The numerical subscript indicates the channel numbered from bottom to top of the cell. The calculations gave: $q_1 = 0.35\%$; $q_2 = 0.32\%$; and $q_3 = 0.30\%$. These imply that the overall radial movement of the menisci for the above conditions as recorded photographically in the ultracentrifuge would be in the region of 0.002 cm, account being taken of the $\times 2$ magnification of the radial cell coordinates by the interference–schlieren optical system of the ultracentrifuge. The variations among the channels is shown to be small, but they do lie within the precision of the instrument. Naturally, should the liquid employed have a larger compressibility and/or density then the observable effect from this source will be increased accordingly, as indicated by eq A16. Again, as for cell deformation, it is anticipated that appropriate precautions for the aforementioned physical effects should be made in accurate sedimentation equilibrium studies employing Rayleigh interference optics.

Acknowledgments. This work was supported in part by a grant (code reference 68337) from the University Grants Committee of New Zealand. In addition we thank Dr. J. W. Lyttleton of the Applied Biochemistry Division, Department of Scientific and Industrial Research, Palmerston North, for his helpful advice and assistance. Furthermore, the encouragement given by Professor G. N. Malcolm of the Chemistry and Biochemistry Department, and that of the members of the Physics and Engineering Department, Massey University is acknowledged.